Toward Molecular Quantum-Dot Cellular Automata:

A Scanning Tunnelling Microscopy Investigation

A thesis presented to the University of Dublin, Trinity College

for the degree of

Doctor of Philosophy in Chemistry

by

Samuel Peter Torsney

Under the supervision of Prof. John J. Boland

School of Chemistry & CRANN

Trinity College Dublin

2018

Declaration

I declare that this thesis has not been submitted as an exercise for a degree at this or any other university and it is entirely my own work.

I agree to deposit this thesis in the University's open access institutional repository or allow the library to do so on my behalf, subject to Irish Copyright Legislation and Trinity College Library conditions of use and acknowledgement.

.....

Samuel Peter Torsney B.A. (Mod.)

The struggle itself towards the heights is enough to fill a man's heart.

ALBERT CAMUS

Summary

Quantum-dot cellular automata (QCA) is one of the computational schemes being developed to take computing past the limits of Moore's law. QCA devices are based on a bistable arrangement of two mobile charges in a square cell, and can be constructed from assemblies of molecules, nanomagnets or metal dots. Molecules are well-suited for QCA applications, and would allow fast switching speeds, exceptional device densities and ultra-low dissipation. However, switching in a molecular-scale QCA system has yet to be demonstrated and many obstacles remain in the path to this goal. Scanning tunnelling microscopy (STM) provides atomic scale information about the structure and electronic properties of conductive surfaces, and can be used to modify both, therefore representing a powerful tool for investigating this kind of system. In the present thesis fundamental challenges associated with demonstrating molecular QCA (MQCA) action with STM are addressed.

Many of the hurdles associated with this are not specific to QCA, but apply to the wider field of molecular surface science. These include issues relating to the deposition of complex molecules in ultra-high vacuum (UHV), controlling the superstructure of self-assembled networks, and the use of engineered substrates with complex molecules and deposition techniques. Meeting these challenges constitutes the main focus of this work.

We have investigated the adsorption behaviour two ferrocene-decorated porphyrins on a range of different substrates. In particular, we have shown how the molecule-substrate interactions must be taken into account when designing supramolecular architectures. The preference for specific adsorption sites, the minimisation of surface energies, and the competing intermolecular interactions all make up a delicate balance which determines the final molecular superstructure.

The challenge of depositing complex molecules on engineered surfaces in UHV is addressed in detail here. Insulator-on-metal systems are necessary to prevent strong perturbation of the electronic structure of a molecule upon adsorption,

while meeting the conductivity requirements associated with STM experiments. We use electrospray deposition (ESD) to deposit molecules various substrates, and show that the electrospray process can alter surface morphologies. Physisiorbed ionic films are shown to be incompatible with ESD, while chemisorbed insulating layers are viable. We have not been successful in sufficiently decoupling molecular states to facilitate charge injection, however we suggest that other substrate systems available in the literature would make such experiments possible.

We have also used ESD to prepare chlorinated copper surfaces *via* reactive landing of chloroform. We have provided new insights into the behaviour of this surface in the coverage regime corresponding to uniaxial compression of the Cl adlayer. A new electronic state has been reported, and assigned as an antibonding interaction between chlorine and copper states. The energy of this interaction was found to depend on the adsorption site, being higher for hexagonal close packed (hcp) sites than for face-centred cubic (fcc) sites. Additionally, we found that the energy of this electronic state was dependent on the size of the domain and upon the distance from the domain edge. This surface did not, however, facilitate decoupling of molecular states.

The electronic properties of both types of ferrocenyl-porphyrins were found to depend on their conformation when adsorbed on metallic substrates. We found that the trench structures on $Cu_2N{-}Cu(100)$ could be used to template the self-assembly of both molecules. The templated wires formed by one of the molecules exhibited interesting electronic structure, which we postulate may be due to intermolecular mixing of molecular orbitals.

Acknowledgements

There's no doubt in my mind that I owe a huge debt of gratitude to everyone who helped me see this thing through. I'd like to take this opportunity to thank some of these people now.

First of all I'd like to thank Professor John Boland, my PhD supervisor, not only for giving me the opportunity to undertake this research, but for his support, encouragement and guidance throughout. John has been a great boss, and it has been a pleasure to work in his group over the last four-and-a-half years.

I'd like to thank Dr. Borislav Naydenov, who taught me pretty much everything I know about surface science. His patience, particularly when I was just getting to grips with STM and UHV equipment, has been incredible, and its been great to have him always there to bounce ideas off. There is no way I could have done it without him. I'd like to thank the rest of the Boland group, members past and present, for all their help over the years and for making it a great place to work. In this regard I'm particularly grateful to Hugh, Xiaopu, Prabhava, Shaun, Peter, Catherine, Felim and Jing. Mary's help with all the admistrative stuff was invaluable in making day-to-day life as smooth and easy as possible.

I'd like to thank all of our collaborators in MolArNet for their work and the EU for providing funding under the FP7 scheme.

I'd also like to thank everyone in the office, in the breakout room and in CRANN in general for all the crack that was had. Special mention here to the PCAM heads and honorary PCAM heads who've made my time in Trinity so memorable. Outside of CRANN, thanks to the lads, who've always been there for a pint when I needed one.

Finally, I'd like to express my gratitude to my family. To my parents, Phil and Tim, for their infinite love and support, for putting up with me, and for everything else, thank you. To Susie, Emily and Robbie, who have always been there for me, to my auntie Imelda and to the rest of the clan, thank you so much for everything.

Contents

List of Figures

List of Acronyms

AFM atomic force microscopy

CA cellular automata

CMOS complementary metal–oxide–semiconductor

CNL charge neutrality level

CPD contact potential difference

CRM charged residue model

CV cyclic voltammetry

CVD chemical vapour deposition

D−B−A donor-bridge-acceptor

DBTJ double-barrier tunnel junction

DFT density functional theory

DOS density of states

ELF electron localisation function

ESD electrospray deposition

ESI electrospray ionisation

fcc face-centred cubic

FET field-effect transistor

FIM field ion microscope

hcp hexagonal close packed

HOMO highest occupied molecular orbital

HOPG highly-ordered pyrolytic graphite

IDIS induced density of interface states

IDOS integrated density of states

IETS inelastic tunnelling spectroscopy

IUPAC International Union of Pure and Applied Chemistry

IVCT intervalence charge transfer

LDOS local density of states

LEED low-energy electron diffraction

LMCT ligand-metal charge-transfer

LUMO lowest unoccupied molecular orbital

MBE molecular beam epitaxy

MLCT metal-ligand charge-transfer

MO molecular orbital

MQCA molecular QCA

MS mass spectroscopy

MV mixed-valence

N-IR near-infrared

NIR negative ion resonance

OMBE organic molecular beam epitaxy

OMO occupied molecular orbital

PDOS projected density of states

PI proportional–integral

PIR positive ion resonance

p-MS preparatory mass spectrometry

QCA quantum-dot cellular automata

QD quantum dot

QMS quadrupole mass spectrometer

RAHB resonance-assisted hydrogen bonding

SAM self-assembled monolayer

SCE saturated calomel electrode

SEXAFS surface-extended X-ray absorption fine structure

STM scanning tunnelling microscopy

STS scanning tunnelling spectroscopy

TIL thin insulating layer

TOF time-of-flight

UHV ultra-high vacuum

WKB Wentzel-Kramers-Brillouin

List of Molecules

Br_2I_2TPP 5,15-di(4-bromophenyl)-10,20-di(4-iodophenyl)porphyrin

Br_2TPP 5,15-di(bromophenyl)-10,20-diphenylporphyrin

Br_4TPP 5,10,15,20-tetra(4-bromophenyl)porphyrin

$CoBr_4TPP$ cobalt 5,10,15,20-tetra(4-bromophenyl)porphyrin

CoTCPP cobalt 5,10,15,20-tetra(4-carboxyphenyl)porphyrin

CoTPP cobalt 5,10,15,20-tetraphenylporphyrin

Cp cyclopentadiene

DNA deoxyribonucleic acid

Fc ferrocenyl

Fc_2Ph_2P 5,15-diferrocenyl-10,20-diphenylporphyrin

H_2TCPP 5,10,15,20-tetra(4-carboxyphenyl)porphyrin

H_2TPP 5,10,15,20-tetraphenylporphyrin

ZnTFcBP zinc 5,10,15,20-tetra[*N*-(1-ferrocenylethyl)benzamide]porphyrin

H_2TFcBP 5,10,15,20-tetra[*N*-(1-ferrocenylethyl)benzamide]porphyrin

$Fc_2(BrPh)_2P$ 5,15-diferrocenyl-10,20-bis(4-bromophenyl)porphyrin

$NiBr_4TPP$ nickel 5,10,15,20-tetra(4-bromophenyl)porphyrin

PDMS polydimethylsiloxane

PEEK polyetheretherketone

PTCDA 3,4,9,10-perylene-tetracarboxylicdianhydride

PTFE polytetrafluoroethylene

TCPP 5,10,15,20-tetra-(4-carboxylphenyl)porphyrin

TFcP 5,10,15,20-tetraferrocenylporphyrin

THF tetrahydrofuran

TPP 5,10,15,20-tetraphenylporphyrin

ZnTCPP zinc 5,10,15,20-tetra(4-carboxyphenyl)porphyrin

ZnTPP zinc 5,10,15,20-tetraphenylporphyrin

Introduction

The use of molecules as device components is one research avenue being pursued to get around the myriad problems associated with continued miniaturisation of conventional semiconductor transistors, which include those related to increasing leakage currents, increasing resistance of the interconnects, and achieving the required resolution with lithography. Within the field of molecular electronics there are two broad strands of research: one trying to implement the familiar device functions with molecular components, and another trying to find completely new ways to perform computations at the molecular scale. Quantum-dot cellular automata (QCA) is an example of the latter, where binary information is represented by the dipole or quadruple orientation of a cell.[1] In this computational paradigm, information is transmitted *via* field interactions between patterned arrays of these cells, rather than by charge transport.[2] Molecular-scale QCA promises high device densities and ultra-low power dissipation, however, while proof-of-concept has been achieved using metal dots, a molecular implementation has yet to be demonstrated.[3]

The goal of this thesis is to make progress towards a demonstration of molecular QCA (MQCA) action with the scanning tunnelling microscopy (STM). The STM is one of the most powerful tools available to surface science.[4] It allows electronic information to be extracted from conductive surfaces in real space. The STM has long been used to study adsorbed molecules,[5] and in recent years has been used to inject charge into molecular systems.[6] This makes STM the perfect tool for MQCA investigations.

However, significant challenges must be overcome in order to achieve this goal. First, suitable molecules must be designed, deposited, and assembled in a useful architecture on a STM-compatible substrate. The molecular orbitals must not couple strongly to the substrate states in order to be able to access the excited states of the molecule. Once this has been accomplished, the challenge remains to inject charge into the molecular cells, and to read out and manipulate the charge configurations in these cells. In this work we tackle these issues, and make some

progress towards the final goal.

The work presented in this thesis has been carried out within the MolArNet consortium, involving six experimental and computational research groups from around Europe. The candidate molecules were synthesised and characterised electrochemically at the University of Bologna, environmental STM was carried out at the Université de Strasbourg, and density functional theory (DFT) calculations were performed at TU Dresden.

This thesis is organised as follows. We introduce the field of molecular electronics in chapter 1, with a particular emphasis on the QCA paradigm. The mixed-valence compounds are introduced, which find applications in all areas of molecular electronics and are key to the implementation of QCA at the molecular scale. We also discuss how we expect the properties of molecules to be perturbed upon adsorption on a surface.

In chapter 2, we explore the theoretical underpinning of STM and scanning tunnelling spectroscopy (STS), the principle techniques used in this work. We outline the origin of the various tunnelling phenomena which arise when molecules are within the tip-sample junction. The operational principles of STM are discussed, along with the experimental details of the equipment used to carry out the measurements presented in this work. The problems associated with depositing complex molecules for STM analysis are outlined in chapter 3, and the electrospray deposition (ESD) technique is introduced. ESD allows almost any type of molecule to be deposited, and we discuss the mechanism behind the process and describe the instrumentation used.

The first of our QCA candidate molecules is described in chapter 4. We compare the adsorption and self-assembly of this ferrocene-functionalised porphyrin on Au(111) and Cu(111), and we find that where the molecule-molecule interaction dominates we observe the square architectures desired for MQCA applications. We examine the electronic properties of these arrays and find good agreement with theoretical predictions made by our collaborations.

We then attempt to assemble these molecular arrays on substrates with insulating spacer layers, and in chapter 5 we outline the difficulties associated with this. We find that physisorbed spacer layers can be modified upon exposure to ESD and suggest that chemisorbed insulating layers should be used when depositing molecules *via* electrospray. We investigate chlorinated copper surfaces for use as spacer layers in chapter 6. We report interesting new electronic effects on the chlorinated copper, but find that it is not useful for decoupling molecular states.

Finally, in chapter 7 we explore the possibility of using surface reactions to assemble covalently-bound QCA devices. We report on the self-assembly and electronic properties of the ferrocene-functionalised porphyrin precursor on both metallic and insulating substrates. The coupling reaction was unsuccessful, however we suggest simple refinements which we believe will facilitate bottom-up assembly of molecular-scale devices.

1

Molecular Electronics

It is now more than fifty years since Gordon Moore made his famous prediction that the number of transistors in an integrated circuit would double approximately every two years.[7] The fundamental limit of this trend lies in atomic scale devices, however significant challenges to continued transistor miniaturisation are encountered even well above this point. In recent years device density has begun to level off, with computational power gains being made up from other sources, such as increasing the mobility in the channel *via* strain engineering. Currently, the most pressing challenge is related to the power dissipation caused by leakage currents which increase as the channel length is reduced. In addition, Moore's lesser-known second law, which states that the cost of building a fabrication facility also increases exponentially over time, may prove more restrictive than any physical or technological issue.

Significant research effort continues to be expended on the search for ways to maintain the computational power gains associated with Moore's first law. One such approach is to fabricate electronic components from the bottom up using molecular building blocks, which constitutes the field of molecular electronics. It is important to note here that performing some useful function with a molecule is not sufficient to classify it as a molecular electronic device. There must be some interface with the macroscopic world, and some way to exchange information with other functional molecules. It must also be possible to cascade arbitrary numbers of these functional molecules in architectures which allow the elementary Boolean operations to be implemented, which in turn requires power gain to prevent the signal decaying over the concatenated network.

The possibility of using individual molecules to perform computing functions

was first proposed by Aviram and Ratner in 1974, who described a molecular rectifier, and provided what seemed to be evidence for its operation.[8] Although it was later found to be an artefact of the experiment, this paper served as the impetus for explosive growth in the field, culminating in 1997 when a functional molecular rectifier was finally demonstrated.[9]

The simplest circuit element is a wire. Multiple molecular wires have been demonstrated,[10] including conjugated hydrocarbons,[11,12] nucleic acid strands,[13,14] carbon nanotubes,[15,16] and porphyrin oligomers.[17,18] In general, molecular wires tend to be highly conjugated, so that the delocalised π-system provides a pathway for electron transport.

A molecular switch can be thought of as a molecule with some measurable property which can be modulated between two states by applying some external stimulus. The bistable property can be structural, electronic, optical or magnetic, among others, while common stimuli include changes in temperature or pH,[19] the introduction (or removal) of some chemical species, gating by some external field or the adsorption of light. Demonstrating a reliable bistable molecule is the first step towards developing a molecular computing machine, since computational logic is essentially based on cascades of switches.[20]

Around the same time as the Aviram and Ratner proposal for electronic devices implemented by molecules, the first mixed-valence compounds were designed.[21,22] A mixed-valence molecule is generally considered to be one where a redox centre, typically a coordinating metal atom, appears more than once with the sites in two (or more) different oxidation states.[23] The redox sites are connected by some bridging structure which allows electronic coupling between the various redox centres.

Mixed-valence compounds originally generated interest for their potential in the study of fundamental properties such as electron transfer, however, as the field of molecular electronics developed, it soon became clear that mixed-valence chemistry would have wide applications in molecular electronics.[24] Since molecular electronics fundamentally depends on electron transfer, it is not surprising that a class of molecules that are good for studying this phenomenon may also provide the opportunity to design specific molecules where electron transfer occurs in ways that are useful from a device point of view. The three Robin-Day classes of mixed-valence molecules,[23] representing those molecules where charge is fully localised on a redox centre (class I), or partially (class II) or completely delocalised (class III) between multiple redox centres, have each been used for different molecular electronic functions. Class III molecules are useful as wires,

where the delocalisation provides fast electron transfer in the nanometer range. Class II molecules have been mooted as potential electronic switches or memory elements, where the reversible trapping of charge enables functionality. The properties of mixed-valence compounds are discussed in detail in the next section.

Many of the molecular electronic devices that have been demonstrated to date are familiar from conventional integrated circuits: wires, rectifiers, transistors, and logic gates.[25,26] However, several more exotic device structures have been proposed, among the most interesting of which are those designed to implement cellular automata (CA)-based computation.

CA are mathematical models consisting of a regular array of "cells" containing one or more discrete variables.[27] The value of the variables in a particular cell are updated at regular time intervals according to rules which depend on the value of the variables in neighbouring cells. The most famous example of a CA is Conway's Game of Life,[28] where each cell in an infinite square grid has only one variable, taking the value of either "alive" or "dead", and which changes depending on the number of "live" neighbours it has. CA were discovered in the 1940s and used to investigate the origins of complexity in in physical and biological systems,[29] soon after it was shown that physical implementations of CA systems were capable of transmitting and processing information.[30,31] In fact, one of the earliest proposals for a molecular computing device was based on CA using conformational switches.[32]

Heinrich *et al.*[33] have demonstrated both fundamental logic operations and the operation of relatively complex logic circuits using this kind of mechanical CA scheme. They used a STM tip to manipulate CO molecules into precise configurations on a Cu(111) surface, where they found that a CO trimer in a "chevron" configuration relaxed to a close-packed arrangement *via* hopping of one of the CO molecules. The chevron and close-packed configurations were assigned as the "0" and "1" logic states, and by placing CO molecules in patterns such that the decay of one chevron configuration would lead to the formation of a new CO chevron, which would then relax itself, *etc*, molecule cascades capable of transmitting these logic states and performing logic operations could be constructed.

More practical molecular CA systems have been demonstrated since,[34] however perhaps the most promising scheme for CA-based computation is QCA, where the charge configuration in a cell containing four redox centres is used to store binary information.[1] Aligning multiple cells allows information to be propagated without the flow of charge, thereby avoiding the power dissipation issue, and more complicated device architectures can allow for the implementation of

logic operations. The QCA paradigm is explored in section 1.2.

To develop a functional molecular electronic structure the components must be designed, synthesised and assembled on a supporting substrate. This should be done first on the single molecule, and tens-of-molecules scale, so that the structures can be fully characterised. Once this has been done, large arrays should be built and patterned. One of the most challenging problems to be overcome is that of how to contact the device so that inputs can be fed in and outputs can be read out. The porphyrin and ferrocene groups which we have identified as promising structural and functional elements for the design of candidates for MQCA, are introduced in section 1.2.3.

Since molecular structures must be supported on a substrate in order to be used as devices, it is important to understand the interaction of molecules with a surface. The molecules must also be stable with respect to diffusion at room temperature, necessitating an appreciable interaction with the substrate. On the other hand, electronic coupling to the substrate can greatly alter the properties of a molecule from its gas-phase state. It is therefore important to keep in mind adsorption effects when designing a molecular electronic system. The electronic effects of adsorption are outlined in section 1.3.

1.1 Mixed-Valence Compounds

A mixed-valence (MV) compound is a molecule containing multiple redox groups, which are identical except for their oxidation state. Although examples of MV compounds have been known for hundreds of years,[35] the field took off in earnest with the publication of the first molecule in which the MV character was designed: the Creutz-Taube ion.[21,22] This was a timely development since it came shortly after Marcus[36–38] and Hush[39] developed their theory of electron transfer. The symmetry of these molecules makes them attractive for studying the mechanisms of electron transfer utilising Marcus-Hush theory, which is indeed what initially generated interest in the field of MV chemistry.[40] The development of numerous classes of MV complexes, and the understanding of the various factors controlling the electron transfer properties in MV compounds, has in recent years led to the exploitation of these molecules as molecular wires and switches.[24]

A two-centre mixed-valence compound can be thought of as a donor-bridge-acceptor (D−B−A) molecule where the donor and acceptor differ only by one electron (or more).[41] The general form of a D−B−A molecule is shown in figure 1.1. Interconversion between the donor and acceptor occurs *via* electron transfer

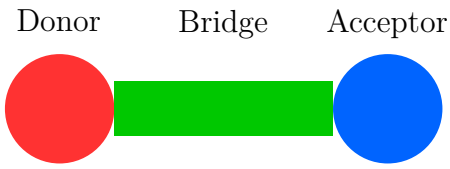

Figure 1.1: Schematic of a donor-bridge-acceptor molecule.

across the bridge. The donor and acceptor groups are usually organometallic moieties, although they can also be organic radical anions and cations.[42] The bridge can range from a simple metal-metal bond to a long organic bridging group, and the nature of this bridge strongly affects the coupling between the donor and acceptor.

Robin and Day classified MV compounds depending on the extent of the delocalisation of the valence electrons.[23] This is described by the mixing of the donor and acceptor wavefunctions, denoted ψ_{d} and ψ_{a}, respectively. The ground state wavefunction is defined by[43]

$$\psi_{\mathrm{MV}} = \sqrt{1 - V_{\mathrm{da}}^2}\psi_d + V_{\mathrm{da}}\psi_a. \tag{1.1}$$

Class I molecules have a high barrier for charge transport between the redox sites, so that $V_{da} = 0$ and the unpaired electron is localised on one of the redox centres and $\psi_{\mathrm{MV}} = \psi_{\mathrm{d}}$. Class III systems have no barrier to interconversion such that the mobile charge is completely delocalised and the ground state wavefunction is a mixture of the donor and acceptor wavefunctions. Here $V_{\mathrm{da}} = 1/\sqrt{2}$, and the oxidation state of each redox centre can be thought of as the average of that on the molecule.[44] In class II compounds there is a small barrier to electron transfer between the donor and acceptor, but the low activation energy allows interconversion upon thermal or optical excitation. The slow rate of electron transfer in class II compounds makes them particularly amenable to study with a variety of techniques. More recently subclasses representing molecules on the border between the primary classes have been added.[45] The delocalised nature of charge in class III compounds suggests that they may be useful as molecular conductors, while if the weak barrier to transfer of charge between the different localised sites in class II compounds can be modulated by an external stimulus, a molecular switch can be conceived.[46]

According to Marcus theory, the potential energy surface for electron transfer from a donor to an acceptor is described by two one-dimensional harmonic potentials along a dimensionless reaction coordinate,[47] as shown in figure 1.2(a).

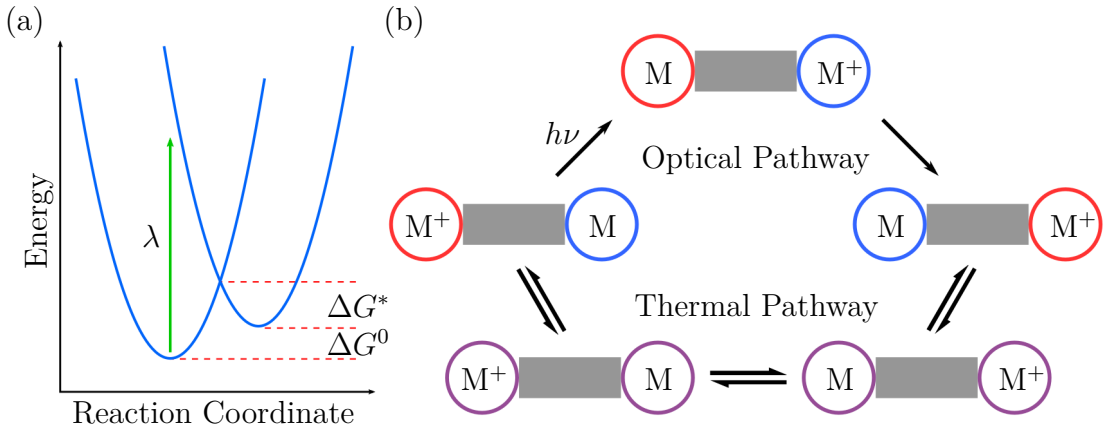

Figure 1.2: (a) The Marcus potential energy surface for an electron transfer reaction between a donor and acceptor. (b) shows a schematic of the optical and thermal pathways for intramolecular charge transfer in a symmetric D−B−A compound. Red and blue circles around the redox centres represent equilibrium intramolecular and solvent configurations for the M^+ and M states, respectively, while the purple circles represent the intramolecular and solvent configuration for the transition state for electron transfer between the two redox centres. Adapted from ref. 40.

There are two pathways for electron transfer from the donor to acceptor, thermal and electronic. These are shown schematically for a symmetric D−B−A molecule in fig. 1.2(b).

For thermal electron transfer to occur, the molecule and surrounding solvent must first form an activated complex with identical configurations around each redox site. The energy required to form the transition state ΔG^* corresponds to the difference between the free energy at the donor minimum and the point at which the diabatic curves cross. Optically induced electron transfer occurs when a photon is adsorbed whose energy corresponds to the vertical difference from the donor minimum to the acceptor diabatic potential. This energy, known as the Marcus reconfiguration energy λ, represents the extra free energy cost associated with the intramolecular and solvent configurations having not yet responded to the change in charge. The Marcus reconfiguration energy has contributions from structural changes within the molecule during charge transfer, known as the inner reorganisation energy λ_i, and from the outer reorganisation energy λ_o which accounts for rearrangement of the surrounding solvent molecules. The optical and thermal pathways are equivalent, leading to a relationship between the activation barrier ΔG^* and the reconfiguration energy λ:

$$\Delta G^* = \frac{(\lambda + \Delta G^0)^2}{4\lambda}, \tag{1.2}$$

where ΔG^0 is the free energy change during the electron transfer reaction, which is zero for the degenerate system in Fig. 1.2(b).

Marcus theory is only applicable to MV compounds belonging to class I, where the diabatic approximation holds. Where there is electronic coupling between the redox sites an adiabatic treatment is required.[39] Hush extended Marcus theory to account for this electronic coupling, which results in an avoided crossing between the potential energy curves of the two states. The resonance energy V_{da} arising from this electronic coupling lowers the barrier for charge transfer:

$$\Delta G^* = \frac{(\lambda - 2V_{\mathrm{da}})^2}{4\lambda}. \tag{1.3}$$

This leads either to a double minimum potential energy curve for a class II compound, when the electronic coupling is smaller than the reconfiguration energy $2V_{\mathrm{da}} < \lambda$, or a single minimum corresponding to the class III case, when $2V_{\mathrm{da}} > \lambda$. MV systems can be classified by their resonance energies V_{AB} according to the Robin-Day scheme:[40]

$$\begin{aligned} &\text{Class I:} && V_{\mathrm{da}} \approx 0, \\ &\text{Class II:} && 0 < V_{\mathrm{da}} < \lambda/2, \\ &\text{Class III:} && V_{\mathrm{da}} \geq \lambda/2, \end{aligned}$$

Potential energy curves for a two-centre MV system, representing each of the three Robin-Day classes, are shown in Fig. 1.3.

The degree of interaction between redox-active groups in a molecule will determine its optoelectronic properties. Class I molecules have properties corresponding to their component parts, whereas class II and III compounds generally have electronic and optical properties which cannot be predicted by looking at each of the components in isolation. This manifests in two ways which are experimentally accessible: separation of the two (or more) sequential redox potentials for the redox-active groups, and the appearance of an intervalence charge transfer (IVCT) band in the near-infrared (N-IR) region of the molecules optical spectrum.

1.1.1 Electrochemical analysis of mixed-valence compounds

Intramolecular electronic coupling in a MV compound implies that once one of the redox centres is oxidised (reduced), oxidation (reduction) of subsequent redox groups requires more energy.[20] This manifests as a shift in the equilibrium of the intramolecular comproportionation reaction, which can be written as

$$\mathrm{M}^{(\mathrm{n}+1)} + \mathrm{M}^{(\mathrm{n}-1)} \rightleftharpoons 2\mathrm{M}^{(\mathrm{n})}.$$

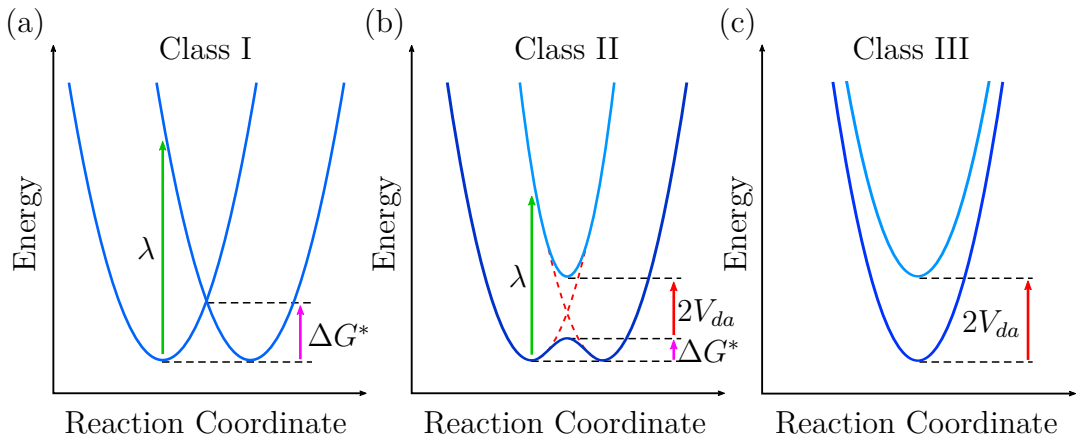

Figure 1.3: Potential energy curves for symmetric MV molecules representing the primary Robin-Day classes. The barrier to electron transfer between the redox centres is denoted ΔG^*, λ is the Marcus reorganisational energy, and V_{da} is the coupling matrix element between the redox centres. (a) Class I molecules have fully localised redox centres such that thermal electron transfer is forbidden between them. (b) The redox centres in Class II molecules are weakly coupled. (c) In Class III molecules charge is delocalised over the redox centres, indicating strong coupling. Adapted from ref. 40.

The equilibrium constant for this reaction is referred to as the comproportionation constant K_c. It describes the stability of the MV state relative to the isovalent state and acts as a measure of the degree of electronic communication between the redox centres. The comproportionation constant is given by

$$K_c = \frac{[\mathrm{M}^{(n)}]^2}{[\mathrm{M}^{(n+1)}][\mathrm{M}^{(n-1)}]}. \tag{1.4}$$

In the limit of no interaction between the redox sites, $K_c = 4$.[48] In this case a single multi-electron peak will be observed in the cyclic voltammetry (CV), whereas for coupled redox centres this peak will be split into multiple waves with redox potentials separated by ΔE. K_c can be determined from electrochemical measurements by utilising the Nernst equation

$$\Delta G^o = -RT(\ln K_c) = -nF(\Delta E), \tag{1.5}$$

where T is the temperature, and R and F are the gas and Faraday constants, respectively.

The comproportionation constant can be used to assign a molecule's Robin-Day class as follows:[20]

$$\begin{aligned} &\text{Class I:} && K_c < 10^2, \\ &\text{Class II:} && 10^2 \leq K_c \leq 10^6, \\ &\text{Class III:} && K_c > 10^6, \end{aligned}$$

However, it has been reported that medium, both the solvent and counter ions, can strongly effect ΔE and therefore delocalisation of excess charge is only one of many contributing factors to large K_c.[49,50] It should not be used as the sole measure of MV behaviour, and is typically combined with analysis of the IVCT band for Robin-Day classification.

1.1.2 Intervalence charge transfer

As we have seen intramolecular electron transfer can occur *via* a thermal or optical pathway (Fig. 1.2). When the interaction between the redox sites is negligible, as for Robin-Day class I molecules, the optical transition occurs at energies

$$h\nu = \lambda = 4\Delta G^*. \tag{1.6}$$

In a class II MV system, electronic coupling between the redox sites gives rise to a new adsorption band associated with charge transfer between the two, referred to as the IVCT. The energy of the IVCT band is related to the Marcus parameters.[39] Hush theory allows the energy of the IVCT, $h\nu_{\max} = \lambda$, to be extracted from the bandwidth of the transition at half its maximum intensity $\Delta\nu_{1/2}$, which can be measured spectroscopically. For a Gaussian absorption band

$$\begin{aligned} \nu_{\max} &= \frac{(\Delta\nu_{1/2})^2}{16\ln(2k_BT)} \\ &= (\Delta\nu_{1/2})^2/2310\ \text{cm}^{-1}. \end{aligned} \tag{1.7}$$

The resonance energy (in wavenumbers) can be obtained from the Mulliken-Hush expression

$$V_{\text{da}} = 2.06 \times 10^{-2} \frac{\sqrt{\nu_{max}\varepsilon_{max}\Delta\nu_{1/2}}}{r_{\text{da}}}, \tag{1.8}$$

where ε_{max} is the molar absorptivity (in units of $\text{mol}^{-1}\,\text{cm}^{-1}$), ν_{max} and $\Delta\nu_{1/2}$ are in wavenumbers, and r_{da} is the separation between the donor and acceptor redox groups in Ångströms.

Since the charge is delocalised in a class III system, there is technically no charge transfer occurring, yet the observed adsorption band is still referred to

as a IVCT band.[51] The single minimum in a class III potential energy surface implies that $h\nu_{\max} = 2V_{ab}$.

Analysis of IVCT bands can be quite challenging for organometallic MV systems since they typically occur in the N-IR region where they may overlap with ligand-metal charge-transfer (LMCT) or metal-ligand charge-transfer (MLCT) bands.[42]

1.1.3 Factors affecting intramolecular electronic coupling in mixed-valence molecules

It is important to understand the factors influencing the communication between redox sites in a mixed-valence compound if we are to design molecules for predefined applications. Essentially, we are interested in how the electronic coupling V_{da} depends on the structural and electronic properties of the molecule.

Class II and III mixed-valence compounds almost always consist of redox groups linked by a conjugated bridge; few examples of appreciable electronic communication through saturated bonds exist, and in those few the end groups are usually held at very close distances.[52,53] The dependence of the electronic coupling on the distance between the end groups and upon the degree of conjugation in the linker was demonstrated nicely for a series of diferrocenyl complexes. Two ferrocenyl (Fc) groups were joined by alkane, alkene and alkyne chains of various lengths, and the mixed-valence character of the resulting compounds were measured electrochemically and by analysis of the IVCT bands. The simplest diferrocenyl compound, biferrocene, consists of two Fc groups linked by a single bond between one of the cyclopentadiene (Cp) rings of each, and is a Class II mixed-valence compound.[54] The insertion of even a single saturated carbon (Fc$-CH_2-$Fc) between the the two Fc groups is sufficient to kill the electronic coupling between the redox units, resulting in a class I molecule.[55] Alkenyl bridges facilitate electronic coupling between the Fc groups, since they are conjugated, and class II behaviour is observed even through a 12-membered alkene chain.[56] However, the magnitude of the coupling decreases exponentially, as expected, as the linker length increases. A similar trend is observed for alkynyl bridges.[57,58]

This implies that anything that reduces the conjugation in the bridge will reduce the communication between the end groups. Chemical factors, such as the bond order, are not the only factors which affect conjugation; geometrical factors such as rotation around a C$-$C bond or bending of the π-system both reduce the overlap between orbitals, which in turn reduces the degree of conjugation.[59] The effect of rotation was demonstrated by calculating the resistance

through a biphenyl molecule, attached to two gold electrodes *via* S···Au bonds, as a function of the angle between the planes defined by each phenyl ring.[60] The resistance was found to increase with the angle between the planes, reaching a maximum at 90°. This explains why interactions between redox sites are greater for molecules in which the various conjugated components are rigidly fixed in relative orientations approaching planarity, and, to a lesser extent, those in which rotations are inhibited by steric hindrance.[43]

The effect of conformation on the degree of electronic coupling between redox groups can be advantageous. If we can alter the conformation of the bridge using some external stimulus, the electronic coupling, and hence electron transport properties, can be altered. The class of molecules where this is possible are known as conformational switches.[61]

Since conjugated groups facilitate efficient electronic coupling between redox groups, aromatic rings and π-conjugated macrocycles are often used as bridging structures. However care must be taken when using cyclical bridges since structural isomers can have different coupling parameters. One of the simplest demonstrations of this is the mixed-valence behaviour of the *ortho*, *meta* and *para* isomers of a diferrocenylbenzene.[62] Upon analysis of the IVCT bands, the *para* isomer was found to exhibit the strongest electronic coupling between the ferrocenyl groups, followed by the *ortho* and, finally, *meta* isomers. The difference in coupling strength was attributed to quantum interference effects between different tunnelling channels. However, this effect is not always observed. No significant difference in coupling strength was observed for the structural isomers of a diferrocenyl cyclobutadiene-CoCp sandwich structure where the ferrocenyl groups are bound to either adjacent, or opposite, vertices of the cyclobutadiene.[58]

The electronic coupling also depends on the difference between the orbital energies on the end groups and bridge, and, as a result, the same bridge may lead to a different distance-coupling relationship between different end groups. The effect of varying the bridge energy was demonstrated using symmetric diferrocenyl molecules where the ferrocenyl groups are bridged by five-membered heterocycles.[63] A series of heterogroups with varying electron donating ability were inserted on the bridge, and the IVCT bands were analysed. The more electron donating the group on the bridge the higher the mixed-valence character of the molecule, as expected for better orbital matching.

The energy of the redox groups can be similarly tuned by substitution of electron donating or withdrawing groups. Indeed, this has already been exploited to break the symmetry between ferrocenyl end groups in a diferrocenyl mixed-

valence complex to fix the order in which the oxidations occur.[64]

Generally, the distance between the redox active elements of the molecule should be 5 Å or less to ensure class II or III mixed-valence behaviour. However, longer-range coupling (10 Å to 12 Å) is possible through the π-system of some linkers, particularly conjugated macrocycles.[65]

In summary, in order to maximise electronic coupling between redox groups, they should be connected at close range through conjugated linkers whose orbital energies align with those of the redox groups. Molecules with large separations, saturated linkers, and/or large energy barriers to electron transport through the linker will tend to exhibit Robin-Day class I mixed-valence behaviour. Care must be taken to ensure a mixed-valence compound, designed for a given application, possesses the properties intended. This is non-trivial given the interplay between the various factors which determine the degree of electronic communication between redox centres in a molecule, and cannot be guaranteed by assembling several well-characterised building blocks.

1.2 Quantum-Dot Cellular Automata

QCA is a computational paradigm based upon quantum mechanical interactions within the QCA cell and Coulombic interactions between cells.[1] A QCA cell consists of a quantum dot (QD) located at each vertex of a square, as shown in figure 1.4(a), where a QD simply refers to a region to which charge can be localised, and can take the form of capacitively-coupled metal islands or redox sites within a molecule. Adding two mobile electrons to a cell leads to a doubly-degenerate ground state where the electrons occupy the dots at opposite vertices of the cell. These degenerate states are used to encode binary information; the different quadrupole orientations represent the "0" and "1" binary states shown in figure 1.4(a).

An isolated cell will have a ground state which corresponds to a superposition of the two degenerate charge configurations. Upon the application of a potential to the cell, the degeneracy is lifted such that the electrons are forced to take on either the "0" or "1" state, depending on the nature of the applied potential. Importantly, the electrostatic interaction with a neighbouring cell is enough to break the degeneracy so that cells aligned side-by-side will adopt identical charge configurations. It is this cell-to-cell interaction which allows the propagation of binary information, and allows Boolean logic operations to be performed.

If we consider the first cell in a line of coupled QCA cells to be the driver,

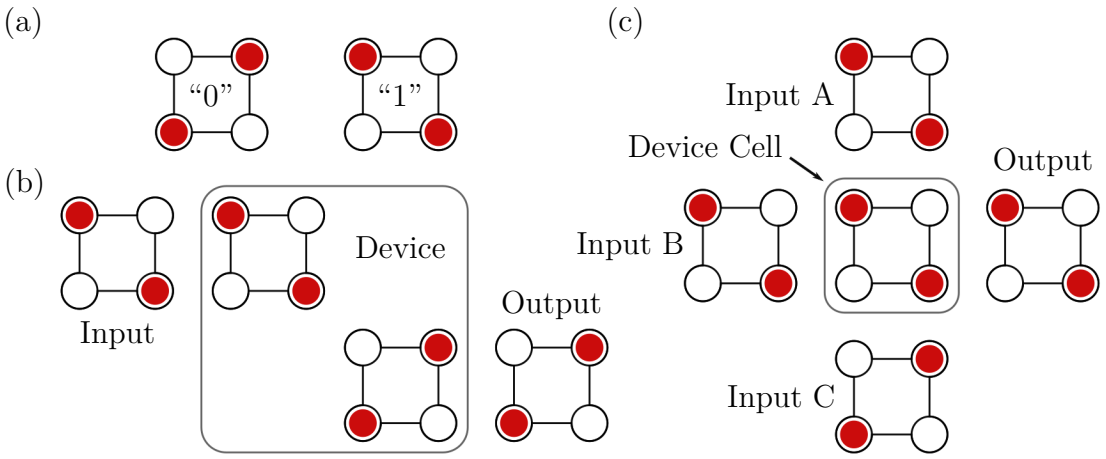

Figure 1.4: (a) The binary states of a QCA cell, where the red dots indicate QDs occupied by a mobile electron and empty dots represent unoccupied QDs. Two of the basic QCA circuit components, the inverter and the majority gate, are shown in (b) and (c), respectively.

the ground state of the line will be the situation where each cell has the same configuration as the driver, so that changing the polarisation of the driver will induce switching in all of the adjacent cells.[66] We then have the simplest QCA device: the wire. In conventional circuits a wire is not usually thought of as a device, however, in QCA transmission of information along the wire depends on proper transfer from cell to cell along the row.

All the elementary device logic elements can be constructed using different layouts of QCA cells.[1] A QCA inverter [Fig. 1.4(b)] consists of a cell shifted by one cell width, in the direction perpendicular to the propagation direction, relative to the neighbouring cell. However, more reliable inverter designs have been conceived.[67] A fan-out structure is simply a T-junction of QCA cells, although it requires power gain which in turn necessitates clocking. A three-input majority gate is built by placing cells in a cross configuration, as shown in figure 1.4(c), which is much simpler than its complementary metal–oxide–semiconductor (CMOS) equivalent.

The device cell adopts the binary state which is dictated by at least two of the three inputs, and propagates this state to the output cell. The AND operation can be implemented with a QCA majority gate by fixing one of the three inputs to "0". The output cell will adopt the "1" configuration if the other two inputs are both in the "1" logic state, and "0" otherwise. Similarly, the majority gate can perform the OR operation by fixing one of its inputs to "1". The inverter corresponds to the NOT operator. Since these three operations allow for complete Boolean logic, QCA then constitutes a scheme for general computing.[68] More

complicated digital systems such as adders[67] and simple microprocessors[69] have already been designed by combining QCA majority gates and inverters in various architectures.

QCA architectures must be clocked to avoid switching errors during transmission of information through a QCA wire with a weak link (such as an imperfectly positioned cell), to avoid the trapping of the switching signal in a metastable cell configuration, and to allow for power gain.[68] Power gain is crucial to allow for signal splitting and to compensate for dissipative processes during transmission which would otherwise lead to the decay in the signal strength.[70]

In a clocked QCA system, the cells are switched between a neutral state, where the charge state is delocalised around the cell, and an active state, representing the "0" or "1" binary state, depending on the external stimulus to the cell. Clocking requires dynamic control of the tunnelling barrier height between the dots in a cell.[71] The clocking signal was originally envisaged as an electric field, however, it was found that introducing an intermediate dot was a more practical approach, particularly for MQCA. The intermediate dot is coupled to clock-electrodes where a bias is applied to generate the clocking action. A positive clocking potential attracts the mobile electron to the clocking dot which then produces the "NULL" state. A negative clocking potential repels the electron which subsequently occupies one of the binary states according to the external potential from adjacent cells.

The clocking signal also allows for the controlled transfer of information along a line. The input cell is polarised as the clocking signal is applied to the line, which causes the state to be transferred along the line. As this signal propagates the input cell is returned to the null state so that the next input can be applied. This is known as a shift register.[70] Clocking even allows latch-type memory devices to be integrated into QCA circuits.[72]

Modern CMOS devices are greatly complicated by large numbers of long interconnect lines. QCA, on the other hand, allows for simplified interconnects since cells communicate only with their nearest neighbours.[73] A QCA computation is implemented by applying inputs to the edges of a system which then relaxes to its ground state. The output of the computation is read from the other edge of the circuit. This "edge-driven" nature of QCA implies that no signal or power lines are necessary within the circuit interior.[71] Another advantage of the QCA scheme stems from the fact that no current flow is associated with the transmission of information, since the intra-cell switching proceeds *via* tunnelling and the inter-cell interaction is mediated by Coulombic forces. This should allow

for extremely low power dissipation, thereby avoiding one of the most pressing challenges in modern microprocessor design.[1] Additionally, the QCA paradigm is not subject to the same scaling limitations as conventional field-effect transistor (FET)-based devices are. In fact, QCA device performance should increase as the device is down-sized.

1.2.1 Implementation of QCA

In this thesis, we consider only conventional, charge-based QCA. However, magnetic QCA, where the electrical dipoles are replaced with magnetic dipoles, is also viable.[74,75] Here, the dots are made up of magnetic domains, and the binary information is represented by the direction of the magnetization vector in the nanomagnet quartets. The magnetic exchange interaction is responsible for intra-cell switching, while ferromagnetic or anti-ferromagnetic coupling mediates the inter-cell interactions. Magnetic QCA operation has been demonstrated at room temperature.[76,77]

It is important to note that the "quantum" in QCA does not imply that a QCA device would be a quantum computer. For quantum computers, system-wide quantum phase coherence is required, whereas in conventional QCA the phase coherence is maintained only within each cell.[1] That being said, quantum computing using coherent QCA has been proposed and is being actively developed.[78,79]

A practical QCA system was first demonstrated for a system comprised of aluminium dots arranged on the vertices of a 60 nm × 60 nm square.[3] Gate electrodes were used to move the electron between the two dots on one half of the cell. Single-electron transistors were used to read the polarisation of the cell.

Since this initial investigation, many more experiments have been performed on metal dot QCA cells,[72,80–82] including the demonstration of a majority gate where voltage inputs were applied to a QCA cell to mimic the potentials of three input cells.[83] The full truth table was reconstructed by varying the input voltages and thus the operation of the majority gate was demonstrated.

Even with cells as large as 60 nm × 60 nm it would be possible to design a microchip capable of outperforming commercially available transistor-based microchips due to enhanced device density and the flexibility of QCA computation. The problem with metal-dot QCA at this scale is that they are functional only at cryogenic temperatures. This is a result of the fact that the kink energy (the difference between the energies of the ground state and the first excited state of the array) is dependent upon the QD capacitance, which increases as the dot

size is reduced. For stable computation this energy must be much greater than k_BT.[1] For room temperature operation, as required for commercial applications, the cell size should be on the order of 2 nm × 2 nm, which is not feasible using metal dots; controlled manufacture of small metal clusters would be exceedingly difficult, and tuning the properties of these clusters would be an insurmountable engineering challenge.

QCA was originally proposed for use with semiconductor QDs, and indeed semiconductor-based QCA has been demonstrated. GaAs/AlGaAs heterostructures with top-gate electrodes were used,[84–86] as were etched Si QDs.[87–89] A functioning QCA cell was demonstrated using phosphorus donors embedded in a silicon surface.[90] However, manufacture of semiconductor QDs is no less challenging than that of metal dots.

The nature of the directional bonding in semiconductors can be exploited to create dots of the required size. Wolkow *et al.* have used dangling bonds on the H−Si(100)-(2×1) surface to form a nanometer-sized QCA cell which was stable at room temperature.[91,92] While this is promising as a proof-of-concept, removing the hydrogen atoms with the STM tip to expose the dangling bond is a time-consuming process and is not suitable for large-scale devices. Additionally, Si dangling bonds are highly reactive and would be passivated on removal from ultra-high vacuum (UHV).

To realise a QCA device capable of functioning at room temperature we need a reliable way to manufacture large numbers of charge-containing dots, which are stable under ambient conditions, in controlled geometries. The most sensible way to do this is to harness the tools of synthetic chemistry to develop molecule-based QCA devices.[2]

1.2.2 Molecular QCA

Molecules naturally fall within the size range required for stable QCA computation at room temperature, can self-organise, and are capable of storing charge. Molecules are therefore natural candidates for use as QCA cells. Synthetic chemistry allows for the controlled manufacture of large numbers of identical, highly tunable molecules with properties which can be engineered to produce functional QCA cells. Implementation of MQCA requires the design of a molecule in which charge can be localised in at least two specific redox-active sites and can tunnel between those sites.[2] The redox sites can be bound together *via* inter- or intra-molecular forces, however, while it is possible that through-space coupling mediated by tunnelling and Coulombic repulsions would be sufficient to drive

QCA switching as it does for metal dots, most of the MQCA systems investigated to date use molecules with two or more redox sites. In this thesis we use both two-dot and four-dot molecules.

Robin-Day class II or III mixed-valence compounds (section 1.1) are prime candidates for QCA cells.[44] Although Class III compounds have no barrier for electron transfer in their unperturbed state, it is expected that the QCA environment will break the symmetry and induce a barrier to charge transfer.[93] However, it is not yet clear under what circumstances the induced barrier would be high enough to confine electrons to specific dots at room temperature. The QCA molecule should be two- or four-fold symmetric (depending on the number of dots) and possess functional groups which allow controlled attachment and orientation on a surface. A means for arranging the molecules into useful architectures and for providing input and reading output at the edge of the arrays is also required for computation using MQCA cells, however this will not be addressed here.

While a functioning MQCA cell has yet to be demonstrated, a considerable number of molecules have been investigated, experimentally and/or computationally, as potential candidates. Some of these molecules are sketched in figure 1.5. One of the first molecules investigated in the context of MQCA already had a long history in molecular electronics: the diallyl radical. This molecule, shown in figure 1.5(a), was proposed for use as a molecular transistor by Aviram,[94] and was later studied by Hush.[95] The unpaired electron can occupy one of the allyl sites, and tunnel between the two, fulfilling the electronic requirements for MQCA candidates. However, the molecule presents no way of anchoring to a surface and no way of self-assembling into the required structures, disqualifying it for practical use. In spite of this, its simple nature made it attractive for computational studies which would be intractable with more complicated molecules. This allowed Lent *et al.*[2] to demonstrate its bistablilty and ability to switch in response to an external driver. Wires composed of parallel diallyl radicals were shown to be capable of transmitting binary information, and the operation of a majority gate was demonstrated computationally.[2] Additionally, a triallyl radical was shown to facilitate clocked QCA.[96,97] Thus, proof-of-concept for MQCA was demonstrated at the computational level.

Since then several more complicated and more practical molecules have been tested experimentally. Fehlner and Long identified a ferrocenyl tetrad as having potential for MQCA applications.[98,99] This molecule, shown in Fig. 1.5(b), had originally been reported in 1978,[100] and is composed of ferrocenyl moieties bound

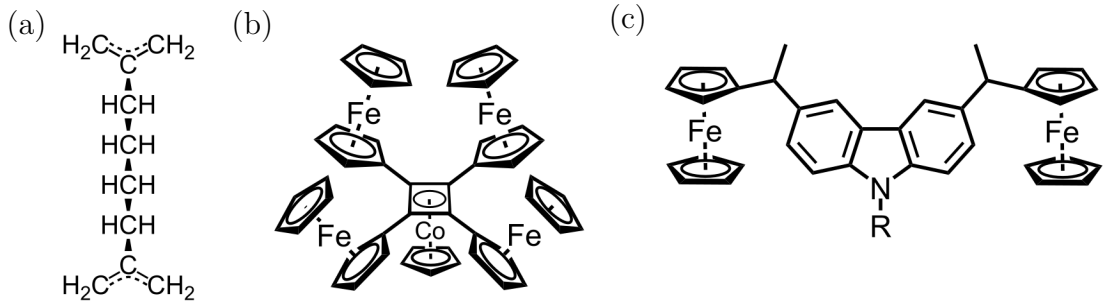

Figure 1.5: Some of the QCA candidate molecules from the literature: (a) the diallyl radical, (b) the Cb−Co−Cp sandwich ferrocenyl tetrad complex, (c) the bisferrocenyl carbazole with some linker R for surface attachment.

to each corner of a cyclobutadiene ring which is itself coordinated in a Cb−Co−Cp sandwich. Electrochemical measurements on this molecule showed four separate reversible one-electron waves, indicating the di-oxidised mixed-valence species should be stable and possible to isolate. Analysis of the IVCT band indicated Robin-Day class II behaviour.[101] Calculations showed that this molecule has two degenerate electronic ground states which are localised on opposite dots, and that the charge configuration could be switched by a neighbouring molecule at 300 K.[102] Despite the square geometry and favourable electronic properties of this molecule, it is not clear how the packing and orientation would be controlled on a surface.

A family of bisferrocenyl carbazoles have received significant study as potential QCA molecules.[103–105] Here a ferrocenyl group was attached symmetrically to either side of a carbazole bridge, as sketched in Fig. 1.5(c), forming a weakly-coupled class II compound with strong charge localisation.[103] The carbazole can be functionalised at various positions, opening up the possibility of fine-tuning the coupling as discussed in section 1.1.3. Functionalisation with an alkanethiol at the R position allows the diad to be attached to a gold surface. The molecule was embedded in a self-assembled monolayer (SAM) and appeared as a double-lobed structure in the STM images, indicating it was stable with respect to rotations at room temperature and under the influence of the STM tip.[103] Computational studies on these molecules indicated that they were clockable and capable of switching in response to a driver.[104] The electrostatic interaction between neighbouring cells has been found to depend strongly on the geometry of both the arrangement of QDs within the cell and the arrangement of the cells themselves, highlighting the need for well designed molecular self-assembly and patterning.[105] The kink energies were shown to be large enough that experimentally reasonable variations in the position and orientation of the bisferrocenyl carbazole are not expected to catastrophically damage the computational process.

The Fehlner group have also synthesised a series of MV molecules based on Ru and Fe metal centres coupled through conjugated linkers.[106] These molecules have been attached to various surfaces,[107,108] with their long axis parallel to the surface, where bistable occupation of the metal centres has been demonstrated.[109] They also deposited a symmetric two-centre ruthenium complex flat on a Au(111) surface where the oxidised (mixed-valence) species was found to pack in structures resembling a QCA wire.[110] The STM contrast was found to relate to the charge on the Ru metal centres.

Two- and three-centre Fe complexes were also characterised and deposited flat on Au(111).[111] The *meta* and *para* isomers of molecules with two (dppe)FeCp groups linked to a central phenyl ring *via* ethynyl linkers were analysed.[112] The *para* isomer is a class III molecule, and retains its delocalised structure on the surface, while the charge on the class II *meta* isomer was found to be localised to one of the Fe centres, indicating that the trends discussed in section 1.1.3 hold for adsorbed MV compounds. The three-centre complex, which has potential for clocking, was observed in its singly- and doubly-oxidised state.[113] The authors did not report any tunnelling between the metal centres, driven by the STM tip, possibly rendered unfavourable by interaction with the PF_6^- counter-ion or with the surface.

These molecules rely on Van der Waals interactions to drive assembly into potentially useful structures. However, Van der Waals interactions are weak and different molecule-substrate interactions could interfere with self-assembly driven by these forces. Additionally, the non-directional nature of Van der Waals interactions makes building functional structures very difficult. We therefore require strong directional intermolecular forces to drive self-assembly into a well-defined architecture irrespective of the substrate.

Another class of molecules which have been investigated for applications in MQCA are ferrocene-functionalised porphyrins.[114] In our opinion, this class of molecules has the potential to overcome several of these challenges and make promising MQCA candidates.

1.2.3 Ferrocene-decorated porphyrins as QCA candidates

To implement MQCA we need to develop a molecule which has two or four "dots", coupled through a suitable linker which facilitates stable attachment to a surface and enables self-assembly into useful patterns. Ferrocene was identified as a good candidate for the active site very early on in the development of MQCA, as is clear from the above discussion, in part because its electrochemistry is well understood.

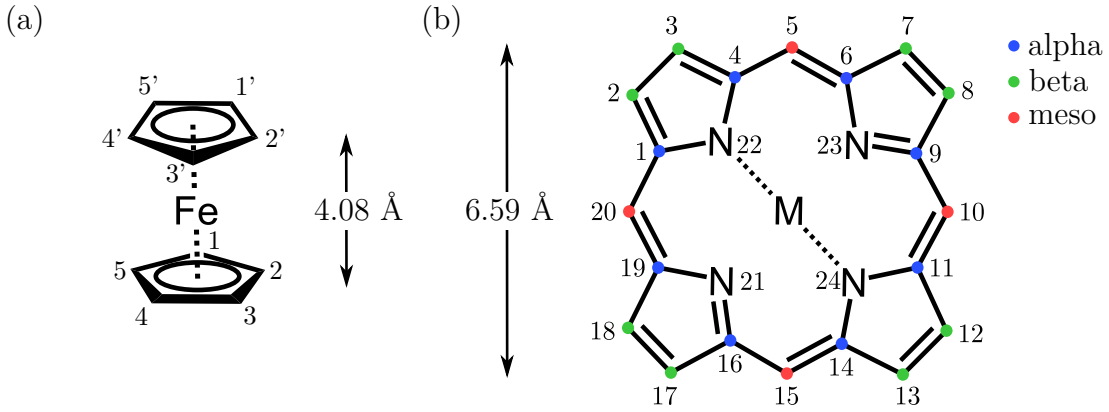

Figure 1.6: Building blocks for the QCA candidates examined in this work. The ferrocene unit shown in (a), which can be oxidised to form the ferrocenium ion, will act as the "quantum dot" in our QCA candidate molecules. The porphyrin macrocycle which has been identified as a promising structural unit is shown in (b), with the α-, β-, and *meso*- positions marked.

Additionally, diferrocenes are among the most studied mixed-valence compounds (as is evident from the discussion in section 1.1.3) and as a result have well-developed synthetic chemistry. The MQCA candidates investigated in this thesis contain ferrocenyl groups as the "dot".

Ferrocene was discovered serendipitously by Kealy and Pauson in 1951 in an attempt to synthesise fulvalene (Cp=Cp) by reacting cyclopentadienylmagnesium bromide over iron(III) chloride.[115] The 1974 Nobel prize in chemistry was awarded for the development of the chemistry of organometallic sandwich compounds, indicating the importance of ferrocene and ferrocene chemistry. It consists of a Fe(II) atom sandwiched between two cyclopentadienyl rings [shown in Fig. 1.6(a)], where the Cp π-orbitals coordinate with the Fe d-orbitals.[116] The Cp rings are eclipsed at equilibrium, giving the molecule D_{5h} symmetry, however, there is only a small barrier to rotation into the staggered conformation, such that rotation is frozen out only below 164 K.[117,118] Ferrocene is reversibly oxidised into ferrocenium, where the iron is in a Fe(III) oxidation state, at a potential of around 0.5 V (depending on the solvent) *vs.* a saturated calomel electrode (SCE).[119]

Porphyrins have long been popular elements of proposed molecular electronic devices,[120] in part due to the versatility of their electronic properties, and in part because they have been shown to enable self-assembly in a wide range of motifs.[121] Both of these properties suggest that porphyrins are promising units for the structural backbone of MQCA devices. The porphyrin macrocycle is conjugated, suggesting favourable electron transfer properties, and indeed it has been shown to be an extremely efficient bridge between ferrocenyl moieties, despite

the relatively large separation between them (∼12 Å).[122] Additionally, a variety of different sites on the macrocycle can be functionalised, and a metal ion can be inserted into the centre of the macrocycle, as indicated in Fig. 1.6(b), which allows fine tuning of the porphyrin electronic properties. The porphyrin ring has 4-fold symmetry, and the *meso*-positions, which are the most accessible sites for functionalisation, present the possibility of creating half-cell or full-cell QCA candidate molecules. The central metal ion also may have potential to act as the extra dot for clocking of QCA cells.

In spite of these favourable attributes, relatively little effort has been expended in developing a porphyrin-based MQCA candidate. However, numerous examples of ferrocenyl-functionalised porphyrins exist already in the literature,[123] the majority of which consist of one or more ferrocenyl groups coupled to the porphyrin *meso*-sites, either directly[124] or *via* some linker.[125] Examples of ferrocenyl groups coupled to the β-sites,[65] or coordinated to a central metal ion,[126] have also been reported. Some of these ferrocenyl-porphyrins have encouraging electrochemical properties.

The first ferrocene-decorated porphyrin reported was 5,10,15,20-tetraferrocenylporphyrin (TFcP), where a ferrocenyl group is attached to each of the porphyrin *meso* sites,[124] as sketched in Fig. 1.7 with $R_i = R_1$. Since it has four redox sites bonded in a square geometry through a conjugated core, it is an obvious candidate for MQCA. There was found to be a relatively strong π-electron interaction between the porphyrin and *meso*-ferrocenyl groups, facilitated by the relative co-planarity of the porphyrin and the *meso*-cyclopentadienyl group.[114] Early electrochemical experiments indicated that the oxidation of each ferrocenyl group occurred very close together,[127] and later tuning found that the first and second waves could be separated somewhat, while the others remained crowded.[128] It is not clear that TFcP would self-assemble as an array of squares aligned side-to-side as required to transmit a binary state in QCA, however, it is conceivable that the β-sites could be functionalised in such a way to drive this geometry.

Adding an electron withdrawing acyl group, R_2 in Fig. 1.7, to the top Cp ring of each ferrocenyl group results in a very promising MQCA candidate.[129] Electrochemical analysis showed two reversible one-electron oxidations followed by a two-electron oxidation wave, all ferrocenyl centred and well separated. Spectroelectrochemical analysis confirmed these results and gave electronic coupling parameters consistent with Robin-Day class II behaviour. The acyl group served not only to reduce the energy of the ferrocenyl orbitals, but also to inhibit rotation of the ferrocenyl groups, both of which increase electronic coupling as discussed

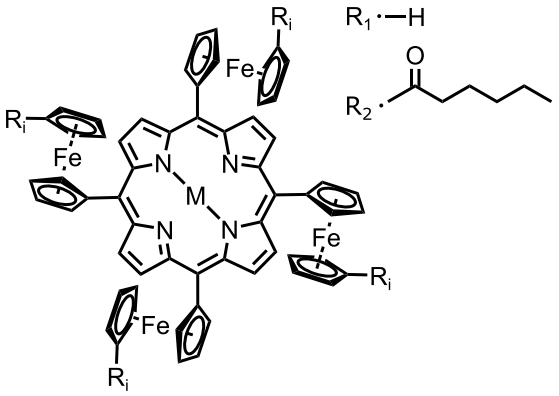

Figure 1.7: Many of the criteria required for QCA are fulfilled by 5,10,15,20-tetraferrocenylporphyrin ($R_i = R_1$), and attaching an acyl group ($R_i = R_2$) to each Fc group results in a very promising QCA candidate.

in section 1.1.3. Additionally, since acyl groups are capable of hydrogen bonding, we would expect this molecule to self-assemble into an array of square cells as required for MQCA. To the best of our knowledge no studies of this molecule adsorbed on a surface have been performed.

Insertion of a phenyl group between the ferrocenyl-groups and the porphyrin core kills the inter-ferrocenyl coupling, resulting in a class I mixed-valence compound.[125] This is attributed to the large angle between the phenyl group and the porphyrin macrocycle, driven by steric interactions between phenyl hydrogens and those of the porphyrinic β-sites, which essentially breaks the conjugation. Similarly, diferrocenyl-porphyrins where the ferrocenyl groups are coupled to the macrocycle *via* an ethylene linker are also class I compounds.[130] As expected, saturated linkers between the ferrocenyl groups and the porphyrin do not facilitate electronic coupling.[131] We therefore expect that the ferrocenyl groups should be directly coupled to the macrocycle in order to create a class II compound.

If we think about using ferrocenyl-functionalised porphyrins in a half-cell geometry, the most obvious molecule is one where a ferrocenyl group is bonded to the *meso*-site either side of the porphyrin. Various permutations of these types of molecules have been synthesised and characterised according to their mixed-valence properties. The general effect of varying the ferrocenyl-porphyrin linker, attachment site, coordinating metal ion (or lack thereof) and the effect of additional substituents on the macrocycle are now understood.

The electrochemical oxidation potentials were studied as a function of the metal ion coordinating to the centre of a diferrocenylporphyrin. The wave-splitting dependence on the coordinating metal ion went, in descending order, as follows: Ni>Zn>MnCl.[132] Additionally, the wave-splitting for the Zn complex

was similar to that for the uncoordinated porphyrin. The effect of the coordinating metal ion has two contributions, the first depending on the electronegativity of the ion, while the second was related to the configuration of the macrocycle. The electronegativity of the metal ion modulates the barrier to electron transfer as discussed in section 1.1.3, and therefore changes the coupling strength. Diferrocenylporphyrins have a highly non-planar porphyrin core configuration, which becomes more planar on coordination of a Ni ion thereby increasing the conjugation and thus the coupling strength.

Structural isomerism is non-negligible for (bis)ferrocenyl-diphenylporphyrins, with the *trans* isomer showing higher coupling than the *cis* isomer, however both compounds were class II.[133] Functionalisation of the porphyrinic β-sites with alkyl groups leads to stronger coupling between the ferrocenyl groups, due to steric effects restricting their rotation relative to the porphyrin core.[122,134]

The effect of surface adsorption on the electronic coupling has received much less attention. Vecchi *et al.*[135] attached TFcP to a Au surface, embedded in a SAM, *via* an alkanethiol linker. They measured a three-electron oxidation peak followed by a one-electron wave corresponding to the three unmodified ferrocenyl groups and the one to which the alkanethiol group was attached, respectively. This was intended for use in a photoelectrochemical cell, and such an attachment scheme would not be useful for MQCA using this molecule or its derivatives (which have more favourable electronic properties).

Since the electronic properties of large molecules such as porphyrins are often only weakly perturbed upon adsorption, even on a metal surface, we propose to adsorb these molecule flat (*i.e.* with the plane of the porphyrin macrocycle approximately parallel to the surface plane) as required for building up QCA architectures with these molecules. To the best of our knowledge there are no published measurements on ferrocenyl-decorated porphyrins adsorbed flat to a surface, besides those carried out recently by our collaborators which will be discussed in chapter 4.

1.3 Molecular Adsorption at Surfaces

We noted in the previous section that the influence of the surface on molecular properties should not be neglected when designing component molecules for molecular electronics. An adsorbate can bind to a substrate *via* Van der Waals, Coulombic and/or covalent interactions. We need to ensure that these interactions are strong enough to immobilise the molecule on the surface, but not so

strong as to have a detrimental effect on the electronic properties of the molecule. In this section we review the effect of surface adsorption on the properties of a molecule.

When an atom or molecule adsorbs on a surface its orbitals broaden, mix and shift in energy.[136] When the interaction is weak, the molecule will exhibit properties very similar to those observed in the gas phase. Strongly-coupled molecules, on the other hand, may be completely unrecognisable from the original species in terms of conformation, chemical reactivity and/or electronic structure. The coupling cannot be neatly divided into strong and weak regimes; in reality, the coupling strength varies continuously between the two. However, it can be instructive to analyse these limiting cases.

1.3.1 The Schottky-Mott limit

In the ideal case of no interaction between the substrate and an adsorbate, where there is no rearrangement of the electron density, it can be assumed that the vacuum levels of the surface and molecule will align. This is the well known Schottky-Mott limit, for which a potential energy diagram is shown in figure 1.8(a). The electron and hole injection barriers, Φ_B^e and Φ_B^h, are given in the Schottky-Mott limit by[137]

$$\Phi_B^e = \Phi_m - E_{\mathrm{A}}, \tag{1.9}$$

$$\Phi_B^h = E_{\mathrm{I}} - \Phi_m, \tag{1.10}$$

where Φ_m is the work function of the metal substrate, and E_{A} and E_{I} are the electron affinity and ionisation potential of the molecule, respectively.

In reality, there is almost always some interaction between the adsorbate and substrate which causes some deviation from the Schottky-Mott limit. Reasons for departure from the Schottky-Mott limit include:

- screening of the molecular polarisability by image charges in the metal surface.
- the formation of an interface dipole, δ.
- hybridization between molecular orbitals (MOs) and the electronic states of the surface.

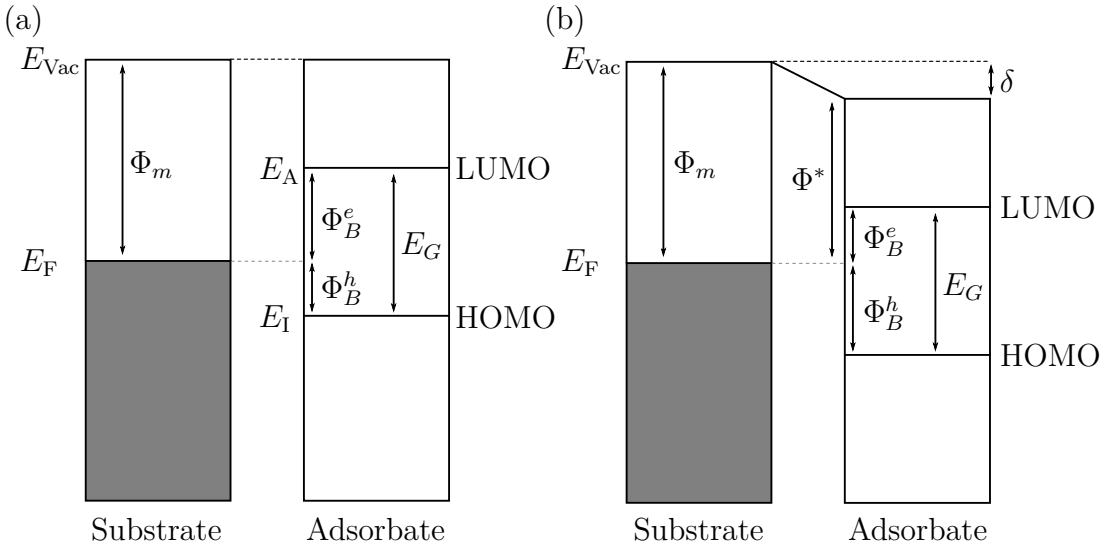

Figure 1.8: Energy level alignment between a substrate and an adsorbate at (a) the Schottky-Mott limit and (b) in the presence of an interface dipole.

1.3.2 Screening by image charges

The adsorption of a charged or dipolar species on a surface will induce redistribution of the electron density within the surface to forming a charge of equal and opposite magnitude below the adsorbed charge.[138] This so-called image charge stabilises the charge in the adsorbate *via* electrostatic interactions. This interaction reduces the ionisation potential and increases electron affinity, narrowing the highest occupied molecular orbital (HOMO)-lowest unoccupied molecular orbital (LUMO) gap.[139,140] The screening parameter S describes the impact of these interactions on the electron/hole injection barrier:

$$S = \frac{\mathrm{d}\Phi_B^e}{\mathrm{d}\Phi_m} = -\frac{\mathrm{d}\Phi_B^h}{\mathrm{d}\Phi_m}. \tag{1.11}$$

The Schottky-Mott limit is observed only on insulating substrates where there are no free charges available to form an image charge, and therefore $S = 1$. Additionally, adsorption on metal surfaces necessarily involves the formation of an interface dipole, even for noble gas atoms, due to the push-back effect.[141,142]

1.3.3 Interface dipoles

A potential energy diagram describing the energy level alignment in the presence of an interface dipole pointing into the surface is shown in figure 1.8(b). The

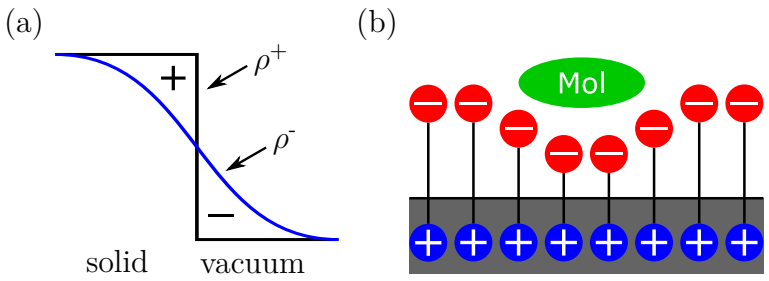

Figure 1.9: The origin of the intrinsic dipole at a metal surface is sketched in (a). The electronic charge density ρ^- (blue) leaks from the solid into the vacuum, whereas the positive charge density ρ^+ (black) drops abruptly to zero at the surface. Pauli repulsion between the electrons in an adsorbed molecule and those leaking from the metal surface compresses this surface dipole, as illustrated in (b). The effective dipole generated by this process is known as the push-back dipole.

injection barriers in the presence of the interface dipole can be written as[137]

$$\Phi_B^e = \Phi_m - E_{\mathrm{A}} - \delta. \tag{1.12}$$

$$\Phi_B^h = E_{\mathrm{I}} - \Phi_m + \delta. \tag{1.13}$$

The total interface dipole is the sum of all the contributing dipoles at the surface, including the push-back dipole δ_{P}, dipoles in the molecule itself δ_{Mol}, which may be permanent or arise from conformational changes upon adsorption, and/or dipoles arising from charge transfer across the interface which we refer to here as the chemisorption dipole δ_{Chem}. The sources of these dipoles are outlined in this section.

Metal surfaces contain an intrinsic dipole because, as illustrated by figure 1.9(a), the positive charge density from the nuclei of the constituent atoms drops abruptly to zero at the surface, whereas the negative charge density leaks into the vacuum.[143] When a molecule adsorbs on this surface, Pauli repulsion between the electrons in the molecule and those leaking from the metal into the surface pushes the metal electrons back towards the surface, reducing the dipole as shown in Fig. 1.9(b). This is known as the push-back effect.

For a physisorbed molecule, no "true" chemical bond is formed, *i.e.* no charge is transferred between the substrate and adsorbate, instead the adsorbate is bound by Van der Waals forces. Here induced and/or permanent dipoles interact with image charges in the polarisable solid, leading to situations where charge transfer is not fully screened. Chemisorption involves the hybridisation of adsorbate states

with those of the substrate. The formation of chemical bond between the two implies a charge rearrangement that will produce a dipole at the interface and will shift the vacuum level. The modification of the electronic structure upon chemisorption is described by the Newns-Anderson model.

1.3.4 Hybridisation between adsorbate and substrate states

The Newns-Anderson model[144,145] describes the interaction of an adsorbate state with energy ε_a with a substrate band with a continuum of states with wave vectors $|k\rangle$ of width W. The degree of hybridisation is governed by the coupling matrix element V_{ak}. This model completely neglects the detailed electronic structure of the adsorbate.[136] Newns developed a Hamiltonian which projects the surface density of states (DOS) onto the adsorbate, which results in a local density of states (LDOS) given by[145]

$$\rho_a(\varepsilon) = \frac{1}{\pi} \frac{\Delta(\varepsilon)}{(\varepsilon - \varepsilon_a - \Lambda(\varepsilon))^2 + \Delta^2(\varepsilon)}, \tag{1.14}$$

where $\Delta(\varepsilon)$ is the chemisorption function describing the width of the adsorbate resonance

$$\Delta(\varepsilon) = \pi \sum_k |V_{ak}|^2 \delta(\varepsilon - \varepsilon_k), \tag{1.15}$$

and the level-mixing shift

$$\Lambda(\varepsilon) = \frac{1}{\pi} \int_{-\infty}^{\infty} \frac{\Delta(\varepsilon')}{\varepsilon - \varepsilon'} \mathrm{d}\varepsilon' = \sum_k \frac{|V_{ak}|^2}{\varepsilon - \varepsilon_k}, \tag{1.16}$$

offsets the resonance to an energy determined by $\varepsilon - \varepsilon_k = \Delta(\varepsilon)$.

If the resonance lies above the Fermi level (adjusted to include the effect of the dipoles) an ionic bond is formed where an electron is transferred from the adsorbate to the substrate. If the resonance lies below the Fermi level an electron is transferred to the adsorbate from the substrate. If the broadened resonance straddles the Fermi level the substrate and adsorbate will be covalently bonded, sharing electrons.

Two limiting cases can be extracted from the Newns-Anderson adsorbate projected density of states (equation 1.14): weak chemisorption, which corresponds to a wide band and $V_{ak} \ll W$, and strong chemisorption, where $V_{ak} \geq W$.

In the case of weak chemisorption, the surface LDOS is assumed to be flat, and therefore $\rho_k(\varepsilon)$ and Δ are independent of energy. Weak coupling implies that $\Lambda(\varepsilon)$ is small. Then the projected DOS corresponds to a Lorentzian of width

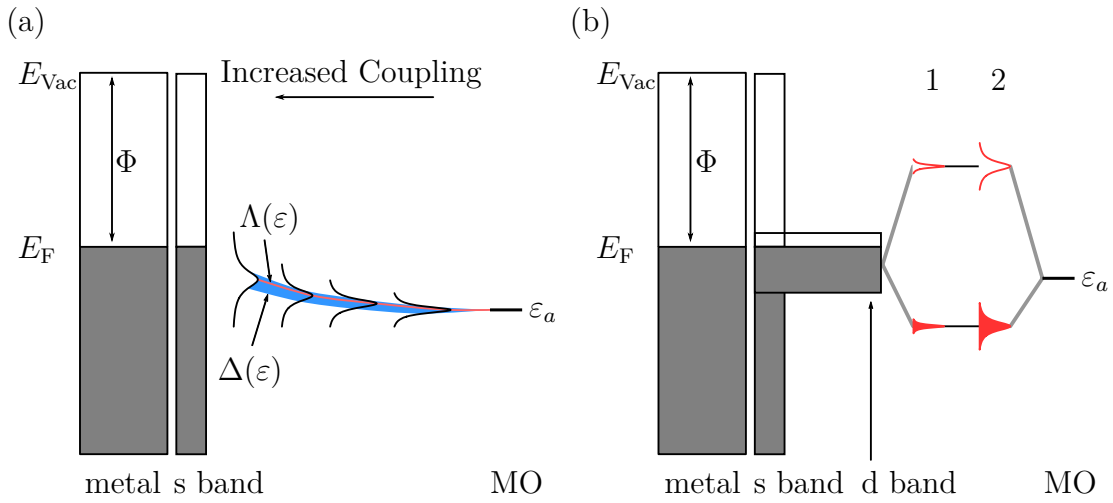

Figure 1.10: The Newns-Anderson model of adsorbate-substrate coupling at (a) the weak, and (b) the strong-coupling limits.

Δ centred around the adsorbate MO energy ε_a. The result is a broadening of the adatom valence level into a resonance with lifetime $\tau = \Delta^{-1}$. Since the charge transfer between the adsorbate and substrate proceeds *via* tunnelling, the tunnelling matrix elements decay exponentially with adsorption distance, the lifetime broadening also decays exponentially with tunnelling distance $\Delta \propto e^{-\alpha z}$. The shift and broadening of the molecular resonance as the distance between the adsorbate and surface is reduced in the weak coupling regime described in figure 1.10(a).

The dipole formed due to weak chemisorption can be predicted by analysis of the induced density of interface states (IDIS) model,[146,147] where the broadening of the adsorbate states implies that there are now finite numbers of states in the energy range of the molecule's HOMO-LUMO gap. This finite DOS in the HOMO-LUMO gap is said to be induced by the surface. This allows charge transfer for any value of Φ. Under the IDIS model, the direction and magnitude of charge transfer between the molecule and the surface is governed by the charge neutrality level (CNL) of the molecule, E_{CNL}. The CNL is an analogue of electronegativity, and can be obtained by filling $\rho_a(\varepsilon)$ up to the level of charge in the neutral and isolated molecule.[147] Charge transfer will occur to try to align E_{CNL} and E_F, however the actual amount of charge transferred will depend on the screening parameter (equation 1.11), which for the IDIS model can be written as

$$S = \frac{1}{1 + 4\pi e^2 \rho_a(E_F) d A^{-1}}, \tag{1.17}$$

where $\rho_a(E_F)$ is the density of states at the Fermi level, d is the adsorbate-substrate distance, and A is the area associated with one molecule. Then[147]

$$\Phi - E_{\mathrm{CNL}} = S(\Phi_m - E_{\mathrm{CNL}}), \tag{1.18}$$

and the dipole induced by the charge transfer is given by

$$\delta_{\mathrm{Chem}} = (1 - S)(\Phi_m - E_{\mathrm{CNL}}). \tag{1.19}$$

Incorporating the dipole arising from the push-back effect, δ_{P}, and the molecular dipole, δ_{Mol}, gives the total interface dipole[148]

$$\delta_{\mathrm{Tot}} = S(\delta_{\mathrm{P}} + \delta_{\mathrm{Mol}}) + (1 - S)(\Phi_m - E_{\mathrm{CNL}}). \tag{1.20}$$

It can be seen that physisorption is the limiting case of weak chemisorption when the chemisorption dipole is zero. We therefore take the cases of physisorption and weak chemisorption together; strong chemisorption yields qualitatively different results.

We can see that when there is no screening the gap will contain no states, and no charge transfer can occur. If the molecular dipole and push-back effect are both negligible, we retrieve the Schottky-Mott limit. For highly screened systems (where $S \sim 0$) the IDIS contains sufficient charge to align Fermi level with the CNL ($E_F \sim E_{\mathrm{CNL}}$), and any additional charge transfer will be compensated with an opposite dipole such that the molecule is pinned to the Fermi level.

In the strong chemisorption limit, shown in figure 1.10(b), the substrate LDOS is strongly energy dependent, as is the case for partially filled d-bands. The increased coupling V_{ak} results in the level-shift function $\Lambda(\varepsilon)$ being strongly energy dependent. $\rho_a(\varepsilon)$ then bears little resemblance to the electronic structure of either the substrate DOS or the adsorbate, but instead gives rise to to MO resonances corresponding to bonding and antibonding interactions between the MO level and the peak in the substrate LDOS. Strong chemisorption can be thought of as a two-step process.[136] The adsorbate states mix with the substrate bands which gives rise to antibonding and bonding resonances (step 1) which are then themselves broadened by interacting with the less energy dependent substrate s,p-bands (step 2). The interaction strength between molecule and substrate is determined by the relative occupancy of these two resonances. If only the bonding states are filled, the bond will be strong; however, increased occupancy of antibonding states weakens the bond strength.

The increased reactivity of steps and kink sites, and non-close-packed surfaces

can be explained in terms of this model. Lower coordination numbers result in a narrower d-band centred on a higher energy. This reduces the filling of the antibonding resonance and therefore results in a stronger interaction.

A similar argument explains why molecules tend to interact only relatively weakly with the noble metals compared with early transition metal surfaces.[149,150] The filling of states depends on the position of the d-states relative to the Fermi level, which varies from metal to metal. Moving from left to right across the row of transition metals, the d-bands shift downwards relative to the Fermi level. Since the interaction of adsorbate states with the metal s,p-bands does not vary much from metal to metal, it is the position of the d-band which controls the interaction strength. The higher the position of the metal d-band, the more empty antibonding states there will be and, consequently, the stronger the adsorbate-metal interaction will be. Noble metals have d-bands well below the Fermi level, which results in a repulsion that tends to cancel out the attraction due to interaction of the adsorbate states with the metal s,p-bands.

The low reactivity characteristic of noble metals tends to result in weak chemisorption, and makes them attractive for use as molecular substrates. We use the Au(111) surface as a preliminary surface to study the self-assembly of our MQCA candidates. However, as will be seen in chapter 4, the lifetime broadening associated with direct adsorption on metal surfaces makes studying the charging properties impossible. To overcome this challenge we use metal surfaces pre-adsorbed with a range of thin insulating layers (TILs). This results in greater separation between metal and adsorbate and therefore reduces hybridisation, while at the same time meeting the conductivity requirements necessary for analysis with STM.

2

Scanning Tunnelling Microscopy

The STM was invented in 1982 by Binnig and Rohrer,[4] for which they were awarded the Nobel prize in 1986. This was revolutionary because it allowed atomic-resolution imaging of a variety of surfaces in real space. Atomic resolution had been observed with the field ion microscope (FIM) as early as 1955,[151] however FIM is limited to the quite exotic structures at the apex of sharp metal tips. STM itself is not without limitations: it is only suitable for conductive materials, and electronic states are only accessible in a window defined by the workfunction of the material and the workfunction of the tip.[152]

The STM consists of an extremely sharp metallic tip which is brought almost into contact with a conductive surface. A potential difference is applied between the tip and the sample, opening up a tunnelling energy window. Quantum tunnelling allows electrons to propagate from the tip, through the vacuum gap, into the sample. The resulting tunnelling current is fed into a feedback loop which controls the tip-sample separation. A map which approximates the surface topography can be built by recording the movement of the tip required to keep the tunnelling current constant as the tip is scanned over the surface.

Early research using the STM mainly involved analysing topographs of various metal and semiconductor surfaces. Atomic resolution with the STM was first achieved on the (1×2) reconstruction of the Au(110) surface.[153] The field of STM began in earnest after the Si(111) - (7×7) reconstructed surface was imaged with atomic resolution, helping to resolve a long-standing dispute about the structure of this reconstruction.[154] The interaction of small (atomic and molecu-

lar) adsorbates with surfaces arose as a target for investigation very early on in the development of the STM. Indeed, Au islands on silicon were one of the first systems investigated.[155] Originally the focus was on studying reconstructions of metal surfaces induced by molecular adsorption,[156] but soon turned to examining the adsorbates themselves. Benzene was the first molecule to be imaged in high resolution,[5] followed shortly by copper phthalocyanine.[157] More recent work has focused on more complicated molecules, and has not been limited to simple imaging.[158,159] Adsorbates are now routinely manipulated with the STM tip,[160,161] allowing structures to be engineered from the bottom up.[162]

An important application of the STM is in STS,[163] where the relationship between the potential difference between the tip and sample, the tip-sample separation, and the tunnelling current is exploited to give information about the electronic properties of the surface. The tunnelling current is related to the LDOS of the tip and the sample, and, coupled with the high lateral resolution of the STM, affords us the ability to map out the electronic structure of a material with atomic resolution.[164]

Today, STM has developed into a powerful tool for studying molecular adsorbates. Controlled functionalisation of tips and the development of TILs as decoupling spacers between molecules and surfaces have allowed molecules to be imaged with incredible resolution.[165,166] The MOs of various adsorbates have been mapped out in detail, and match the shapes predicted by DFT.[167] Making and breaking of bonds has also been demonstrated with STM,[168,169] opening the door for single-molecule chemistry.

In this chapter, we outline the operating principles of STM and the details of the instrument itself. In section 2.1 we examine the physical principle underlying STM. We introduce quantum tunnelling and show how the electronic properties of the sample being examined relate to the observed data. In section 2.2, we elaborate on this for the case of molecules adsorbed on the substrate. In particular, we examine how the different coupling regimes outlined in section 1.3 affect the tunnelling characteristics. Section 2.3 explores the STM from an instrumentation point of view, and the details of the STM used to carry out the experiments presented in this thesis are described in section 2.4.

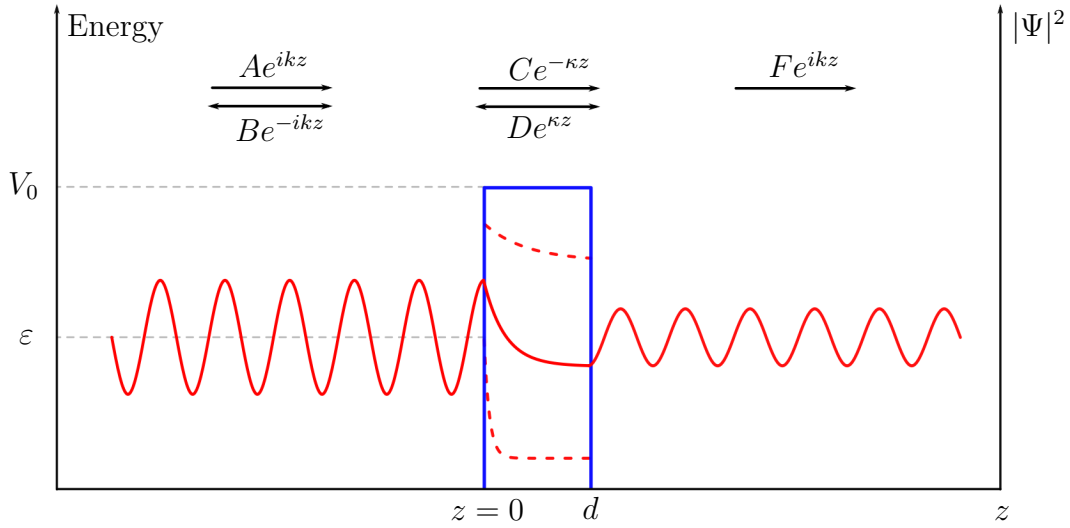

Figure 2.1: Tunneling through a 1D potential barrier.

2.1 Theoretical Background

2.1.1 Elastic tunnelling through a one-dimensional square barrier

The operating principle of STM is based upon quantum tunnelling, where quantum particles, such as electrons, can leak into, or pass through a sufficiently thin classically-forbidden region. To illustrate this phenomenon, and how it relates to the STM, we first consider the case of elastic tunnelling through a 1D square potential barrier.[170]

The potential barrier $V(z)$, shown in figure 2.1, is of height V_0 above the bottom of the potential ($V = 0$) in the region between $z = 0$ and $z = d$:

$$V(z) = \begin{cases} 0, & \text{for } z < 0 \text{ and } z > d, \\ V_0, & \text{for } 0 \leq z \leq d. \end{cases} \tag{2.1}$$

Since the potential is not time dependent, the spatial dependence of the wavefunction is obtained from the time-independent Schrödinger equation, which, in the one-dimensional case, for an electron with energy ε is

$$\frac{\hbar^2}{2m}\frac{\partial^2}{\partial z^2}\psi(z) = [V(z) - \varepsilon]\psi(z). \tag{2.2}$$

Outside the barrier, the potential is zero, and the wavefunction corresponds to an oscillating plane wave for a free electron:

$$\psi_{\text{free}}(z) \propto e^{ikz}, \tag{2.3}$$

where $k = \sqrt{2m\varepsilon}/\hbar$.

Inside the barrier, the potential is V_0, and if the electron energy is less than the potential $\varepsilon < V_0$, the electronic wavefunction is described by an exponentially decaying real wave:

$$\psi_{\text{barrier}}(z) \propto e^{-\kappa z}, \tag{2.4}$$

where $\kappa = \sqrt{2m(V_0 - \varepsilon)}/\hbar$. The exponent κ controls how fast the wavefunction decays inside the barrier. Since κ is proportional to the square root of the difference between the electron energy and the barrier height, states furthest from the top of the barrier are attenuated most strongly. This energy dependence is shown by the dashed curves inside the barrier in figure 2.1.

If we assume the incident wavefunction travels from left to right, the general solution is

$$\psi(z) = \begin{cases} Ae^{ikz} + Be^{-ikz}, & \text{for } z < 0, \\ Ce^{-\kappa z} + De^{\kappa z}, & \text{for } 0 \leq z \leq d, \\ Fe^{ikz}, & \text{for } z > d, \end{cases} \tag{2.5}$$

where A is the amplitude of the incident wave, which we take to be unity, B is the amplitude of the reflected wave, C is the amplitude of the decaying wave inside the barrier, D is the amplitude of the wave reflected from the drop in potential at $z = d$ and F is the amplitude of the transmitted wave. These amplitudes can be found by solving for the wavefunctions at the boundaries $z = 0$ and $z = d$.

The transmission probability is given by the absolute square of the amplitude of the transmitted wave:

$$T = |F|^2 = \frac{4k^2\kappa^2}{(k^2 + \kappa^2)^2 \sinh^2(\kappa d) + 4k^2\kappa^2}. \tag{2.6}$$

For a tall, wide barrier $\kappa d \gg 1$, so we can say that $\sinh^2(\kappa d) \sim (1/4)e^{2\kappa d}$ and we can neglect the $4k^2\kappa^2$ term from the denominator, which gives

$$\begin{aligned} T &= \frac{16k^2\kappa^2}{(k^2 + \kappa^2)^2}\, e^{-2\kappa d} \\ &= \frac{16\varepsilon(V_0 - \varepsilon)}{V_0^2}\, \exp\left[-2d\frac{\sqrt{2m(V_0 - \varepsilon)}}{\hbar}\right]. \end{aligned} \tag{2.7}$$

It is important to note that the transmission function decays exponentially

with the barrier width. This is the source of the extreme resolution achievable with the STM.[4]

2.1.2 The WKB approximation

The Wentzel-Kramers-Brillouin (WKB) approximation is a semi-classical method for describing quantum mechanical behaviour.[170] It can be used to extend the solution for the 1D square potential barrier to more general barrier shapes.

As shown in section 2.1.1, it is the phase, ikz, of the wavefunction that is modified by a potential V_0. We can break a spatially varying 1D potential into small segments of constant potential - a series of infinitesimal rectangular barriers of height $V(z)$ and thickness $\mathrm{d}z$. The wavefunction still takes the form of a plane wave, with the total phase shift being given by integration of the infinitesimal phase shifts from z_0 to z_1.

$$\psi(z_1) = \psi(z_0)\, \exp\left[i \int_{z_0}^{z_1} \sqrt{V(z) - \varepsilon}\, \mathrm{d}z\right]. \tag{2.8}$$

For an electron with energy lower than the potential barrier $\varepsilon < V(z)$, the transmission factor can be written, under the WKB approximation, as:

$$T = \left|\frac{\psi(z_1)}{\psi(z_0)}\right|^2 = \exp\left[-\frac{2\sqrt{2m}}{\hbar} \int_{z_0}^{z_1} \sqrt{V(z) - \varepsilon}\, \mathrm{d}z\right]. \tag{2.9}$$

Using the trapezoidal approximation, the potential barrier in the STM tip-sample junction can be written as

$$V(eV) = \Phi + \frac{eV}{2}, \tag{2.10}$$

where Φ is the tunnelling barrier height. The transmission coefficient is then

$$T(\varepsilon, eV, z) = \exp\left[-\alpha z \sqrt{\Phi + \frac{eV}{2} - \varepsilon}\right], \tag{2.11}$$

where $\alpha = 2\sqrt{2m}/\hbar$. The exponential decay of the tunnelling probability with the barrier width and the square root of the difference between the electron energy and the barrier height is retained for barriers of arbitrary shape treated under the WKB approximation.

2.1.3 The Bardeen model of the tunnelling current

Bardeen developed a model for tunnelling in metal-insulator-metal junctions long before the STM was invented.[171] In his model, the two electrodes are considered

to be two separate systems, whose electronic states can be found by solving the time-independent Schrödinger equation for each. The transition of an electron in an initial state to a final state in the other electrode is treated as a scattering problem within time-dependent perturbation theory.

When applying Bardeen's model to the STM, the electrodes correspond to the sample and the tip. In our case the tip is grounded and the potential is applied to the sample. In the zero temperature limit, the energy levels in each electrode are filled up to the Fermi level, and empty above. Then, if a potential difference V_b is applied between the two electrodes, the energy levels of the sample are shifted by eV_b relative to the tip. This means that there are states between $E_{F,t}$ and $E_{F,s} + eV_b$ which are filled in the tip and empty in the sample, or *vice versa* depending on the polarity of the applied bias, allowing electrons to scatter from one to the other. This energy range is known as the tunnelling window.

Bardeen used Fermi's golden rule[170] to calculate the transition rate for an electron in an initial tip state i at $E_{t,i}$ to a final sample state f at $E_{s,f}$:

$$w_{t,i\to s,f} = \frac{2\pi}{\hbar} |M_{fi}|^2 \, \delta \left(E_{s,f} - E_{t,i}\right), \tag{2.12}$$

where M_{fi} is the tunnelling matrix element.

The Dirac delta function in equation 2.12 implies that electrons can tunnel only between two states with equal energy, so the total tunnelling rate is calculated by summing over all pairs of final and initial states in the tunnelling window, giving

$$w_{t\to s} = \frac{2\pi}{\hbar} \sum_{i,f} |M_{fi}|^2 \, \delta \left(E_f - E_i\right). \tag{2.13}$$

Exploiting the fact that, for the Dirac delta function, $\int_{-\infty}^{\infty} f(\varepsilon)\delta(\varepsilon - E_f) = f(E_f)$, and writing the tunnelling matrix element as a function of energy, the transition rate becomes

$$w_{t\to s} = \frac{2\pi}{\hbar} \int_{E_{F,s}}^{E_{F,t}} |M_\varepsilon|^2 \sum_i \delta \left(\varepsilon - E_i\right) \sum_f \delta \left(\varepsilon - E_f\right) \mathrm{d}\varepsilon, \tag{2.14}$$

and since $\rho(E) = \sum_n \delta(E - E_n)$, the tunnelling current can then be obtained by multiplying the transition rate by the twice the electronic charge:

$$I = 2ew_{t\to s} = \frac{4\pi e}{\hbar} \int_0^{eV_b} \rho_t(\varepsilon - eV_b)\rho_s(\varepsilon)|M(\varepsilon)|^2 \mathrm{d}\varepsilon, \tag{2.15}$$

where the factor of 2 accounts for electron spin degeneracy, and the energies are referenced to the sample Fermi energy, such that $E_{F,s} = 0$ and $E_{F,t} = eV_b$.

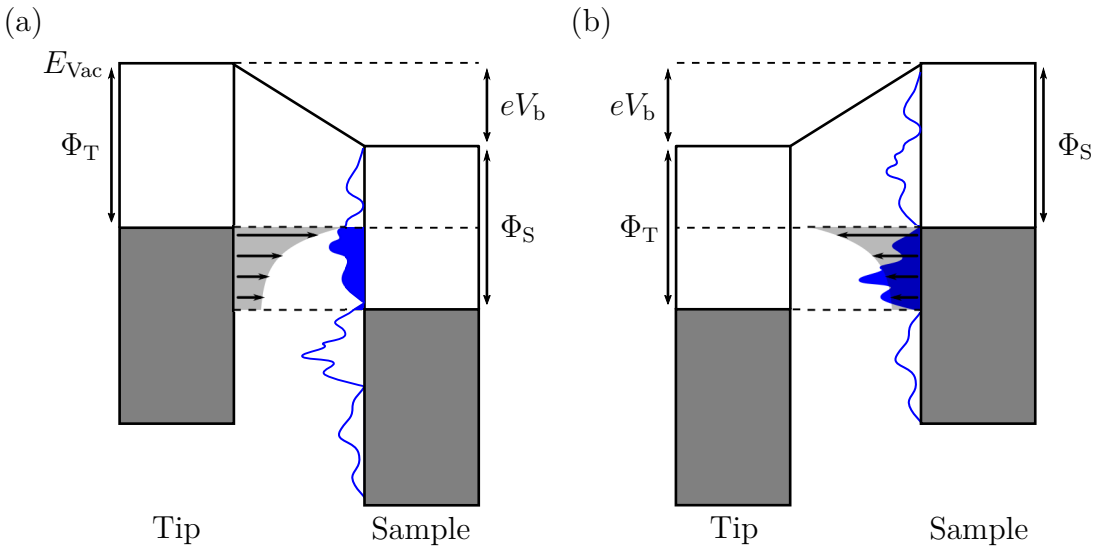

Figure 2.2: Potential energy diagram for the STM under (a) positive sample bias, where electrons tunnel from the tip into the empty states of the sample, and, (b) negative sample bias, where electrons tunnel from the sample filled states into the tip empty states. The transmission coefficient is illustrated by the grey curve and black arrows in the tip-sample gap. The sample LDOS is shown in blue, with the portion available in the tunnelling window filled in. The tip is assumed to have constant LDOS.

We then have an expression for the tunnelling current which depends on the tip and sample LDOS, ρ_t and ρ_s respectively, and on the tunnelling matrix element, which can be approximated using the 1D WKB transmission factor (equation 2.11), $T(\varepsilon, eV_b, z) = |M(\varepsilon)|^2$:[152]

$$I = \frac{4\pi e}{\hbar} \int_0^{eV_b} \rho_t(\varepsilon - eV_b)\rho_s(\varepsilon)T(\varepsilon, eV_b, z)\mathrm{d}\varepsilon. \tag{2.16}$$

Figure 2.2 illustrates the various contributions to the tunnelling current implied by equation 2.16. The workfunction varies from material to material, and is also dependent on orientation and geometry. When a tip and sample with different workfunctions are brought into contact, tunnelling occurs between the two, forming an electric field which aligns the respective Fermi levels. This electric field is known as the contact potential difference (CPD). Here, for the sake of simplicity, we will assume that the workfunction of the tip, Φ_T, and the workfunction of the sample Φ_S are the same, $\Phi_T = \Phi_S = \Phi$, and therefore $V_{\mathrm{CPD}} = 0$. The Fermi level can then be referenced to the vacuum level such that $E_F = -\Phi$.

Here we assume that the tip has a constant LDOS over the energy range spanned by the tunnelling window, as is reasonable for tips prepared as described in section 2.4.3. When a positive bias is applied to the sample, the sample

states are shifted down relative to the tip states, as shown in figure 2.2(a). This opens a tunnelling window of width eV_b within which electrons can tunnel from filled states in the tip to the sample's empty states. The transmission function (equation 2.11) is illustrated by the grey shaded curve in the gap region, and implies that states near the top of the tunnelling window dominate the tunnelling current. When the sample is positively biased, states nearest the Fermi energy of the tip tunnel most strongly into the states at $E_{F,s} + eV_b$. As the bias is scanned over the positive range, it is the LDOS of the sample which dominates the tunnelling current. The reverse is true for negative biases, which highlights the importance of a flat tip LDOS when performing STS.

2.1.4 LDOS extraction

The quantity of interest in most STS experiments is the LDOS of the sample. According to equation 2.16, the tunnelling current at a given voltage also depends on the tip LDOS and the tip-sample separation. A straightforward method of determining $\rho_s(eV_b)$ is not immediately obvious. In early STS experiments, $\mathrm{d}I/\mathrm{d}V(eV_b)$ was used to approximate the sample LDOS,[172] however it is clear that while $\mathrm{d}I/\mathrm{d}V$ provides the contribution to the tunnelling current of the states at $\varepsilon = eV_b$, it is not a good measure of $\rho_s(eV_b)$.[173] Attempts to improve this approximation by normalising the $\mathrm{d}I/\mathrm{d}V$ signal were introduced, first by calculating $\mathrm{d}\ln I/\mathrm{d}\ln V$,[174] and more recently by calculating $(\mathrm{d}I/\mathrm{d}V)/(I/V)$.[175] This method is still widely used, despite evidence that the approximation is flawed and not independent of tip-sample separation.[176] Modelling the system under the WKB approximation has led to the development of a number of methods for extracting LDOS data from STS measurements.[177] The method used in this thesis was developed by Naydenov *et al.*,[178] and is briefly outlined here.

Bardeen's equation for the tunnelling current (equation 2.16) can be differentiated using the mean value theorem for integrals, to give the following expression for the differential conductance $dI/dV(V_b)$:

$$\begin{aligned}\frac{\mathrm{d}I}{\mathrm{d}V}(V_b) = \rho_s(V_b)\rho_t(0)T(eV_b, eV_b, z) - \frac{\alpha z}{\beta\sqrt{\Phi}}I(V_b) \\ + \int_0^{eV_b} \rho_s(\varepsilon)T(\varepsilon, eV_b, z)\frac{\mathrm{d}\rho_t(\varepsilon - eV_b)}{\mathrm{d}V_b}\mathrm{d}\varepsilon,\end{aligned} \tag{2.17}$$

where $\beta = \beta(V_b, \Phi, z) \simeq 4$.

This can be rearranged to give

$$\frac{\mathrm{d}I}{\mathrm{d}V_b}(V_b) - \frac{\alpha z}{\beta\sqrt{\Phi}} I(V_b) = \rho_s(V_b) T(eV_b, eV_b, z) \left[\rho_t(0) + \int_0^{eV_b} P_{s,t}(\varepsilon, eV_b, z) \frac{\mathrm{d}\rho_t(\varepsilon - eV_b)}{\mathrm{d}V_b} \mathrm{d}\varepsilon \right], \tag{2.18}$$

where

$$P_{s,t}(\varepsilon, eV_b, z) = \frac{\rho_s(\varepsilon)}{\rho_s(V)} \frac{T(\varepsilon, eV_b, z)}{T(eV_b, eV_b, z)}. \tag{2.19}$$

If we say that $\rho_s(\varepsilon)$ changes slowly compared to $T(\varepsilon)$, we can say that $P_{s,t} \simeq const. = 1$, and replacing $\mathrm{d}\rho_t(\varepsilon - eV_b)/\mathrm{d}V_b$ with $-\mathrm{d}\rho_t(\varepsilon - eV_b)/\mathrm{d}\varepsilon$, the expression inside the square brackets in equation 2.18 simplifies to $\rho_t(-eV_b)$. We are then left with the combined tip-sample LDOS:

$$\rho_{s,t}(V_b) = \rho_s(V_b)\rho_t(-V_b) \approx \left[\frac{\mathrm{d}I}{\mathrm{d}V_b}(V_b) - \frac{\alpha z}{\beta\sqrt{\Phi}} I(V_b) \right] \exp\left[\alpha z \sqrt{\Phi - \frac{eV}{2}} \right], \tag{2.20}$$

Then only unknown parameters are then the absolute tip-sample separation z and the barrier height Φ. These parameters can be calculated by measuring an $I(V)$ curve and its bias derivative $dI(V)/dV$ at two different tip-sample separations and applying equation 2.20 to each set of measurements. The recovered LDOS should be constant for all tip-sample separations, so we can define

$$\Delta R_{1,2} = \left| 1 - \frac{\rho_{s,t}(V_b, z_1)}{\rho_{s,t}(V_b, z_2)} \right|, \tag{2.21}$$

and find the Φ_0 and z_0 values which give the minimum value for $\Delta R_{1,2}$.

In order to recover the sample LDOS, the ρ_t must be known. The atomic composition and configuration of the tip is usually unknown, but the tip LDOS can be calculated by performing combined tip-sample LDOS measurements on a well-known surface structure. Generally, a good STM probe should have a relatively flat LDOS which would contribute a background $\rho_t(0)$ to the combined tip-sample LDOS, so that the structure of the combined LDOS spectrum reflects that of the sample LDOS.

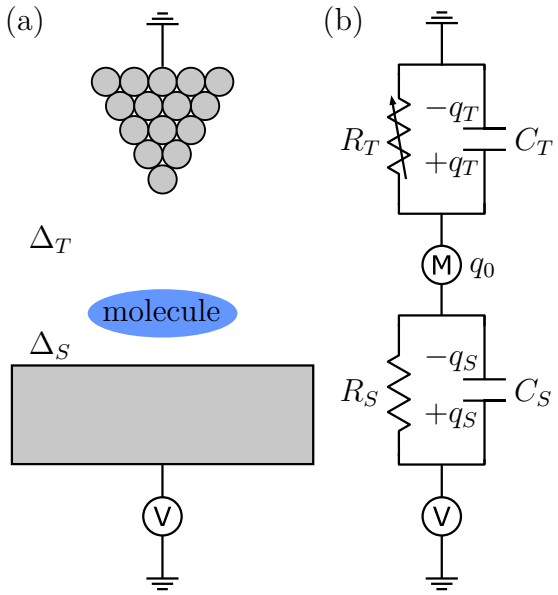

Figure 2.3: A schematic of the DBTJ is shown in (a) where the coupling between a molecule and the substrate is denoted Δ_S and the coupling between the molecule and the tip is denoted Δ_T. Tunnelling in this set-up can be described by the equivalent circuit shown in (b), where R_S and C_S represent the resistance and capacitance, respectively, of the molecule-substrate junction, and the corresponding values for the tip-molecule junction are R_T and C_T. The charges on the molecule-substrate and tip-molecule junctions are denoted q_S and q_T, respectively, while q_0 is a background charge.

2.2 Molecules in the Tip-Sample Junction

As we saw in section 1.3, a molecule has different properties in the gas phase and when coupled to a surface. A molecule in the tip-sample junction is described by two coupling parameters, Δ_T and Δ_S, corresponding to the tip-molecule coupling and molecule-substrate coupling, respectively, as shown in figure 2.3(a). Tunnelling through such a junction can be described by the double-barrier tunnel junction (DBTJ) equivalent circuit,[179] shown in Fig. 2.3(b). The molecule is represented by the circuit element M, which has some predefined voltage response, and resistor-capacitor parallel sub-circuits represent tunnelling through the tip-molecule junction and molecule-substrate junction. Tunnelling through the vacuum gap is modelled by a variable resistor as a reflection of the fact that the tip-sample separation is under experimental control. Since molecules are unstable at small tip-sample separations and high currents, we work under the assumption that $R_S \gg R_T$ and $C_S \gg C_T$. The resistance R_S and capacitance C_S represent the junction between the molecule and the surface.

We treat the cases of strong and weak molecule-substrate coupling separately.

Where the molecule is strongly coupled to the surface, the relevant tunnelling rate will be high, and thus R_S will be very low such that the effect of C_S is negligible. Here weak coupling is considered to correspond to a situation where the MOs of weakly coupled molecules are localised on the molecule itself and do not undergo significant hybridisation with the underlying substrate states. We therefore require that the time an electron spends in the molecular states is greater than the fundamental uncertainty in time described by the uncertainty principle[180]

$$t \gg \Delta t \geq \frac{h}{\Delta E}. \tag{2.22}$$

Since the energy uncertainty of the electron is less than the applied potential $\Delta E < eV_b$, and since the current I cannot exceed e/t because we require that the electrons tunnel into weakly coupled molecules one at a time, we can write the minimum resistance $R_{\min}$ value for R_S and R_T for the molecule to be considered weakly coupled as[180]

$$R_{\min} = \frac{V_b}{I} \gg \frac{h}{e^2} = 25813\ \Omega. \tag{2.23}$$

Note that this should be considered as an order of magnitude calculation, however, more rigorous treatments come to similar conclusions.[181]

In the following, we outline the tunnelling phenomena associated with tunnelling through adsorbed molecules in the strong and weak coupling regimes. Particular attention is paid to the weak coupling regime, where the long excited state lifetimes can give rise to very unusual tunnelling characteristics.

2.2.1 Strongly-coupled molecules

Molecules, especially small ones, generally couple strongly to the metal surface upon which they are adsorbed. As described in section 1.3, strong substrate-molecule coupling causes the discrete molecular levels to broaden, shift and mix.[145] The coupling between the adsorbate and substrate can be described by a perturbation to the Hamiltonian, which causes the delta function-like DOS of the molecule to broaden to a Lorentzian, with a width on the order of an electron volt. The effects of this strong coupling and the resulting implications for the local barrier and LDOS has been described in section 1.3. Tunnelling into the strongly-adsorbed molecule-surface system will result in a current reflective of this modified barrier and LDOS, governed by the principles discussed in section 2.1.3.

The tunnelling current measured on applying some bias V_b has contributions from multiple MOs, even those with energies far from the substrate Fermi level, because of the broadening of MOs.[182] Tunnelling electrons can also excite the vibrational modes of the molecule. Coupling to vibrational modes transfers some of the energy of the tunnelling electron to the molecule where it is dissipated vibrationally. For this reason tunnelling is said to be inelastic, and forms the basis of a spectroscopy, inelastic tunnelling spectroscopy (IETS).[183]

Inelastic tunnelling spectroscopy

Like many of the phenomena observed in STM, IETS was originally developed for metal–insulator–metal junctions.[184] Excitation of phonons during tunnelling increases the tunnelling rate and therefore appear as steps in the differential conductance $\mathrm{d}I/\mathrm{d}V$ at tunnelling voltages which coincide with the energy of a vibrational mode $\hbar\omega_i$.[185] IETS spectra are usually presented as plots of the second derivative of the current with respect to junction bias $\mathrm{d}^2I/\mathrm{d}V^2$ against the junction bias where the vibrational modes appear as peaks. The intensities of these peaks are largest for modes which modify the tunnelling pathway of electrons through the junction, by stretching the C−C bond in a π-conjugated molecule,[185] for example.

Inelastic electron tunnelling may also cause chemical bond-breaking and chemical rearrangement in the tunnelling medium, either by electron-induced consecutive excitation or *via* transient formation of a negative ion.[186] Inelastic tunnelling can also be used to manipulate an adsorbate. or induce conformational changes in a molecule. Detailed discussions of IETS can be found elsewhere.[187]

2.2.2 Weakly-coupled molecules

The tunnelling characteristics of a molecule coupled weakly to the underlying substrate are drastically different to those in the case of strong coupling. Some of the phenomena arising from tunnelling into a weakly-coupled molecule are outlined here. As discussed previously, if the tunnelling rates through the tip-molecule and molecule-substrate junctions are sufficiently low (*i.e.* R_T and R_S are greater than the minimum tunnelling resistance defined in equation 2.23) transport through the junction occurs in a two-step process, known as sequential tunnelling.[188] Depending on the lifetime of the tunnelling electron in the weakly-coupled molecule, the vibrational structure of the molecule may couple to the electronic states, giving rise to new features in the STS, or, if the lifetime is

sufficiently long, the molecule and its environment may relax, stabilising the charge on the adsorbate and resulting in "charge capture".

One effect of this two-step tunnelling process is to give rise to a capacitive charging energy E_C which offsets the energy at which the MOs of weakly-coupled molecules contribute to the tunnelling current.[189] This can be explained through electrostatic modelling of the DBTJ equivalent circuit.

The double-barrier tunnel junction

The weak coupling regime corresponds to a DBTJ structure, the equivalent circuit for which has already been introduced in Fig. 2.3. Analysis of the electrostatic properties of the DBTJ circuit is a very powerful tool for understanding charge transport in the real system.[180]

We start by noting that the charge over each capacitor is $q_i = C_i V_i$ for $i = S, T$, and that the total charge on the molecule is $q = ne = q_T - q_S + q_0$, where $n = n_s + n_T$ is the number of electrons occupying the molecule, and q_0 is a background charge. The potential over C_S is

$$V_S = \frac{C_T V_b + ne - q_0}{C_S + C_T}, \tag{2.24}$$

and the voltage over C_T is

$$V_T = \frac{C_S V_b + ne - q_0}{C_S + C_T}. \tag{2.25}$$

The electrostatic energy stored in the circuit is

$$E_C = \frac{q_S^2}{2C_S} + \frac{q_T^2}{2C_T} = \frac{C_S C_T V_b^2 + (ne - q_0)^2}{2(C_S + C_T)}. \tag{2.26}$$

Electron tunnelling between the molecule and the substrate requires work to be done by the voltage source. The change in the voltage over C_S due to electron tunnelling is

$$\Delta V = V_q - V_{q+e} = -\frac{e}{C_S + C_T}, \tag{2.27}$$

which in turn results in a change in the charge on the capacitor

$$\Delta q_S = C_T \Delta V = -\frac{eC_T}{C_S + C_T}, \tag{2.28}$$

so that the work done by the voltage source can be written

$$W = -\frac{eC_T V_b}{C_S + C_T}. \tag{2.29}$$

A similar expression is valid for the other junction. The Helmholtz free energy can be obtained by subtracting the total work from the electrostatic energy in the circuit:

$$\begin{aligned} F(n_S, n_T) &= \frac{q_S^2}{2C_S} + \frac{q_T^2}{2C_T} + \frac{neC_T V_b}{C_S + C_T} + \frac{neC_S V_b}{C_S + C_T} \\ &= \frac{1}{C_S + C_T}\left\{\frac{1}{2}\left[C_S C_T V_b^2 + (ne - q_0)^2\right] + eV_b(C_S n_T + C_T n_S)\right\}. \end{aligned} \tag{2.30}$$

From this expression we can calculate the free energy change when an electron tunnels through each of the barriers

$$\Delta F_S^{\pm} = F(n_S \pm 1, n_T) - F(n_S, n_T) = \frac{e}{C_S + C_T}\left[\frac{e}{2} \pm (ne - q_0) \pm C_T V_b\right]. \tag{2.31}$$

$$\Delta F_T^{\pm} = F(n_S, n_T \pm 1) - F(n_S, n_T) = \frac{e}{C_S + C_T}\left[\frac{e}{2} \pm (ne - q_0) \mp C_S V_b\right]. \tag{2.32}$$

Using Fermi's golden rule, we can write the rate of tunnelling in terms of the free energy change and the tunnelling resistances $R = R_S, R_T$ [190]

$$\Gamma(\Delta F) = -\frac{\Delta F}{e^2 R(1 - e^{\Delta F/k_B T})}. \tag{2.33}$$

The tunnelling rate between the tip and molecule is much slower than between the molecule and the surface in STM measurements under normal conditions.[191] This means that on average, from the point of view of the tip, the molecule is always in its neutral state.[180] Then we need only consider the change in free energy upon tunnelling through the tip-molecule junction. For tunnelling to occur spontaneously we require the free energy change to be negative. Neglecting the background charge q_0, inserting a factor α to account for the voltage drop over the molecule-substrate junction (equation 2.24),[189] and setting $\Delta F = 0$ in equation

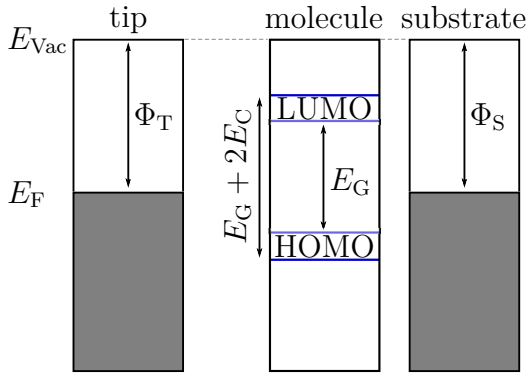

Figure 2.4: Electrostatic charging causes the measured HOMO-LUMO of a molecule adsorbed in a DBTJ configuration to be larger than that of the isolated molecule.

2.31 for $C_S \gg C_T$ gives

$$E_C = \alpha e V_b = \frac{(2n+1)e^2}{2C_S}, \tag{2.34}$$

which is the well-known Coulomb staircase.

The Coulomb staircase is rarely seen for DBTJ structures with a central molecular island because of the presence of multiple conduction channels (MOs) in its energy spectrum.[189] However, the charging energy due to Coulomb blockade has the effect of shifting the energies at which the MOs appear in STS.

When an electron tunnels into the molecular affinity level, it does so at an energy $E_A + E_C$, where E_C is given by equation 2.34, and, similarly, tunnelling into the ionisation level occurs at an energy $E_I + E_C$. This is the source of the difference between the STM transport gap ΔV_{STM} and the molecular HOMO-LUMO gap E_{G}:[192,193]

$$\begin{aligned} \alpha e \Delta V_{\mathrm{STM}} &= \Delta E_{\mathrm{G}} + 2|E_C| = \Delta E_{\mathrm{opt}} - J_{e,h} \\ &= \Delta E_{\mathrm{G}} + \frac{e^2}{C_S} \end{aligned} \tag{2.35}$$

where ΔE_{opt} is the optical gap, $J_{e,h}$ is the electron-hole attraction energy. The increase in the transport gap of a weakly-adsorbed molecule in a DBTJ is illustrated in figure 2.4.

Sequential tunnelling

As previously mentioned, tunnelling through a weakly-coupled molecule occurs one electron (or hole) at a time in a step-wise process known as sequential tunnelling. Figure 2.5(a) shows the potential energy diagram for sequential tunnelling through a positively-biased DBTJ. When an electron tunnels from the tip into the affinity level of the molecule, as represented by the green arrow in figure 2.5(a), it forms a transient molecular ion known as the negative ion resonance (NIR) of the molecule.[192] Since the ground state conformation of the charged state of a molecule is different to the ground state conformation of the neutral species, and since tunnelling is fast compared to nuclear motions (the Born-Oppenheimer approximation), the molecular ion formed on tunnelling into the affinity level is in a vibrationally-excited state. Provided that the lifetime of the NIR is short, such that the electron tunnels into the substrate [red arrow in figure 2.5(a)] before it has time to relax to the ground state conformation of the molecular ion, the spatial distribution of the NIR level corresponds to that of the LUMO.[167] Similarly, the spatial distribution of the positive ion resonance (PIR) corresponds to that of the HOMO, and sequential tunnelling process through the ionisation level is shown in figure 2.5(b). Thus, tunnelling into a weakly-coupled molecule allows its MOs to be mapped out with the STM. However, because the resonances correspond to temporary charging of the molecules, the energies at which they appear in the STS are different to the energies of the MOs, as discussed above.

The parameter α describing the bias drop over the molecule-substrate junction can greatly influence the tunnelling characteristics of the system, and is related to the relative tunnelling rates through each of the junctions, which is dependent on the tip-sample distance. Additionally, when the weak coupling has been introduced by placing a TIL between the molecule and the substrate, α will depend on the thickness and local polarisability of the TIL.[193,194]

Co-tunnelling

Weakly-coupled molecules are visible in STM images measured at tunnelling biases within the transport gap of the molecule. Since we usually adsorb the molecule on a TIL to achieve weak coupling, the push-back effect is expected to be minimal. Molecular dipoles will play a role, however contrast is seen even for molecules without an intrinsic dipole. To explain the source of the extra contrast we look to virtual states.[180]

The overall free energy change for tunnelling between tip and sample is neg-

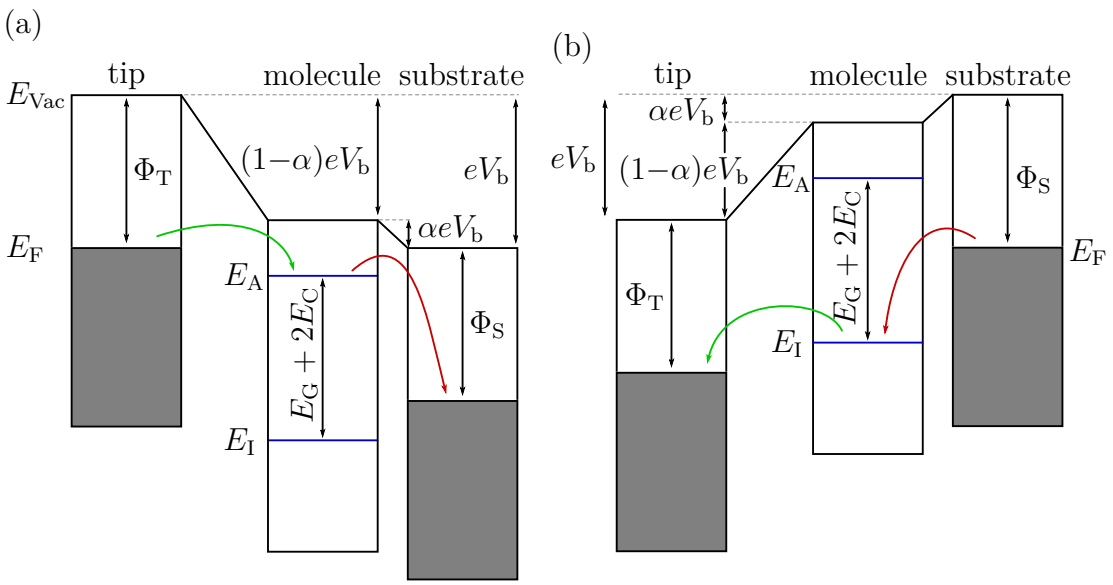

Figure 2.5: When a positive bias potential V_b is applied to the sample, the vacuum level E_{Vac} of the substrate shifts downward by eV_b, and, due to the finite bias drop between the adsorbate and the substrate αV_b, the vacuum level of the adsorbate shifts by $(1-\alpha)eV_b$. When the applied voltage is sufficiently high for the tunnelling window to contain the affinity level E_A, an electron can tunnel into the affinity level (represented by the green arrow), forming a NIR of the adsorbate. After some time τ_{NIR}, which depends on the coupling between the adsorbate and the substrate, the electron tunnels into the substrate, as represented by the red arrow. A similar process occurs for negative sample biases, where holes tunnel through the ionisation level E_I, which is shown in (b).

ative ($\Delta F = -e|V_b|$) even for biases where the free energy change for tunnelling through the individual junctions is positive. This suggests that a second-order process is possible, where electrons simultaneously travel through each of the junctions. This is known as co-tunnelling and is shown schematically in figure 2.6(a), where the electron tunnels through the affinity level such that an energy uncertainty $\Delta E = E_F - E_A - (1-\alpha)eV_b$ is required to conserve of energy. The maximum residence time is then $> \hbar/2\Delta E$.[180]

Lifetime of transient molecular ions

So far we have depicted sequential tunnelling as a process where a charge tunnels into a molecular resonance to form a transient ion, which then relaxes back into the neutral state when the charge tunnels into the other electrode. This is valid for short-lived molecular ions. More complicated processes can occur when the lifetime of the transient state increases, *i.e.* when the coupling between the molecule and the substrate is reduced. When the transient molecular ion lifetime is on the order of a period of a molecular vibration, the tunnelling electron can

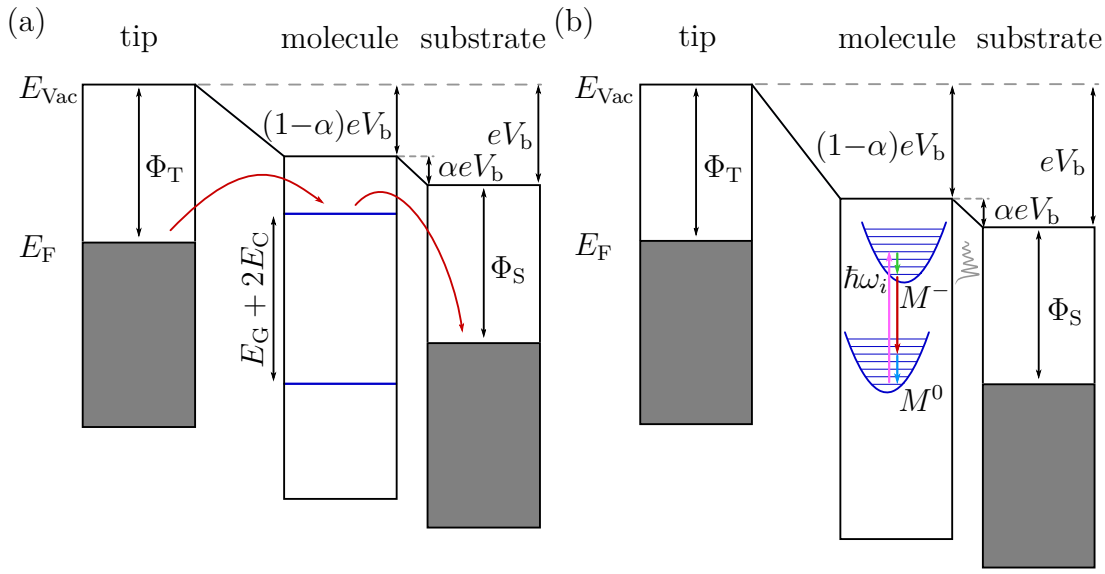

Figure 2.6: The potential energy diagram for the co-tunnelling process is shown in (a), where an electron (or hole) occupies an electronic state outside the tunnelling window for such a short time that the energy is considered conserved because of its corresponding uncertainty. When the lifetime of the molecular resonance is comparable to a vibrational period, the tunnelling electron can couple to the vibronic states of the resonance, as shown in (b). Increasing the magnitude of the potential applied to the sample by $\hbar\omega_i$, where ω_i is the frequency of the excited vibration, adds a new tunnelling channel, such that a Franck-Condon progression associated with the transient molecular ion can be observed in the STS.

couple to the associated vibronic levels.[195] This can lead to satellite peaks for the elastic peak representing a Franck-Condon envelope of vibronic states,[196,197] as shown in Fig. 2.6(b).

The lifetime of the resonance is important, but so too are the relative tunnelling rates into, and out of, the molecule. These quantities are related. As mentioned before molecules are unstable under high currents, corresponding to small tip-sample distances and high tunnelling rates through the vacuum. Therefore we consider that the tip-molecule junction is the bottleneck for tunnelling. The asymmetry in the tunnelling rates means that coupling to vibronic states will appear more strongly for resonant tunnelling through the affinity level than through the ionisation level.[198] The reason for this is illustrated in figure 2.6(b). At positive sample bias corresponding to the ground vibrational level of a molecular resonance ($\alpha eV_b = E_{\mathrm{LUMO+n}} + E_C = E_{A,n}$) an electron tunnels from the tip, through the vacuum gap, into a molecular affinity level. The electron resides on the molecule for some time τ before tunnelling into the substrate. Since in the sequential tunnelling regime the electrons can occupy the molecule only one at a time, and since tunnelling through the DBTJ is limited by the tunnelling rate

through the vacuum gap, any increase in this rate will lead to an increase in the tunnelling current. The tunnelling rate through the vacuum gap depends not only on the tip-sample separation, but also on the number of channels available within the tunnelling window. A molecular vibrational mode, or combination of modes, with energy $\hbar\omega_i$, which is vibronically coupled to the resonance level we are tunnelling into, will contribute an additional tunnelling channel when the magnitude of the sample bias is increased by the energy of the vibration (corrected for the bias drop across the junction), *i.e.*, when $\alpha e\Delta V_b = \hbar\omega_i$. This leads to vibronic replicas of the resonance peak separated by $\hbar\omega_i/\alpha$.

The case of tunnelling into an ionisation level results in weaker, possibly negligible, effects of vibronic coupling on the STS. Here ($eV_b < 0$) an electron tunnels from the substrate through the TIL into the molecule, where it is resident for time τ before tunnelling through the TIL in the rate limiting step. Opening new channels by increasing the bias by $\alpha e\Delta V_b = \hbar\omega_i$ affects only the tunnelling rate into the sample. Since in this regime electrons can tunnel only one at a time, and since the tunnelling current is dominated by the tunnelling rate through the vacuum, the effect of the extra tunnelling channels will be suppressed. In the case of bipolar tunnelling, strong vibronic coupling is possible at either polarity.[194]

It is important to note that the vibrational states seen in the $\mathrm{d}I/\mathrm{d}V$ are those of the transient molecular ion and not of the neutral molecule.[199] We have assumed here that the transient molecular ion relaxes into its ground vibrational state before the electron tunnels out of the molecule. This may not be the case, particularly if there are large conformational differences between the neutral and charged states, in which case the molecular ion may only be able to relax to a local minimum in its conformational potential energy surface. Longer-lived transient states have more time to relax which increases the probability of adopting the lowest energy conformation for that state.

We have also assumed that the molecule is left in its vibrational ground state when the tunnelling electron vacates the level it tunnelled into. This also may not be the case, and if it is not the molecule may or may not have time to relax before another electron is injected. This can have implications for manipulation of weakly-coupled molecules, and for the making or breaking of bonds.[195]

Charge capture

As mentioned in the previous section, the longer-lived a transient molecular ion is, the more likely it is to adopt its lowest energy nuclear configuration. This is equivalent to inner-shell relaxation which was described in section 1.1. Outer-shell

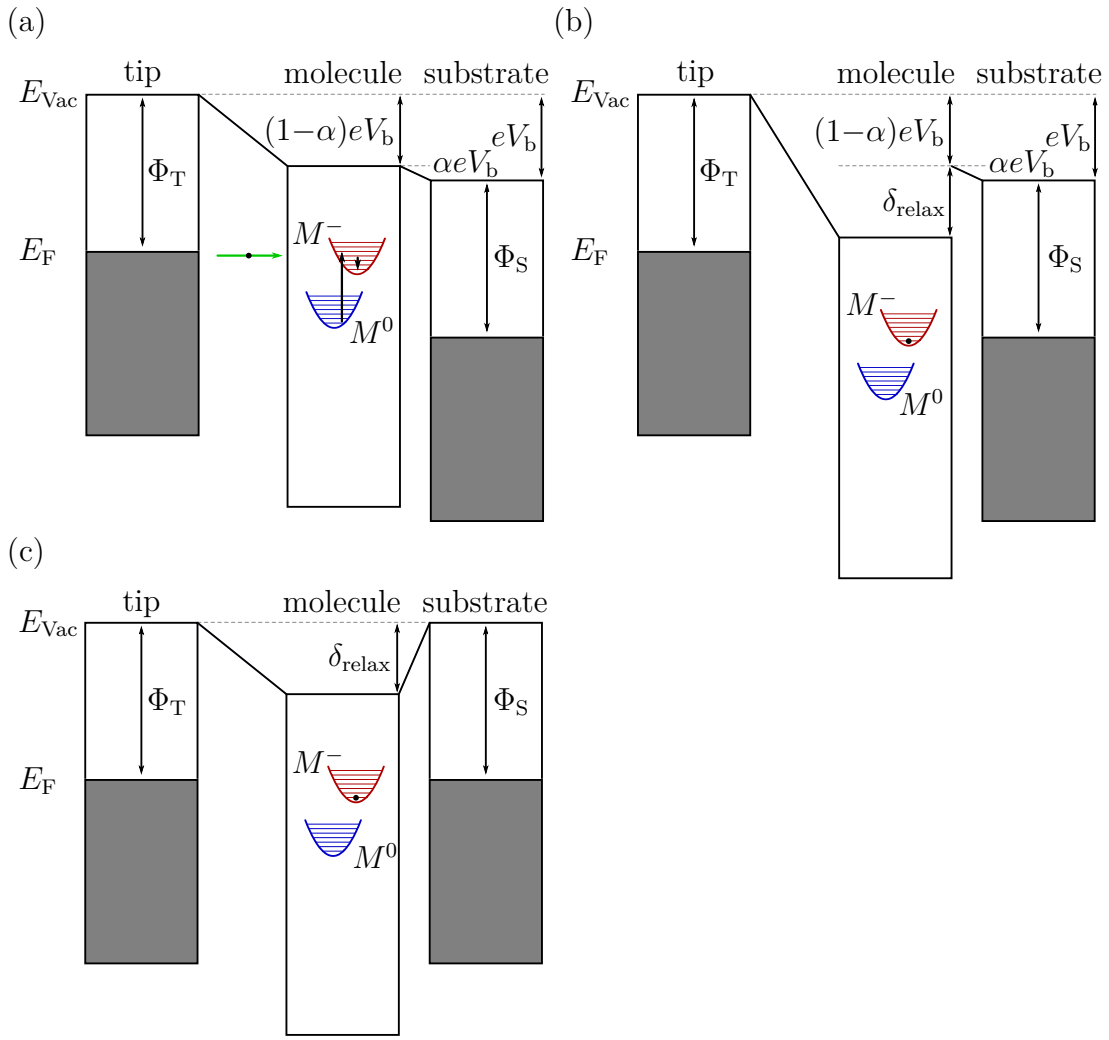

Figure 2.7: The process of charge capture during sequential tunnelling. In (a) an electron tunnels into the affinity level of the adsorbate, forming a transient charged state, M^-. If the lifetime of this state is sufficiently long for inner and outer sphere relaxations to take place, and its energy is sufficiently close to the Fermi level for these relaxations to shift it below E_F, charge capture will take place. Inner sphere relaxations involve configurational changes of the molecule to bring it into the vibrational ground state of M^-, while outer sphere relaxations involve the adsorbate environment and which may produce a dipole δ_{relax}, stabilising the charged state, as shown in (b). Then, when the bias potential is removed, the energy of the charged state will remain below the system Fermi level and the charge will remain on the molecule, as shown in (c).

relaxation is also possible. This refers to relaxations in the geometry of the underlying TIL lattice structure, changes in the image charge induced by the molecule in the underlying substrate, relaxations in the geometry of adjacent molecules, and any other changes in the environment of the molecular ion which lower the total energy of the system. Even if they do not stabilise a charged state, coupling to the vibrations in the supporting lattice can cause a broadening in the

line-shape of the resonance.[167] Inner-shell relaxations lower the relative energy of the excited state, and outer-shell relaxations create potentials which act to oppose the effect of the charge in the excited state.

If the affinity level (or ionisation level) of the molecule is sufficiently close to the Fermi level, the inner and outer shell relaxations can shift the state across the Fermi level, resulting in a stable molecular ion.[6,200] This "charge capture" mechanism is shown schematically in figure 2.7. This was first demonstrated by Repp *et al.*[201] where Au adatoms on NaCl bilayers were charged reversibly. Here the lifetime of the Au^- state was sufficiently long to allow coupling to the vibrations of the NaCl ionic lattice and for relaxations in that lattice to take place. Bistable charge states have subsequently been observed in a range of molecules on surfaces including NaCl/Cu(111),[158] Al_2O_3/NiAl(110),[6] and h-BN/Ir(111).[193] In all cases the relaxation of the TIL lattice was the dominant factor driving the stabilisation of the charged state. A hysteretic $I(V)$ loop is the signature of a bistable charge state in an adsorbate.

2.3 Instrumentation

2.3.1 The scanning tunnelling microscope

A schematic of an STM is shown in figure 2.8. The STM consists of an atomically-sharp metallic tip mounted on a piezo-electric actuator which is capable of controlling the tip position with an accuracy below 1 Å in x and y and at least 0.01 Å in z.[152] Many different configurations of the piezoelectric actuator have been used to achieve this positional stability. Here we show a tube scanner, which is one of the most widely used configurations due to its high resonance frequency, which helps minimise vibration transmission and allows high speed imaging.[202] The tube scanner has three sets of electrodes, controlling deformation in x, y and z. The potentials applied to the x and y electrodes are specified by the user to scan over an area of a known size (once the piezo constants have been calibrated using a reference sample).

To begin a STM experiment, the tip must first be brought within tunnelling range of the sample. First, the tip is brought macroscopically close to the surface using the course approach mechanism which moves the entire piezotube using stick-slip motion of piezoelectric actuators. An automated approach mechanism is then used to bring the tip 4 Å to 7 Å from the sample. Here the dynamic range of the z-piezo is swept while the circuit searches for the set-point current. If this

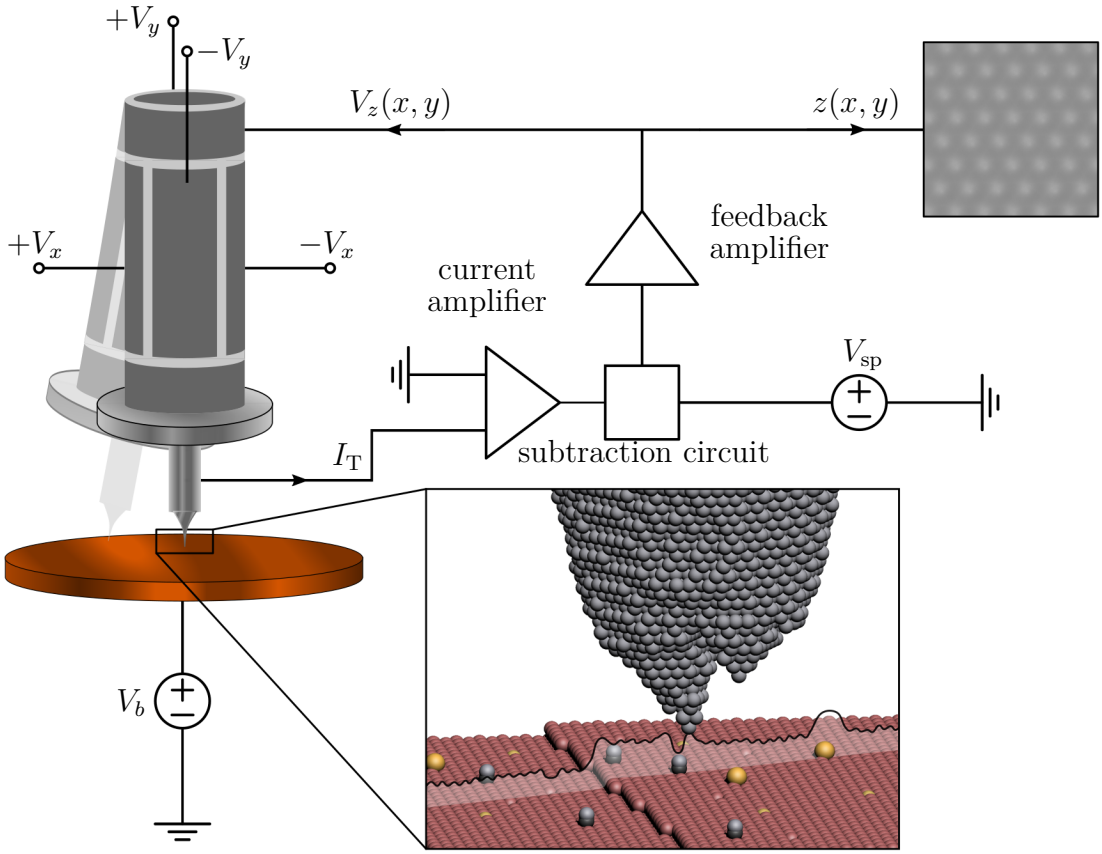

Figure 2.8: Schematic of a scanning tunnelling microscopy.

current is not available, a course approach step is taken which is smaller than the dynamic range of the z-scanner. This process is repeated until the tip is close enough to the sample to draw the set-point current.

We have experimental control over two out of three parameters during an STM experiment: the sample bias V_b, the set-point current I_{sp}, and the tip-sample separation z_{piezo}. There are two primary modes used for STM imaging: constant-current mode, where V_b and I_{sp} are fixed while z_{piezo} is recorded, and constant-height mode, where V_b and z_{piezo} are fixed while I_T is recorded.

2.3.2 STM imaging modes

In **constant-current** mode, the potential applied to the z-electrode is obtained from a feedback mechanism, where the measured tunnelling current (typically 2 pA - 2 nA) is amplified and converted to a voltage using an operational amplifier (with a gain of $1 \times 10^9\,\mathrm{V\,A^{-1}}$, and a cut-off frequency of 1.1 kHz) in the current-amplification mode. This signal is then subtracted from a reference voltage corresponding to the set-point current. The resulting voltage signal is amplified and fed back to the z-piezo, so that the tip-sample separation is adjusted

to minimise $|I_T - I_{sp}|$ using a digital proportional–integral (PI) controller. We use only the integral term, with a time constant on the order of 400 µs. We therefore obtain a set of coordinates of the form $z_{\text{piezo}}(x, y)$. This can be plotted as a contour map, commonly referred to as a topological map, however it does not necessarily correspond to the geometrical topography of the sample. The measured z_{piezo} does not exactly correspond to the absolute separation of the tip and sample, but is dependent upon the local electronic properties of the sample at the tunnelling bias. The $z_{\text{piezo}}(x, y)$ map is in reality a map of the surface of constant LDOS at the applied bias.[203] A schematic feedback mechanism is shown in Fig. 2.8, with the inset showing the path of the tip above a surface during imaging in constant-current mode.

The other imaging mode is the **constant-height** mode. Here the tip is rastered in x and y with the feedback loop is disconnected. The tunnelling current is measured, so that we get a map of the current magnitude at every point $I_T(x, y)$. The absence of a feedback mechanism allows for high frequency imaging, however it is extremely risky, since the current can reach very high values if a surface feature approaches the set-point tip-sample separation. Additionally, the background plane of the sample must be carefully defined, which can be very difficult in the presence of drift. For this reason, constant-current imaging is much more widely used.

2.3.3 Scanning tunnelling spectroscopy

Two of the three experimental parameters V_b, I_{sp}, and z_{piezo}, can be independently varied over a point on the surface, while measuring the third, to provide a wealth of information about the electronic properties at that point. There are three primary tunnelling spectroscopies:[152]

- $I(V_b, z)$ spectroscopy, which is known as constant-height spectroscopy if z is fixed, or variable-height spectroscopy if z varies in a predefined way.
- $Z(V_b)$ spectroscopy, which is known as constant-current spectroscopy.
- $I(z)$ spectroscopy.

To record an $I(V_b, z)$ spectrum, we measure the tunnelling current as V_b and z vary in some pre-programmed way.[178] Since the tunnelling current is an integral over all the states in the bias range from the Fermi level to V_b (equation 2.16), the differential conductance signal $\mathrm{d}I/\mathrm{d}V$ is often measured using a lock-in amplifier to track a small AC signal (10 mV, 966 Hz) applied over V_b, to identify the

contribution of the state at V_b to the tunnelling current. At bias ranges where the current is quite flat, the current can be measured as the bias is scanned at constant height, while maintaining a high signal-to-noise ratio. Over larger bias ranges, z should be varied to keep the measured current high enough for low noise, and low enough to avoid modifying the tip and/or sample. Moreover, measuring $I(V_b, z)$ at two different tip-sample offsets while recording the $\mathrm{d}I/\mathrm{d}V$ signal allows the LDOS to be extracted as described in section 2.1.4.

In constant-current spectroscopy we measure the response of z_{piezo} as the sample bias is swept, while keeping the current fixed at some set-point. This allows large bias ranges to be measured without losing resolution, however care must be taken with biases close to the Fermi level and with samples with a band-gap since the tip-sample distance may be reduced to very small distances in these regions to try to obtain the set-point current which can modify the tip and/or surface. Here we also tend to look at the $\mathrm{d}I/\mathrm{d}V$ signal for ease of identifying states of interest.

We can also fix the sample bias, and vary the tip-sample distance while monitoring the current response. This is $I(z)$ spectroscopy. In the tunnelling regime, we expect an exponential increase of the current as the tip-sample separation is reduced, as governed by the transmission coefficient (equation 2.11). The exponent of this decay provides an estimate of the apparent barrier height, provided there are no sharp peaks in the LDOS near the sample bias at which the measurement is carried out.

The $\mathrm{d}I/\mathrm{d}V$ signal can also be recorded while imaging. As mentioned above, the $\mathrm{d}I/\mathrm{d}V$ signal corresponds to the contribution of the states at V_b to the tunnelling current. Therefore the $\mathrm{d}I/\mathrm{d}V$ signal obtained while scanning maps out the relative intensity of the square of the sample wavefunction at energy eV_b.

2.4 Experimental Details

2.4.1 The UHV system

The STM apparatus, shown in figure 2.9, consists of three UHV chambers: the STM chamber, the preparation chamber, and the load-lock. The load-lock can be vented and pumped independently of the other two chambers *via* a turbo-molecular pump, enabling transfer of samples and tips without breaking the vacuum. The load-lock has a base pressure of 1×10^{-10} mbar after a 48 hour bake. An ESD system, described in the next chapter, is mounted on the load-lock.

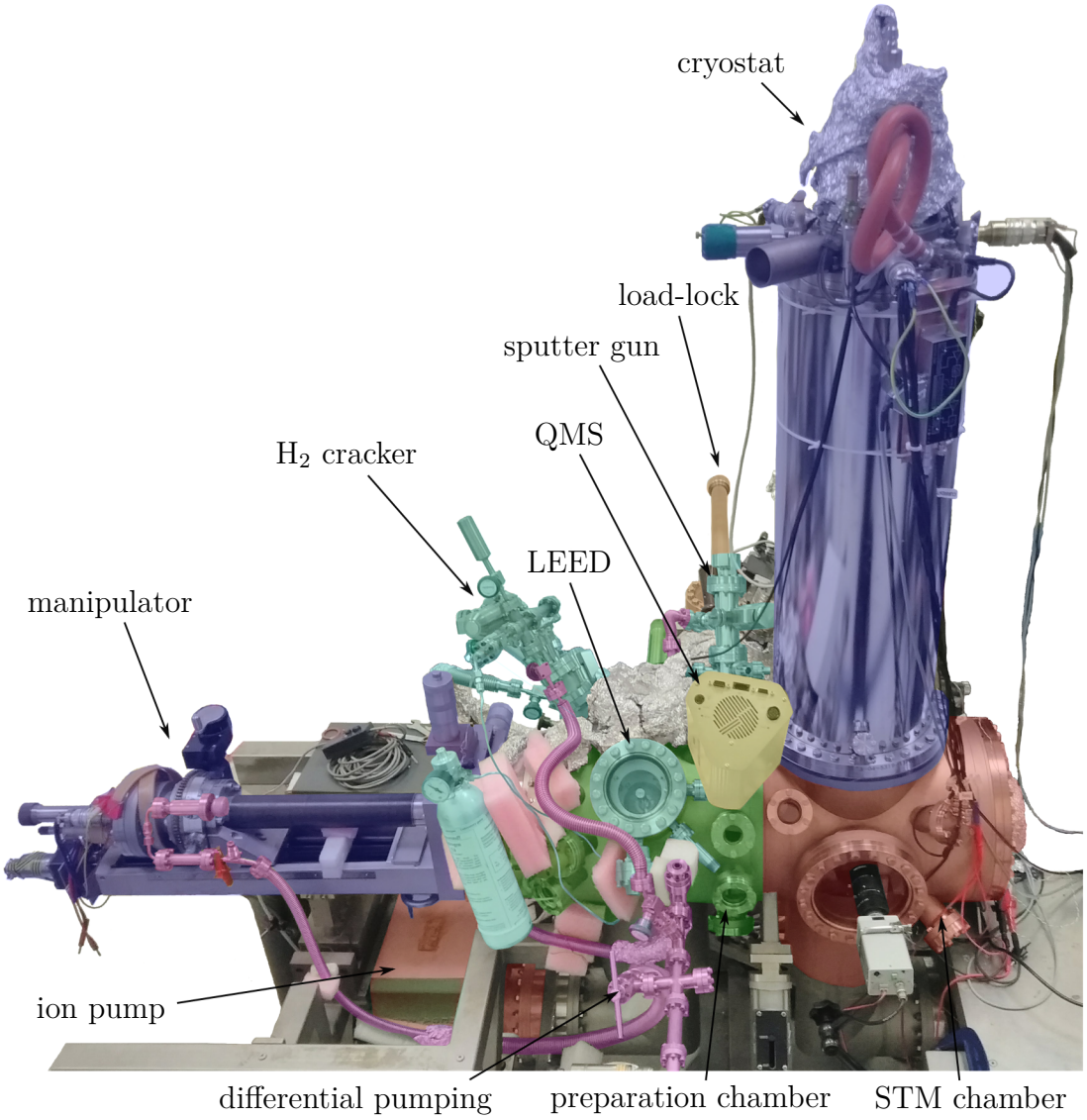

Figure 2.9: The UHV system used in this work, which consists of three chambers: the STM chamber which is cooled by a cryostat and houses the CreaTec STM, the preparation chamber which has various attachments for preparing and analysing samples, and the load-lock chamber which allows new samples to be introduced to the system without breaking the vacuum in the preparation and STM chambers.

The preparation chamber has a base pressure of 5×10^{-11} mbar, and contains various tools for preparing and analysing a sample. The preparation chamber is equipped with a quadrupole mass spectrometer (QMS), a sample storage stage with spaces for up to five samples and an additional vertical sample mount for NaCl deposition, a sputtering gun, a low-energy electron diffraction (LEED) apparatus, and a H_2 cracker for hydrogen passivation of silicon. The system is equipped with a manipulator which allows transfer of samples between the chambers. The manipulator is generally kept at room temperature, but can be cooled

by liquid nitrogen if necessary. The preparation chamber is pumped by an ion pump, equipped with a titanium sublimation pump, and is separated from both the STM chamber and load-lock by gate valves. The STM chamber (base pressure $<3 \times 10^{-11}$ mbar) houses the scanner assembly which is cooled by a bath-type cryostat.

Since diffusion is an activated process, it can be frozen out at low temperatures, affording us highly stable surfaces where individual features can be studied for long periods of time. Additionally, operation of the STM in UHV means that the sample remains clean almost indefinitely. The cryostat also helps to reduce the pressure by acting as a cryopump. The cryostat has two stages: a 4 L inner cryostat, which is itself cooled by the 15 L outer cryostat. Both cryostats are kept at 77 K using liquid nitrogen, however the inner cryostat can be further cooled to liquid helium temperatures. In addition to freezing out atomic and molecular motion, working at lower temperatures reduces the thermal drift and sharpens the Fermi surface of the sample under investigation.

Since the tip-sample distance is one of the critical experimental parameters, the microscope must be very stable with respect to vibrational excitation. Successful operation of a STM therefore requires adequate mechanical isolation. The tip-sample distance should be stable to within 0.01 Å to allow operation at tunnelling current set-points in the pA range.[152] The STM and preparation chambers are pumped by ion pumps which have no moving parts and emit no vibrations, and during scanning the load-lock turbo pump is switched off. As mentioned above, all elements of the STM scanner assembly are designed to be compact and rigid so that it has a high resonance frequency and a low transfer function for ambient vibrational frequencies. This comes down even to the choice of material used for the tip, where tungsten and PtIr are popular choices, partly because of their high stiffness. Additionally, a number of vibration isolation techniques are used to filter out vibrations which are transmitted through the frame or in the ambient. The whole UHV system is suspended on Newport pneumatic dampers, and vibrations transmitted to the system are excluded from the scanner by the combination of suspension springs with eddie-current dampers which attach the STM head to the cryostat.

2.4.2 The CreaTec low-temperature STM

The microscope used in the experiments presented in this thesis is a commercially available CreaTec LT-STM. The microscope head, shown in Fig. 2.10 is based on the Pan-type slider.[204] This design is structurally rigid which aids in avoiding

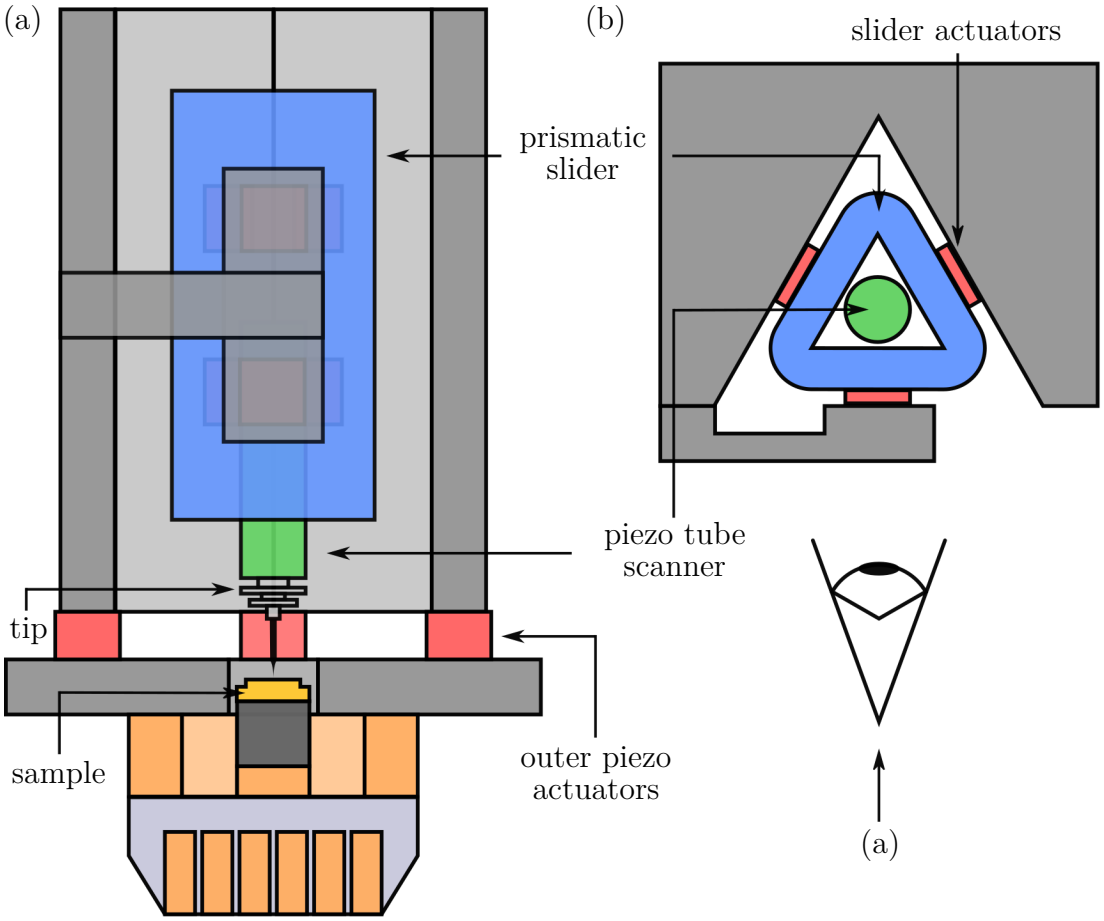

Figure 2.10: A front (a) and top (b) view of the CreaTec Pan-type slider STM scanner assembly.

transfer of mechanical vibrations as already discussed. In the Pan-type scanner, a triangular prism with polished sides is attached to the STM body by a pair of shear piezoeletric actuators on each side.[205] Two of the actuator pairs are mounted directly to STM body, while the other is mounted onto a beam that is pushed down by a stiff plate spring. The prism can be manipulated in the z-direction using slip-stick motion of the piezo stacks.

The prism itself is hollow, and a piezoelectric tube scanner is mounted inside. Contacts for mounting the STM tip or qPlus sensor are attached to the top of the scanner tube. This whole assembly is mounted on piezoelectric actuators which allow for course positioning in x and y. During scanning z is finely controlled by the tube scanner, while the (x, y) position can be controlled either by the tube scanner or by the outer piezo stacks. We use the tube scanner for (x, y) positioning in the work presented in this thesis.

2.4.3 Tip preparation

The tip plays a crucial role in determining the quality of data acquired in STM experiments. The reciprocity principle states that the electrode with the sharper wavefunction will image that with the more diffuse one,[203] which in practice means that the tip must be sharp to avoid experimental artefacts such as multiple tips. Additionally, as we have seen in equation 2.16, STS measures a convolution between the LDOS of the tip and the sample. We therefore require the tip LDOS to be featureless in the tunnelling bias range. This is particularly important in analysis of the filled states, where tip features dominate the spectra [see Fig. 2.2(b)]. For these reasons we take particular care to prepare and characterise the STM tips.

STM tips are etched from tungsten wire using 2 M NaOH and the DC current method described by Ibe *et al.*[206]. Here, a length of high purity tungsten wire is placed above the centre of the NaOH beaker. A stainless steel loop is positioned in the liquid, centred on the tungsten wire. A potential difference of $\sim$5 V is applied between the tungsten wire anode and the stainless steel cathode. The exact value of the etching voltage governs the resulting tip aspect ratio. Since etching occurs mainly at the meniscus, the wire is dipped into and retracted from the liquid several times to remove the oxide and smoothen it. The tip is then etched, by immersing the end of the wire in the NaOH with the circuit on. The electrochemical reaction proceeds as follows:

$$\begin{aligned}
&\text{Anode:} && \mathrm{W} + 8\mathrm{OH}^- \longrightarrow \mathrm{WO_4}^{2-} + 4\mathrm{H_2O} + 6\,\mathrm{e}^- \\
&\text{Cathode:} && 6\,\mathrm{H_2O} + 6\,\mathrm{e}^- \longrightarrow 3\,\mathrm{H_2} + 6\,\mathrm{OH}^- \\
&\text{Overall:} && \mathrm{W} + 2\mathrm{OH}^- + 2\,\mathrm{H_2O} \longrightarrow \mathrm{WO_4}^{2-} + 3\,\mathrm{H_2}
\end{aligned}$$

A neck forms at the meniscus, as shown in figure 2.11(a), and when it becomes sufficiently small for the weight of the section below to overcome the tensile strength of the neck, the neck breaks, leaving an extremely sharp tip. The control circuit, which monitors the current differential, shuts off the power when this occurs to avoid the newly formed tip being blunted by the etching process. Any residual salt from the etching process is removed by immersion in deionised water. When loaded into the UHV chamber, these tips are annealed to approximately 1000 K using electron bombardment to remove the wet oxide resulting from the etch process.

Since we are mainly interested in examining the STS of molecular systems, it is important to have a reliable probe with known chemical composition and $\rho_T(E)$, due to the convolution of tip and sample LDOS. To ensure we have a

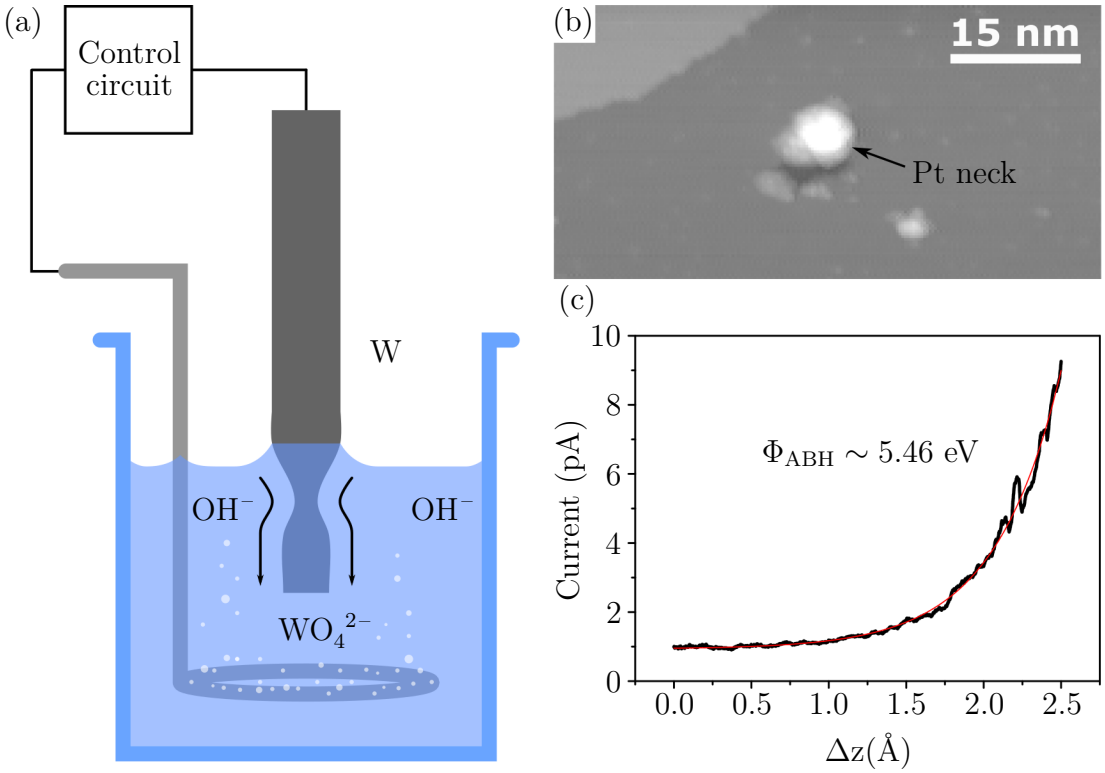

Figure 2.11: High quality STM tips are prepared by etching tungsten wire in a NaOH solution as shown in (a). These tips are then inked on Pt(111), by locally melting the surface by forming a contact with the tip. Withdrawing the tip from the surface forms a neck, an example of which is presented in (b). The composition of the tip is confirmed by carrying out $I(z)$ spectroscopy (section 2.3.3) where an apparent barrier height of approximately 5.5 eV is expected between a Pt tip and surface.

metallic tip with relatively flat density of states, tips are inked and characterised on a single crystal Pt(111), using the method described by Naydenov *et al.*[207] The inking process involves approaching the tip to contact, and locally melting the Pt surface in the contact area. A Pt neck is extruded from the surface as the tip is withdrawn, which eventually breaks, leaving Pt atoms forming the apex of the tip and a feature on the surface, an example of which is shown in figure 2.11(b). This process is repeated until the resulting tip is sharp, which can be verified by scanning over the Pt surface feature left after inking, and has a featureless $\rho_T(E)$, and until the tip is thoroughly covered in Pt, as confirmed by the observation of an apparent barrier height of 5.5 eV in the $I(z)$ spectra. A representative $I(z)$ spectrum between a Pt tip and a Pt(111) surface is shown in Fig. 2.11(c).

3

Electrospray Deposition

The first problem to be overcome in any surface science investigation is that of preparing the substrate surface and to deposit on it the target system to be investigated. Since here we are interested in probing QCA candidate molecules with STM and STS in UHV, we need a technique capable of depositing these molecules on conductive substrates with controllable coverage. This is non-trivial given the complexity implicit in any MQCA candidate and the low tolerance for impurities.

The study of adsorbates has a long history in surface science, with the development of new techniques being required to enable the deposition of increasingly complex adsorbates. Simple metals are usually deposited by sputtering or evaporation, while more complicated materials can be deposited by molecular beam epitaxy (MBE)[208] or chemical vapour deposition (CVD).[209] Gas-phase molecules are introduced to a UHV system through a leak valve, where their sticking coefficient on a surface can be controlled by varying the sample temperature.

Molecules are often transferred to a clean surface in vacuum *via* sublimation,[210] however this is limited to molecules which are relatively volatile and thermally stable.[211] Vapour pressure tends to decrease with molecular weight, which in turn leads to higher temperatures being required to sublimate the molecule in experimentally useful quantities. At some point the thermal energy required for sublimation will approach the energy of the weakest bond in the molecule, leading to fragmentation. When considering highly-functionalised molecules designed specifically for applications such as molecular electronics, this threshold is easily reached. As will be seen in the next section, our QCA candidate molecules are not compatible with sublimation-based deposition. It is clear then that alternative

strategies for surface preparation are needed.

One approach is to build the QCA structure from the bottom-up by depositing and assembling molecular precursors.[212] This approach has been quite successful, for example in the case of graphene-like macromolecules which can be constructed from relatively simple building blocks.[213–216] However, an obvious limitation of bottom-up assembly, which will be discussed in more detail in chapter 7, is that it must be possible to deposit precursors by conventional methods and they must survive the assembly conditions.

In section 3.1 some alternative strategies for preparing thin films of complex molecules are reviewed and, of these, ESD is identified as the most promising. ESD is a technique that has its origins in mass spectroscopy (MS),[217,218] where it is used to produce gas-phase ions of fragile analytes. This technique has since been adapted to prepare samples for analysis in UHV.[219] Section 3.2 lays out theoretical framework behind ESD, while the experimental details of the ESD set-up are outlined in section 3.3. Finally, in section 3.4, we discuss the impurities that are an unavoidable consequence of exposing a surface to an electrosprayed solution.

3.1 Molecular Deposition Strategies

By far the most common method of depositing molecules onto a surface in UHV involves sublimating the molecules from a Knudsen cell.[210] Molecules are heated in a crucible until they enter the gas phase, where they then impinge on the sample *in vacuo*. This technique is often referred to as organic molecular beam epitaxy (OMBE), despite the fact that the growth may or may not be epitaxial, depending on the details of the molecule-substrate interaction.[220] OMBE is ubiquitous in molecular surface science, primarily because the coverage can be finely controlled after careful calibration. Additionally, OMBE is an extremely clean deposition method, provided the source material is of high purity and has been well degassed.

Of course, OMBE is not without its limitations. To facilitate OMBE, the molecule should be thermally stable at least up to the sublimation temperature, otherwise unwanted reactions will compete with the formation of the molecular beam. Dissociation occurs when the thermal energy approaches the intramolecular binding energies (typically 2 eV to 4 eV), but other types of reactions, such as polymerisations, are possible.[221] In general, OMBE is suitable for molecules with a molecular weight not exceeding $1000\,\mathrm{g\,mol^{-1}}$.[222]

Due to the their large size and fragility, many biologically and electroni-

cally interesting molecules have traditionally been out of reach of the powerful tools developed for UHV surface analysis.[223,224] Since, as we saw in chapter 1, MQCA candidates require a certain level of complexity in order to incorporate the electronic, structural and organisational properties required for viable QCA functionality, we anticipate that it is likely they will be thermally labile. Indeed, other groups have found that their QCA candidate molecules were not OMBE-compatible.[110–113,225]

3.1.1 Decomposition of MQCA candidates upon sublimation

To prove the need for an alternative to OMBE, we attempted to sublimate our MQCA candidate molecule in UHV. The molecule used here, ZnTFcBP, is shown in figure 3.1(b) and consists of a TPP molecule with the hydrogen at the 4-position on each phenyl ring exchanged for N-(1-ferrocenylethyl)acetamide. This molecule is described in greater detail in chapter 4. First, we formed an OMBE source by electrospraying multilayer coverages of ZnTFcBP onto a clean Au(111) surface in UHV. This sample was held in front of a second Au(111) sample and annealed to approximately 800 K. The resulting surface was then analysed with STM, and is shown in figure 3.1.

As can be seen from figure 3.1(a), well-organised molecular islands are found on the otherwise relatively clean surface. The rod-like species observed on the surface is an impurity species we see after every deposition by electrospray, which seems to have been co-deposited with the molecule during OMBE. These contaminants are described in greater detail in section 3.4. The other features on the surface are due to tip-forming in the vicinity.

These molecular islands appear qualitatively different from those observed when the intact molecules assemble on Au(111), which are described in section 4.3. Here, particularly in Fig. 3.1(f), we clearly resolve the porphyrin core of the molecule, as well as the phenyl rings. Most of the porphyrin rings are in the planar configuration, while some have a saddle geometry, as can be distinguished from the elevated position of two opposite pyrrole rings in the topography.[226] However, we observe no feature which can be attributed to the Fc groups, which leads us to conclude that they have detached from the molecule during sublimation. The square unit cell of the molecular islands has a side length of ∼19 Å, very similar to that measured for islands of 5,10,15,20-tetra-(4-carboxylphenyl)porphyrin (TCPP) which self-assemble with a cyclic hydrogen bonding structure.[227] We cannot say with any certainty exactly which bond has been broken, however, since TPP molecules pack with a nearest-neighbour distance of 14 Å,[228] we be-

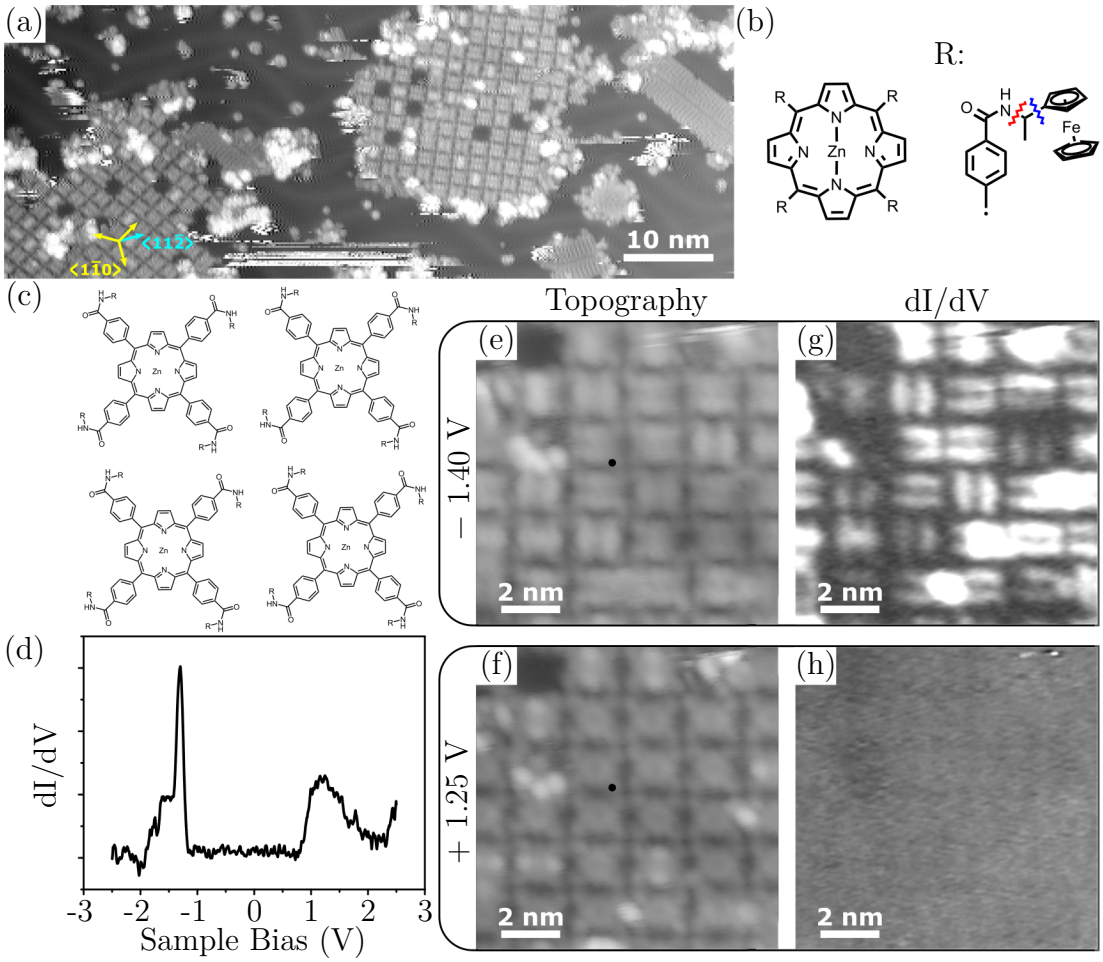

Figure 3.1: OMBE of ZnTFcBP [sketched in (b)] onto Au(111) results in the surface shown in (a). No feature corresponding to the Fc groups are observed indicating the molecule has fragmented, and possible fragmentation points are shown in red and blue in (b). The structure of the assembly is proposed in (c). Variable-height STS on the π-system of molecular fragments at is shown in (d), recorded at the location marked by the black dot in (e) and (f).

lieve that the hydrogen bonding groups are still attached. In the sketch of the molecule in Fig. 3.1(b), the red and blue markers indicate bonds which may have been broken. A proposed packing model is shown in Fig. 3.1(c).

We have also performed STS on these islands. In the spectrum presented in Fig. 3.1(d), we see a sharp peak at −1.4 V in the filled states, corresponding to the HOMO, and a broad LUMO peak at 1.25 V. Topographic maps of the HOMO and LUMO are shown in Fig. 3.1(e) and (f), respectively, while the corresponding $\mathrm{d}I/\mathrm{d}V$ intensity maps are shown in Fig. 3.1(g) and (h). The HOMO has a double lobe structure, while the LUMO is delocalised over the entire molecular island.

It is clear that our MQCA candidates are not OMBE compatible, and that an alternative deposition strategy is required.

3.1.2 Alternatives to OMBE

Molecular thermolability does not, however, rule out deposition by sublimation. Fragmentation during OMBE can be minimised by exploiting the kinetics of the sublimation and dissociation processes. Since the fragmentation and sublimation processes will have different activation energies, there will be a temperature regime at which the rate of one process is strongly favoured over the other. Here we will assume that the activation energy for sublimation is lower than that for fragmentation, such that at high temperatures sublimation is favoured. Then, by supplying thermal energy to the molecules on a short time-scale, far more molecules should enter the gas phase than dissociate. This is the rapid heating deposition technique.[229] Crucibles are generally incapable of the time-response required for deposition *via* rapid heating, so analyte-covered filaments or laser pulses are more often used.[222,230] Rapid heating can be an effective way of depositing molecules, however it can be difficult to obtain high-coverages with this technique, and very large molecules or nanomaterials may still present difficulties.[231]

These very large molecular structures can be transferred to the surface using a technique known as dry contact transfer.[232] Here, a fibreglass brush is covered in a powder of the analyte species, which is then transferred to the UHV chamber and brought into direct contact with the sample. Some analyte particles will be transferred to the sample surface. The primary drawback of this technique is that large clusters are often transferred to the sample, which can destroy a STM tip, and when only single analyte species are transferred they can be very difficult to find. However, for non-volatile, insoluble species such as carbon nanotubes, the dry contact transfer method can be the most viable option.[233]

For soluble analytes, pulsed valve deposition is possible.[223] Here, a solution containing the analyte species is introduced to the vacuum chamber through a very small aperture (50 µm to 500 µm) which is opened for a very short period of time (∼100 ms). The coverage is controlled by varying the number of solution pulses incident on the sample, however this is not very reproducible due to the complex fluid dynamics involved. During pulsed valve deposition, very high pressures of up to 1×10^{-5} mbar can be reached. Solvent molecules have been reported to stick to the surface even when deposition takes place far above the reported desorption temperature of the solvent.[234,235] MQCA candidates investigated by other groups were deposited *via* pulsed valve.[110–113,225]

The main advantage of the pulsed valve method is that solubility is the only limiting factor in terms of the kinds of species which can be deposited. ESD is

a technique which retains this advantage, but allows for better coverage control and lower operational pressures.[219] Here, ionised droplets are produced from an electrified solution. These droplets undergo a desolvation process, eventually forming gas-phase ions which are subsequently introduced to vacuum through a differentially-pumped controlled leak, where they subsequently impinge on a sample. ESD allows different types of molecules to be deposited under the same conditions, forgoing the need for arduous calibration processes for each. This is attractive for our work where the properties of QCA candidate molecules may need to be tuned. Additionally, it has been reported that molecules electrosprayed onto insulating substrates can retain the charge they picked up during the ESD process,[236–238] which may be useful for MQCA applications. In the next section we outline the ESD process.

3.2 Principles of ESD

The challenge of non-destructively generating gas-phase ions from complex molecules, particularly biologically relevant ones such as proteins, was a long standing issue in mass spectroscopy. Many "soft" ionisation process have been devised to this end,[239–242] and electrospray ionisation (ESI) has emerged as the most popular of these.[218] ESI was pioneered by Dole[217] and developed by Fenn,[243] and is now ubiquitous in mass spectroscopy. It is now possible to produce intact ionised species with molecular weights greater than 1×10^8 Da using ESI-MS.[244–246]

Instead of being fed into a mass spectrometer, the ionised molecular beam can instead be directed onto a surface where the material is deposited. This is known as preparatory mass spectrometry (p-MS), and was originally used for separating nuclear isotopes as part of the Manhattan project.[247] The first use of electrospray-based p-MS was in preparing thin films of radioactive material for use as alpha particle sources.[248] Later, ESD was used for fabrication and deposition of nanoparticles,[249–252] and for producing thin films of polymers[253] and biomolecules.[254,255] Thundat *et al.*[256] used electrospray to deposit DNA on a Au sample for ambient STM analysis. Electrospray was brought to UHV as early as 1977 where it was used to modify metal surfaces.[257] However, it was James O'Shea's group at Nottingham who pioneered the development of electrospray as a technique for depositing intact analytes onto surfaces in UHV to be analysed with conventional surface science tools.[258]

The electrospray ionisation process occurs in three stages.[259] First, the solution containing the analyte species is extruded through an electrified capillary,

where the high electric field causes the surface tension of the liquid to be overcome by the electrostatic repulsion of the molecules within the solution. This leads to the formation of a conical meniscus at the end of the capillary. Within a certain potential range, small charged droplets are emitted from the apex of the cone. In second stage of the ESI process, solvent molecules evaporate from the droplets, leading to an increase in repulsive forces between the charges within each droplet. Above a threshold charge-to-volume ratio, these droplets undergo a "Coulomb explosion", where the droplet splits up into many progeny droplets. This process continues until ionised molecules are formed in the third stage of the ESI process. There are competing models for the formation of ions from the droplets, and which of these models is a better description of the ion formation process depends on the properties of the analyte species.

These three stages of ESI are described in more detail below.

3.2.1 Formation of the Taylor cone

In the first stage of the ESI process, a solution containing the species of interest is fed from a reservoir to a narrow, conductive capillary. This capillary, known as the emitter, is held at a very high potential relative to the entrance capillary to the vacuum system, which acts as the counter-electrode. If the counter-electrode is large and planar compared to the emitter, the electric field, E_C in the air at the emitter tip can be approximated as[260,261]

$$E_C = \frac{2V_C}{r_C \ln\left(4d/r_C\right)}, \tag{3.1}$$

where r_C is the outer radius of the emitter capillary, V_C is the applied potential and d is the distance between the emitter and the entrance capillary. This field is sufficient to oxidise some of the molecules and causes a separation of charge in the liquid droplet at the emitter tip.[262] When a positive bias is applied to the emitter, as is the case in the work described in this thesis, positively charged species in the solution will be repelled from the emitter. The balance of the repulsive electrostatic interactions between these positive charges at the liquid surface and the surface tension of the liquid determines the shape of the droplet at the emitter tip.

The shape of the liquid meniscus at the emitter tip is thus strongly dependent on the magnitude of the applied potential, but is also influenced by many other variables, such as the electrical conductivity, the surface tension and viscosity of the liquid, the liquid flow rate, the ESD system geometry, and the dielectric

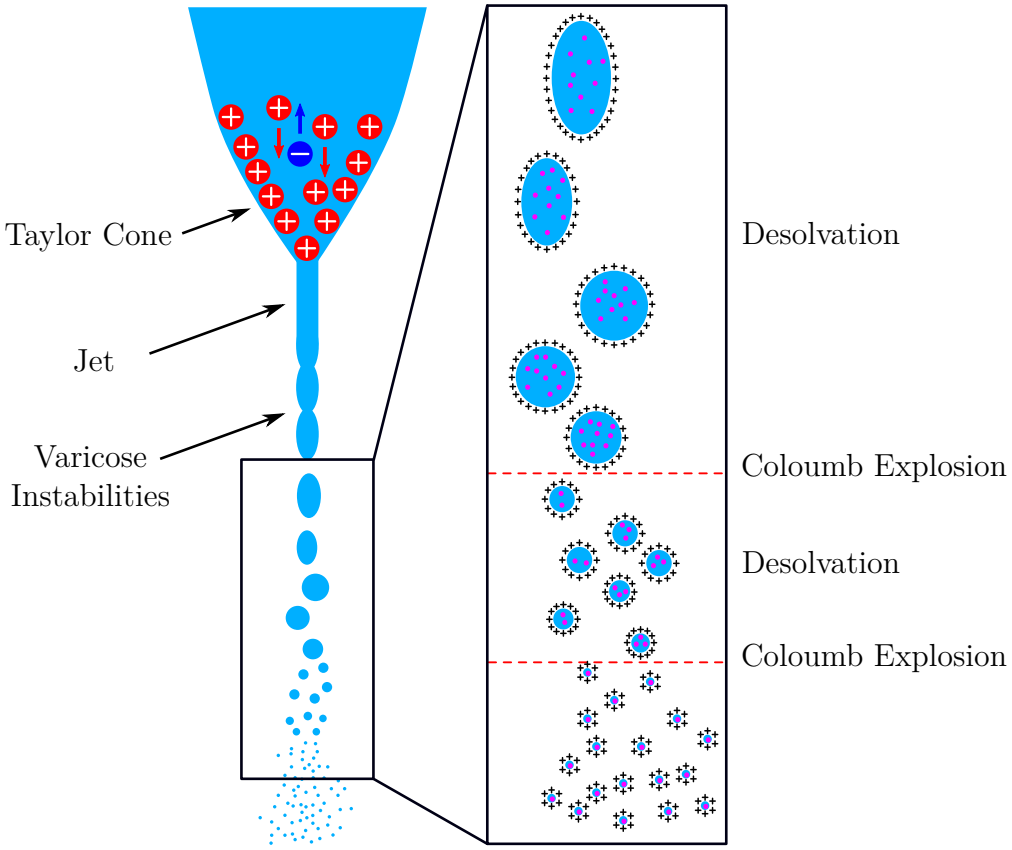

Figure 3.2: Charge separation in an electrified solution extruded from a capillary. Under a range of biases a cone-jet is formed where a stream of liquid is emitted from the tip of a cone. Varicose instabilities cause this stream to break into charged droplets, which then undergo successive desolvation - Coulomb explosion cycles.

strength of the ambient medium.[263] The prototypical droplet shape is known as the Taylor cone, although it was first observed by Zeleny.[264,265] Taylor, who described it mathematically, showed that the electrostatic and capillary pressures are at equilibrium at each point on the surface for a cone with a half-angle at the apex of 49.3°.[266] Therefore, the ideal Taylor cone exists only for a single value of the applied potential; however, stable conical menisci exist for a range of applied potentials.

Charged droplets are emitted from the apex of these conical menisci for a range of field strengths, typically on the order of $10^6\,\mathrm{V\,m^{-1}}$ to $10^7\,\mathrm{V\,m^{-1}}$. The stable droplet-emitting conical menisci are collectively known as cone-jets.[267] The high field at the surface of the cone pushes positive ions towards the apex. These ions drag the liquid with them, producing a filament of liquid, known as a "jet", down-field along the long axis of the emitter.[259]

At the location of the jet, the charge density is so large that the surface tension

is overcome and can no longer hold the fluid together. Varicose instabilities cause the jet to break up into charged droplets,[268,269] which are then accelerated towards the counter-electrode. The sign of the charge on each droplet is the same and is governed by the polarity of the applied potential. The droplets therefore repel each other and form a conical "electrospray". Evaporating solvent causes these droplets to shrink which eventually makes them unstable, leading to the second stage of the ESI process.

3.2.2 The desolvation process

As the charged droplets are accelerated towards, and enter, the entrance capillary to the vacuum, solvent evaporates from the droplets. This leads to an increase in the droplet charge-to-volume ratio because the charge level in the droplet remains the same. When the droplet approaches the "Rayleigh stability limit", defined by the Rayleigh equation, it undergoes a Coulomb explosion process, which generates many, much smaller, progeny droplets.[270] The Rayleigh equation is defined as follows:[271]

$$q_R = 2\pi(2\epsilon_0\gamma r^3)^{1/2}, \tag{3.2}$$

where q_R is the charge on a droplet with radius r, γ is the surface tension of the liquid, and ϵ_0 is the permittivity of the vacuum. Electrosprayed droplets tend to undergo Coulomb fission at charge-to-volume ratios lower than that defined by equation 3.2, due to deviations from perfect spherical symmetry.[272]

Studies of Coulomb explosions suggest that that the fission is uneven, where offspring droplets contain in the region of 1% of the mass of the parent droplet, but $\sim$ 15% of its charge.[273] This is a more stable configuration, because, although the charge-to-volume ratio is increased in the offspring droplets relative to the parent droplet, the charge is spread over a greater total surface area, which reduces the repulsive interactions between the charges. As solvent evaporates from these droplets, they too undergo successive Coulomb explosions. This process continues until the droplets impinge on the surface, or until single, charged analyte ions are formed. There are several models describing how gas-phase ions are produced from charged droplets, the two most common of which are discussed in the following section.

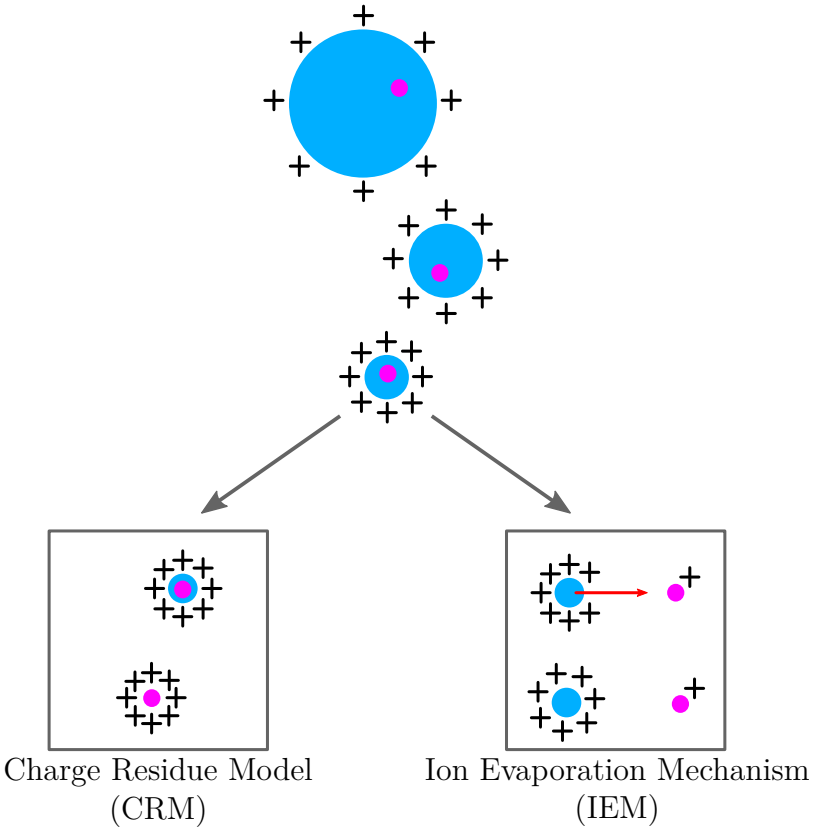

Figure 3.3: Schematic of the charged residue model (CRM) and the ion evaporation mechanism (IEM) of ion formation.

3.2.3 Formation of gas-phase ions

The first model of ion formation in ESI was proposed by Dole and co-workers, and is known as the charged residue model (CRM).[217,274] In the CRM the original concentration is assumed to have been quite low, such that after successive Coulomb explosions only a single analyte ion is left from the droplet. After the last solvent molecule evaporates, the analyte molecule forms a gas phase ion with the residual charge of the droplet. A schematic of the CRM is drawn in Fig. 3.3.

An alternative model, known as the IEM, was developed by Iribarne and Thompson.[275,276] This model postulates that when a droplet reaches a certain size (which is above the Rayleigh limit), the analyte is ejected as a gas-phase ion due to the interaction of the charged analyte with the droplet's internal electric field, as sketched figure 3.3.

The difference between the two models is that in the CRM the ion is formed through the action of successive Coulomb fission events, while in the IEM the analyte evaporates from the droplet into the gas phase through the action of the electric field on the droplet surface. However, the distinction between these

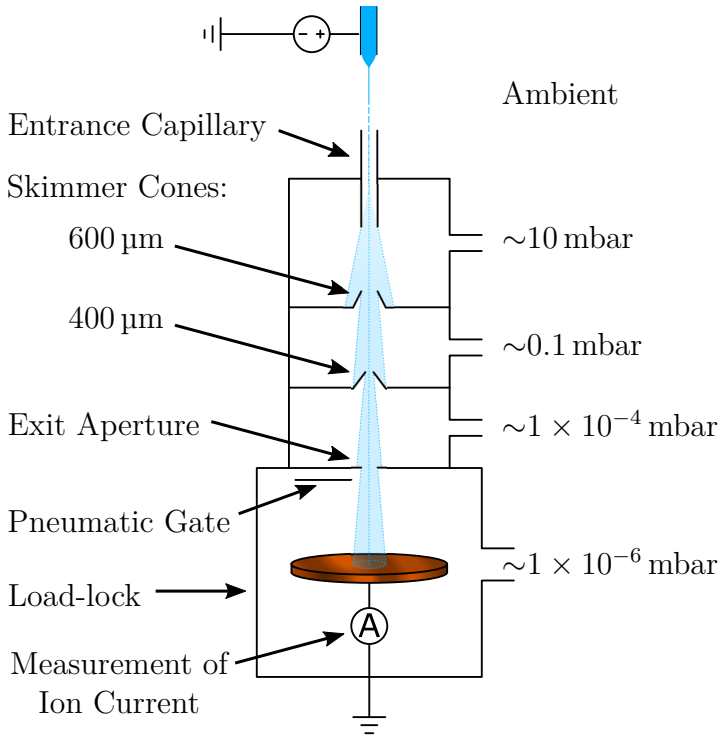

Figure 3.4: Schematic of the electrospray apparatus.

two models is unclear when the droplet is very small such that the expulsion of the analyte ion could be regarded as a final Coulomb fission. In any case, there is some consensus that, in general, the IEM is applicable for smaller molecules, whereas the ionization of molecules whose extended length is greater than the size of the charged droplet are better described by the CRM.[277]

Both of these mechanisms for the formation of gas-phase ions are softer than most other methods. One reason for this is that the internal energy of the analyte and solvent molecules in the droplet may be dissipated as the solvent desorbs.[262] This leads to little fragmentation of analyte molecules in ESI-MS and it has been shown that non-covalent interactions can be preserved throughout the ionisation process,[278] leading to the possibility of depositing 3-D structures which have been assembled in solution.

3.3 The Electrospray Apparatus

For the work in this thesis we use a commercially-available ESD system manufactured by *MolecularSpray*. Here, the plume of ionised droplets is formed in ambient, as discussed in the previous section, before being introduced to vacuum through differential pumping stages. The ESD system is shown in figure 3.4.

The ESI stage of the system consists of an emitter capillary, with an internal diameter of 100 µm into which the solution to be deposited is fed. This emitter capillary is equipped with a polyetheretherketone (PEEK) sheath to insulate it and to increase its mechanical stability. A very high positive bias (0.5 kV to 5 kV) relative to the grounded entrance capillary is applied to the emitter through a liquid junction. The distance between the tip of the emitter and the entrance capillary is between 1 mm and 3 mm, which translates to an electric field in the region of 1 MV m^{-1}. The entrance capillary has an inner diameter of 0.25 mm, and is essentially a controlled leak. The spray of droplets passes through the entrance capillary to the differential pumping stages, where it freely expands in vacuum.

The differential pumping has three stages, pumped by two rotary pumps and a turbo-molecular pump, which have operational pressures on the order of 10 mbar, 0.1 mbar and 4×10^{-4} mbar, respectively. These pumping chambers are separated by skimmer cones whose apertures are 600 µm and 400 µm in diameter, which serve to collimate the molecular ion beam. The droplets pass through a final aperture (1 mm in diameter) into the deposition chamber, which has a base pressure of 1×10^{-10} mbar. A pneumatic gate valve is located between the exit aperture and the deposition chamber, which allows the deposition time to be accurately controlled.

The sample is situated in the deposition chamber on a custom-built stage which allows positioning of the sample in x and y with millimetre precision. The distance between the emitter and the sample is 50 cm. Correct alignment between the entrance capillary and the sample is confirmed by shining a light through the entrance capillary and observing its reflection from the sample surface. The sample stage is electrically-connected to an electrode which allows the ion current to be measured, and, if necessary, a potential to be applied to the sample.

With the gate valve open, the deposition chamber pressure is of the order 5×10^{-9} mbar, which rises to $\sim 1 \times 10^{-6}$ mbar during ESD. When the gate is closed the pressure drops to 1×10^{-8} mbar within two minutes, 1×10^{-9} mbar within 20 minutes and to the base pressure within one hour. It is important to note here that these pressures are measured with a vacuum gauge which is located far from the sample, so that the real pressure at the sample during ESD may be significantly higher than indicated.

A solution must be conductive in order to be ESD compatible. For molecules which are soluble only in non-conductive organic solvents, small quantities of acid or base can be added to increase the conductivity of the solution, or mixtures

of different solvents can be used. In the work presented here we use chloroform, chloroform and methanol mixtures, or tetrahydrofuran (THF) and methanol mixtures as the solvents. It is important to minimise the transport of bubbles to the emitter, as these give rise to an unstable cone-jet. Additionally, the solution concentration should be within certain levels; too low concentrations will necessitate long deposition times, which can lead to co-deposition of large quantities of impurities (see section 3.4), while high concentrations can lead to blockages of the entrance capillary. We find that the optimum range is between $0.01\,\mathrm{g\,l^{-1}}$ to $0.3\,\mathrm{g\,l^{-1}}$.

3.3.1 Electrospray Deposition Rate

As already mentioned, the ion current incident on the sample during ESD can be measured. This electrical current is related to the material flux on the sample. Assuming the ion current I_S is carried by singly charged ions of the analyte species, the coverage Θ after exposure of the sample to ESD for time t can be estimated as

$$\Theta = \frac{Q_{\mathrm{tot}}}{e}\frac{A_{\mathrm{mol}}}{A_{\mathrm{sub}}} = \frac{I_S}{e}\frac{A_{\mathrm{mol}}}{A_{\mathrm{sub}}}t, \tag{3.3}$$

where Q_{tot} is the total charge incident on the surface, A_{mol} is the area covered by the adsorbed molecule, and A_{sub} is the area of the substrate.

A representative ion current measurement during ESD is shown in Fig. 3.5. Here, a $0.1\,\mathrm{g\,L^{-1}}$ solution of ZnTFcBP in THF:CH_3OH was electrosprayed onto a Au(111) surface for 4 minutes, with the emitter held at 1.5 kV relative to the entrance capillary. Integrating the current over the duration gives the total charge transported to the surface as 5.6 nC. We have estimated the electrospray beam diameter to be approximately 2 mm, by measuring the ion current as the sample was moved, keeping all other parameters constant. Then, assuming one charge per molecule and a molecular area of $\sim 3.25\,\mathrm{nm^2}$ (see chapter 4), according to equation 3.3, we get a coverage of approximately 4×10^{-4} monolayers in the region where the electrospray was incident.

A standard STM measurement involves scanning an area of approximately $200\,\mathrm{nm} \times 200\,\mathrm{nm}$. At $\sim 4 \times 10^{-4}$ monolayers coverage, we would, on average, expect to find just five molecules per scan in the region exposed to ESD. However, in repeated experiments where molecules have been deposited under similar conditions, we find significantly higher coverages. This is because several of the assumptions made in equation 3.3 are not justified.

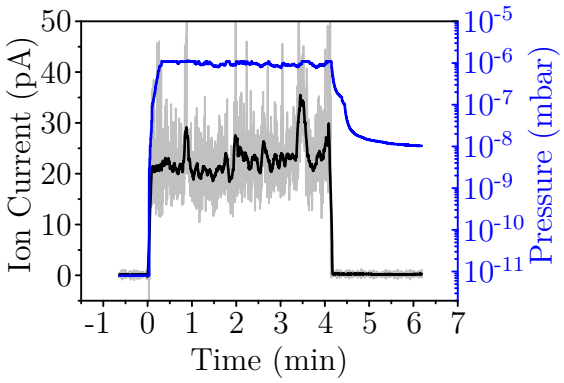

Figure 3.5: The ion current (black) and chamber pressure (blue) during a 4 minute ESD of ZnTFcBP/THF:CH_3OH onto Au(111).

First of all, equation 3.3 assumes that the coverage resulting from ESD is uniform in the region of the sample where the electrospray beam was incident. It is well-known, however, that the coverage profile is approximately Gaussian. While uniform coverages are usually desirable when depositing thin molecular films for device purposes, it can be very useful to have a gradient of molecular densities in surface science experiments. A non-uniform coverage profile allows investigation of different molecular densities with the same parameters, which can be particularly useful when the molecular packing structure is coverage dependent. However, uniform coverages can be achieved by adding electrostatic lenses, if required.

We observe significant coverage in areas even far from the center of the beam. Diffusion plays a role here, but cannot explain why the total coverage is obviously far higher than the ion current would suggest. In deriving equation 3.3 we have assumed that the molecules arrive as single ions, however it is clear that this is not the case. We observe significant variations in coverage even on the micrometer scale, suggesting that the molecules arrive on the surface in droplets containing multiple molecules.

Full experimental control of the ESD dose can be achieved with a significantly more complicated set-up, including an ion funnel, quadrupole mass selection, retarding grid analysers and time-of-flight (TOF)-MS.[279] However, for our purposes this is not necessary. By monitoring the ion current and chamber pressure during deposition, a qualitative measure of coverage can be attained. When combined with the coverage gradient, we can reproducibly prepare surfaces with large areas in the requisite molecular density regime.

The electrical contact to the sample can also be useful for other purposes. It has been reported that some molecules, particularly proteins, can fragment

if their kinetic energy is too high when they impact the surface.[280,281] A potential can be applied to the sample to bring this energy below the fragmentation threshold (typically <10 eV).[282] Alternatively, it may be desirable to accelerate the molecules, particularly if surface modification is the goal.[283,284] We have never observed significant quantities of fragmented molecules after ESD, possibly due to their landing in small droplets where the solvent sheath dissipates the kinetic energy.

3.4 Impurities Introduced During ESD

As we have seen, ESD involves exposure of the sample to a beam of charged droplets at relatively high pressures. The cleanliness of the resulting surface is limited by the purity of the solution and by the contaminants introduced during the electrospray process. Care must be taken that both the source material of the target molecule and the solvent in which it is dissolved are pure. Additionally, it is important to check the compatibility of the solvent with the surface since some surfaces can crack solvent molecules, leading to unwanted adsorbates, or indeed react with the solvent itself. Since we often desire to deposit molecules which are only weakly soluble, it can be difficult to identify solvents which are compatible with both the molecule and the surface. However, we found that no matter how much care was taken to eliminate the introduction of impurities in the analyte solution, it was impossible to eradicate contaminants from the surface altogether.

The Au(111) surface provides a convenient way of examining the introduction of impurities during ESD. It is an unreactive surface and, as a result, solvent compatibility is generally not an issue. However, the herringbone reconstruction generates relatively reactive kink sites were molecules preferentially adsorb, so that by monitoring the cleanliness of the kink sites, as well as the step edges, we can get a qualitative idea of the surface cleanliness.

Opening the gate valve to the electrospray system while there is no solution flow, *i.e.*, when only air enters the UHV chamber, results in a surface where the vast majority of kinks and step edges are clean. In contrast, the kinks are always occupied after exposure of the sample to the active electrospray, regardless of the solution contents and even when the sample is not in the direct path of the droplet beam. Larger defects are seen when the sample is in the path of the spray, examples of which are shown in figure 3.6.

In general, the contaminants introduced by ESD fall into two categories: solvent-dependent and solvent independent, both of which are seen in figure

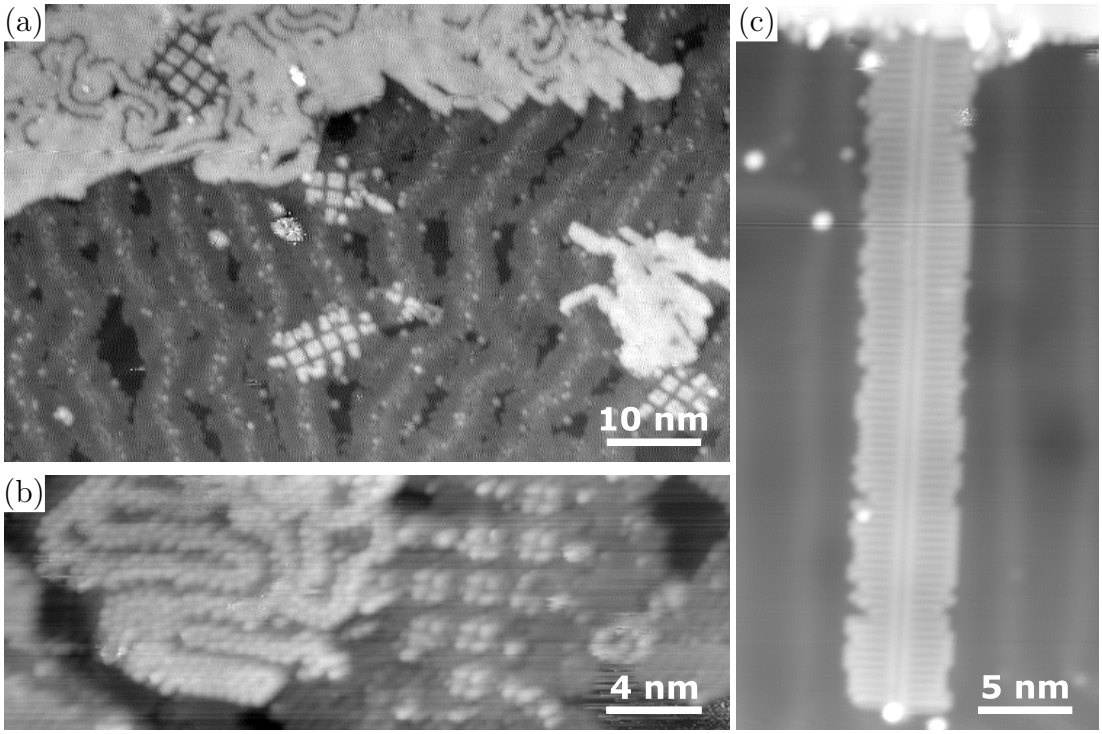

Figure 3.6: Impurities co-adsorbed with target molecules after ESD. Three species can be distinguished in (a): the target molecule (square features), contaminants originating from the solvent (labyrinthine feature), and contaminant from elsewhere [rod-like features covering the Au(111) herringbones]. These are shown in greater detail in (b). The rod-like features are shown after a cleaner deposition in (c).

3.6(a). Here, we have removed the exit aperture from the apparatus (see Fig. 3.4) and deposited a solution of ZnTFcBP in THF:methanol. The square features arising from the ZnTFcBP molecule can be seen to blend seamlessly into the contaminant features so that we can say that ZnTFcBP is adsorbed in a contaminant matrix. The removal of the exit aperture results in a much higher concentration of contaminants than we see from a standard deposition. The rod-like defects which cover the herringbone features are observed after every deposition and as a result are not related to the nature of the solvent. The other type of contaminant is dependent on the solvent, and appears as a disordered chain-like structure. Other groups have observed almost identical features when depositing molecules *via* pulsed valve, which they attribute to THF.[111] The THF feature is resolved in greater detail in figure 3.6(b).

A higher resolution STM topograph of the rod-like contaminants is presented in Fig. 3.6(c). The rods vary slightly in length but are usually on the order of 30 Å. This length variation suggests that the rod-like species are polymeric fragments. On Au(111) they self-assemble in a double row structure along the herringbone,

whereas on Cu(111) they pack along one of the close-packed directions of the substrate. The rods align with the close-packed directions on Cl−Cu(111) also, however they have only been observed isolated rather than packed into islands.

Assigning the origin of these features is more difficult. Since we see these features after ESD of solvent only, the purity of the target molecule is not the critical factor. Some of the solvents used are quite aggressive, and as a result one explanation could be that they are removing some material from the PEEK fittings in the electrospray apparatus. However, these features were still present when the PEEK parts were replaced with solvent-resistant polytetrafluoroethylene (PTFE). Examining the contaminant peaks commonly seen in ESI-MS, we find that they include those corresponding to polysiloxanes, a polymeric compound which is ubiquitous in labware coatings, especially syringes, and is even found in the ambient.[285] A polydimethylsiloxane (PDMS) chain ten units in length is approximately the size of the rods we see in the STM topographs. Thus, we postulate that these are the source of the solvent-independent contaminants.

Both the THF features and the rod-like features can be removed by annealing the sample.[286] However, since the MQCA candidates are thermally sensitive, and since we can prepare surfaces with only small quantities of contaminants, this is not necessary.

4

Functionalised Porphyrins on Noble Metals

In chapter 1 we described the requirements for a good MQCA candidate, and settled on ferrocene-decorated porphyrins as the basis of those we would explore. Porphyrins are known to self-assemble in a multitude of different patterns, many of which have the fourfold symmetry we require.[121] To ensure that our architectures are stable with respect to variations in temperature and electric field, we require that they are bound with strong intermolecular forces. Hydrogen bonds are relatively strong and allow separation of the design of the electronic properties of the molecular network from the design of its topology. This makes them attractive for use in molecular device components, and therefore we have chosen to add functional groups which facilitate hydrogen-bonding to our ferrocene-decorated porphyrins.

In this chapter we describe the properties of metal-supported hydrogen bonded networks of these ferrocene-decorated porphyrins. We first provide an introduction to hydrogen bonding and outline how hydrogen bonding can be exploited to build functional architectures. We then detail the structure and electrochemical properties of the molecules investigated in this chapter. In section 4.2, we briefly describe the Au(111) and Cu(111) surfaces upon which the candidate molecules are adsorbed. The adsorption and self-assembly characteristics on these substrates are explored in section 4.3. Finally, in section 4.4 we explore the electronic properties of these self-assembled molecules from both an experimental and theoretical viewpoint.

The work presented in this chapter[287] has contributions from several different

groups. The molecule was synthesised by Pier Giorgio Cozzi's group, and characterised electrochemically by Francesco Paolucci's group, both at the University of Bologna. Our collaborators in the Samori group at the Université de Strasbourg carried out the *in situ* STM measurements. Finally, DFT calculations were carried out by Alejandro Santana-Bonilla of the Cuniberti group in Dresden.[288]

4.1 Hydrogen-Bonded Porphyrin Networks for Molecular QCA

Supramolecular chemistry is the field of chemistry which considers the design and assembly of functional molecular networks.[289] By designing a molecular component with appropriate electronic properties and with "molecular recognition" groups which interact non-covalently in a pre-programmed manner with other components, a supramolecular device can be built from the bottom-up. Hydrogen bonding interactions are one type of these non-covalent intermolecular interactions, and are widely exploited in the engineering of supramolecular architectures. Hydrogen bonds can span a wide range of interaction strengths, from 0.2 eV to 1.7 eV, which is ideal for assembling stable molecular networks, but which remain reversible, such that the thermal energy at room temperature is sufficient to allow these networks to self-heal.[290] Additionally, the directional nature of hydrogen bonds allows for high selectivity in supramolecular design.[289]

The hydrogen bond is a cohesive force arising from a complex electrostatic interaction between a dipole, generated when a electronegative atom X bonds to hydrogen, and an electron cloud.[290] The X−H bond is polarised by the electron-withdrawing nature of X, which creates a partial positive charge at the hydrogen site.[291] This so-called "donor" can interact with the partial negative charge on an "acceptor" group, which commonly takes the form of a lone pair or π-system. The donor-acceptor interaction is shown schematically for an amide dimer in figure 4.1(a), where each N−H donor interacts with the acceptor group arising from the lone pair on the oxygen atom on the other amide group.

Hydrogen bonds are typically classified as strong, moderate (conventional), or weak, however the line between these groups is rather arbitrary.[291] In general, the hydrogen bond strength tends to increase with increasing acidity of the XH group, and increasing basicity of the donor. The strongest hydrogen bonds are in ionic systems, since the electrostatic interaction between a monopole and a dipole tends to be stronger than an equivalent interaction involving two dipoles.[292] The strongest known hydrogen bond occurs between HF and F^-, where the bonding

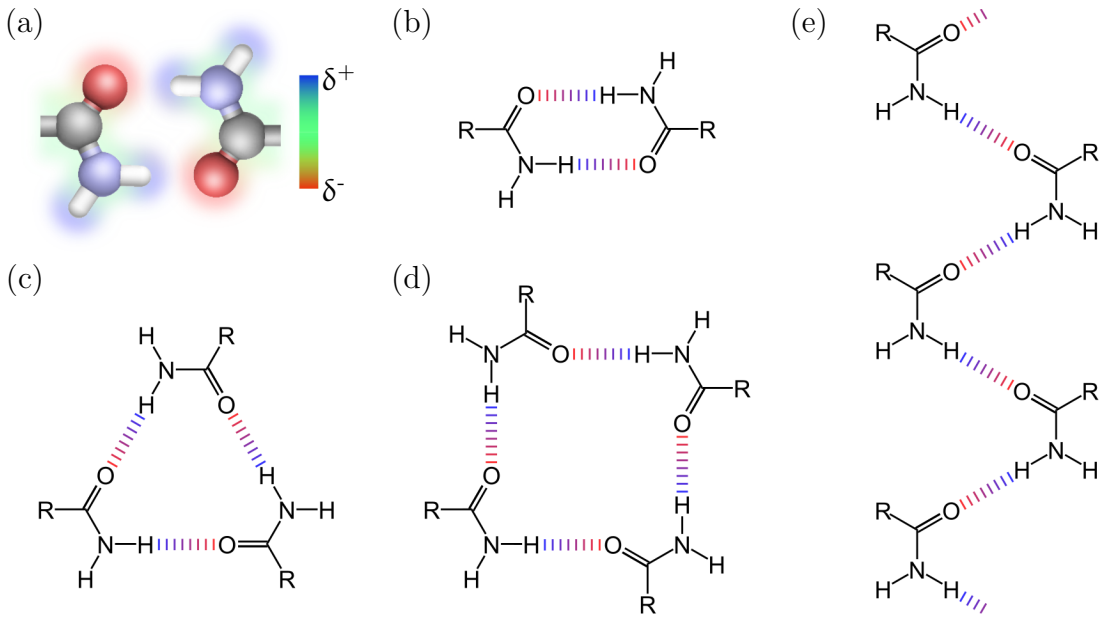

Figure 4.1: Hydrogen bonding interactions between amine groups. The electrostatic origin of the hydrogen bonding interaction is sketched in (a), where the electronegative N atom withdraws electron density from the H atoms bound to it. The resulting electron deficient areas on these H atoms can then interact with the electron-rich O lone pairs. Hydrogen-bonded dimer, trimer, tetramer and catameric motifs are shown in (b)-(e), respectively. The R group will play a major role in determining the self-assembly structure.

is best described by an ionic model corresponding to the $[F{-}H{-}F]^-$ system.[293] Hydrogen bonds involving charged donors and/or acceptors tend to have energies between 0.65 eV to 1.7 eV and corresponding H···A distances from 1.2 Å to 1.5 Å.[292] On the other hand, the weakest hydrogen bonds generally involve C−H···A and X−H···π interactions, with CH_4···FCH_3 being the weakest example.[294] These weak hydrogen bonds are characterised by H···A distances greater than 2.2 Å, and energies less than 0.2 eV. The moderate strength, or conventional, hydrogen bonds are favoured for the engineering of supermolecules. These tend to involve N−H···O=C and O−H···O=C interactions where the bond energies and distances are between 0.2 eV to 0.65 eV, and 1.5 Å to 2.2 Å, respectively.

Besides a dependence on the character of the donor and acceptor, and upon the separation between them, the strength of hydrogen bonds also have an angular dependence.[291] Hydrogen bonds are strongest in a linear configuration, however the angular dependence is weak and deviations from 180° are often observed to accommodate multiple hydrogen bonds. In the majority of cases, biological and engineered, hydrogen bonded synthons (molecular subunits of a supermolecule) form arrays where the X atom in the acceptor group simultane-

ously acts as a donor, which is what gives rise to the multitude of complicated ice crystal phases.[291] Additionally, functional groups such as carboxyl groups and amide groups contain both hydrogen bonding donors and acceptors, allowing them to bond in a multitude of configurations. Some of the possible configurations are shown for an amide in figure 4.1(b)-(e), where the structure formed will depend on the nature of the R group, and if confined to a surface, on the molecule-substrate interaction. The tandem nature of these hydrogen bonds is not confined to homo-molecular recognition, as is well known for the DNA base pairs.

Another interesting thing to note about these multiple hydrogen bonds is that they are cooperative: the overall bonding interaction is stronger than the sum of the constituent bonds. This can occur, for example, in water where alignment of multiple O−H bonds increases the dipole within each. When hydrogen donor and acceptor groups are linked by π-bonds, the delocalised nature of the electrons can lead to polarisation across multiple bonds.[291] In this case the increased interaction strength is known as resonance-assisted hydrogen bonding (RAHB).[295,296] The configurations in figure 4.1(b)-(e) all benefit from RAHB.

A variety of 2D porphyrin-based hydrogen-bonded networks have been reported. These can take on a variety of architectures, depending on the symmetry of the functionalisation[297] and on the selectivity of the attached hydrogen bonding group.[298] TPPs functionalised with hydrogen bonding groups at the 4-positions of the meso-phenyl groups are known to self-assemble into square patterns,[227,299,300] with the nature of the network depending on the details of the molecule-substrate interaction.[301,302] Here we have chosen amide groups as the functional group for self-assembly, which form relatively strong hydrogen bonds and can bond in a conformationally flexible manner, as we have already seen. Amides are similar to carboxylic acids in terms of hydrogen bonding, so that we would expect a TPP molecule functionalised with amides at each of the 4-positions of the meso-phenyl rings to self-assemble in a manner similar to that reported for TCPP.[227,299,301,302]

The other reason amide groups were chosen is to allow for simple molecular synthesis. The amide coupling reaction, where an amide is formed by treating a carboxylic acid with an amine, offers a convenient way to attach Fc groups. This allowed our collaborators to create a four-fold symmetric ferrocene-decorated porphyrin by reacting commercially-available TCPP with a ferrocenylamine.[303] Both the free-base and Zn-metallated analogues were synthesised and their properties are discussed below. The molecules are known as 5,10,15,20-tetra[*N*-(1-ferrocenylethyl)benzamide]porphyrin and zinc 5,10,15,20-tetra[*N*-(1-

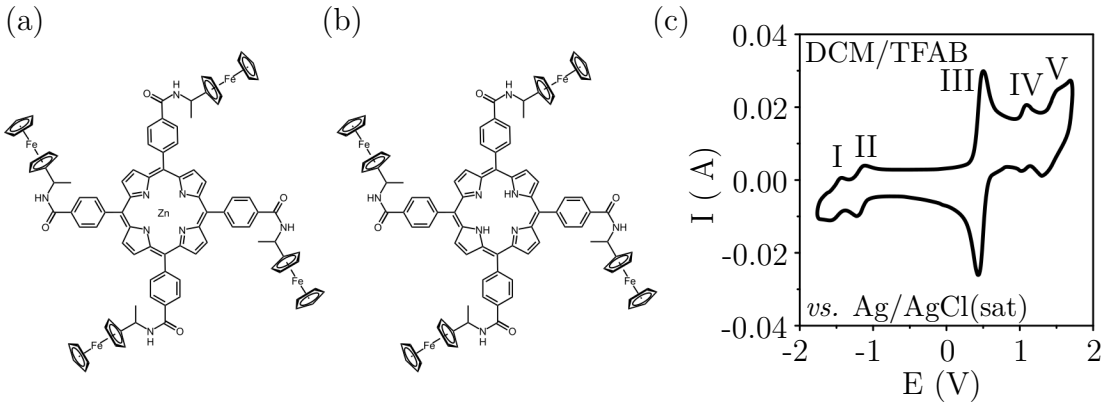

Figure 4.2: Molecular structure of ZnTFcBP (a) and H_2TFcBP (b). A CV of a H_2TFcBP analogue measured by El Garah *et al.*[303] is shown in (c), where peaks I, II, IV and V are all single electron redox peaks originating from the porphyrin core, and peak III is a four-electron oxidation of the equivalent ferrocene groups. The CV was performed in DCM under ultra-dry conditions, using TBAH as a supporting electrolyte. A glass-sealed platinum disk ultramicroelectrode, with a 125 µm diameter, was used as the working electrode, while the platinum and silver spirals were used as counter electrodes and quasi-reference electrodes, respectively. Potentials were measured with decamethylferrocene standard and were referenced to Ag/AgCl(sat).

ferrocenylethyl)benzamide]porphyrin, and will be referred to as H_2TFcBP and ZnTFcBP throughout this chapter. ZnTFcBP and H_2TFcBP are sketched in figure 4.2(a) and (b), respectively.

Since the phenyl groups are out of plane with the porphyrin ring, they serve as spacers only and we would not expect electronic interaction between the ferrocenyl units even if the linker did not contain a saturated bond.[304] This has been confirmed by our collaborators, who performed electrochemical analysis of an analogue of H_2TFcBP.[303] The resulting CV, reproduced in figure 4.2(c), shows a single four-electron oxidation peak originating from the equivalent ferrocenyl groups, as well as peaks corresponding to oxidations and reductions of the porphyrin core. The analogue investigated differs only in the attachment of a dodecyl chain to the carbon atom linking the Fc group to the amide, where we have a methyl group. This alkyl chain increases the solubility of the molecule but is not expected to alter its electronic properties, therefore ZnTFcBP and H_2TFcBP can be assigned as Robin-Day class I molecules. In chapter 1 we listed Robin-Day class II behaviour as a requirement for potential QCA molecules. However, it is possible that supramolecular mixed-valency could render these molecules viable.

There are now several examples of mixed-valence supermolecules, where redox centres in different molecules are coupled across a set of hydrogen bonds.[305,306]

Mixed-valence behaviour in a hydrogen-bonded dimer can be very strong, with at least one example of class III behaviour reported.[307] Additionally, it is possible that through-space coupling between the Fc groups, which is highly sensitive to the separation between the redox centres,[308] could be sufficient to facilitate the kind of mixed-valence behaviour required for MQCA. However, Paolucci *et al.*, who carried out the electrochemical measurements, found no evidence of electronic coupling of any kind between the Fc groups when the molecules were assembled on the highly-ordered pyrolytic graphite (HOPG) surface.[303]

While the lack of electronic coupling between Fc groups within and between these molecules is not ideal for MQCA applications, modulating the distances between the Fc units within a cell and between adjacent cells will favour intra-cell tunnelling stimulated by inter-cell electrostatic interactions. Regardless, we believe that ZnTFcBP and H_2TFcBP are valuable as a reference point, and as a first iteration towards a functional system. These molecules should allow us to investigate the behaviour of self-assembled ferrocenyl-decorated porphyrins, and the effects of injecting charge into these systems. We hope that limiting the interactions to electrostatic and through-space tunnelling will allow us to better understand these assemblies before the complexity of a through-molecule channel is added. If indeed we are able to create a supramolecular mixed-valence analogue of this system, by substituting the saturated linker between the aminyl-nitrogen and the Fc group for a conjugated one, having ZnTFcBP/H_2TFcBP as a reference point will be very valuable.

4.2 The Au(111) and Cu(111) Surfaces

We first characterise the behaviour of ZnTFcBP and H_2TFcBP molecules on Au(111) and Cu(111), before attempting to decouple the molecules from the surface. As we discussed in section 1.3, the noble metals are relatively inert, and the close-packed surfaces of these are the least reactive of all. Since both gold and copper have a face-centred cubic (fcc) crystal structure, the (111) plane is the close-packed plane. The ease of preparing these substrates, combined with the aforementioned inertness explains the ubiquity of Au(111) and Cu(111) in UHV molecular characterisation. The bulk lattice constant of gold is 4.08 Å, which leads to a nearest neighbour distance of 2.88 Å and a step height of 2.36 Å on the (111) surface, while the corresponding values for copper are 3.61 Å, 2.55 Å and 2.08 Å, respectively.[309]

The Au(111) surface has an interesting structure, unlike most fcc metals,

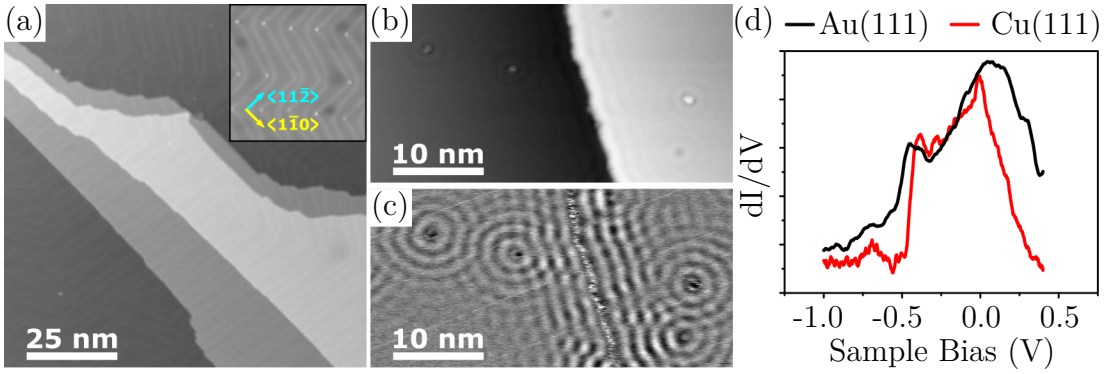

Figure 4.3: Topographic and electronic properties of the Au(111) and Cu(111) surfaces. An STM topograph of the Au(111) surface is shown in (a) where the step height is 2.36 Å. The herringbones can clearly be resolved in the inset (same scale), where impurities can be seen to preferentially adsorb at the kink sites. The scattering of the Cu(111) surface state from the step edges and from small adsorbates, likely water (depressions) and CO protrusions, can be seen in the topographic map in (b). This scattering can be more clearly resolved in the $\mathrm{d}I/\mathrm{d}V$ channel, as can be seen from (c). The onset of the surface state can be measured using STS and, as shown in (d), appears at −0.55 V on Au(111) (black), and at −0.45 V on Cu(111) (red). Imaging conditions: (a) 50 pA, 1 V; inset 20 pA, −2 V; (b), (c) 100 pA, −150 mV.

its (111) surface undergoes a reconstruction.[310] Elastic strain drives a uniaxial compression of the top atomic plane by 4.55% in the $[0\bar{1}1]$ direction, leading to alternating fcc and hexagonal close packed (hcp) domains, and a $23 \times \sqrt{3}$ unit cell.[311,312] The atoms between the fcc and hcp domains occupy less symmetric sites and, as a result, are displaced normal to the surface. These "herringbones" or soliton lines appear as ∼0.2 Å protrusions running along the [112], and symmetry equivalent, directions in STM topographs, such as that shown in figure 4.3(a).[313,314] They run for approximately 250 Å before changing direction by ±120°. The corners where a herringbone changes direction are known as kink sites, and are preferential adsorption sites.[297,315] Since the herringbones can be observed at almost all STM imaging conditions, and often through a molecular layer, they can be very useful since the packing direction of adsorbed molecules can be assigned without having to achieve atomic resolution which can be very difficult to achieve without disrupting the adsorbed species.[316]

Additionally, a Shockley-like surface state is present on both the Au(111) and Cu(111) surfaces, with a band edge energy of −0.52 eV and −0.45 eV, relative to the Fermi level, respectively.[317–320] STS showing the Au(111) and Cu(111) surface states are shown in Fig. 4.3(d), in black and red, respectively. The herringbone reconstruction on Au(111) acts as a superlattice for this surface state.[319]

The surface state manifests as a freely-diffusing 2D electron gas, and can scatter from, or form an interface state with, adsorbed atoms or molecules.[321,322] Figure 4.3(b) shows a Cu(111) surface with an atomic step and some adsorbates, and the scattering of the surface state from these features can be seen in Fig. 4.3(c). The workfunctions of the Au(111) and Cu(111) surfaces are 5.31 eV and 4.94 eV, respectively.[323]

4.3 Adsorption and Self-Assembly of MQCA Candidates

Single crystals of Au(111) and Cu(111) (*MaTeck*, Germany) were prepared by multiple cycles of Ar^+ bombardment followed by annealing up to 800 K. Surface quality was confirmed with LEED before deposition of molecules. ZnTFcBP and H_2TFcBP were deposited *via* ESD, from a solution prepared by dissolving the molecules in a solvent appropriate to the surface (chloroform or THF for Au(111) and THF for Cu(111), and in both cases methanol was added in a 1:1 ratio to improve conductivity).

Deposition of ZnTFcBP onto Au(111) results in the formation of large molecular islands characterised by prominent square features at most biases, as shown in figure 4.4(a). The unit mesh is approximately square, measuring (23.0 ± 1.0) Å $\times$ (21.5 ± 1.0) Å. This is in good agreement with the structure of ZnTFcBP at the solid-liquid interface, as can be seen from the *in situ* STM image in Fig. 4.4(b), which has a square unit mesh with side length 22 Å. The Fc groups dominate the contrast in UHV, whereas at the solid-liquid interface the TPP backbone of the molecule is primarily resolved.

The fact that the same structure is observed on HOPG and Au(111), in air, in 1-phenyloctane, and in UHV, for both the free-base and Zn-metallated versions of the molecule, suggests that the surface plays a minimal role in the self-assembly, and it is the intermolecular interactions which drive the self-assembly structure. This is supported by the fact that we see the molecules growing over a step edge in a carpet-like fashion, indicated by the green arrow in Fig. 4.4(a). In fact, ZnTPP is known to adsorb preferentially at Au(111) step edges due to the lower coordination number,[316] but the continuous growth of the molecular island over the step indicates that the molecule-molecule interaction is favoured over the molecule-substrate interaction.

However, having said that, it is clear that the surface plays a role in directing the self-assembly on Au(111). We observe molecular domains rotated by multiples of 60°, which reflects the symmetry of the underlying substrate. One of the unit

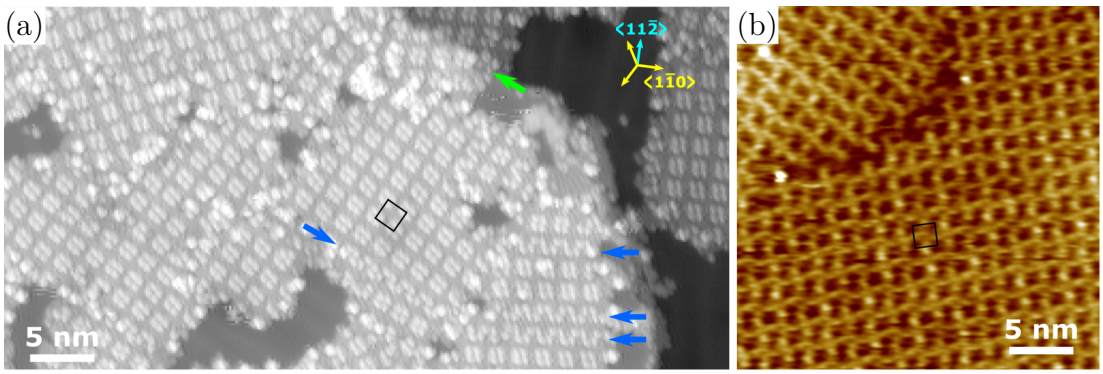

Figure 4.4: Self-assembled ZnTFcBP islands are shown on Au(111) in (a) where they were measured with LT-STM in UHV, and (b) at the 1-phenyloctane/HOPG interface where they were analysed using *in situ* STM. The structure of the molecular islands is identical with a square unit cell of side length ∼22 Å (indicated by black square), however the source of contrast is the Fc groups in UHV and the TPP backbone *in situ*. The green arrow in (a) indicates a molecular island overgrowing a step edge, while the blue arrows indicate packing faults. Imaging conditions: (a) 10 pA, 1 V, (b) 25 pA, −650 mV.

cell vectors is aligned with the herringbone directions, which means that the other unit cell vector is aligned with one of the close packed directions of the surface, *i.e.*, the unit mesh is aligned at multiples of 60° with the [11$\bar{2}$] and [1$\bar{1}$0] directions.

A model of the packing structure is shown in the bottom half of figure 4.5. Each molecule is bound to four others by hydrogen bonding in the so-called cyclic dimeric structure,[324] where the amide donor and acceptors are separated by approximately 1.75 Å, which is within the range of a typical N−H···O hydrogen bond length (see section 4.1). This differs from the cyclic tetramer structure adopted by the ZnTFcBP fragments we saw in section 3.1.1, and from the structure of TCPP observed at the air/HOPG interface,[227] but is almost identical to the structure of CoTCPP on Au(111) in acidic solution reported by Yoshimoto *et al.*[301]

Yoshimoto *et al.*[301] attribute the change in self-assembly architecture, relative to that observed for H_2TCPP, to the increased molecule-substrate interaction driven by the presence of the Co metal center. Since we see the same structure for ZnTFcBP and H_2TFcBP, we do not attribute the formation of the cyclic dimeric structure to the molecule-substrate interaction, but to steric interactions between Fc groups in the pores left by the hydrogen bonded TPP backbones. Interestingly, the network structure is almost identical to that in a layer of ZnTCPP molecular sieves, where the pores are kept open by molecular templating.[325,326]

Four molecules each contribute one Fc group to a quartet as highlighted in red in figure 4.5. These Fc quartets resemble the type of structures we would

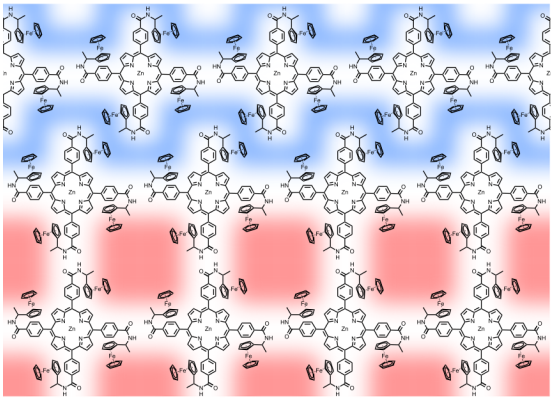

Figure 4.5: Structural model of the square and zig-zag self-assembly motifs. The square features observed on Au(111) for both ZnTFcBP and H_2TFcBP originate from a ferrocene quartet, highlighted in red, where each Fc group is bound to a different molecule. When the hydrogen-bonded molecular rows are offset from each other by half a unit cell, a zigzag structure is visible in the STM topography. The zigzag arises from groups of two ferrocenes from a molecule either side, as highlighted in blue.

require for MQCA. It is well-known that Fc groups prefer to pack orthogonal to each other,[327,328] however we were unable to resolve differences between the Fc groups in the STM topography as can be seen from the higher resolution images in Fig. 4.6(a) and (b).

The square structure is formed when the molecule-molecule interactions dominate over the molecule-substrate interactions. However, as we already mentioned, the alignment of the overlayer with the high-symmetry directions of the surface indicates that the molecule-surface interaction is not irrelevant. Indeed, the molecular periodicity appears to be quasi-commensurate, with a unit cell length corresponding to 8 atomic distances along the close-packed directions. When ZnTFcBP is adsorbed on the Cu(111) surface, which is slightly more reactive and known to interact more strongly with TPPs than Au(111) does,[329] we observe the familiar square features in a minority phase. The favoured structure appears to be a fully commensurate (9×9) overlayer, with unit mesh vectors 23 Å in length, separated by 60°. This structure is shown in Fig. 4.6(c).

It should be noted that the unit cell vectors along the close-packed direction are identical for the square and zigzag motifs formed on Au(111) and Cu(111), respectively, indicating that the hydrogen bonding is preserved in rows along this direction. Additionally, we know from observing the zigzag features within the molecular islands on Au(111) [as indicated by the blue arrows in figure 4.4(a)] that the molecules are not rotated relative to one another (since the square periodicity is maintained either side of the zigzag row) but shifted by half a unit cell length.

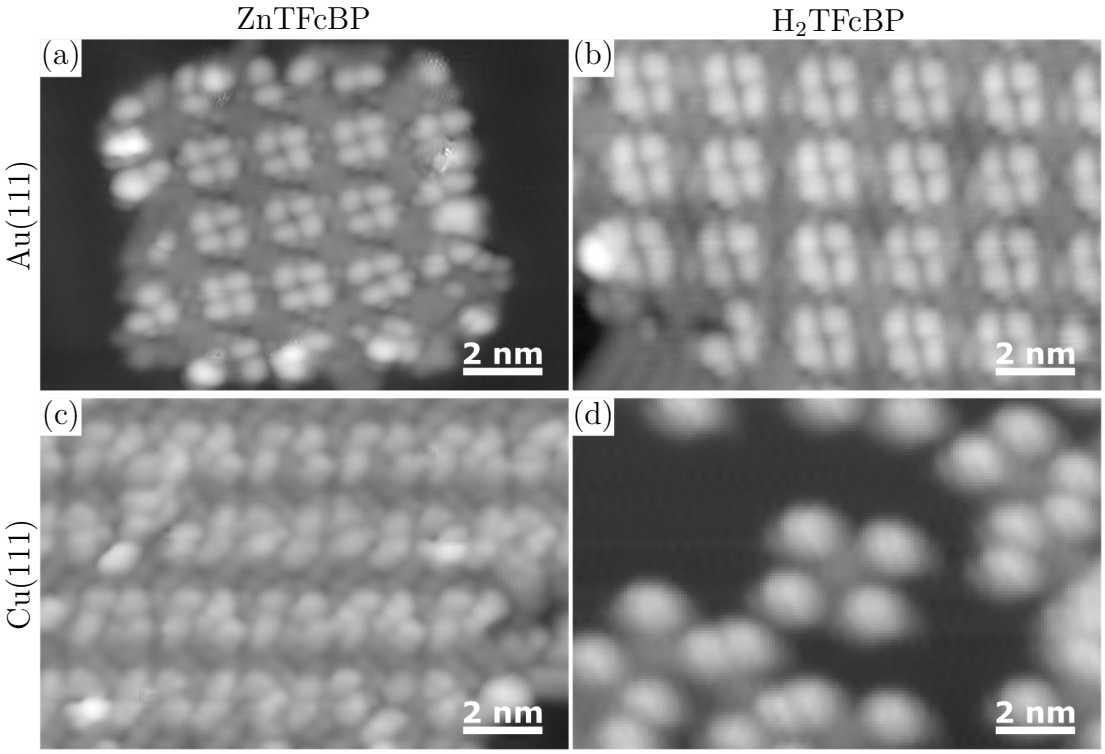

Figure 4.6: ZnTFcBP and H_2TFcBP both assemble into molecular islands with a square unit cell on Au(111), shown in (a) and (b), respectively. On Cu(111), however, the molecule-substrate interaction is stronger, which favours assembly of ZnTFcBP into a zig-zag pattern (c), and prevents self-assembly of H_2TFcBP completely resulting in the isolated molecules shown in (d). Imaging conditions: (a) 10 pA, −1 V, (b)-(d) 20 pA, −1 V.

Figure 4.5 shows the transition between the two packing motifs, and the blue feature shows how the zigzag feature arises.

The driving force for this structure is less obvious. Since the amide-amide hydrogen bond energy is approximately 0.5 eV,[330–333] the energy cost of ∼1 eV associated with breaking two of these bonds per molecule must be compensated by a total energy reduction associated with forming the commensurate structure on Cu(111). The most obvious source is that associated with adsorption of each molecule in the site which provides the highest adsorption energy. However, while adsorption with the metal ion over the top site is favoured, the reported difference between that and the bridge or hollow site is on the order of 50 meV.[334,335] Additionally, metallated TPPs are known to self-assemble with the same incommensurate structure on Au(111), Ag(111) and Cu(111), irrespective of the central metal ion.[228,336–344] Since, for metallated TPPs, the difference in molecule-substrate interaction strength is controlled by the d_{z^2} orbital occupancy, and we do not see an incommensurate-commensurate transition going from CoTPP/Au(111) to

CoTPP/Cu(111), we would not expect to see this for a Zn metal center, which has a filled d_{z^2} orbital and therefore interacts less strongly with the surface than does Co.[345]

ZnTFcBP is more complicated than TPPs, and it is well known that the nature of the termination of the phenyl groups can have an impact on the mobility of the molecule.[341] For example, metallated 5,10,15,20-tetra(4-bromophenyl)porphyrins (Br_4TPPs) are known to be immobile on Cu(111) if in a saddle configuration, but mobile if planar.[346,347] The large contribution to the STM topography from the Fc groups in the filled states where the porphyrin conformation is most easily distinguished makes it difficult access the porphyrin core, however we believe that ZnTFcBP remains planar on Cu(111). Additionally, there is no reason to believe that a saddle distortion would interfere with hydrogen bonding.[298]

We instead attribute the different structures on Au(111) and Cu(111) to the difference in surface energies between these substrates. Au(111) has a surface energy of 80 meV $Å^{-2}$, while the corresponding value for Cu(111) is 112 meV $Å^{-2}$.[348] The (9×9) structure is more close packed than the incommensurate square structure, with an area of 460 $Å^2$/molecule compared to 530 $Å^2$/molecule. The increased density helps to minimise the surface free energy.[227]

In contrast, the behaviour of H_2TFcBP on Cu(111) is much better understood. As can be seen from Fig. 4.6(d), H_2TFcBP does not self-assemble on Cu(111), instead isolated molecules are observed. The molecules typically measure 20 Å $\times$ 17 Å, with some disorder in the position of the Fc lobes, attributed to their conformational flexibility with respect to the rest of the molecule. Additionally, each Fc group appears considerably larger than when the molecule is organised into molecular islands, suggesting that they may be able to move under the influence of the tip. The isolated molecules are found with a relative orientation of 60°, further reflecting the strong molecule-substrate interaction.[342]

H_2TPP is well-known to be immobilised on Cu(111), where its iminic (−N=) nitrogen interacts strongly with the underlying substrate, pushing the aminic (−NH−) nitrogens away from the surface plan, thereby driving a saddle deformation in the usually planar porphyrin core.[349] This saddle deformation is accompanied by deformation of two pyrrole rings toward the surface and two away from the surface, and a rotation of the phenyl rings more in plane with the porphyrin. It has been suggested that free-base porphyrins have strongly preferred adsorption sites,[343] and more recently that Cu atoms are partially extracted from the surface,[350] forming an intermediate to the Cu-metallated porphyrin which is formed at higher temperatures where the aminic hydrogens can desorb.[228] It

would be interesting to self-metallate H_2TFcBP on the Cu(111) surface and see if the (9×9) structure is retrieved, since this would provide further evidence for our attribution of the structure driving force to a surface energy minimisation rather than a specific interaction between the metal center and the surface.[351] However, this has not been attempted due to the thermolability of the Fc groups (see section 3.1.1).

The diffusion barrier is significantly increased for H_2TPP/Cu(111), however the molecules are mobile at room temperature as demonstrated by the separation of H_2TPP and CoTPP, which self-assembles on Cu(111).[329] This, combined with fact that the (9×9) structure is commensurate means that the preferred adsorption site is not the only factor impeding self-assembly. This confirms the intermolecular repulsion mechanism put forward by Rojas *et al.*[342] Indeed, we observe scattering of the Cu(111) surface state from H_2TFcBP, as has been seen for H_2TPP.[352] Thus, we can say that the strong H_2TFcBP-Cu(111) interaction is due to the interaction of the TPP core of the molecule with the underlying Cu(111).

The difference in adsorption properties of ZnTFcBP and H_2TFcBP suggests that the molecules interact with the surface primarily through the TPP core of the molecule. However, due to the convolution of the geometric and electronic properties in STM measurements, and since these molecules are quite large, it is not possible to confirm this with STM alone. To assign the adsorption configuration, we turn to DFT calculations carried out by our collaborators in the Cuniberti group at TU Dresden. Here, they calculated the total energy of the surface as a function of adsorption distance (referenced to the Fe-surface separation, averaged over the four Fc groups) for two configurations of both ZnTFcBP and H_2TFcBP; one where the porphyrin core is closest to the Au(111) surface and the Fc groups are pointing away, and the other where the Fc groups are closer to the surface. These configurations are shown in Fig. 4.7, and from the total energy curves it can be seen that for both molecules the lower energy configuration is the former.

We have already noted that the conformation of adsorbed porphyrin derivatives can greatly impact the self-assembly of those molecules. In figure 4.8(a) and (b), contour maps highlighting the calculated deformation of the porphyrin macrocycle at the center of ZnTFcBP and H_2TFcBP are shown. From these it can be seen that the porphyrin macrocycle is best described as ruffled, according to the standard classification of porphyrin distortions, for both ZnTFcBP and H_2TFcBP. The calculated deviations from planarity are quite modest; when Fc

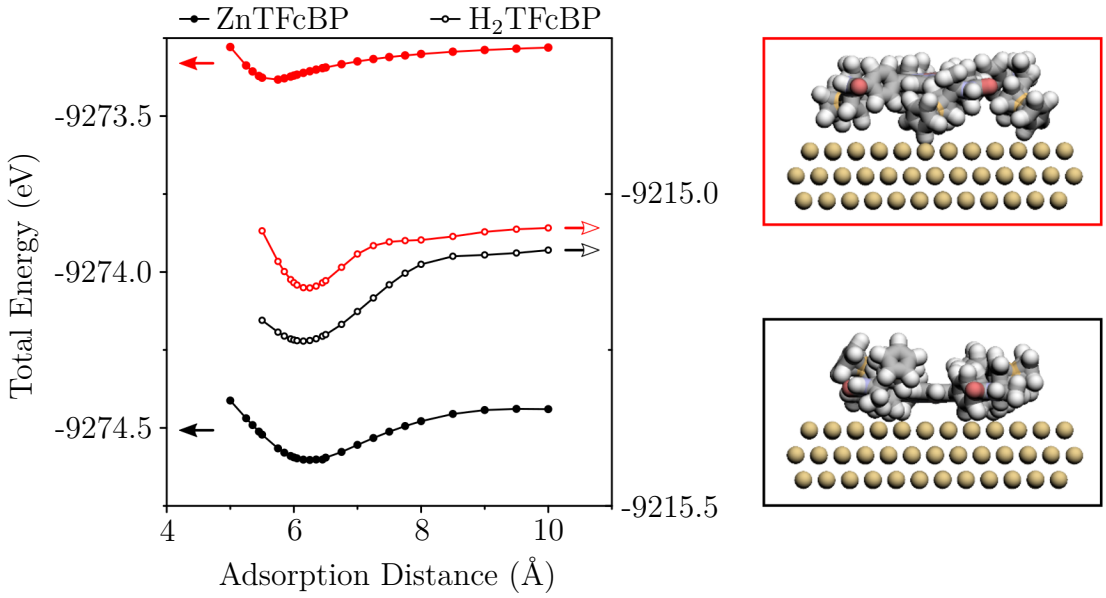

Figure 4.7: DFT calculations of the total energy of the molecule-substrate system for both ZnTFcBP and H_2TFcBP show that the adsorption configuration with the ferrocene groups facing away from the surface (black) is energetically preferable to that where they are closer to the surface (red).

groups are directly bound to the porphyrin macrocycle, out of plan distortions up to ±0.6 Å are expected,[353] although no data for these molecules adsorbed on a surface are available, which could restrict the deformation in order to maximise interaction with the surface. The large angles between the phenyl groups and the plane of the porphyrin (58° - 88°) are consistent with ruffling, whereas for a saddle deformation, angles below 30° are expected.[341,354]

As previously mentioned, STM topography is a convolution of geometric and electronic information, and, as a result, we do not expect to be able to resolve the moderate ruffling of the porphyrin. Indeed, at biases where we resolve the porphyrin, it appears planar for ZnTFcBP, as can be seen from Fig. 4.8(d). A small depression is observed at the centre corresponding to the filled Zn d_{z^2} orbital.[355,356] However, for H_2TFcBP, while most of the macrocycles appear as a hollow ring, we see some with prominent features along the diagonal of the porphyrin *meso-meso* axis. These features are well known to arise when a porphyrin adopts a saddle conformation,[226] and have been reported many times in the past even within the same molecular island.[298,357] Indeed, Zhang *et al.*[358] have reported that they observe two porphyrin conformations, even when the difference in adsorption energy approaches 1 eV. We reported this for the ZnTFcBP fragments on Au(111) in chapter 3, however we did not observe any of the intact molecules in the saddle conformation. Two H_2TFcBP molecules with flat macrocycles and

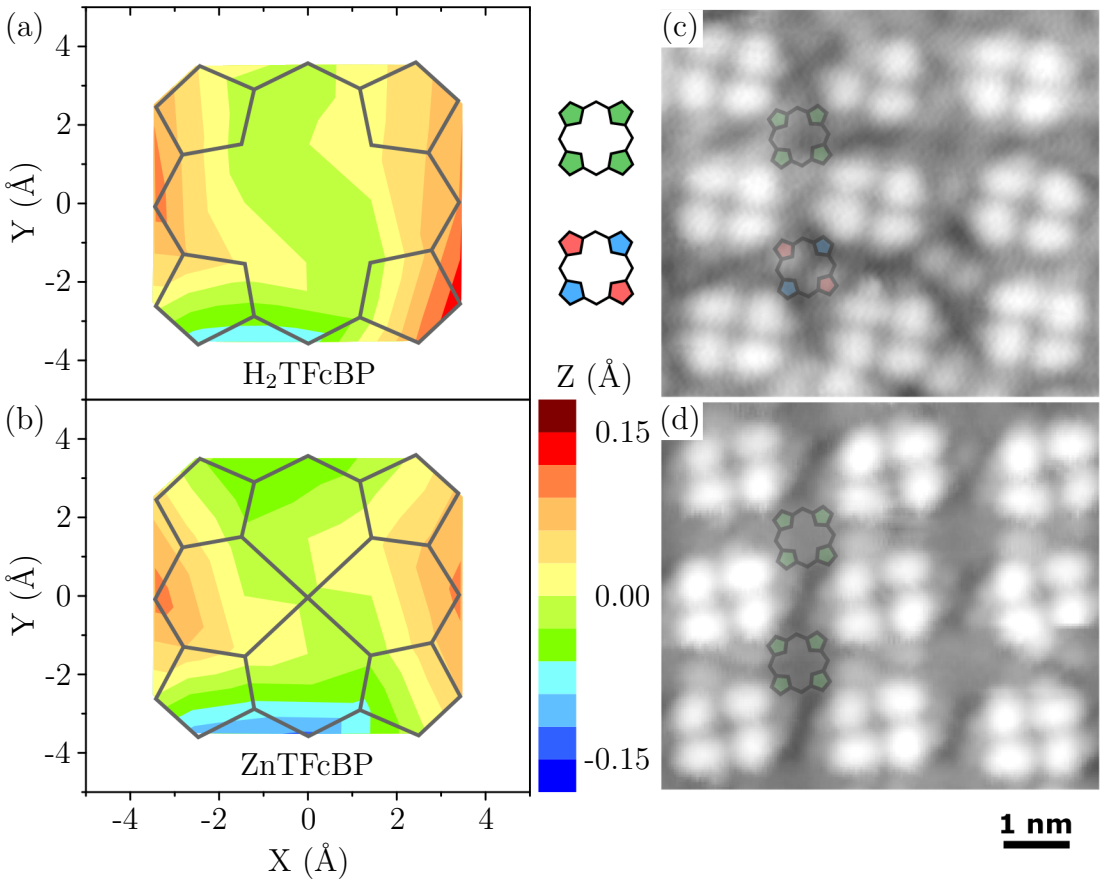

Figure 4.8: The porphyrin macrocycle at the centre of H_2TFcBP and ZnTFcBP adopts a non-planar conformation when adsorbed on Au(111), as shown in (a) and (b) respectively, according to DFT calculations. In some of the H_2TFcBP molecules on Au(111) the porphyrin core appears flat with a central depression, while in others two protrusions are observed along a molecular diagonal [shown in (c)] which are due to the deflections of the pyrrole rings in the saddle conformation. For ZnTFcBP, all of the porphyrin cores look identical as shown in (d). Imaging conditions: (a) 25 pA, −0.575 V, (a) 20 pA, −1.5 V.

two with saddle conformations (indicated by the sketches of the porphyrin ring showing the deflection of pyrrole groups) are shown in figure 4.8(c), where the pyrrole groups protrude by ∼0.4 Å.

In summary, we have found that ZnTFcBP and H_2TFcBP both interact with Cu(111) and Au(111) primarily with their TPP backbones. The porphyrin has a ruffled macrocycle when adsorbed on the surface, which, for H_2TFcBP, can undergo a saddle deformation. On Cu(111) there is a significant molecule-substrate interaction for ZnTFcBP and H_2TFcBP which prevents self-assembly into the square patterns they were designed to form. The Au(111) surface, on the other hand, both molecules self-assemble in this square pattern, driven by four sets of cyclic dimeric hydrogen bonds, which results in Fc quartets resembling the type

of structures necessary for MQCA applications.

4.4 Electronic Properties of Molecular Networks

Now that the adsorption and self-assembly of our MQCA candidates have been fully characterised, we describe the electronic properties of these assemblies.[287] We begin by analysing the projected density of states (PDOS) calculated by our collaborators in Dresden, and the details of the calculations can be found elsewhere.[287,288] The PDOS of ZnTFcBP and H_2TFcBP, calculated both in the gas-phase and adsorbed on Au(111), are presented in the top and middle panel of Fig. 4.9, respectively. The similarity between the gas-phase and adsorbed PDOS is expected for weakly adsorbed molecules. The calculated electron localisation function (ELF) takes the value of 0.2 to 0.5 in the region between the molecule and the surface, indicating that no significant charge transfer takes place and that the interaction between the molecule and the surface is non-covalent in nature.[359] The minor changes to the PDOS upon adsorption are attributed to conformational changes, where the Fc units tilt and undergo torsional distortions with respect to the phenyl rings. Additionally, it can be seen that, as expected,[360,361] the coordination of a zinc metal center to the porphyrin macrocycle has very little effect on the PDOS.

The calculated HOMO-LUMO gap of both ZnTFcBP and H_2TFcBP is reduced from ∼3.2 eV in the gas phase to ∼2.7 eV upon adsorption, which is attributed to screening by image charges, as discussed in section 1.3, in addition to the small conformational changes already mentioned. This compares quite well with the 2.3 eV transport gap measured from the STS, shown in the bottom panel of Fig. 4.9. Despite the fact that DFT often underestimates the HOMO-LUMO gap,[362] the overestimate observed here is comparable to that reported for similar systems.[356] Additionally, the position of the porphyrin-centred LUMO, which is relatively insensitive to the conformation of the porphyrin macrocycle,[335,363] is in good agreement with the reported values for TPPs,[338,356,358] including that reported for the ZnTFcBP fragment in chapter 3.

As described in section 2.1, the STM current is proportional to the integral of the LDOS over the tunnelling window, weighted by the transmission function. The $\mathrm{d}I/\mathrm{d}V$ signal, on the other hand, corresponds to the LDOS intensity at the selected bias voltage, and therefore we can directly compare $\mathrm{d}I/\mathrm{d}V$ maps to the MOs at various energies. The MOs are very closely separated and are broadened by the presence of the surface, as outlined in section 1.3, so that the $\mathrm{d}I/\mathrm{d}V$

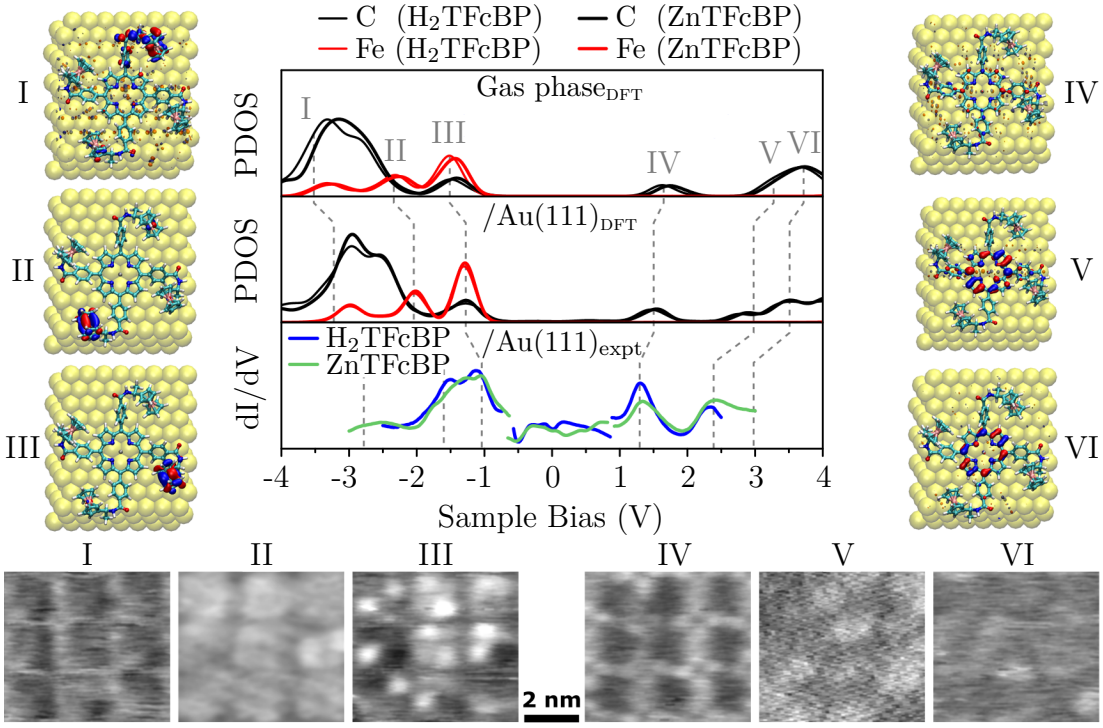

Figure 4.9: Comparison of calculated PDOS and MO spatial distribution to STS data and dI/dV maps. The PDOS for organised ZnTFcBP and H_2TFcBP molecules in the gas phase and adsorbed on Au(111) are shown in the top and middle panels, respectively. These are compared to STS data for the two molecules, shown in the lower panel, and relatively good agreement is observed once the energy scales have been adjusted. We compare the calculated MOs to dI/dV maps at energies marked by the grey lines (I-VI), and here too we find good agreement.

maps correspond to a superposition of MOs. Starting from the filled states at a bias −3 V, the PDOS intensity is localised on the C atoms, and the MO marked I is localised predominantly on the TPP part of the molecule. We find good agreement between the spatial distribution of the MO in I and the corresponding dI/dV map. Similarly, both the MO distribution and dI/dV maps between −2 V to −1 V, marked II and III respectively, show localisation to the Fc sites.

In the empty states region of the spectrum (positive biases), there is negligible contribution from the Fe atoms, and the PDOS is localised entirely on the C backbone of the molecule. At 1.3 V (IV) we clearly map out the TPP core in the dI/dV channel, in good agreement with the MO distribution. Moving to higher biases, we begin to lose contrast in the dI/dV map, since the MOs are more evenly distributed throughout the molecule. Some contrast is available for peak V, at ∼2.3 V, where it mainly appears between adjacent molecules, across the amidophenyl groups, but this contrast disappears at 3 V.

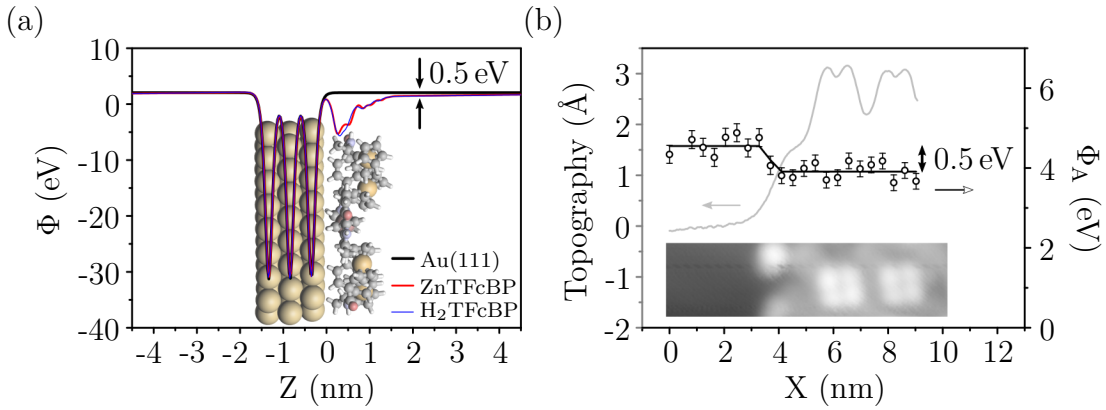

Figure 4.10: The workfunction is altered by ∼0.5 eV upon adsorption of ZnTFcBP and H_2TFcBP. In (a) we show the calculated plane-averaged electrostatic potential profile through the relaxed slab, with a model of the surface behind the plot. Far from the surface, the electrostatic potential with and without the each of the molecules reveals a workfunction difference of 0.5 eV. We compare this to experimental data in (b), where we have extracted the apparent barrier height from $I(z)$ data measured along a line from the bare Au(111) to over the molecular island. We again find a reduction of 0.5 eV on the molecular island relative to the Au(111).

In the modelling we have detected a surface dipole, which lowers the effective workfunction of the system by 0.5 eV, as shown in figure 4.10(a). Here, the plane-averaged electrostatic potential is shown for a cross-section of the molecule adsorbed on the three-layer Au(111) slab, and far from the surface there is a 0.5 eV difference between the electrostatic potential for the bare slab and that with either of the adsorbed molecules. This dipole was identical for ZnTFcBP and H_2TFcBP, as expected from the similarity of the PDOS. We have compared this to the difference in apparent barrier height, extracted from the $I \propto e^{-\alpha\sqrt{\Phi_A}z}$ relationship as discussed in chapter 2, measured from $I(z)$ spectra along a line going from the bare Au(111) to above the molecular island. The resulting Φ_A values are shown in figure 4.10(b), with the topographic profile along the line on which the spectra were measured shown on the other axis, and a STM image of the area in the inset. We find approximately a 0.5 eV difference between the barrier height measured above the bare Au(111) surface and above the molecular island, in excellent agreement with the theory.

Both the intrinsic molecular dipole and the charge transfer dipoles are very small for this system and we therefore attribute the formation of the surface dipole to the push-back effect, as discussed in section 1.3. The $\Delta\Phi = -0.5$ eV measured here is slightly less than literature results for CoTPP/Ag(111) where $\Delta\Phi = -0.7$ eV,[364] and ZnTPP/Ag(111) where $\Delta\Phi = -0.86$ eV.[345] However, con-

sidering the larger molecule-surface separation (∼4 Å for ZnTFcBP compared to ∼3 Å for CoTPP) and larger molecular area we expect a smaller push-back dipole.

The fact that we see molecular contrast even within the bias window corresponding to the HOMO-LUMO gap can, at least partly, be attributed to the presence of the surface dipole induced by adsorption of the molecule. In the bias range between −3 V and 1 V, the Fc groups dominate the STM contrast, which should indicate that the magnitude of surface dipole is greatest at these locations. Unfortunately, the apparent barrier height cannot be measured with submolecular resolution, since a finite area of the surface is sampled during $I(z)$ spectroscopy. Since the surface dipole is mainly due to the push-back effect, we expect it to be greatest above those parts of the molecule which are closest to the surface. The Fc moieties are situated 2 Å to 3 Å further from the surface than the porphyrin core, and therefore we expect that the surface dipole cannot account for the observed contrast. It is possible that the modulation of the Au(111) surface state by the molecule could account for the STM contrast within the HOMO-LUMO gap. However, as we will see below, ZnTFcBP and H_2TFcBP have different effects on the surface state, which if this were the cause of the molecular contrast would lead to differences in the topography of ZnTFcBP and H_2TFcBP in the low bias regime, which was not observed. Another possibility is that tunnelling through virtual states at the Fc sites increases the tunnelling rate and therefore the current, as discussed in section 2.2.2.

As we have already mentioned, the surface dipole is primarily due to the push-back effect. Since the push-back effect involves suppressing the leakage of electrons into the vacuum, it is reasonable to expect it to have some effect on the surface state which is localised to this region. It is well-known that molecular adsorption can quench or shift the surface state.[322,365,366] To investigate the effect of adsorption on the surface state, we integrated the PDOS in the region of the surface state, from −0.5 V to 0 V, and the resulting integrated density of states (IDOS) maps are shown in Fig. 4.11(a). We can clearly see that the modulation pattern is different for H_2TFcBP and ZnTFcBP.

To compare the IDOS maps in Fig. 4.11(a) with experimental results, we have extracted LDOS data from $I(V_b, z)$ spectra (as outlined in section 2.3.3) measured across both H_2TFcBP and ZnTFcBP. Colour maps displaying the LDOS, measured across the section of molecule shown in figure 4.11(b), are shown in figure 4.11(c), where the shaded regions exclude energies outside the surface state. Again, we can clearly see that the surface state is detected in different locations. The areas in which the surface state is detected are shown schematically in figure

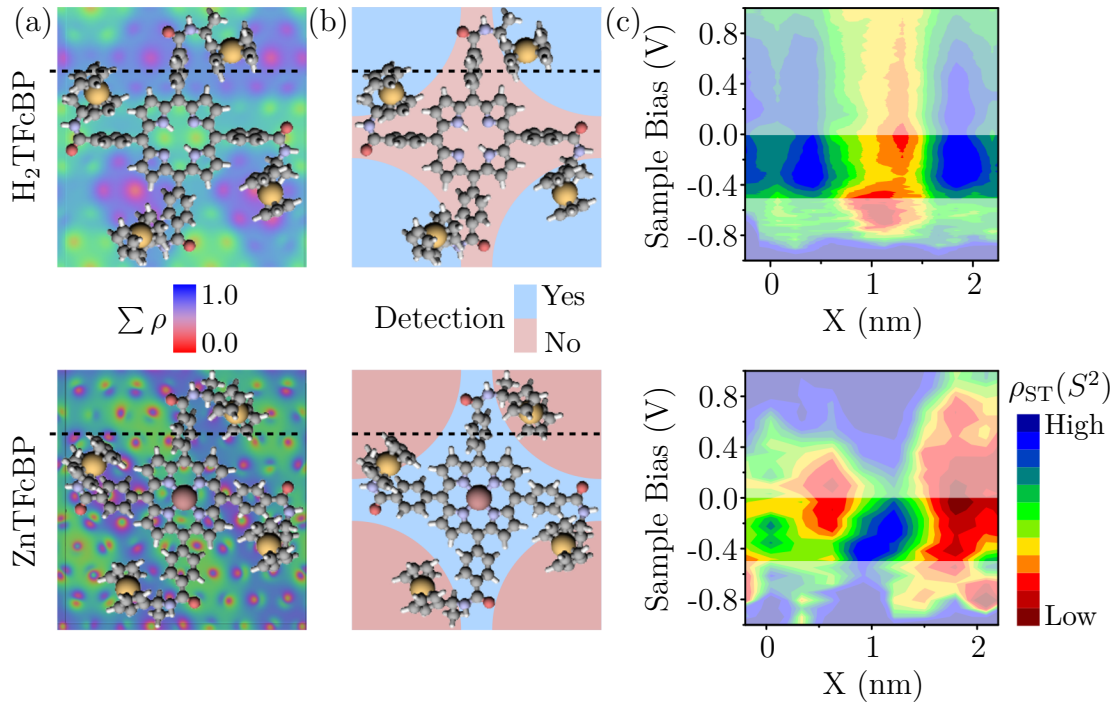

Figure 4.11: DFT and STS mapping of the modulation of the Au(111) surface state by the adsorbed molecule. Maps of the relative intensity of the surface localised DOS, calculated by integrating the PDOS from −0.5 V to 0 V are shown in (a) for H_2TFcBP (top) and ZnTFcBP (bottom). A schematic of the regions in which the surface state was detected for each of the molecules are shown in (b). The detection regions were taken from (c) where LDOS maps were extracted from $I(V_b, z)$ data recorded across the line indicated in (b). The regions outside the surface state region are made opaque, and it can be seen that H_2TFcBP and ZnTFcBP have different effects on the Au(111) surface state.

4.11(b), and we can assert that overall there is reasonably good agreement between the theoretical and experimental patterns of the surface localised density of states.

On closer inspection of the $\mathrm{d}I/\mathrm{d}V$ map corresponding to peak III in figure 4.9, it can be seen that the Fc groups have varying LDOS intensity at this bias. A larger image of this $\mathrm{d}I/\mathrm{d}V$ map is presented in Fig. 4.12(a). To investigate the origin of this behaviour we measured $Z(V_b)$ spectra along the line in Fig. 4.12(b), and constructed a contour map to visualise the evolution of the spectra, which is shown in Fig. 4.12(c). It is clear that the porphyrin-centred LUMO state is constant in energy, whereas the empty states show a Fc-based peak which is strongly modulated in space.

We have estimated the centres of the states by fitting each spectrum with Gaussian curves (two on the filled states side, and one in the empty states) whose widths were fixed at 0.45 V, and these centres are indicated for each spectrum

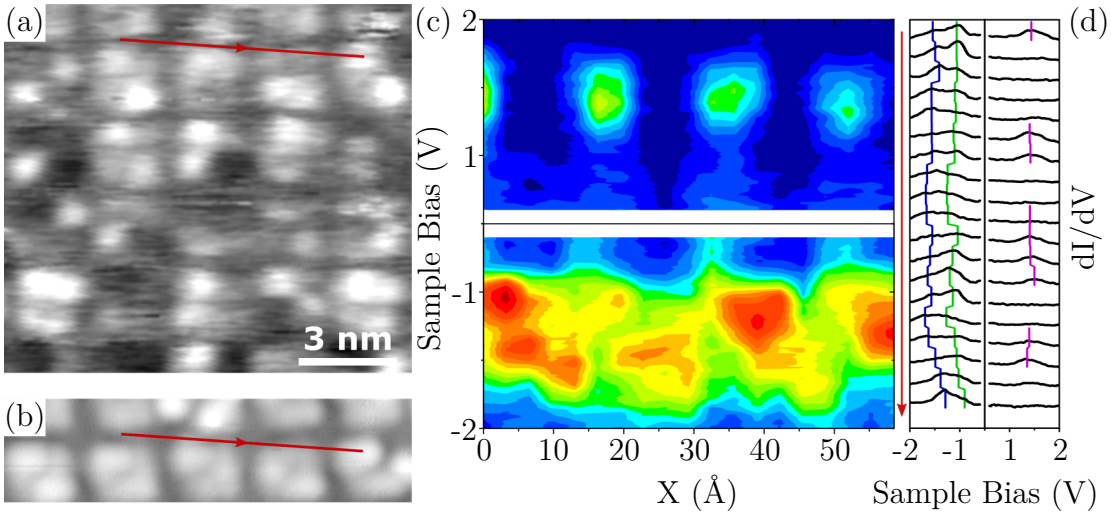

Figure 4.12: The dI/dV map for peak III in figure 4.9 shows a position depended intensity, as is shown for a larger area in (a). To ascertain the origin of this behaviour we have constructed a dI/dV heat map from constant-current spectra measured along the line in (b). This heat map is shown in (c), and it is clear that the LUMO, which is localised on the molecules conjugated backbone, is constant in energy, whereas the Fc-derived OMOs shift in energy. By tracking the centres of these peaks in (d), which were obtained by fitting Gaussian curves with FWHM of 0.45 V, we can see that the Fc-based peaks are shifting in a concerted manner, while the TPP-derived peak is approximately constant in energy.

in Fig. 4.12(d). It should be noted here that the Fc peak is detected across the island, while the state localised to the conjugated backbone of the molecule is not, due to the relative heights of the respective parts of the molecule and the finite extent of the tip. The porphyrin-derived state is approximately constant in energy, varying by ±0.08 V around a center of 1.42 V. On the other side, the Fc based peaks shift around −1.10 V and −1.55 V by ±0.2 V. The separation between the two filled states appears to be constant at 0.44 V, with an error comparable to that of the LUMO which is taken as the experimental error here.

The concerted nature of the shifting OMO states suggests that it is a modulation of the local surface dipole which is driving this behaviour. The linker between the Fc groups and the amide is conformationally flexible, and indeed DFT calculations of the relaxed structure show that each Fc group in the molecule has a different conformation. The Fc groups in ZnTFcBP range from being almost parallel to the surface to having a 30° rotation, and the Fe ions at the center of these groups varying at heights from 6 Å to 6.7 Å relative to the surface. While this small height difference should not appreciably impact the push-back dipole, which in any case is expected to be greatest beneath the TPP backbone of the molecule, it can still shift the MO energies in the hundreds of mV range, primarily

due to screening effects.[367] While DFT predicts just four Fc conformations, in the real system we expect a continuum of possible orientations due to finite island size, the influence of the underlying herringbone reconstruction, packing faults, and entropic effects.

The pattern of LDOS intensity modulation in Fig. 4.12(a) appears random, suggesting that conformational variations do not propagate through the island. We attempted to modify the conformation of the Fc groups in a quartet to investigate this, however the molecular islands were found to be extremely stable and detectable changes in conformation could not be made without also modifying the tip.

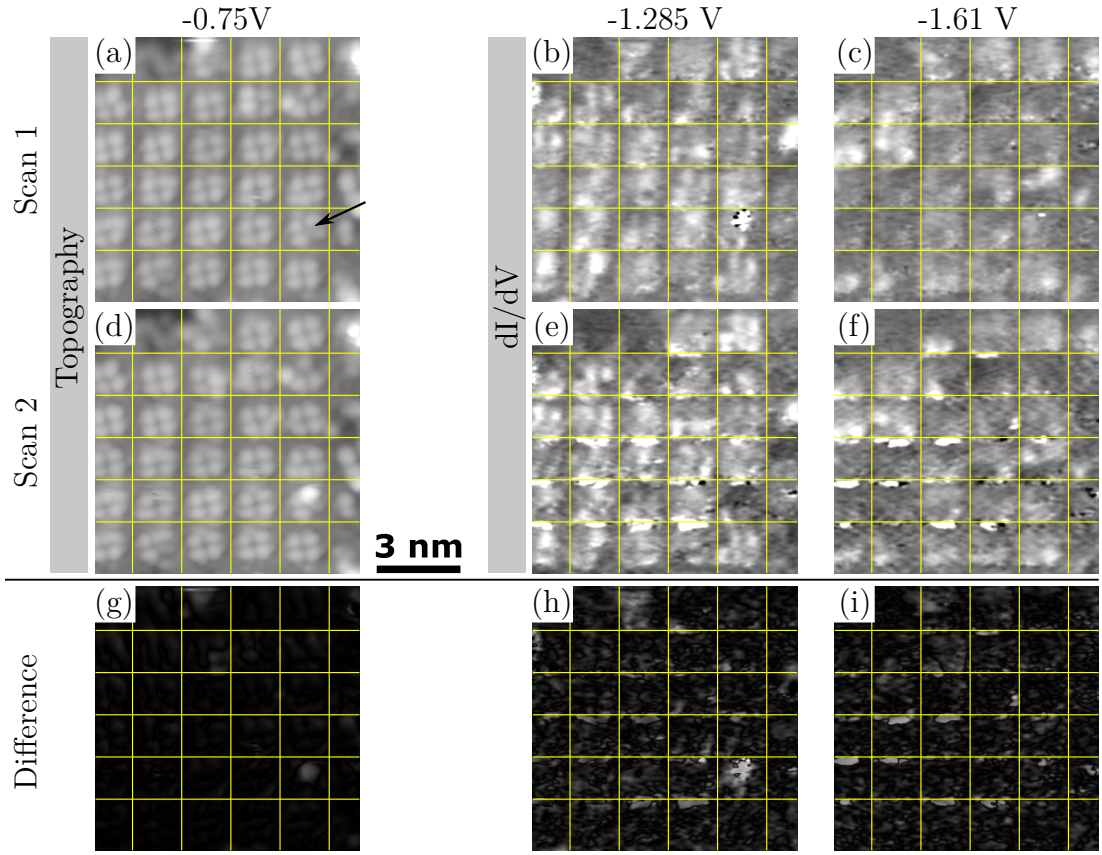

Figure 4.13: The conformational influence on the LDOS intensity variations was investigated by scanning a molecular island before and after modifying it, by moving the STM tip 6 Å towards the surface with the sample bias set to 0 V, at the location indicated by the arrow. The topography is shown at a sample bias of −0.75 V for the first and second scans in (a) and (d), respectively, and the difference map in (g) highlights the changes. Comparing the $\mathrm{d}I/\mathrm{d}V$ maps in (b) and (c) to those in (e) and (f) results in the difference maps in (h) and (i), which show that large variations in the $\mathrm{d}I/\mathrm{d}V$ intensity between the two scans occurs only in those Fc quartets where topographical changes can be resolved, *i.e.*, where the island was modified and near its edge at the top left of the image.

In figure 4.13 we show two STM measurements of an organised ZnTFcBP island where the local geometry has been slightly altered between the scans by approaching the tip 6 Å toward the surface with the bias set to 0 V. The topographs in Fig. 4.13(a) and (d) were measured at −0.75 V in order to minimise the contribution from the LDOS localised on the Fc groups. The conformational changes, insofar as they manifest in the STM apparent height, are visualised in figure 4.13(g), which was constructed by taking the absolute value of the differences between the height values in Fig. 4.13(a) and (d).

Comparing the $\mathrm{d}I/\mathrm{d}V$ maps at −1.285 V and −1.61 V for each of the two scans [Fig. 4.13(b) and (e) and Fig. 4.13(c) and (f), respectively], it is clear that the tip has indeed been modified in the process of modifying the molecular island. In the second scan, the tip is noisy in the region between the Fc quartets, indicating an unstable tip apex. In spite of this, the LDOS intensity distribution is consistent between the two scans, at both biases, except in those cells which show topographic differences from one scan to the other. This is visualised in the difference maps presented in Fig. 4.13(h) and (i). We conclude from this that, while the electronic properties of these assemblies depend on the local conformation, conformational irregularities are not strongly propagated, and that moderate steric interactions between the Fc units would not be expected to spuriously switch the charge configuration in a QCA device constructed from these molecules.

As discussed in chapter 1, upon changing the oxidation state of the Fc groups, we expect some conformational reorganisation of the molecule. Since we have seen that ZnTFcBP and H_2TFcBP form very stable self-assembled structures where conformational differences are not propagated, it is reasonable to expect that charging some of the Fc groups would not disrupt the molecular packing. To test this hypothesis, we require that the Fc groups be sufficiently decoupled from the underlying substrate that the lifetime of the resonance is sufficiently long to facilitate charge capture as outlined in chapter 2. Despite the fact that the Fc groups are located quite far from the surface, and that they are decoupled from the rest of the molecule through the saturated linker, we find no evidence of the self-decoupling which has been observed in other systems.[368] In fact, the broad width of the Fc-derived states is indicative of coupling to the underlying substrate. Rigidity of the system is reported to be an important factor for effective self-decoupling,[368] and as we have seen the Fc groups are not rigidly bound. In order to investigate the effects of injecting charge into these systems, we therefore need to insert a spacer layer between the metallic substrate and the molecular

assembly, which will be the focus of the next chapter.

4.5 Conclusions

In this chapter we have described a molecule which forms stable hydrogen-bonded molecular islands with a square architecture. While ZnTFcBP and H_2TFcBP lack the Fc-Fc electronic coupling which is required for MQCA, we believe they represent a valuable model system for MQCA. However, in order to investigate the properties of these assemblies when some of the Fc groups have been oxidised, we need to decouple the molecular states from those of the substrate. This task is the focus of the next chapter.

We found that the adsorption properties are similar in many ways to those of the TPP molecule on which these molecules are based. Both ZnTFcBP and H_2TFcBP bind to the surface predominantly *via* Van der Waals interactions which are strongest beneath this TPP backbone. We have reported that the molecule-molecule interactions drive a square packing motif for both the free-base and Zn-metallated versions of the molecule on Au(111) in UHV, in air and at the solid-liquid interface, and at the air- and liquid-HOPG interfaces. We have also shown that surfaces with stronger molecule-substrate interactions, such as Cu(111), can drive deviations from the desired square architecture, or in the case of H_2TFcBP disrupt self-assembly altogether. We have also shown that while the ruffled macrocycle geometry is favoured for this molecule, and that the conformational flexibility distinctive of TPP derivatives is retained.

By comparing STS measurements to DFT calculations of the PDOS and MOs, we have shown that the HOMO and LUMO are localised to the Fc and TPP parts of the molecule, respectively. We find good agreement between experiment and theory for the presence of a 0.5 eV reduction of the workfunction upon adsorption of ZnTFcBP or H_2TFcBP on Au(111), and in the modulation pattern of the surface state by the molecules. We have also observed variations in the energies of the OMOs localised on different Fc groups which we have attributed to conformational disparities between them. The shifts of these states appear not to be propagated over the molecular assembly which leads us to believe that these islands may be insensitive to the conformational changes which are expected to occur upon charge injection. If this conformational flexibility were to hold upon replacement of the saturated amine-ferrocene linker with a conjugated version, such that intermolecular Fc-Fc coupling was introduced through the hydrogen bonds, the result would be a highly promising system for demonstrating MQCA.

5

Functionalised Porphyrins on Thin Insulating Layers

In the previous chapter we showed that we could create square arrays of functional molecules on surfaces where the molecule-molecule interaction dominates. We found that these arrays had interesting electronic properties, with molecular states well-localised on different parts of the molecule. However, these states were hybridized with the electronic states of the underlying metal, and, as described in section 2.2, we require them to be weakly coupled to the substrate states in order to probe their excited states. We saw in section 1.3 that orbital overlap is the key parameter influencing the coupling of adsorbate and substrate states. Therefore, the adsorbate can be protected from hybridisation with the substrate states by increasing the separation between the two.

There are three popular strategies to minimise the perturbation of adsorbate electronic structure on adsorption: self-decoupling through the use of bulky side-groups,[369,370] pre-depositing a sacrificial adsorbate layer,[371,372] and inserting a TIL between the molecule and substrate.[373,374] Additionally, in very specific cases lateral intermolecular interactions have been shown to result in weakly coupled molecules,[375,376] however this is not generally applicable. Self-decoupling would add another layer of complexity onto an already demanding list of design requirements, while using a sacrificial adsorbate layer may result in favoured adsorption sites and interfere with the self-assembly, and, as a result, neither of these strategies are pursued here.

The use of TILs is based on the fact that, in order to hybridise, adsorbate and substrate states not only need to be in close spatial proximity, but need to have

similar energies. Insulators have no states within the band gap so that the frontier MOs cannot hybridise with the insulator states in the band gap region. Defect states lie within the band gap, facilitating coupling with the adsorbate, and as a result the quality of the insulating film is very important.[377] For STM we require a conductive substrate, ruling out bulk insulators. However, insulating films thin enough to allow tunnelling are STM-compatible, and have been demonstrated to exhibit a band gap approaching that of the bulk.[373]

Depositing molecules on TIL-on-metal systems is by far the most popular strategy for investigating weakly-perturbed adsorbate states, and has had facilitated some extraordinary experiments. The frontier MOs of pentacene have been mapped out with STM in astonishing detail, and were found to match extremely well the shapes predicted by theory.[167] This has subsequently been repeated for other molecules.[378] Additionally, charge has been injected into atomic and molecular adsorbates,[158,192,379,380] and single-molecule chemistry has been performed.[159,381,382]

The ability to tune substrate properties is clearly a very powerful tool in STM experiments. In this chapter we outline our attempts to investigate self-assembled arrays of QCA candidate molecules on various different spacer layers, and the challenges associated with using ESD with complex substrates. We start by describing the substrate systems used, then in section 5.2, we show that some of these are incompatible with ESD. Finally, in section 5.3 we show limited success in decoupling molecules using Cu_2N−Cu(100), while our molecules are strongly bound to the Cu_3N−Cu(110) surface.

5.1 TILs for Decoupling MQCA Candidates

A variety of thin film systems have been reported as effective decoupling layers in the literature, including inorganic salts,[373,383–386] inorganic and metal nitrides[193,387–389] and oxides,[390–393] alkanethiol films,[394] noble gas layers,[378,395,396] and passivated semiconductors.[397] We focus here on three systems: NaCl(100) on Au(111) and the surface nitrides of Cu(100) and Cu(110).

5.1.1 NaCl/Au(111)

NaCl(100) is one of the most widely used TILs in surface science and indeed has played a role in STM experiments for more than two decades.[383] Bulk NaCl is an insulating ionic crystal with a cubic crystal structure, where each Na^+ ion is surrounded by six Cl^- ions, and *vice versa*, at a separation of 5.63 Å.[309] This

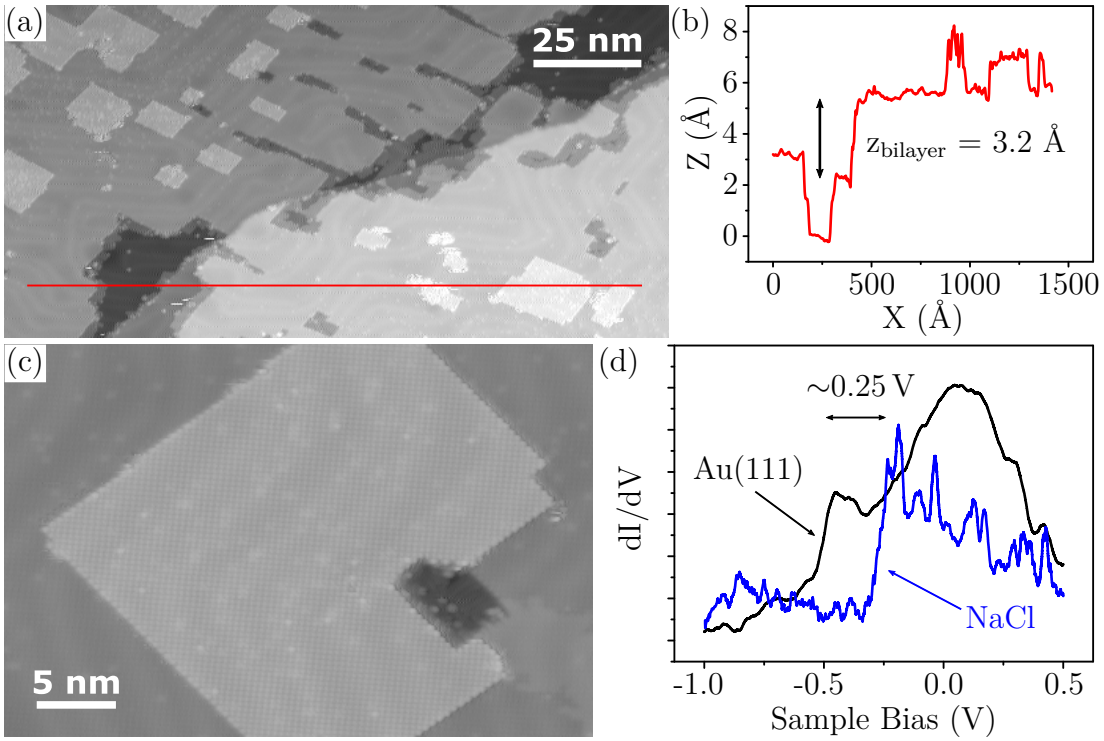

Figure 5.1: NaCl(100) on Au(111). (a) shows large bilayer NaCl(100) islands smoothly overgrowing Au(111) steps, with trilayer islands beginning to go on top. The apparent height of the bilayer is 3.2 Å, with the third layer 1.8 Å high, which is shown by the line profiles in (b). The high resolution image of a third-layer islands in (c) shows perfect non-polar step edges and atomic resolution of the Cl^- species. The Au(111) surface state is shifted ~250 mV towards the Fermi level upon adsorption of NaCl(100), as illustrated by the $I(V_b, z)$ spectra plotted in (d). Imaging conditions: (a) −1 V, 20 pA; (c) −2 V, 20 pA

structure maximises the contact between unlike charges. The bulk band gap is approximately 8.5 eV, which is established in very thin films.[398]

Thin films displaying the NaCl(100) facet have been grown on a range of substrates, including Ge(100),[399] Cu(111),[400] Cu(110),[401] Cu(211),[402] Ag(100),[403] Al(111), Al(100)[404] and Au(111).[405] The (100) plane is favoured since it is electrically neutral, *i.e.*, each layer contains the same number of Na^+ and Cl^- ions. It is for this same reason that islands with four-fold symmetry and 90° angles between edges are exclusively observed, minimising the appearance of unstable kinks. These islands overgrow steps in a carpet-like fashion, where they tend to align their polar axis parallel with the step edge due to Coulombic interactions with the Smoluchowski dipole at the step.[406] This can be seen for the bilayer/trilayer NaCl(100) films grown on Au(111) in Fig. 5.1(a), from which it is also clear that adsorption of NaCl does not modify the herringbone reconstruction on the Au(111) surface.

These films are prepared by sublimating NaCl from a crucible in UHV, which allows for precise control of the layer thickness. Sublimated material travels as Na^+Cl^- clusters, thus maintaining the stoichiometry.[407] Monolayer NaCl can be grown if the sample is held at low temperature during deposition, but is unstable at room temperature where it spontaneously converts to bilayer.[408] For both monolayer and bilayer growth, the next layer begins to grow before previous layer has terminated, as can be seen from figure 5.1(a). All of the films used in our experiments were prepared at room temperature. Annealing the bilayer/substrate system to 470 K promotes its conversion into predominantly trilayer NaCl(100).[409] The apparent height of an NaCl(100) bilayer is 3.2 Å, less than twice that of a single layer (1.8 Å), while the third layer appears as a 1.5 Å step, as can be seen in figure 5.1(b).[409]

A high resolution image of a third layer island on top of a NaCl bilayer is shown in figure 5.1(c). Here we clearly resolve atomic corrugation, with a nearest neighbour distance of ∼4 Å. This corresponds to the 3.99 Å spacing between two ions of the same species in the bulk (100) plane. It has been reported that under normal conditions we resolve the Cl^- ions in STM irrespective of the applied bias,[383,404] although the Na^+ ions have also been resolved.[366] The nearest-neighbour distances for the NaCl(100) layer are modulated by the underlying herringbone reconstruction, which can clearly be seen through the NaCl(100) layers in Fig. 5.1(a).

The NaCl film compresses the charge density leaking from the underlying substrate as discussed in section 1.3, forming a push-back dipole which reduces the workfunction by 1.1 eV on Au(111).[408] Adsorption of a NaCl(100) bilayer also transforms the Au(111) Shockley surface state into an interface state localised between the metal and the film, and shifts its energy by ∼250 meV, as can be seen in the STS plots shown in Fig. 5.1(d). The shift in the band onset energy is attributed to a reduction in the image potential upon adsorption of a NaCl film.[410] In fact, the onset of the interface state is modulated by the Au(111) herringbone reconstruction, with a 60 meV shift towards the Fermi level over the fcc domains compared to the hcp domains.[366]

This interface state is extremely useful for investigating the excited states of adsorbates since it can be used to probe the charge state of an adsorbed atom or molecule.[407] The layer itself decouples an adsorbate efficiently enough that its ion resonances may have experimentally accessible lifetimes.[158] The electrostatic interaction between an adsorbate and the interface state electrons depends on the charge of that adsorbate. Neutral adsorbates have a short-range repulsive

potential which should only weakly scatter interface electrons. A negatively-charged adsorbate will have a longer-range potential and therefore strongly scatter the interface state. On the other hand, a positively-charged atom or molecule will interact attractively with the interface electrons, localising them below the adsorbate.[411]

While NaCl bilayers efficiently decouple adsorbate states from those of the underlying substrate, the adsorbates states can still be broadened by coupling to vibrations in the NaCl lattice.[167,412] This can be advantageous since it may help stabilise the charged states of an adsorbate, as outlined in section 2.2, however, when probing the electronic structure of an adsorbate, as little perturbation as possible is desired. Using heavier ions can mitigate this electron-phonon coupling, as has recently been demonstrated using RbI films.[378]

5.1.2 Cu_2N−Cu(100)

The nitrides of the close-packed surfaces of copper are also popular choices as spacer layers. In the bulk, Cu_3N has an *anti*-ReO_3 structure, where nitrogen atoms occupy the corner sites of a cubic unit cell, with a Cu atom along the edge between each pair of nitrogen atoms.[413] The unit cell vector is 3.819 Å in length. Atomically thin copper nitride layers can be formed on all of the close-packed copper surfaces.[414–416]

Molecular nitrogen is physisorbed on Cu(100) at low temperatures,[417] but not at room temperature.[418,419] Nitrogen chemisorption must be activated, and is commonly achieved by electron irradiation,[419] decomposition of NH_3,[420,421] or by bombarding a copper surface with nitrogen ions.[422] Such a N overlayer is stable up to temperatures around 770 K.[423]

Chemisorbed nitrogen atoms occupy every other fourfold hollow site on the Cu(100) surface, forming a c(2 × 2) overlayer structure which has a Cu−N bond length of 1.85 Å.[421] Cu_2N islands, such as that shown in figure 5.2(a), consist of alternating rows of Cu and CuN.[387] The $c(2 \times 2)$-N layer is incommensurate with the underlying substrate, leading to strain in the film.[424] This strain gives rise to two different coverage regimes in which the elastic strain manifests in different ways.

In the low coverage regime, corresponding to $\Theta < 0.5$ ML, adsorbed nitrogen atoms attract each other to form c(2 × 2) islands with edges running in the ⟨100⟩ directions. Strain limits the size of these Cu_2N islands to ∼52 Å.[425] As the coverage increases, these rectangular islands come closer and closer together until they form a grid-like array. The low-coverage Cu_2N−Cu(100) surface is shown in

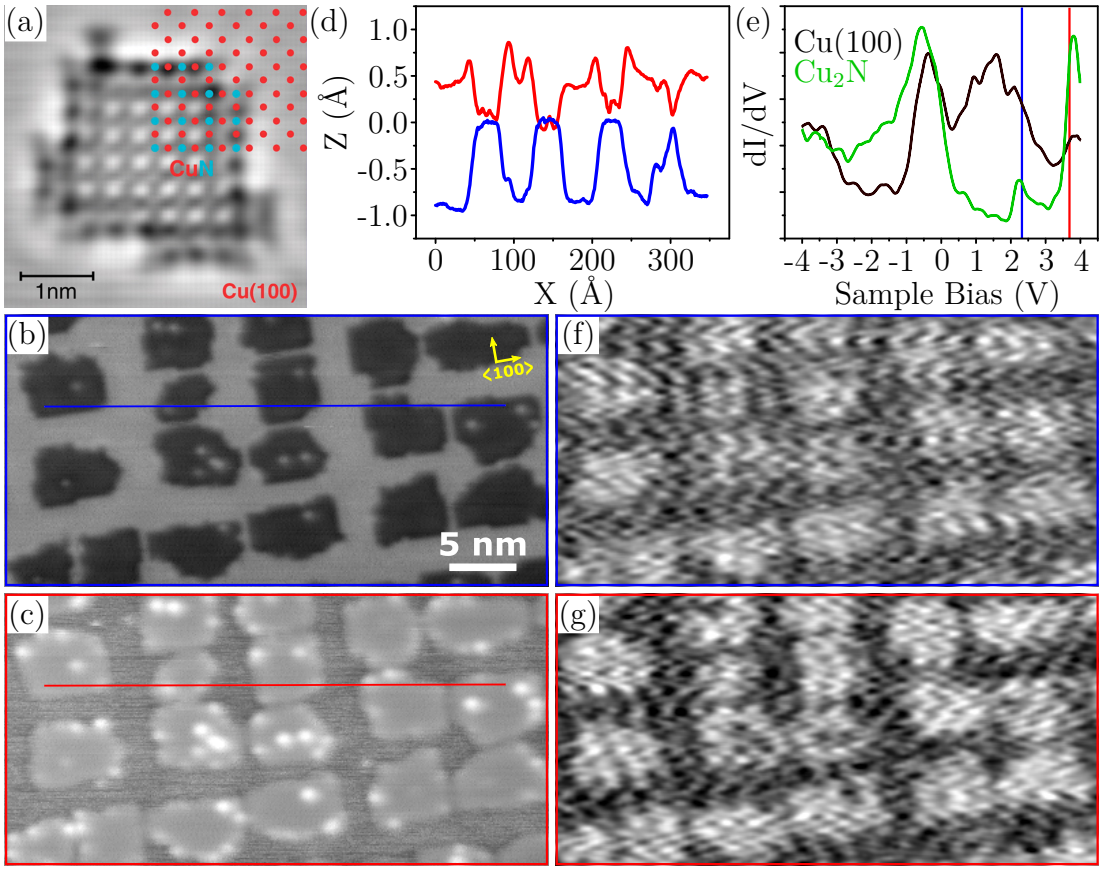

Figure 5.2: The structure of a c(2 × 2)-N island is illustrated in (a), which has been reproduced from Hirjibehedin *et al.*[387] The topographs in (b) and (c), and the corresponding line profiles in (d), show the self-organised array of these rectangular islands, and that the STM contrast is primarily electronic in origin, and inverts above ∼3 V. This contrast dependence can be explained by looking at the variable-height spectra in (e), where the Cu_2N LDOS is suppressed, with electronic states appearing at ∼2.3 V and ∼3.9 V These states are mapped out in the dI/dV maps in (f) and (g) corresponding to the topography in (b) and (c), respectively, and it can be seen that they are localised on the Cu_2N islands. Imaging conditions: (b), (f) 2.3 V, 20 pA ; (c), (g) 3.7 V, 20 pA.

figure 5.2(a), where the Cu_2N islands appear as ∼0.8 Å depressions in the topography at a sample bias of 2.3 V.

Despite this apparent height difference, the N atoms are very close to coplanar with the Cu(100) surface.[415] As for many other systems, the observed contrast reflects spatial variations in the LDOS, rather than the geometric corrugation.[426] Indeed, this can be seen in Fig. 5.2(c), which shows the same area as Fig. 5.2(b), but measured with the sample held at 3.7 V such that the contrast is inverted. Line profiles across the blue and red lines in Fig. 5.2(b) and (c), respectively, are shown in Fig. 5.2(d) where the relative apparent heights can be compared.

The variable-height spectra displayed in Fig. 5.2(e) for Cu(100) and Cu_2N

show the origin of this contrast inversion. On the Cu(100) areas we observe a broad peak centred on 1.8 V, attributed to an unoccupied surface state,[427] which is suppressed on Cu_2N. The Cu_2N islands have electronic states at 2.2 V and 3.9 V, the origin of which is still unclear.[428] The dI/dV maps corresponding to these peaks [Fig. 5.2(f) and (g)] show that they are localised to the Cu_2N islands. The feature close to the Fermi level on the filled states side is due to an asymmetry in the tip LDOS, and the close approach of the tip during the measurement upon which the Cu_2N layer is known to become leaky.[428] From Fig. 5.2(e) the dI/dV intensities for the Cu(100) and Cu_2N can be seen to cross at approximately 3.5 V, which is indeed close to where the topographic contrast inversion occurs. The Cu_2N layer suppresses the DOS over a range of at least 4 eV,[428] allowing it to efficiently decouple atomic and molecular states from the underlying Cu(100).[388,429] Additionally, the workfunction is increased by 0.9 eV upon chemisorption of nitrogen, which is attributed to the charge transfer from the surface to the N atoms in the formation of the polar Cu−N bonds.[430]

In Fig. 5.2(b) and (c), bright spots can be seen on the Cu_2N islands. These protrusions have been attributed to nitrogen vacancies.[431] The occurrence of these defects in the Cu_2N surface may be beneficial, since although molecules are more strongly coupled to the substrate at defect sites,[374] defects in TILs act as anchors for molecules.[432] This is important since the sticking coefficient is generally significantly smaller on the TIL than on a metal, such that diffusing molecules will tend to be found on the metal,[431] and, as mentioned in chapter 3, we are limited to room temperature deposition.

An alternative way to ensure that some of the target molecules can be found adsorbed on the spacer film is simply to minimise the area of bare metal exposed. The c(2 × 2)N overlayer is incommensurate with the Cu(100) surface and, as a result, full coverage cannot be achieved. However the high coverage surface may suffice. As mentioned above, the strain arising from the incommensurability manifests in different ways for the high and low coverage regimes. In the high coverage regime, c(2 × 2) terraces are separated by narrow trenches which may contain some remnant Cu(100), depending on the terrace size, as can be seen from the STM topograph shown in figure 5.3(a).[424] The line profiles in Fig. 5.3(b) and (c) show that these trenches are one atomic layer deep (1.8 Å), ∼16 Å wide, and run for tens of nanometers in the ⟨110⟩ directions. The trenches relieve strain by allowing the Cu_2N islands to expand outward.[425] The remnant Cu(100) forms cross structures which resemble the island structure at low coverage and show the same apparent height difference, indicating they are coplanar with the Cu_2N

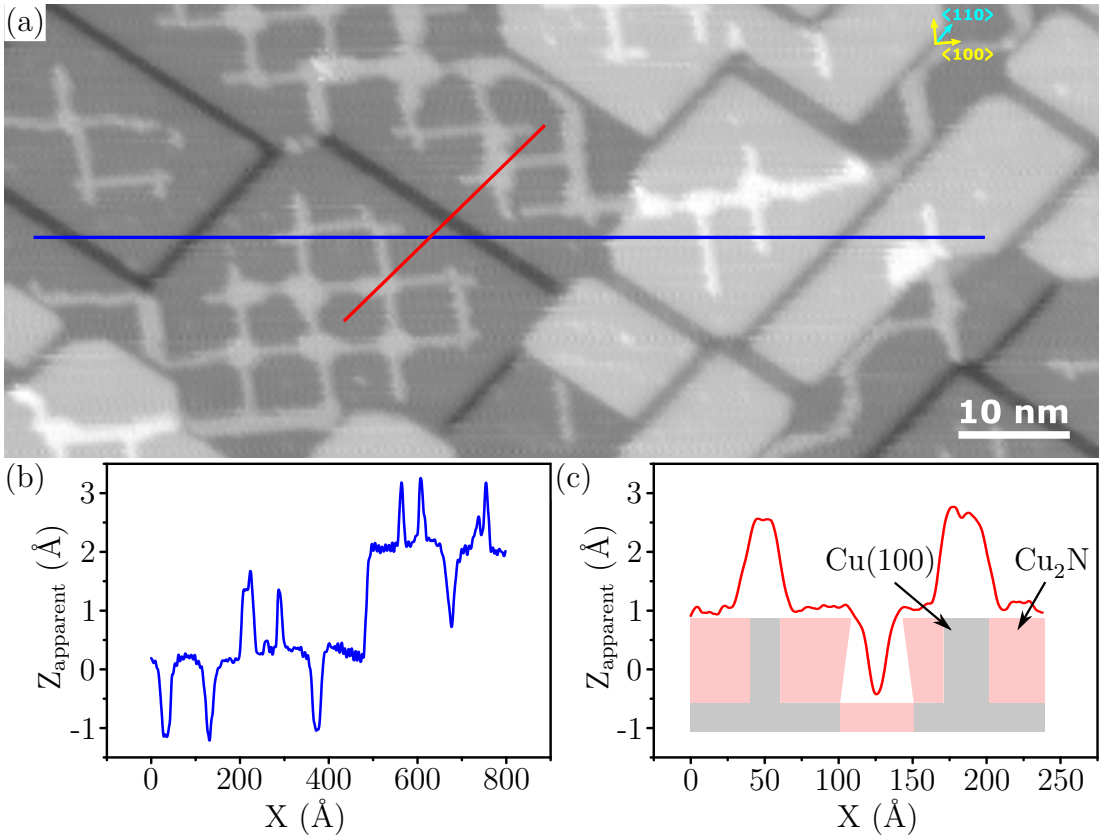

Figure 5.3: A STM topograph of the high coverage Cu_2N−Cu(100) surface is shown in (a), showing Cu_2N terraces separated by strain-relieving trenches and Cu(100) crosses. Imaging conditions: 1.5 V, 35 pA. The apparent height profiles in (b) and (c) show that the steps correspond to the Cu(100) steps, with height 1.8 Å, and that the trenches are also one atomic layer deep and ∼16 Å wide. The schematic in (c) shows Cu(100) in grey and Cu_2N in light red, with the outward relaxation exaggerated for illustration purposes.

terrace. The width of the crosses and trenches depends on the phase of the adjacent islands.[433]

5.1.3 Cu_3N−Cu(110)

Activated N^+ ion bombardment of the Cu(110) surface also results in a surface nitride,[414] which exhibits a band gap exceeding 3 eV.[434] This nitride has a p(2×3) structure, with a periodicity of 10.8 Å in the [100] direction and 5.1 Å in the [1$\bar{1}$0] direction,[414] corresponding to a coverage of 0.65 ML.[434] An STM topograph of Cu_3N−Cu(110) is shown in figure 5.4(a). This surface structure is described by a pseudo-(100) surface reconstruction, where two close-packed [1$\bar{1}$0] Cu rows form chains with N atoms adsorbed in the fourfold hollows between them.[434] It is these N_t atoms which are imaged prominently in figure 5.4(a). Between these chains

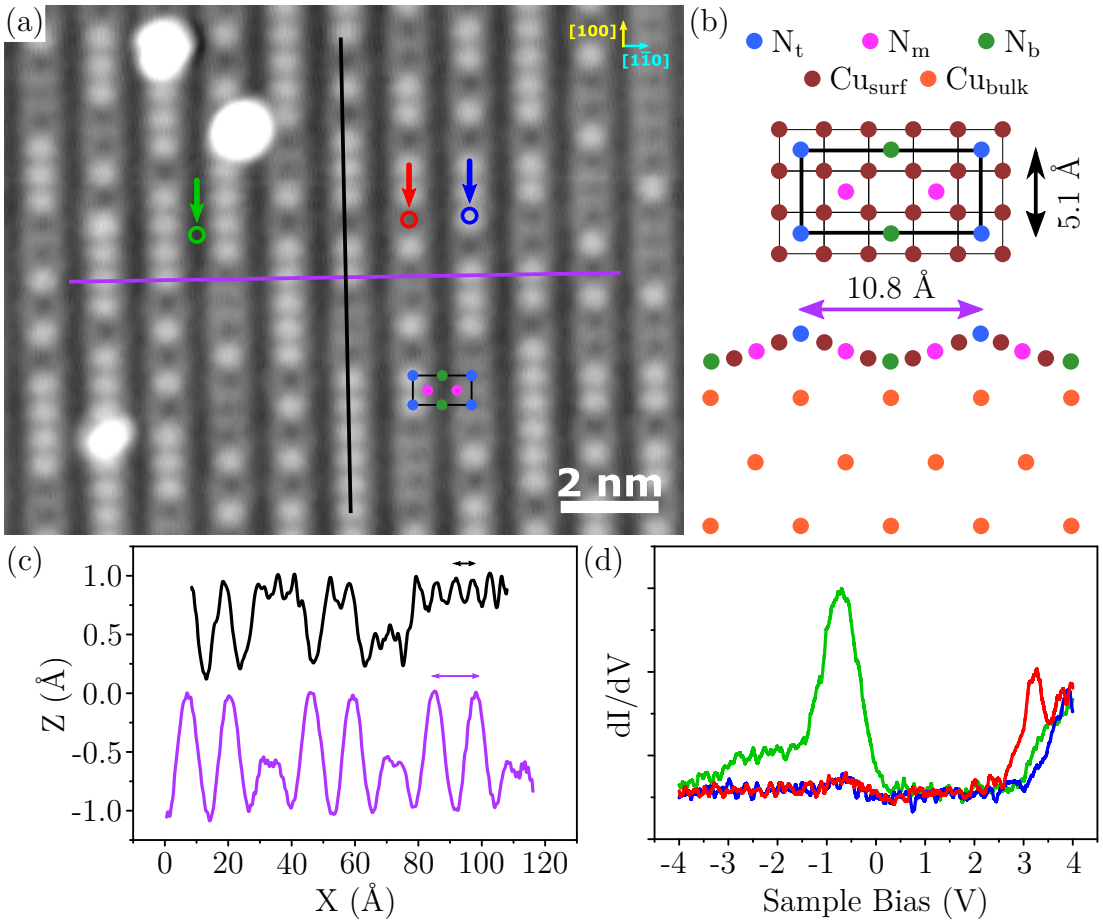

Figure 5.4: The topography of the Cu_3N−Cu(110) is shown in (a), where the protrusions correspond to nitrogen atoms in the top sites and are indicated in blue in the unit cell shown in (b). Imaging conditions: −0.75 V, 20 pA. The line profiles in (c) show a periodicity of 11 Å in the [100] direction and 5 Å in the [1$\bar{1}$0] direction, in good agreement with the literature. The different surface sites have different spectroscopic signatures as shown in (d) for the locations indicated by the green, red and blue arrows in (a).

is a missing row, which forms the depression in the topography. N atoms are adsorbed in two other fourfold hollow sites, labelled N_m and N_b in Fig. 5.4(b). The N_m atoms can be seen between the N_t atoms along a chain, and are more clearly resolved when the N_t atom is missing. The N_b atoms are located at the bottom of the missing rows and are not resolved here. The line profiles in figure 5.4(c) show a 11 Å × 5 Å unit cell and a corrugation amplitude of ∼0.5 Å which is in good agreement with the expected values.[434]

It can clearly be seen in figure 5.4(a) that some of the N_t atoms are missing so that the [1$\bar{1}$0] chains are imaged. The nitrogen atoms preferentially desorb from these "top" sites indicating that this surface was over-annealed after ion bombardment. The binding energy is higher at the nitrogen vacancy sites than

at other surface sites.[435] Another type of defect that arises is in imperfections in the spacing between the chain structures, where they are occasionally found beside each other instead of being separated by a missing row. These 1D defects shift all adjacent rows by the same amount.[414]

The different sites on the Cu_3N−Cu(110) surface show different spectroscopic signatures. We observe a peak at −0.5 V which is due to the asymmetry of the sample density of states around the Fermi level,[436] combined with the approach of the tip during variable-height STS. This peak is stronger over the N_b site than over the occupied and vacancy N_t sites due to the surface corrugation and the finite size of the tip apex, which allow for closer effective tip-sample distances.[437] Over N_t and N_b the state with an onset energy of approximately 3 V has been attributed to the N 2p states, and is broader over the N_b sites due to contributions from more N states.[436] We find an additional state beginning at ∼2.5 V on the N vacancy sites. Other groups have reported a state at 2.0 V which we do not see here. Bhattacharjee *et al.*[436] have postulated that this state is an interface state arising from the Cu(110) surface state at ∼2.0 V. If this is correct, the high density of nitrogen vacancies could strongly scatter the interface state, rendering it undetectable, however more data is needed to confirm this.

5.2 Compatibility of ESD with TILs

The standard method of depositing molecules onto TILs is to use OMBE, with the substrate held at low temperatures.[438] Here, as established in chapter 3, we are limited to ESD at room temperature. Other groups have successfully deposited molecules on TILs at room temperature, however they generally worked with high coverages, saturating any exposed metal to drive adsorption on the TIL.[439,440] Since ESD does not provide the precise coverage control that is possible with OMBE, we first wanted to confirm that it was possible to image molecules on TILs under the moderate coverage conditions expected with ESD.

In chapter 4 we established that the molecule-substrate interaction occurs primarily between the TPP core and the surface. We therefore deposit ZnTFcBP onto NaCl/Au(111) *via* OMBE in the same way as was done in section 3.1. Although we know the molecule fragments at the linker between the amide and the Fc groups, if we can observe ZnTFcBP fragments on the NaCl bilayers, we expect to be able to image intact ZnTFcBP also. The result of such a deposition is shown in figure 5.5(a), where the ZnTFcBP fragments cover the metal surface, leaving large areas of bare NaCl exposed, as expected. However, it can be seen

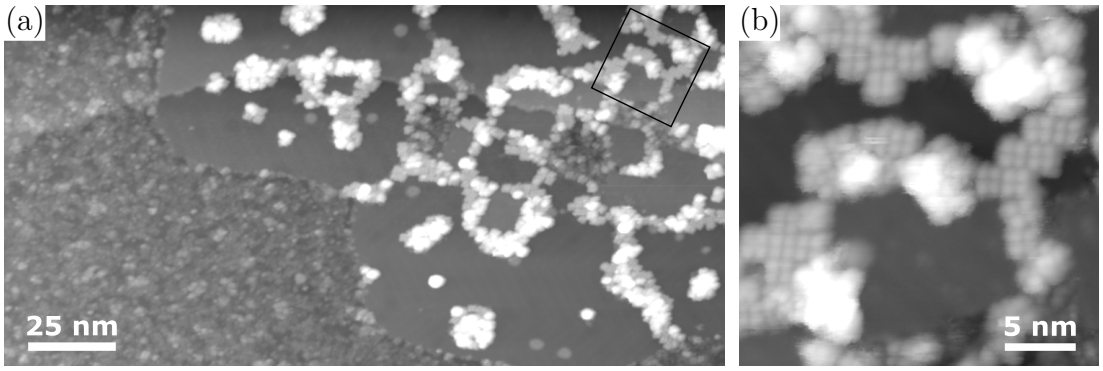

Figure 5.5: Fragmentative OMBE of ZnTFcBP onto Au(111) partially covered with bilayer NaCl(100). The molecules preferentially adsorb on the bare metal, as can be seen from (a), but can also be found at defect sites and third-layer island edges on the NaCl, where they appear as the four-lobed features seen clearly in (b). Imaging conditions: −2.5 V, 10 pA.

that there are many adsorbates on the NaCl bilayer, anchored at the edges of third-layer islands and other defects.

Looking at the higher resolution image in Fig. 5.5(b) it can be seen that the ZnTFcBP fragments appear as four-lobed squares. Third layer step edges are known to be preferential adsorption sites,[441] possibly stabilised here by electrostatic interactions between the amide groups and the ions in the NaCl(100) edges. The molecules at these step edges also act as nucleation sites for self-organised islands to grow on the NaCl. It is clear from the relative coverages on the metal and NaCl that quite high total coverages must be deposited. To achieve the necessary coverages we have exploited the non-uniform deposition profiles of the electrospray and the NaCl source. We deposited overlapping areas of both as shown schematically in figure 5.6(a), where the green circle represents NaCl coverage and the pink circle represents the area exposed to the electrospray.

STM topographs corresponding to the areas indicated in Fig. 5.6(a) are shown in figure 5.6(b)-(i). Figure 5.6(b) was measured far from the area exposed directly to the ESD beam, and the familiar NaCl(100) bilayer is observed, with small third layer islands, and some of the rod-like impurity species discussed in section 3.4. Moving towards the center of the area exposed to the NaCl source, we see almost a complete bilayer of NaCl(100) with third- and fourth-layer islands on top, as is shown in figure 5.6(c). In Fig. 5.6(d) and (e), the NaCl morphology is changed, favouring smaller and/or pitted islands with comparable bilayer and trilayer coverage, along with many unstable features. The regions in which these were measured correspond to those in which the edge of the electrospray beam overlaps with the NaCl coverage. Where the NaCl coverage begins to fall off in

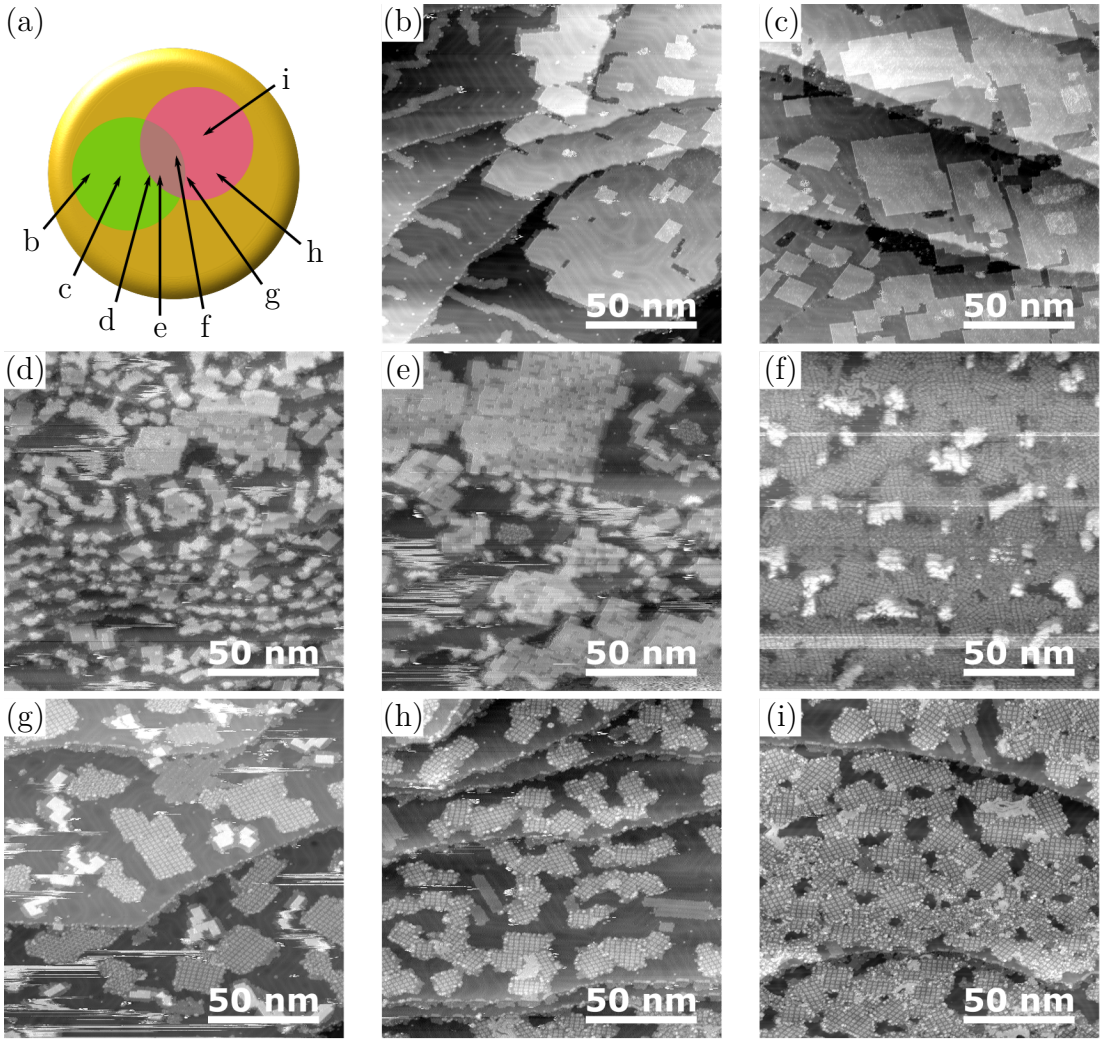

Figure 5.6: ESD of ZnTFcBP onto NaCl was attempted by exposing a partially NaCl-covered Au(111) surface to the electrospray. The areas exposed to the NaCl (green) and electrospray (pink) sources are shown schematically in (a), where the approximate locations of topographs (b)-(i) are also indicated. On one side we have clean NaCl(100) bilayers and on the other we have large ZnTFcBP coverages, however the morphology of the NaCl is clearly modified where the exposures overlap. Additionally, there were large areas of the surface where no stable imaging conditions could be found.

areas exposed to electrospray, we see quite large ZnTFcBP coverages surrounding irregular NaCl islands which seem to favour a triangular shape and an apparent height between 5 Å and 8 Å. In Fig. 5.6(g), we have small NaCl islands and some of the square ZnTFcBP domains, and moving to figure 5.6(h) and (i) we see no NaCl islands but high ZnTFcBP coverage. In the region of the sample between the areas shown in Fig. 5.6(e) and (f) we could find no imaging conditions at which the system was stable.

It is clear that the NaCl(100) layers are modified by exposure to the elec-

trospray. The triangular shape of the crystallites, seen most clearly in Fig. 5.6(f), is indicative of NaCl(111). In fact, Hebenstreit *et al.*[442] have reported that NaCl(100) can be converted to non-stoichiometric NaCl(111) on Al(100) by depositing excess Na. They report that these NaCl(111) islands are unstable under the STM tip, and that even more complicated structures develop in the presence of additional adsorbates.

While the mechanism driving the changes in the NaCl layer is unclear, it could be that the electrospray removes some of the Cl^- ions, effectively creating an excess of Na. Alternatively, the modification of the NaCl film could be driven by charge injection during ESD. It is well-known that NaCl layers can be modified using charge injection from the tip.[443] Bulk alkali halides form rectangular pits similar to those in Fig. 5.6(e) upon exposure to electron beams.[444] Momentum transfer from ion bombardment or exposure to plasma can also modify alkali halide surfaces.[445,446] During electrospray the surface is exposed to adsorbates and bombarded with ions whose momentum and/or charge may be transferred, which means that several factors could play a role. It should be noted here that Hinaut *et al.*[447] have successfully imaged organic molecules electrosprayed on a bulk KBr(100) crystal using atomic force microscopy (AFM), where they observed some pitting, but no large-scale surface modification.[447] Due to the low-stability of the NaCl(111) crystallites during STM imaging, further study of this system was not undertaken.

We have established that NaCl is incompatible with ESD, at least under the conditions in our experiment, and we expect other adsorbed ionic crystals to be similarly affected. TILs which are covalently bound to the surface should be more resistant to modification. We then turn to the copper nitride surfaces introduced in section 5.1. As we already described, the Cu(100) c(2 × 2)-N structure is incommensurate, preventing formation of a complete monolayer, such that bare Cu(100) is always exposed. This is problematic since the Cu(100) surface is quite reactive and, unlike Cu(111) or Au(111), tends to react with the solvents in which the molecule is dissolved,[448] and may crack the molecule itself.

To illustrate this, we have exploited the sputtering intensity profile to prepare a Cu(100) surface with a N coverage gradient such that at one side of the sample we have bare Cu(100), in the middle we have the low coverage Cu_2N structure, and on the other side we have the high-coverage structure. We have then exposed this sample to a 2:1 mixture of methanol and THF, which are the solvents used for deposition of QCA candidates. Topographs of the resulting surface are shown in figure 5.7, where it can be seen that the formerly flat Cu(100) is now rough

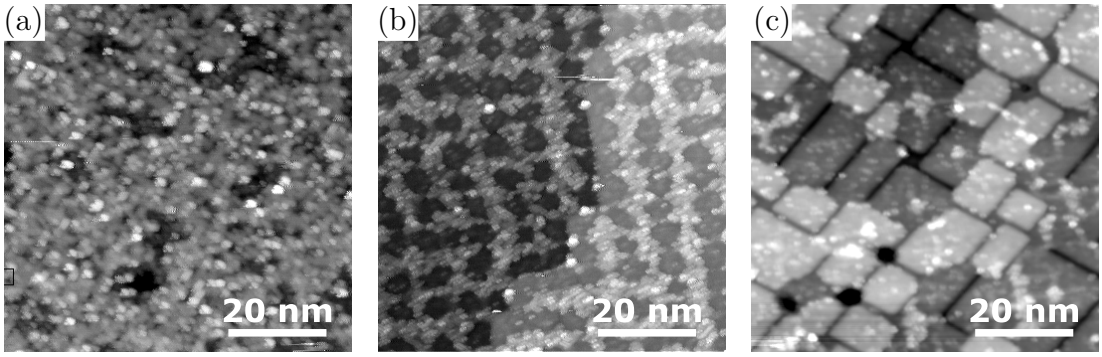

Figure 5.7: TILs can protect surfaces from reaction with solvent molecules during electrospray. Bare Cu(100) reacts with electrosprayed solvent as shown in (a). The topograph in (b) shows that Cu_2N islands remain clean after exposure to solvent. However, only the high-coverage $Cu_2N{-}Cu(100)$ surface is deemed ESD-compatible, since only the Cu cross structures are contaminated as shown in (c).

and inhomogeneous. While all of the exposed metal in figure 5.7(b) has reacted, the Cu_2N islands are clean and intact. The high coverage Cu_2N surface is only affected at the Cu crosses, and is therefore a suitable ESD substrate.

5.3 Compatibility Issues Between Molecules and TILs

ESD of ZnTFcBP onto $Cu_2N{-}Cu(100)$ results in a surface such as that shown in figure 5.8(a). At first glance this surface looks disordered, however upon closer inspection it can be seen that there are small areas of molecules organised in the square structure described in the previous chapter. These organised areas follow the trenches, extending no more than two unit cells either side. As previously noted, adsorbates on TILs are commonly found at defect sites and not in the center of terraces, which explains the preferential alignment along the trenches. Fig. 5.8(c) shows a high-resolution topograph of one of these organised islands, where it appears that the molecules are suspended on the edge of the trench and tilt down into it to form hydrogen bonds. However, the reduced LDOS at the center of the bridge may be contributing to the apparent height, obscuring the planarity of the molecules.

The Cu_2N layer facilitates much better resolution than was possible on the metal substrates, as shown in Fig. 5.8(c), where both the TPP core and the Fc groups are clearly resolved. This is reflected in the STS, plotted in Fig. 5.8(b), where both the ferrocene-centred HOMO and porphyrin-centred LUMO have a significantly narrower width on Cu_2N relative to Au(111). The HOMO-LUMO gap is also measured to be increased by 0.4 V on the nitride film. An increased

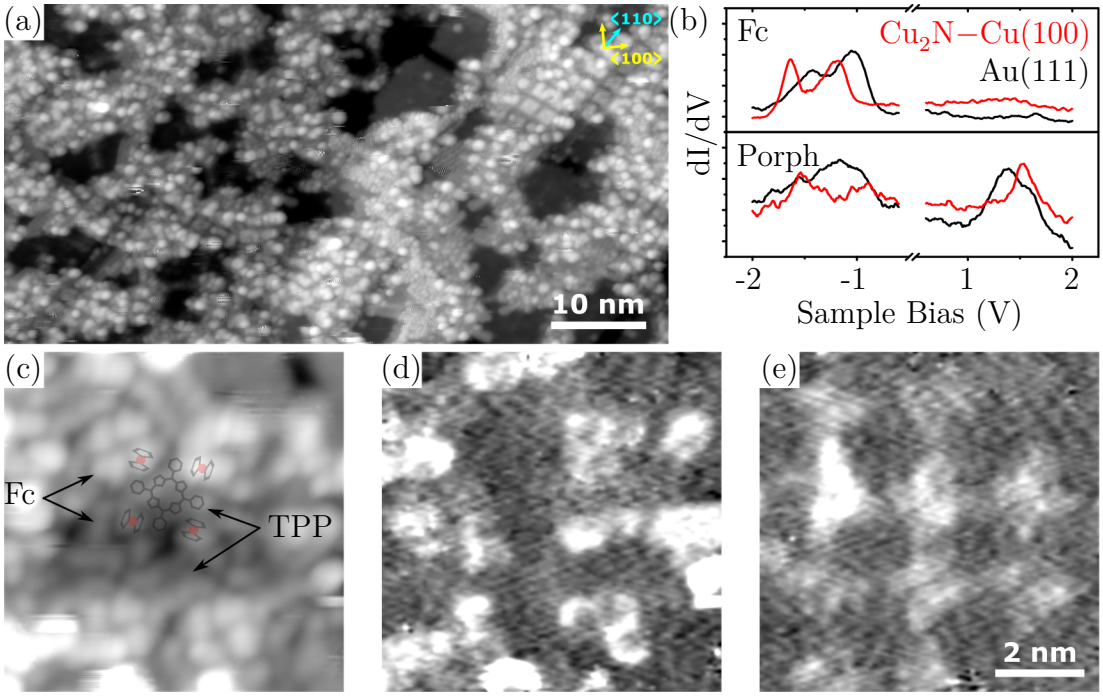

Figure 5.8: The small terrace sizes inhibit molecular self-assembly, which occurs preferentially at the Cu_2N trenches, as shown in (a). The reduced widths of the electronic states on Cu_2N relative to Au(111), compared in (b), indicates reduced coupling. This is corroborated by the higher resolution attainable, where the topograph in (c) shows that the TPP core and Fc groups can be clearly resolved. The HOMO shows site dependent intensity in the dI/dV map in (d), while that associated with the LUMO does not vary from molecule to molecule, as shown in (e). Imaging conditions: (a) −2.0 V, 10 pA ; (c) −1.5 V, 20 pA ; (d) −1.5 V, 20 pA ; (e) 1.5 V, 20 pA.

measured gap is expected when the molecule is adsorbed on a TIL due to reduced screening, as discussed in chapter 1. However, since there is no clean metal available on this surface it was not possible to ensure that the wider gap could not be attributed to a gap on the tip. Fig. 5.8(d) and (e) show that while the porphyrin-centred LUMO has approximately constant dI/dV intensity on each molecule, the Fc states vary from site to site, as was the case for the molecules adsorbed on Au(111).

We did not observe any vibronic replicas of the STS peaks nor any hysteresis in the spectra indicating were we able to inject charge into the system, which as outlined in section 2.2.2 are signatures of the weak coupling regime. This indicates that while the hybridisation of molecule and substrate states was reduced, it was not sufficiently small for our purposes. It is known that at defect sites the coupling is greater,[374] which indicates that we should probe molecules at the center of the Cu_2N terraces. Unfortunately, the terraces are small and the copper features act

as nucleation sites for impurities, disrupting the molecular ordering. We therefore move to the Cu_3N−Cu(110) surface which is commensurate and should allow for molecular ordering on a large scale.

Depositing ZnTFcBP on Cu_3N−Cu(110) results in an unexpected structure. Here, the molecules are aligned in the [001] direction with the TPP core perpendicular to the surface. An STM image of this surface is shown in figure 5.9(a), and a model of the adsorption configuration is shown in figure 5.9(b). Careful inspection of figure 5.9(a) reveals that the molecules are adsorbed in a specific site: along the $[1\bar{1}0]$ chains with the center of the molecular feature approximately in line with the "link" in the chain corresponding to the N_m positions. Here we assign the molecule as having two "legs" pointing down into the valleys of the corrugated Cu_3N surface such that the molecule straddles one of the chain structures. The molecules, when found together, are spaced at approximately 12.1 Å intervals and appear ∼10.7 Å wide, as can be seen from Fig. 5.9(c) and (d), respectively. The molecules are also found in two different orientations, labelled "R" and "L" in figure 5.9(a), and appear to favour opposite orientations when packing in adjacent rows.

Porphyrins adsorb with the molecular plane perpendicular to the surface when π-π stacking is the dominant intermolecular interaction and has an energy which is greater than molecule-surface interaction energy in the flat geometry.[303] For this molecule, however, hydrogen bonding dominates the intermolecular interactions, which is stronger than π-π stacking interactions. Additionally, the fact that we see isolated ZnTFcBP molecules in the edge orientation rules out π-π stacking as the driving force for this adsorption geometry. The apparent preference for a clearly defined adsorption site indicates some specific interaction between the molecule and the substrate. We note here that the surface shown does not correspond to a complete Cu_3N layer, but is nitrogen deficient since almost all of the N_t sites are unoccupied. These vacancies are reported to be preferential adsorption sites,[435] however it is difficult to see here how the upright molecular configuration would maximise the interaction with these sites.

The vacancy sites may however be related to the driving force for this molecular configuration. Carboxylic acids are known to deprotonate on Cu(110), leaving a carboxylate anion which interacts strongly with the surface atoms.[449,450] This has been reproduced recently for a ferrocene derivative, with a COOH group bound to each Cp ring, on Cu_3N−Cu(110).[435] Additionally the H−N−C=O groups of guanine, cytosine, thymine and adenine are deprotonated on contact with Cu(110), allowing the resulting lone pair on the N atom, as well as that of

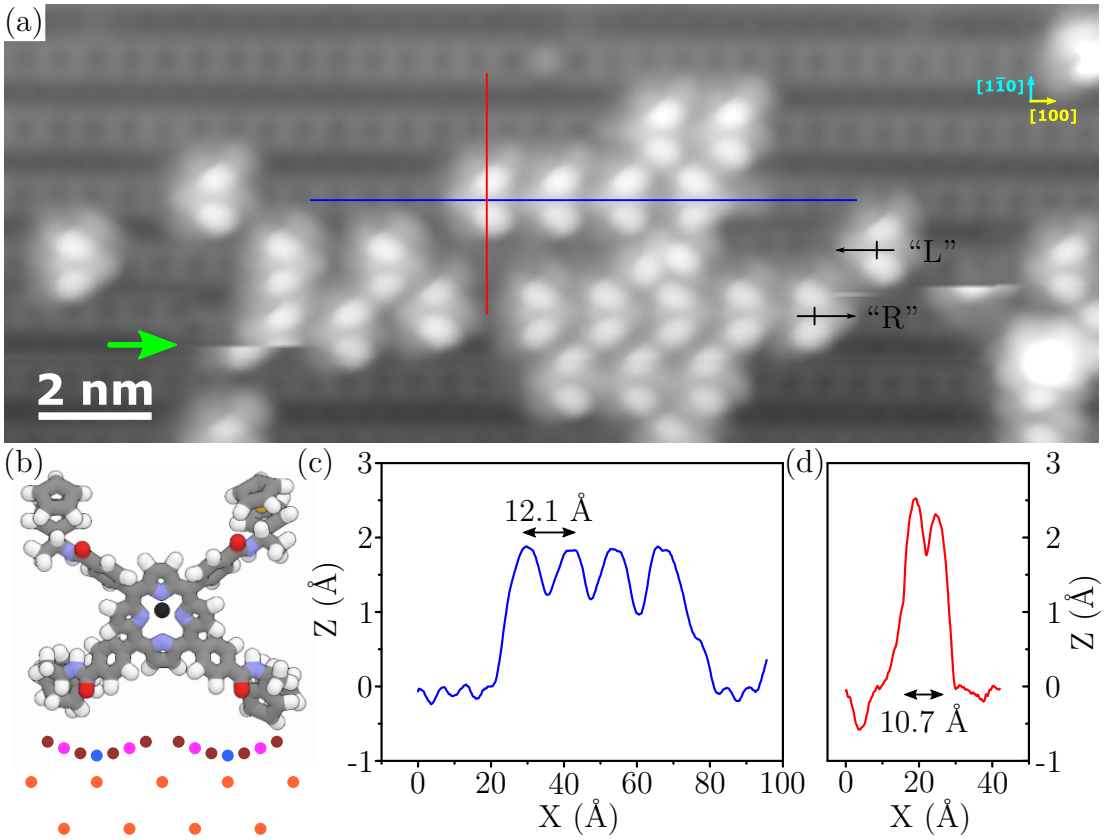

Figure 5.9: A STM scan of ZnTFcBP adsorbed on nitrogen-deficient Cu_3N−Cu(110) is shown in (a), where the molecule appear as two-lobed features straddling a N_t vacancy. Imaging conditions: (a) −1.5 V, 10 pA. The green arrow indicates where one of the molecules has flipped from the "R" to the "L" orientation under the influence of the STM tip. A tentative assignment of the adsorption configuration is presented in b), where the molecule interacts with the surface in the missing-row depressions through its amide group. When the molecules pack together they are spaced by ∼12.1 Å as indicated in (d), and adjacent rows have opposite directions. The line profile across the molecule in (d) gives a feature size of approximately 10.7 Å.

the C=O group, to interact with the surface Cu atoms.[451] For these DNA bases, the reaction proceeds *via* an enolic intermediate, and it is possible that in our case a tautomerisation of the amide into an imidic acid facilitates the deprotonation reaction.

Berger *et al.*[435] noted that their Cu_3N surface was missing the N_t atoms, and postulated that these nitrogen atoms may react with the cleaved H atom and desorb as NH_3. It has been reported that surface oxygen facilitates the deprotonation of aniline on Cu(110) by reacting to form water molecules which subsequently desorb,[452] which lends credence to this hypothesis. It is, on the other hand, possible that the N_t vacancies were generated by over-annealing the surface

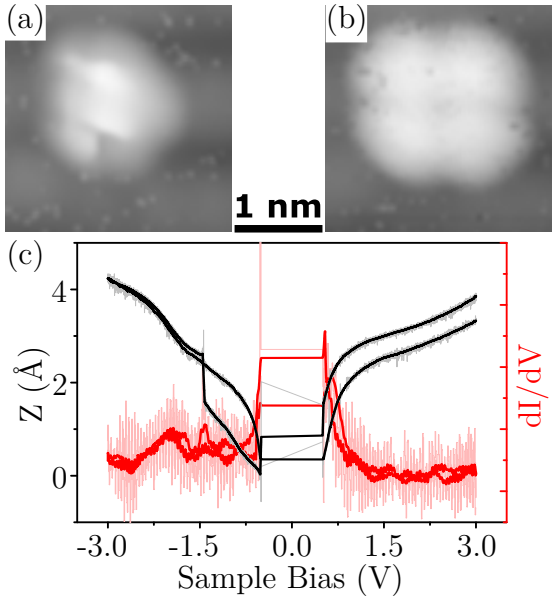

Figure 5.10: We observed a ZnTFcBP molecule switching from an upright conformation (a) to a flat conformation (b) on Cu_3N−Cu(110) during measurement of the $Z(V_b)$ spectrum shown in (c). We were not successful in attempts to repeat this, indicating that the molecule is strongly bound to the surface.

as in Fig. 5.4, and were therefore already present on the surface before deposition. Alternatively, some other species could have reacted with the N_t atoms during electrospray. While more data is needed to establish if the missing atoms are generated by the deprotonation reaction, or indeed if the N_t vacancies allow the deprotonation to take place, the high stability of the upright conformation supports the deprotonation hypothesis.

During $Z(V_b)$ spectroscopy we observed a molecule switching from a two-lobed structure to a four-lobed one, corresponding to a conformational change from upright to flat. The molecule is shown before (a) and after (b) the spectrum shown in figure 5.10(c), where the switch occurs at approximately $-1.5\,\mathrm{V}$. However, this switching behaviour could not be reproduced, even when subjected to more aggressive manipulation attempts. This indicates that the molecule is strongly bound to the surface, since if the molecules were bound to the surface by a dipolar interaction, between the surface Cu atoms and the oxygen lone pairs for example, it should be possible to manipulate them with the STM tip. Additionally, during scanning we observed that molecules occasionally appeared to rotate. This can be seen from the feature indicated by the arrow in figure 5.9, which we attribute to an inversion of the molecule which keeps the covalently-bound anchor points fixed.

In the flat configuration shown in Fig. 5.10(b), the molecule appears as a four-

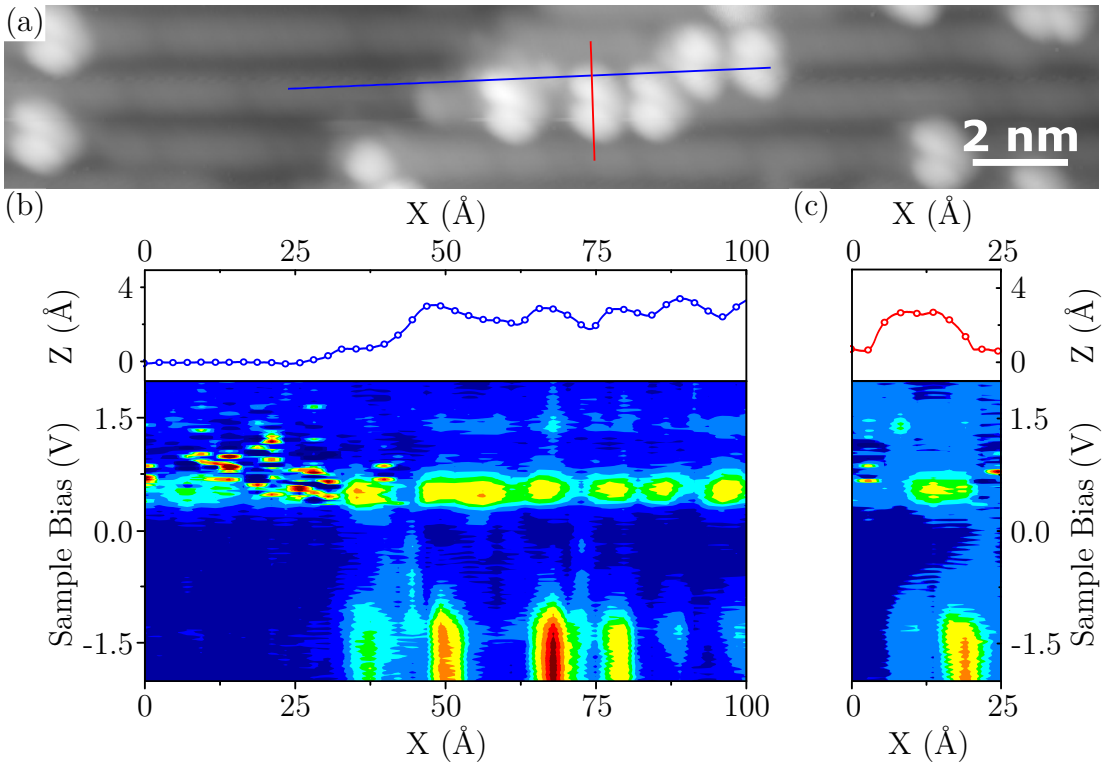

Figure 5.11: Contour maps illustrating the evolution of variable-height spectra across the blue and red lines in (a) are shown in (b) and (c), respectively. It can be seen that there is a tip state at ∼0.5 V, and a state below −1 V corresponding to the Fc-based peaks observed already for ZnTFcBP.

lobed structure measuring (13.5 ± 0.1) Å on each side. We note that it appears almost identical to the ZnTFcBP fragment on NaCl(100)/Au(111) shown in figure 5.5. This raises the possibility that the molecule has been cracked by the surface. It is plausible that the N−C bond linking the ethyl ferrocene group to the rest of the molecule is cleaved by the Cu_3N−Cu(110) surface *via* the same mechanism as the deprotonation process. We expect the ethyl ferrocene product of such a reaction to desorb at room temperature, leaving no indicative trace for STM.

On the other hand, the molecules show a spectroscopic signature which suggests that the molecules are intact. Variable-height spectra measured across the blue and red lines in Fig. 5.11(a) were compiled into contour maps, shown in Fig. 5.11(b) and (c), respectively. Here we see a tip state at ∼0.6 V, and a state at −1.5 V which is localised on the molecule. This corresponds to the location of the Fc-derived HOMO for ZnTFcBP, however, it is possible that it has some other origin. Computational modelling is needed to elucidate the interaction of ZnTFcBP with the Cu_3N−Cu(110) surface, however it is clear that the complex nature of this system makes it unsuitable for studying the excited states of organised ZnTFcBP arrays.

5.4 Conclusions

In this chapter we have introduced some TILs commonly used to decouple molecular adsorbates from metallic substrates, and outlined some of the challenges associated with depositing molecules onto these spacer layers *via* ESD. We have shown that NaCl(100) films on Au(111) are modified during ESD, possibly forming NaCl(111) crystallites. We expect that other ionic crystals would be similarly modified, and therefore suggest that only those films which are chemically bound to the underlying metal constitute ESD-compatible surfaces. The nitrides of the close-packed copper faces meet this criterion, however they present their own difficulties.

Cu(100) is reactive so that any exposed metal is contaminated by solvent molecules, and since the c(2 × 2)-N overlayer is incommensurate, exposed metal is unavoidable. Bare metal makes up only a small fraction of the high coverage Cu_2N−Cu(100) surface, which is therefore considered ESD compatible. However, the small terrace sizes on this surface are not conducive to self-assembly, especially for large molecules such as ZnTFcBP, and as a result organisation is observed almost exclusively at the trench edges.

Cu_3N−Cu(110) is commensurate, allowing full coverage to be achieved. The surface appears to be suitable for examining electrosprayed molecules, however it is possible that some species introduced *via* electrospray has led to the large quantities on nitrogen vacancies on the surface. Molecule-substrate interactions were found to dominate the adsorption properties of ZnTFcBP on this substrate, prohibiting the study of self-assembled arrays of these molecules. The observed upright adsorption configuration is believed to be due to a specific interaction between deprotonated amide groups on the molecule and the surface Cu atoms. It is possible that the molecule is cracked by the surface, perhaps by the same mechanism as the proposed deprotonation. From analysis of the topography alone, we have not been able to confirm whether or not the molecule is still intact, however, the STS signature is indicative of attached Fc groups. More data is needed to fully elucidate the interaction of ZnTFcBP with Cu_3N−Cu(110), however the complexity of this system renders it unfavourable for our purposes and a systematic study is not undertaken here.

Other TILs have been reported in the literature which we believe would be useful for STM investigation of self-assembled molecular networks deposited using ESD, notably h-BN/Cu(111)[453] and Al_2O_3−NiAl(100),[374] and these will be investigated in the future. In the next chapter we investigate whether Cl atoms

can effectively decouple molecular states from Cu(111) states, and present some new findings on the interactions between chlorine atoms on the Cu(111) surface.

6

Functionalised Porphyrins on Chlorinated Copper

As we saw from the previous chapter, none of the standard TILs investigated were compatible with electrosprayed ZnTFcBP/H_2TFcBP. In order to decouple the molecular assemblies from the underlying metal we need to identify an ESD-compatible TIL, which has defect-free terraces large enough to facilitate self-assembly. While several potentially useful alternative TILs exist in the literature, notably Al_2O_3−NiAl(100)[197] and h-BN/Cu(111),[453] these are complicated to prepare.

During the course of our research we found that we could prepare stable chlorinated copper surfaces by simply exposing a clean Cu(111) surface to chloroform introduced to vacuum *via* ESD. Since bulk Cu(I)Cl has a band-gap of 3.25 eV,[454] and since ultra-thin insulating films can exhibit a band gap approaching that of the bulk even when only a few atomic layers thick,[455] it is possible that Cl−Cu(111) would be an effective surface for decoupling molecules. Indeed, Xe monolayers have been found to effectively decouple molecular adsorbates.[378,395,396]

Beyond this, the Cl−Cu(111) system is interesting in its own right, as evidenced by the fact that it has been studied continuously for more than three decades.[456–460] In this chapter we describe the evolution of the Cl−Cu(111) surface with increasing Cl coverage, and provide new insight into the electronic properties of this surface (section 6.1), which we published in *Physical Review B*.[461] Then, in section 6.2, we describe the behaviour of our MQCA candidate molecules adsorbed on the Cl−Cu(111) surface.

6.1 Properties of the Chlorinated Cu(111) Surface

The structure of chlorine adsorbed on Cu(111) has already been studied extensively. The initial studies used LEED[456] but more recently these have been followed by photoelectron diffraction,[462] surface-extended X-ray absorption fine structure (SEXAFS),[463] and x-ray standing wave techniques.[457,464] The introduction of STM[465] has allowed investigation of local features, with atomic resolution, which are averaged out by other techniques. Most of the published research has been focused on the structure and desorption behaviour of the chlorine adlayer,[466] with the electronic properties of the Cl−Cu(111) surface being less well studied. Some first principles calculations have been performed, including a detailed paper by Peljhan and Kokalj, which describes the electronic properties of the surface at various Cl coverages.[467]

6.1.1 Chlorination of Cu(111)

Almost all existing studies focus on surfaces that are formed *via* dissociation of molecular chlorine in vacuum. Chlorine gas is extremely reactive, and exposure to even low pressures of Cl_2 can cause corrosion and damage of UHV equipment. For this reason, chlorine-emitting electrochemical cells are used instead of the leak valves used for less reactive gases.[468] These electrochemical cells are highly controllable and therefore facilitate the deposition of a finely controlled dosage.

Jones and Clifford reported that chloroform adsorbs dissociatively on Cu(111) at room temperature.[469] Initially the chloroform molecules physisorb, before the C−Cl bonds break sequentially, leaving three Cl atoms and a C−H radical adsorbed on the surface. The C−H radical diffuses on the surface until it meets another, and it reacts to form ethyne, which then desorbs.[469] While ESD of chloroform does not have the same degree of experimental control as the electrochemical cell in terms of the resulting Cl coverage, a saturated monolayer is all that is required for use as a spacer layer.

The reaction of chloroform with Cu(111) was previously reported to self-terminate at the $(\sqrt{3} \times \sqrt{3})$ R30° structure (1/3 ML).[469] However, we find that electrospray deposition of chloroform onto Cu(111) results in a Cl adlayer with coverage between 3/8 and 7/19 ML. We attribute the higher coverage obtained here to the action of the electrospray. During exposure of the sample to the well-collimated electrosprayed molecular beam, there is high pressure at the sample and the adsorbed Cl atoms may be temporarily displaced, allowing an excess of chloroform to react with the surface.

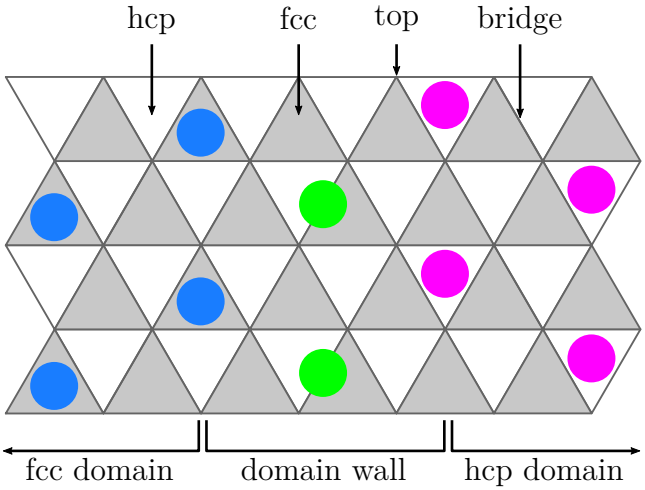

Figure 6.1: The different adsorption sites on an fcc(111) surface. The vertices of the triangular grid represent surface atoms, with the shaded triangles representing fcc sites and the empty triangles representing hcp sites. The blue, pink and green circles represent adatoms in fcc, hcp, and bridge sites, respectively. This colour scheme is used throughout this chapter.

6.1.2 Structure-coverage relationship

Figure 6.1 shows the various adsorption sites on a fcc(111) surface. In this figure and throughout the paper, adatoms in fcc, hcp, and bridge sites are coloured blue, pink, and green, respectively. As Cl atoms are added to the Cu(111) surface they form chains, where the adjacent atoms alternate between adsorption in fcc and hcp sites, or small $(\sqrt{3} \times \sqrt{3})$ R30° islands with the Cl atoms in fcc sites.[460] As the coverage increases, a porous structure is formed, with voids enclosed by the aforementioned Cl chains or $(\sqrt{3} \times \sqrt{3})$ R30° ribbons. The voids close as more Cl atoms are added to the surface, until the coverage reaches 1/3 ML, where a uniform $(\sqrt{3} \times \sqrt{3})$ R30° adlayer is formed.[456]

Above 1/3 ML, Cl atoms form crowdion interstitials where some of the Cl atoms surrounding the interstitial are displaced from fcc sites to hcp or bridge sites.[470] These crowdion interstitials condense into domain walls as the number density increases.[459] A section of a domain wall is shown in Fig. 6.1, where the Cl atoms transition from a $(\sqrt{3}\times\sqrt{3})$ R30° domain in which the Cl atoms occupy fcc sites, to one in which they occupy hcp sites, by passing through a line of atoms in bridge sites. The size of these domains shrinks with increasing Cl coverage until, at 0.4 ML, the fcc and hcp domains are each one atomic row wide.[470] Between 0.4 ML and 5/12 ML, the mesh is further compressed such that some of the Cl atomic rows are in sites intermediate between bridge and hollow. Above 5/12 ML, further uniaxial compression of the surface mesh is unfavourable because it

would result in Cl-Cl nearest-neighbour distances smaller than the Van der Waals diameter of chlorine.[471]

Figures 6.2(a) and 6.2(b) show the $(19 \times \sqrt{3})$ structure, corresponding to a coverage of 7/19 ML. Here domains, alternating between two and three atomic rows wide, are separated by rows of Cl atoms adsorbed in bridge sites. The atoms in bridge sites can be distinguished from those in hollow sites by analysing the topography. Since the inter-row distance is shorter between a row of Cl atoms in hollow sites and a row of Cl atoms in bridge sites than between two rows of atoms in hollow sites, the contrast between the atoms is reduced. Therefore, where there is greater contrast between two atomic rows, indicated by the cyan arrow in Fig. 6.2(a), atoms in these rows can be assigned to hollow sites. Where there is reduced contrast between an atomic row and the row on either side of it, indicated by yellow arrows, the atoms in this row can be assigned to bridge sites. Alternatively, the bridge sites can be identified by noticing that atomic rows in adjacent domains do not align exactly. The atomic row (along the uncompressed direction) where there is an offset between adjacent rows in both of the other two (compressed) directions, as indicated by the black lines in Fig. 6.2(b), can be identified as the bridge site.

Due to the symmetry of the structure, the fcc domains cannot be differentiated from the hcp domains by analysis of the topography alone. To identify the adsorption site, this adlayer was modified by locally applying a large current and desorbing some of the Cl atoms to form large domains [see left side of Fig. 6.2(c)]. Since it was previously established that Cl atoms occupy fcc sites in the $(\sqrt{3} \times \sqrt{3})$ R30° adlayer,[463] due to the slightly larger adsorption energy relative to the hcp sites,[472] the large domain is assumed to consist of Cl atoms occupying fcc sites.

The relationship between Cl coverage and structure in the uniaxial compression regime is described in Fig. 6.3. At 1/3 ML the chlorine atoms occupy the Cu(111) fcc sites in the isotropic $(\sqrt{3}\times\sqrt{3})$ R30° structure,[456,458] which is marked by the lower dashed line in Fig. 6.3(a) and shown schematically in Fig. 6.3(b). As the coverage increases crowdion interstitials appear on the surface, which then condense into domain walls resulting in a non-uniform uniaxial compression of the $(\sqrt{3} \times \sqrt{3})$ R30° structure.[470] The domains get progressively smaller as the coverage increases. The $(8 \times \sqrt{3})$ structure shown in Fig. 6.2(a) is indicated in Fig. 6.3(a), and shown schematically in Fig. 6.3(c). The $(19 \times \sqrt{3})$ structure, shown schematically in Fig. 6.3(d), was also observed after electrospraying chloroform on clean Cu(111). The $(5 \times \sqrt{3})$ structure, indicated in Fig. 6.3(a),

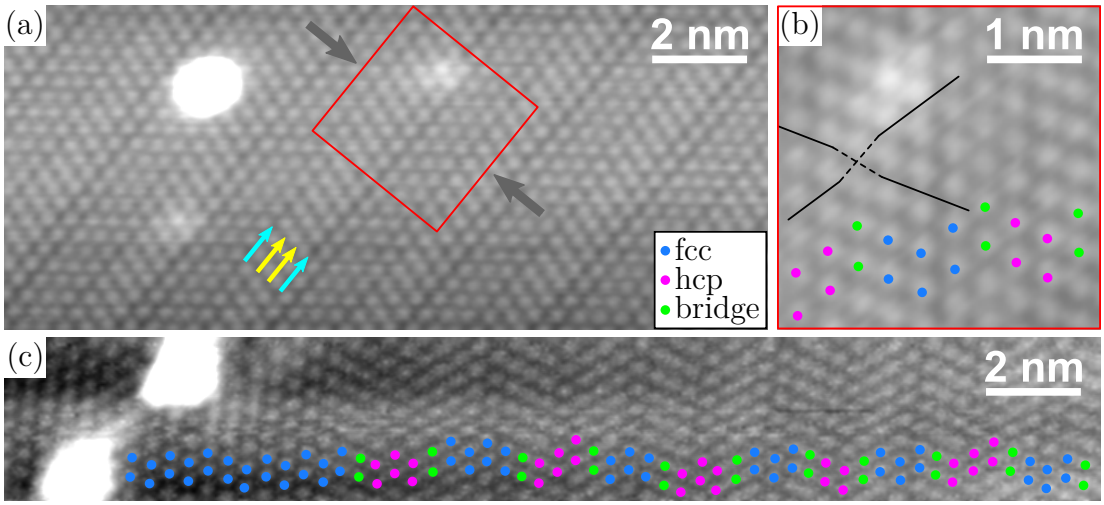

Figure 6.2: Topographic images of uniaxially compressed Cl adlayers on Cu(111). The compression direction is indicated with grey arrows. Part (a) shows atomic resolution of the Cl adlayer, imaged at 1.0 V, 50 pA. The striped pattern allows us to differentiate between Cl atoms adsorbed in hollow sites and those in bridge sites. Part (b) shows the enlarged area indicated by the red square in (a). Here, atoms in bridge sites can be distinguished by following the atomic rows along the compressed axes. The blue, pink, and green circles represent Cl atoms occupying fcc, hcp, and bridge sites, respectively. These were assigned by analysing the image in panel (c), where high current was applied to desorb some of the Cl atoms, forming a large $(\sqrt{3} \times \sqrt{3})$ R30° domain. Since in the uncompressed $(\sqrt{3} \times \sqrt{3})$ R30° structure, the Cl atoms all occupy fcc sites, we assign the Cl atoms in the largest domain to fcc sites.

corresponding to alternating fcc and hcp domains one atomic row in width, has been previously reported for Cl on Ag(111).[470]

Between 1/3 and 2/5 ML, where Cl atoms occupy fcc, hcp, and bridge sites only, the relationship between coverage in monolayers Θ, the number of chlorine atoms per unit cell N_A, and the length of the unit cell L are given by:

$$\Theta = \frac{N_A}{2L}, \tag{6.1}$$

where N_A is related to the number of atomic rows in the fcc domain R_{fcc} and the number of atomic rows in the hcp domain R_{hcp} according to the following equation:

$$N_A = (b+1)(R_{\mathrm{fcc}} + R_{\mathrm{hcp}} + 2), \tag{6.2}$$

and the unit-cell length is:

$$L = \frac{b+1}{2}(3R_{\mathrm{fcc}} + 3R_{\mathrm{hcp}} + 4), \tag{6.3}$$

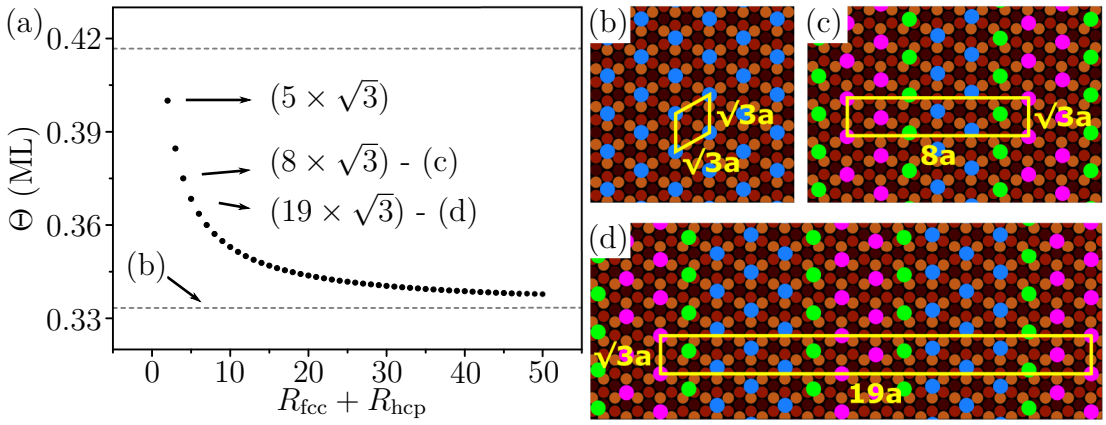

Figure 6.3: Coverage vs structure relationship in the uniaxial compression regime. R_{fcc} and R_{hcp} represent the number of atomic rows in the fcc and hcp domains, respectively. The orange, light brown, and dark brown circles represent the copper atoms in the first, second, and third layer from the surface, respectively. Blue, pink, and green circles represent Cl atoms occupying fcc, hcp, and bridge sites, respectively. Part (a) shows the coverage decaying exponentially to 1/3 ML (indicated by the lower dashed line), corresponding to the $(\sqrt{3} \times \sqrt{3})$ R30° structure [presented in (b)], as the domain widths increase. The upper dashed line in (a) corresponds to the maximum coverage structure in the uniaxial compression regime. Part (c) shows the $(8 \times \sqrt{3})$ structure where domains, two atomic rows wide, of Cl atoms occupying fcc sites are separated from hcp domains by a row of Cl atoms in bridge sites. Part (d) shows a model of the $(19 \times \sqrt{3})$ structure, shown in Fig. 6.2(a), where the fcc and hcp domains are both three and two atomic rows wide, respectively.

where $b = (R_{fcc} + R_{hcp}) \bmod 2$.

At coverages between 0.4 ML and 5/12 ML, single row fcc and hcp domains are separated by domain walls several rows wide, where the chlorine atoms occupy adsorption sites that are less symmetric than bridge sites. The most compressed structure possible under the uniaxial compression regime is the $(12 \times \sqrt{3})$ structure,[459,471] corresponding to a coverage of 5/12 ML [indicated by the upper dashed line in Fig. 6.3(a)].

6.1.3 Electronic properties of uniaxially compressed chlorine adlayers

The Cl−Cu(111)-$(\sqrt{3} \times \sqrt{3})$ R30° surface is shown in Fig. 6.4(a). The Cl atoms occupy the fcc sites, with a nearest neighbour distance of $d_{\text{Cl-Cl}} = \sqrt{3} a_{\text{Cu(111)}} = 4.4\,\text{Å}$. We have measured STS on this surface [figure 6.4(b)] and found a single peak, at 1.6 V, in the tunnelling window between ±3.5 V. Since the Cl p_x and p_y orbitals are doubly occupied, and therefore below the Fermi energy, we assign the observed STS peak to an interface state between the Cu d orbitals and the

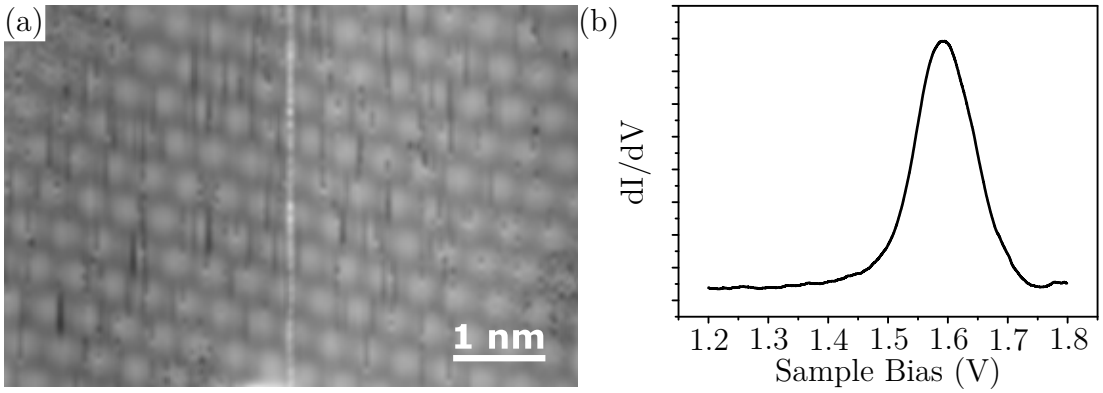

Figure 6.4: The topography (a) and STS (b) of the Cl−Cu(111)-($\sqrt{3} \times \sqrt{3}$) R30° surface.

Cl 3 p_z state. While there are no significant antibonding features in the PDOS spectrum calculated by Peljhan and Kokalj,[467] the calculated spectrum only extends 2 eV into the empty states. Considering that calculated energy scales often need adjusting to match experimental results, and that the antibonding Cu d - Cl 3 p_z interaction is expected to be strong, this state may simply lie outside the calculated range. Since the Cu s, d - Cl 3 p_z bonding interaction, the Cu s, d - Cl 3 $p_{x,y}$ bonding interaction, and the Cu d - Cl 3 $p_{x,y}$ antibonding interaction are accounted for in the calculated PDOS, we anticipate the antibonding interaction between the Cu d and Cl 3 p_z states to be the next state available in the wider energy range for tunnelling in these measurements.

STS data for the ($8 \times \sqrt{3}$) Cl overlayer are presented in Fig. 6.5. The differential conductance, measured between ±1.0 V and ±3.0 V using constant-current spectroscopy is plotted in Fig. 6.5(a). Variable-height spectroscopy was used to access the low bias range between ±1.0 V. These data were used to extract the combined tip-sample LDOS $\rho_{S,t}(V)$. Constant-current spectroscopy, variable-height spectroscopy, and the approach used to extract the LDOS from the resulting data, are described in chapter 2.

We make several observations from Fig. 6.5(a). The first is that for spectra measured over each domain type, as for the ($\sqrt{3} \times \sqrt{3}$) R30° system, we observe only a single peak in the tunnelling window between 3.5 V and −3.5 V. Here the center of the peak measured on the fcc domain is at ∼1.8 V, whereas this state appeared at approximately 1.6 V for the uniform adlayer in Fig. 6.4. We attribute this difference to the effect of the domain size; as we will see below, the energy of this electronic state shifts towards the Fermi level as the domain size increases. However, we first focus on the effect of the domain registry on the antibonding interaction, namely, that the state is further blue-shifted by approximately 200 mV

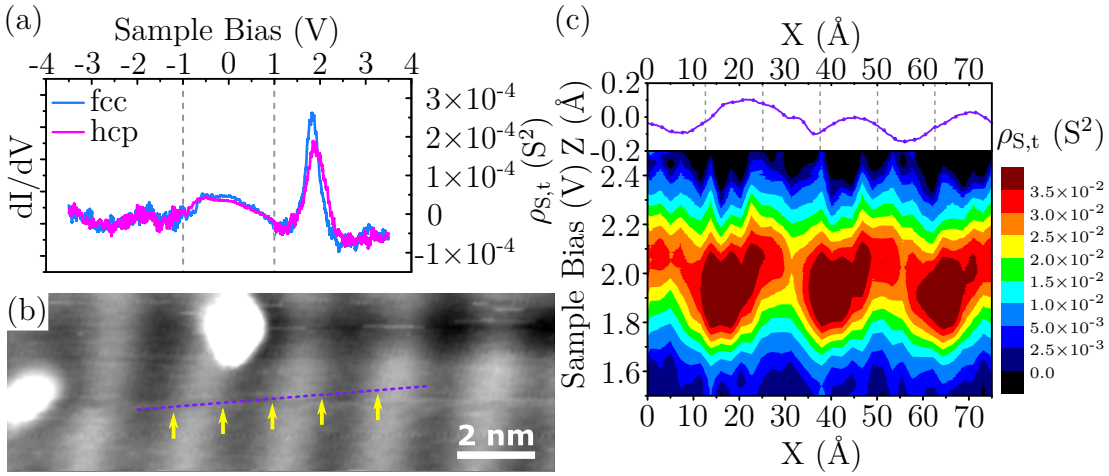

Figure 6.5: STS measured over the fcc (blue) and hcp (pink) domains on a $(8 \times \sqrt{3})$ Cl overlayer are shown in (a). From ±1.0 V to ±3.0 V the differential conductance was measured using $Z(V_b)$ spectroscopy, and Between −1.0 V and 1.0 V, the LDOS, extracted from variable-height spectra,[178] is shown. The peak at 1.8 V is attributed to the interaction of the Cl 3 p_z state with the Cu d states. This state is blue-shifted by approximately 200 mV on the hcp site relative to the fcc site. A STM topograph recorded at 2.0 V is shown in (b), where the fcc domains appear as ridges and the hcp domains appear as valleys. The energetic shift in the observed state between the fcc and hcp domains is shown more clearly in the LDOS contour map in (c). The maxima can be seen to follow the domain type. Approximate positions of the Cl bridging rows are indicated by the yellow arrows in (b) and dashed lines in (c).

when measured on a hcp domain compared to a fcc domain.

This dependence of the energy of the antibonding interaction on the domain registry gives rise to corrugation in topography. A topographic map of the $(8 \times \sqrt{3})$ structure [shown schematically in Fig. 6.3(c)] at 2.0 V is presented in Fig. 6.5(b). At this bias we lose atomic resolution and the fcc domains appear as ridges in the topography. Similar features have been observed in the topography of Cl adlayers on Ag(111), where the dark features they observe in the topography at 1.98 V were attributed to areas of increased chlorine density, *i.e.*, centred around the bridging rows.[470] If this were true, the topographic feature would be centred on, and have the same periodicity as, the bridging rows which are indicated by the yellow arrows in Fig. 6.5(b) [and the dashed lines in the topographic profile in Fig. 6.5(c)]. Since this is not the case, we are confident in assigning its origin to the shifting electronic state, and we attribute the bright features to fcc domains, and the dark features to hcp sites.

The shift of the observed state is shown in more detail in Fig. 6.5(c), where the combined tip-sample LDOS has been extracted, as above, from variable-height

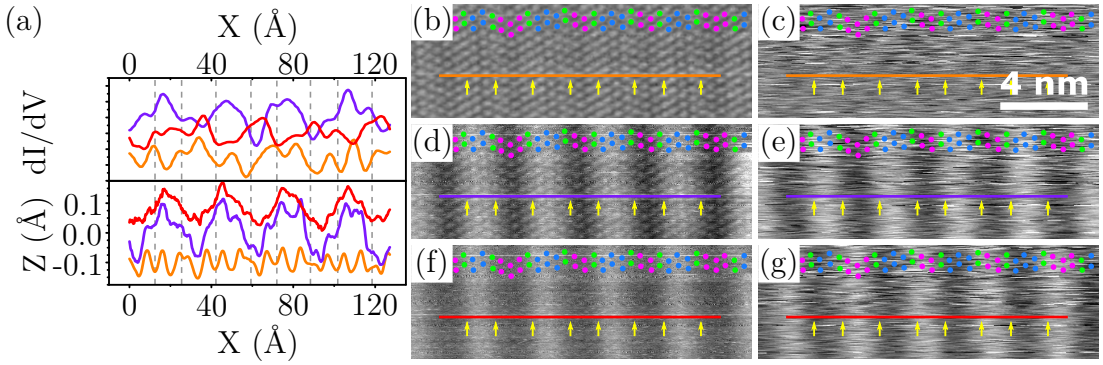

Figure 6.6: Multi-channel STM data for a $(19 \times \sqrt{3})$ Cl adlayer on Cu(111). (b), (d) and (f) show topographic maps of the surface at 1.5 V, 1.8 V and 2.1 V, respectively, while (c), (e) and (g) show corresponding differential conductance maps. Blue, pink and green circles indicate Cl atoms adsorbed in Cu(111) fcc, hcp and bridge sites, respectively. (a) shows topographic (bottom) and dI/dV profiles (top) along the orange (1.5 V), purple (1.8 V) and red (2.1 V) lines in (b)-(g). The dashed lines in (a) mark the positions of bridge rows [indicated by the yellow arrows in (b)-(g)].

spectra measured across several domains [purple dashed line in Fig. 6.5(b)]. There was a small lateral drift during the acquisition of the spectra, which appears as an offset in the angle of the line across which the spectra were measured, so that these data were not precisely recorded perpendicular to the long axis of the domains. The maxima in the LDOS contour map in Fig. 6.5(c) can be seen to shift smoothly from approximately 1.9 V on the fcc domains to approximately 2.1 V on the hcp domains. We note here that it is unclear why no distinct state is observed for the Cl atoms occupying bridge sites, despite the difference in Cl adsorption energy between hollow and bridge sites being only ∼80−90 meV.[460]

The shift of the STS peak with domain registry is shown more clearly in figure 6.6. Line profiles for the topographic [Fig. 6.6(b),(d),(f)] and dI/dV maps [Fig. 6.6(c),(e),(g)], recorded concurrently at 1.5 V, 1.8 V, and 2.1 V, respectively, are shown in figure 6.6(a). It is clear that the states at 1.8 V and 2.1 V are anti-phase to each other and arise from the domain registry. Additionally, we can confirm from Fig. 6.6 that the topographic feature that appears above ∼1.7 V is related to this STS peak, and is centred on the fcc domain, rather than on the domain walls.

To investigate the origin of the blue-shift of the Cu d -Cl 3 p_z antibonding interaction, two Gaussians were fitted to each spectrum. The widths of the Gaussians were set to be equal within each fit. The average width across all the spectra was obtained and the peaks were re-fit with the widths fixed at the average value of 0.4 V, and the centres free to vary. The average value of the two peak centres

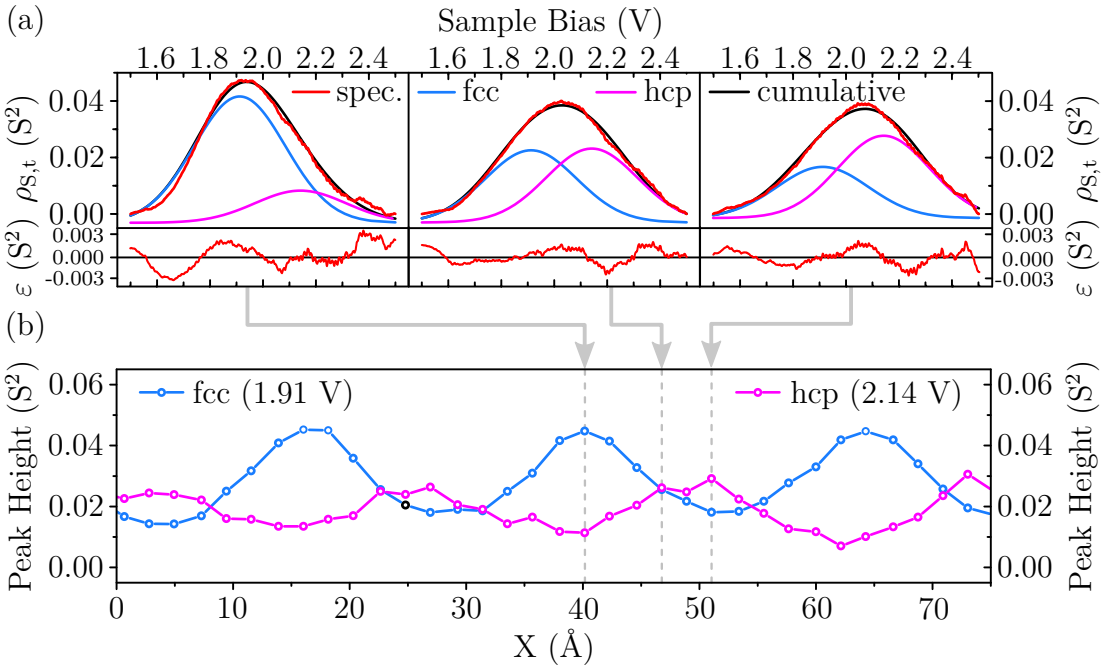

Figure 6.7: Deconvolution of the LDOS measurements from Fig. 6.5(c) into components from the fcc and hcp sites. A linear background was subtracted from each LDOS spectrum, and two Gaussians with equal widths were fitted to each. Representative fits for spectra on the fcc, bridge, and hcp sites are shown in (a). Residuals from these fits are shown at the bottom of the panel. The variation of the peak height is shown in (b). The two peaks are anti-phase and correlate with the topography. The peak at 1.91 V corresponds to the interface state between fcc Cl atoms and the Cu(111), and the peak at 2.14 V is attributed to the corresponding state for Cl atoms adsorbed in hcp sites.

was (1.91 ± 0.07) V and (2.14 ± 0.06) V, respectively. Each spectrum was re-fit with the peak centres fixed at these values. Samples of the fits are shown in Fig. 6.7(a). The amplitudes of the two peaks for the spectra in Fig. 6.5(c) are shown in Fig. 6.7(b). The peak heights are anti-phase to each other, and follow the topography, with the peak at 1.91 V being strongest on the fcc domains and the peak at 2.14 V being strongest on the hcp sites, consistent with Fig. 6.6. The observed shift is therefore due to the variation in the amplitude of the relative local contribution from the fcc-Cl and hcp-Cl peaks, rather than a shift in the energy of either of these peaks. Since the amplitude of the fcc peak is non-zero in the hcp domains, and *vice versa*, it is clear that these states are not strongly localized.

We postulate that the energy difference between the fcc state and the hcp state is due to the change in magnitude of the dipole between the two sites. No difference in the measured apparent barrier height could be resolved between the two domains, possibly due to the fact that the expected difference is similar

to the margin of error of the measurement. However, DFT calculations show that the charge on a Cl atom occupying a hcp site is higher than on one in a fcc site[467] due to the increased number of immediate Cu neighbours, and that the workfunction is expected to be 0.04 eV higher for a hcp domain than for a fcc domain.[473] Indeed, calculations of uniform Cl adlayers on Ag(111), which is closely analogous to Cu(111), show that the excess charge on the hcp-Cl atom resides, at least partially, in the p_z orbital.[474] The additional charge at Cl atoms adsorbed at the hcp site is likely responsible for the observed shift in the hcp unoccupied p_z state to higher energies.

As we mentioned above, the state is found at lower energies on the uniform $(\sqrt{3} \times \sqrt{3})$ R30° adlayer relative to the compressed adlayers. To investigate the origin of this effect, domains of various sizes were produced by applying high current as in Fig. 6.2. The larger domains were assumed to have fcc registry, while the domains which remained largely unchanged were assigned as hcp. This area is shown in Fig. 6.8(a). The LDOS was extracted from spectra measured across these domains, along the blue dotted line in Fig. 6.8(a), as previously described. The resulting contour map is shown in Fig. 6.8(b). Analysis of this plot leads to two observations:

1. The energy of the interface state shifts closer to the Fermi level as the domain size increases.

2. The energy of the interface state is greater at the edge of a domain, near the bridge sites constituting the domain wall, and decays towards the center of the domain.

We now explore the latter in more detail, by examining the peak behaviour across the largest domain in Fig. 6.8(a) [between ∼150−210 Å in Fig. 6.8(b)]. A plot of the interface state energy (approximated by the bias voltage corresponding to the maximum LDOS value) with increasing distance from the bridging row is shown in Fig. 6.8(c). It can be seen that, going from the domain edge towards the center, the bias value corresponding to the energy of the interface state tends asymptotically toward 1.6 V. We note that the interface state appears at 1.6 V in the STS of a uniform $(\sqrt{3}\times\sqrt{3})$ R30° Cl adlayer, where every Cl atom is adsorbed in a fcc site (see Fig. 6.4). This suggests that the presence of the domain walls perturbs the interface state, and shifts it to higher energies. However, it is unclear whether this is due to the increased Cl density in the vicinity of the bridge rows, or because of a specific interaction of the fcc Cl−Cu(111) interface state with the corresponding bridge Cl state (which was not detected in the available tunnelling

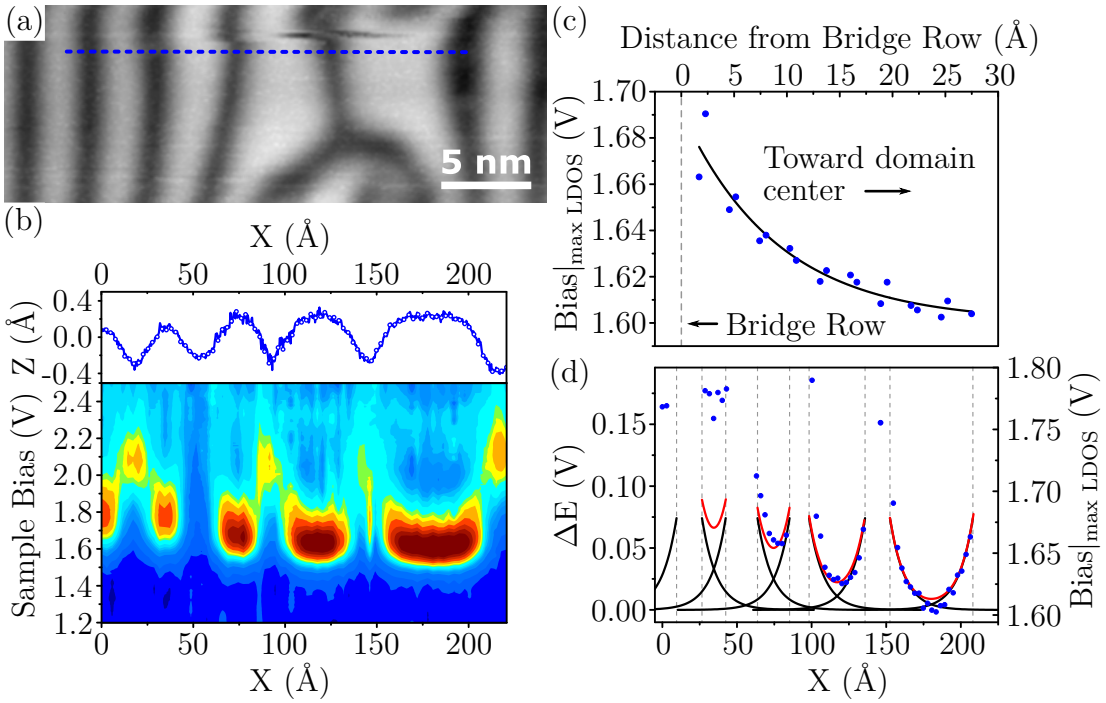

Figure 6.8: A topographic map of an area that has been modified with the tip to form domains of varying sizes is shown in (a). The LDOS along the blue dotted line in (a) is shown in (b). The energy of the interface state on the fcc domains shifts closer to the Fermi level as the domain gets larger, but does not vary from 2.1 V for the hcp domains which have constant width. The position of the peak maximum in the largest domain is plotted in (c) as a function of the distance to the domain edge. As the distance from the domain edge increased, the peak maximum asymptotically approaches 1.6 V, the peak position for a uniform $(\sqrt{3}\times\sqrt{3})$ R30° Cl adlayer. The domain size effect was modelled in (d) by placing the curve extracted in (c) at the locations of the bridging rows in (b). The red curves are the sums of the asymptotic curves, and the blue circles represent the measured peak positions.

window).

The effect of domain size on the energy of the Cl−Cu(111) interface state was modelled using the relationship derived above. The approximate positions of the bridge rows, estimated from Fig. 6.8(b), are represented by dashed vertical lines in Fig. 6.8(d). The observed peak voltage - distance relationship, fitted in Fig. 6.8(c), was then inserted at each of these positions. Next, the domain walls on either side were assumed to contribute additively, and the resulting predicted peak energy at every point across each fcc domain was calculated [indicated by the red curves in Fig. 6.8(d)]. Finally, this was compared to the measured energy of the interface state at various locations on each fcc domain, indicated by the blue circles, and it is clear that for larger domains very good agreement between

the predicted and measured values is obtained. For the smallest domain, however, this simple model significantly underestimates the effect of the domain size on the energy of the interface state, and therefore the interaction between the domain walls and the Cl−Cu(111) interface state for the smallest domains is not well described by adding the contributions from two non-interacting domain walls.

In summary, we have produced uniaxially compressed chlorine adlayers on Cu(111) by exploiting the decomposition of chloroform on this surface. We have described the relationship between coverage and structure in the uniaxial compression regime, and provided new information about the electronic properties of these surfaces. In particular, we have identified a single electronic state arising from the adsorption of Cl on Cu(111), and attributed it to an antibonding interaction between the Cl 3 p_z and Cu d states. The energy of this state was found to depend on the registry and size of the Cl domains, being blue-shifted for hcp domains compared to fcc domains, and for small domains compared to large domains.

6.2 ZnTFcBP on Chlorinated Cu(111)

To test how well the Cl adlayer performs in decoupling molecules from the underlying Cu(111), we electrosprayed ZnTFcBP onto a pre-formed Cl−Cu(111) surface. The molecules self-assemble into a square array, driven by hydrogen bonds between the amine groups, as was described in chapter 4 for ZnTFcBP/Au(111). This indicates that, as expected, the molecule-molecule interaction dominates, rather than the molecule-surface interaction. An STM topograph of ZnTFcBP islands on the Cl−Cu(111) is shown in Fig. 6.9(a), with the unit cell marked in blue.

Figure 6.9(b) shows a higher resolution image of the area marked by the black box in Fig. 6.9(a). Here we clearly resolve the TPP core of the molecule. The improved topographic resolution could be a result of reduced coupling between ZnTFcBP and the underlying metal as we saw for the molecules at the Cu_2N−Cu(100) trenches in chapter 5, however, it may also be due to the STM tip. Occasionally Cl atoms are picked up by the tip, and are known to increase imaging resolution due to the Cl p orbitals terminating the tip.[366,475] These relatively mobile Cl atoms can also be problematic for STS experiments.

We performed STS measurements on the ZnTFcBP/Cl−Cu(111) in the hope that the ionic resonances and/or vibronic states would be experimentally accessible. No spectroscopic signature of weak molecule-substrate coupling was

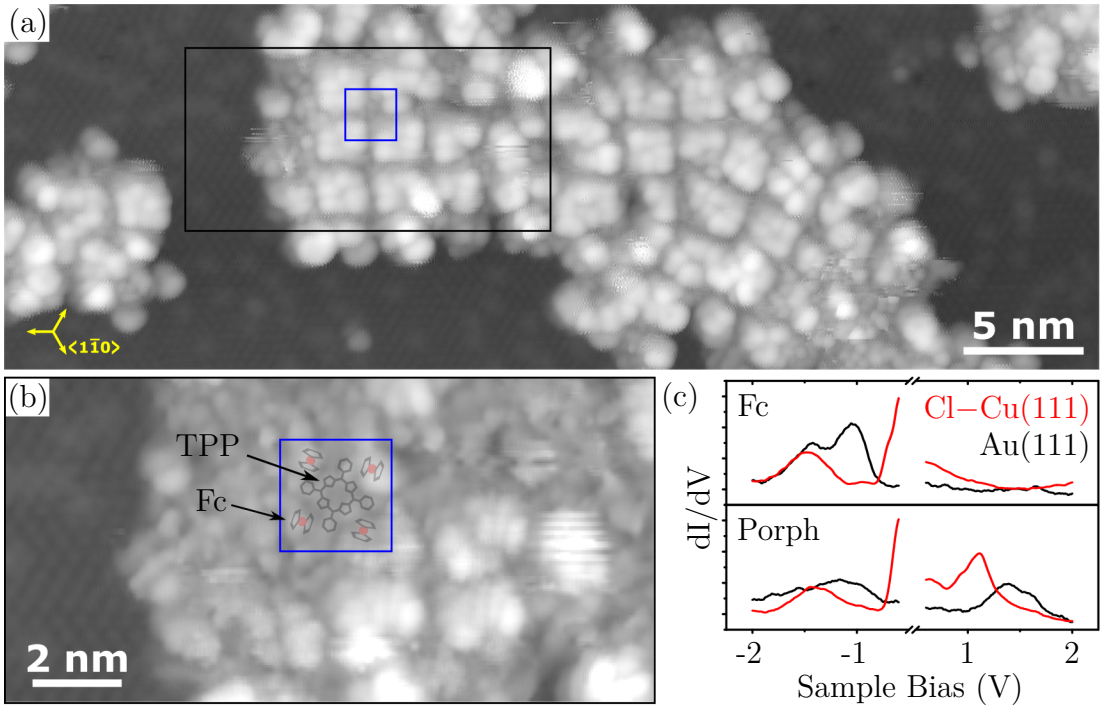

Figure 6.9: It can be seen from (a) that ZnTFcBP self-assembles in a square pattern on Cl−Cu(111), identical to that found on Au(111). On the Cl−Cu(111) surface we can resolve clearly the TPP core of the molecule, as can be seen in (b). The dI/dV signals, recorded during $Z(V_b)$ spectroscopy on Au(111) (black) and Cl−Cu(111) (red), are compared in (c). The states corresponding to the Fc groups and π-system are shifted in energy by −0.5 V on Cl−Cu(111) relative to Au(111). Imaging conditions: (a) 20 pA, −2.5 V; (b) 20 pA, −0.75 V.

observed, indicating that the Cl−Cu(111) surface is not an effective spacer layer. Molecular spectra are qualitatively similar on Au(111) and Cl−Cu(111), as can be seen from Fig. 6.9(c). On both surfaces we observe a peak in the filled states localised to the Fc groups, and one in the empty states centred on the π-system of the porphyrin.

Both peaks are down-shifted by ∼0.5 V on the Cl−Cu(111) compared to Au(111). This shift can be explained by comparing the workfunctions of the two surfaces. The workfunction of Cu(111) is 4.94 eV,[323] which increases by ∼0.8 eV upon adsorption of Cl at a coverage of approximately 1/3 monolayers according to Goddard *et al.*[456] The Au(111) surface has a workfunction of 5.31 eV.[323] The difference in workfunction between the two surfaces ($\Delta\Phi = \Phi_{\text{Au(111)}} - \Phi_{\text{Cl-Cu(111)}} = -0.43$ eV ≈ -0.5 eV) accounts for the shift in the energy of the ferrocene- and porphyrin-based electronic states on the different surfaces.

6.3 Conclusions

We report STS data for uniaxially compressed Cl adlayers on Cu(111), formed by exploiting the dissociative interaction of electrosprayed chloroform with the copper surface. We observe a single peak in the empty states, which we attribute to the antibonding interaction between the Cl 3 p_z orbital and the Cu d states. The energy of this peak was found to be higher on the hcp domains than on the fcc domains. Decomposition of the peak into contributions from each of the adsorption sites reveals that the hcp Cl−Cu(111) interaction is approximately 230 mV more antibonding than the equivalent fcc interaction, and that the states are not well localized but leak into adjacent domains. We suggest that this energy shift is due to more charge transfer from Cu to Cl adatoms at hcp sites.

The energy of the interface state in large fcc domains was found to depend on the distance from the domain edge. The peak position was found to approach that for a pristine $(\sqrt{3}\times\sqrt{3})$ R30° - Cl adlayer, where all the adatoms are in fcc sites, as the distance from the domain edge increases. The peak position was modelled for domains of different sizes based on this asymptotic energy - distance relationship, and the predicted peak position was found to match closely the measured value, except for small domains where the peak position is underestimated. We postulate that the observed asymptotic relationship originates in the interaction between the electronic states due to Cl atoms adsorbed in bridge sites and those in fcc sites. There was no peak due to the bridging site observed in the available tunnelling window. We believe these results shed important light on the ordering and interaction between Cl adatoms on Cu(111) and their influence of the local electronic structure of the surface.

The adsorption and self-assembly behaviour of ZnTFcBP/Cl−Cu(111) was found to be identical to that on Au(111). The molecule is spectroscopically very similar on the two surfaces also. We observe a rigid shift in the spectra over both the Fc sites and the π-system of the molecule, which we attribute to the workfunction difference between the two surfaces.

The single layer of Cl atoms is not sufficient to prevent hybridization of the MOs with the Cu(111) electronic states, which may be due to the small size of the Cl atoms. It is possible that using larger halide adlayers, such as $(\sqrt{3}\times\sqrt{3})$ R30°−I,[476] would be more effective. We instead examine a different molecule which has more favourable properties for MQCA, including the possibility to couple the molecules into covalently-bonded wires.

7

Towards Covalently-Coupled QCA Devices

In the work presented so far we have relied on self-assembly driven by hydrogen bonds to create molecular networks. These non-covalent networks have the advantage of being reversible and, as a result, tend to adopt the lowest energy configuration and heal defects in the network. However, these bonds are quite weak (0.05 eV to 0.7 eV), which can allow molecules to diffuse relative to the other molecules in the network, and prevents transfer of the network from substrate to substrate.

Covalent bonds are significantly stronger (on the order of several eV) and therefore covalently-bonded networks are significantly more thermally, chemically and structurally stable than those held together with non-covalent interactions. The highly directional nature of covalent bonds allows for well-defined structures to be designed and assembled from the bottom-up.[477] However, the irreversibility of covalent bonds means that any defects introduced into the network are permanent.[478] While complicated structures can be engineered in solution using the tools of synthetic chemistry, their size and nature are often limited by solubility.[479] To be useful for device purposes, these assemblies usually need to be supported on a substrate. Intact molecular networks get progressively more difficult to deposit onto a substrate as their size increases, though significant progress in this area has been made in recent years.[224,480,481]

An alternative approach is to use pre-deposited building blocks to assemble a molecular network on a substrate.[482] To assemble the molecular networks, a bond in some functional group within the molecular building block must be bro-

ken, and a new one formed between the activated precursors. This requires the supply of energy, which is commonly achieved by heating the sample, or in some instances using a STM tip. While allowing for the construction of extremely precise, well-defined architectures, assembling a network using STM-induced molecular manipulation and bond scission is extremely time consuming. Annealing a sample to initiate the reaction is a much more efficient way to build large networks, however it often results in significant numbers of defects, as mentioned already. Additionally, the functional group involved in network formation must have an activation energy that is sufficiently low that the reaction can be initiated without degrading the rest of the building block.

The topology of such a network is determined by the number and nature of the functional groups which undergo the reaction to form the covalent bonds, as well as by the symmetry of the building block itself.[483] The properties of the network are governed by the nature of the building block "core" and the bonds linking the building blocks.[484]

In this chapter we investigate a molecule designed specifically for forming covalently-bonded wires *via* surface-catalysed coupling reactions. This molecule is described in section 7.2. We were not successful in coupling the molecules, as is discussed in section 7.5. However, the intact molecule was found to self-assemble on both Au(111) and Cu_2N−Cu(100), and found to exhibit interesting electronic properties on both surfaces, as discussed in sections 7.3 and 7.4, respectively.

7.1 Covalent Coupling at Surfaces

Multiple types of surface reactions have been demonstrated to date, including condensation polymerisation, Glaser coupling, alkane polymerization, boronic acid condensation, decarboxylative polymerization, imine coupling, acylation reaction, dimerization of N-heterocyclic carbenes, azide-alkyne cycloadditions and Bergman cyclizations.[485–494] Ullmann coupling was the first of these covalent coupling reactions to be adapted for surface engineering, and remains one of the most widely used today.

The Ullmann coupling reaction is a well-developed tool in organic synthesis for coupling aryl groups. The classic Ullmann reaction involved the synthesis of symmetric biaryls, where a copper catalyst forms an activated intermediate with an aryl-halide.[495,496] This activated species reacts oxidatively with the second aryl-halide, forming a complex which eliminates the copper halide upon reduction, leaving the coupled biaryl. It has been developed since then, allowing for a varied

range of applications and less harsh reaction conditions.[497,498]

In 1992, Brian Bent's group showed that an analogous reaction could be performed on a metal surface in UHV.[499] They deposited iodobenzene onto Cu(111) at low temperature, where they saw that the C−I bond dissociated at 175 K and the resulting phenyl radicals reacted to form biphenyl above 300 K. Hla *et al.*[169] successfully induced bond scission of the C−I bond in iodobenzene deposited on Cu(111) using electrons injected with the STM tip. They showed that the residual phenyl groups could be manipulated next to one another, and a reaction induced by inelastic tunnelling which rotates the unfulfilled C atom away from the stabilising Cu(111) step edge.

Grill *et al.*[212] were the first to adapt the surface Ullmann coupling reaction for molecular engineering. They showed that with appropriate precursor design various network morphologies could be produced, and that a stepwise coupling reaction could be induced by using a precursor with two different halides,[500] opening the door for the design and synthesis of complicated molecular networks on a surface. The Ullmann coupling reaction has since been demonstrated for a variety of precursors on many different surfaces.[483]

The surface usually plays a role in the reaction beyond simply acting as a support. For example, using a more reactive surface can lower the temperature required to break the C−X bond, which is generally the reaction limiting step.[501] Additionally, some surfaces, such as Cu(110), impart a preferred orientation onto molecular islands, which helps to minimise the presence of defects in a network.[502] Insulating surfaces are often required for device applications, and the Ullmann coupling reaction has been shown to be possible on an insulator.[503,504] It is possible to transfer covalently-bonded molecular layers between substrates, which would be useful for device applications.[505]

Most of the surface reactions published to date have used relatively simple precursors and have aimed at building molecular networks with interesting emergent properties, rather than harnessing the properties of the precursors in a controlled way. For example, these reactions are most often used to assemble graphene-like structures with precise architectures which are predicted to give rise to desirable electronic properties, such as a band-gap.[506] These graphene structures include porous graphenes[507] and graphene nanoribbons with well-defined edge structures.[214]

The work presented in this chapter has a different aim. We intend to utilize the surface Ullmann coupling reaction to create a covalent scaffold on which electronically-interesting functional groups are aligned in a well-defined pattern.

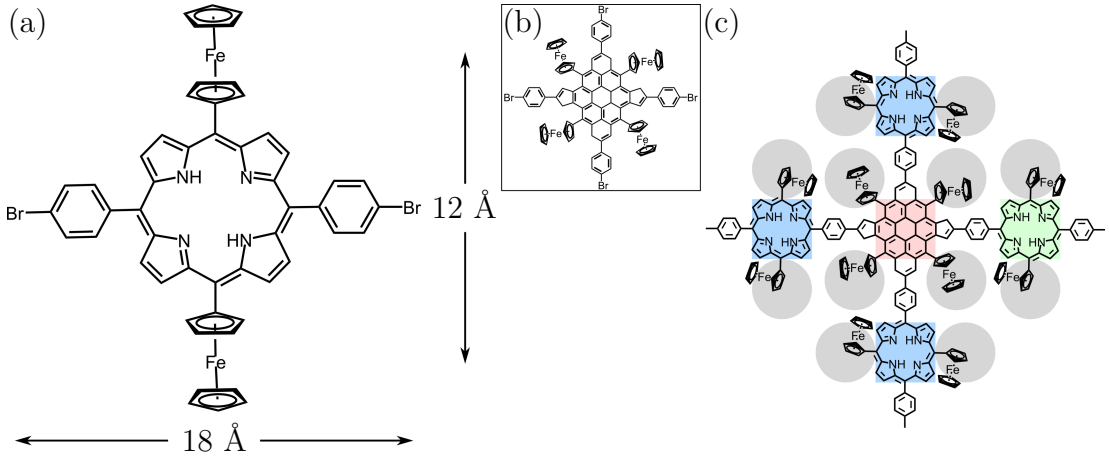

Figure 7.1: Structure of $Fc_2(BrPh)_2P$ and expected dimensions are shown in (a). Hydrogen atoms not explicitly shown. A molecule such as that shown in (b) could be used to couple four $Fc_2(BrPh)_2P$ molecules into a majority gate structure, as depicted in (c). Blue, red and green squares indicate the input, active and output cells, respectively.

7.2 Precursor to Functional Molecular Networks

The molecule investigated in this chapter is a porphyrin derivative inspired by the seminal work of the Grill group,[212] and was synthesised by Stefano Masiero at the University of Bologna. It consists of two ferrocenyl groups bound to opposite *meso*-positions on the porphyrin ring and with bromophenyl groups in *trans*-configuration in the other two *meso*-positions. The IUPAC name for the molecule is 5,15-diferrocenyl-10,20-bis(4-bromophenyl)porphyrin, but it will be referred to as $Fc_2(BrPh)_2P$ from this point in. A structural model of $Fc_2(BrPh)_2P$ is shown in Fig. 7.1(a).

As outlined in section 1.2.3 there exist in the literature a variety of similar molecules, with ferrocenyl units directly linked to a porphyrin core, which allows us to predict some of the properties of $Fc_2(BrPh)_2P$. In fact, Nemykin *et al.*[353] have synthesised an almost identical molecule, with the Br atoms on the phenyl rings replaced by hydrogen atoms, analysed its IVCT bands, and performed DFT calculations. They found it to possess Robin-Day class II character, and predicted that the porphyrin macrocycle was highly distorted from planarity in the gas phase, primarily due to steric interactions between the porphyrin β-hydrogen atoms and those on the ferrocenyl-Cp rings. Since the presence of the Br atoms on the phenyl groups should have no effect on the coupling between the ferrocenyl moieties, it is reasonable to expect $Fc_2(BrPh)_2P$ to exhibit the mixed-valence behaviour we require for MQCA applications. These properties, combined with

the potential for breaking the phenyl−Br bond, and creating covalently-coupled chains *via* the Ullmann coupling reaction, as discussed in the previous section, are what makes $Fc_2(BrPh)_2P$ interesting for device purposes.

It is easy to see that a covalently-linked $Fc_2(BrPh)_2P$ chain would be useful as a MQCA wire. The strong coupling between the Fc groups in each porphyrin-centred half-cell should be preserved (provided it is not disrupted by molecule-substrate interactions) while the intra-cell coupling is expected to be mediated by electrostatic interactions only. Furthermore, the intra-cell coupling could be tuned by inserting a suitable linker between the $Fc_2(BrPh)_2P$ units.

Beyond the MQCA wire, it is conceivable that computationally-useful structures could be engineered based on $Fc_2(BrPh)_2P$. Co-depositing $Fc_2(BrPh)_2P$ with a small proportion of a molecule designed to link the molecular wires in a cross geometry, and subsequent annealing of the surface should result in a random network of wires and majority gate structures. An example of such a molecule is shown in Fig. 7.1(b), and the resulting majority gate is shown in Fig. 7.1(c) where the input, output and active cells are highlighted in blue, green and red, respectively. While this molecule may not be synthetically feasible it illustrates how molecules can be designed to act as MQCA device components. Similarly, a precursor molecule designed to create inverter architectures could be envisaged. While the random nature of the resulting networks would not allow for a useful device to be fabricated, they could be used for proof-of-concept demonstrations of molecular implementation of QCA logic functions. Combining multiple analogues of $Fc_2(BrPh)_2P$ with different functional groups for stepwise coupling, could, in theory, provide a way to controllably create useful molecular architectures, however significant progress in synthetic chemistry at surfaces would have to be made before this became a realistic possibility.

7.3 $Fc_2(BrPh)_2P$ on Au(111)

Before we attempt to couple the $Fc_2(BrPh)_2P$ units, we first characterise them on Au(111).

7.3.1 Self-assembly

$Fc_2(BrPh)_2P$ does not possess any functional groups which drive directional self-assembly. Halogens can participate in hydrogen bonds, or can form halogen bonds,[508] neither of which are expected to be very strong or directional for this molecule. The molecule is relatively large, so that packing to maximise Van der

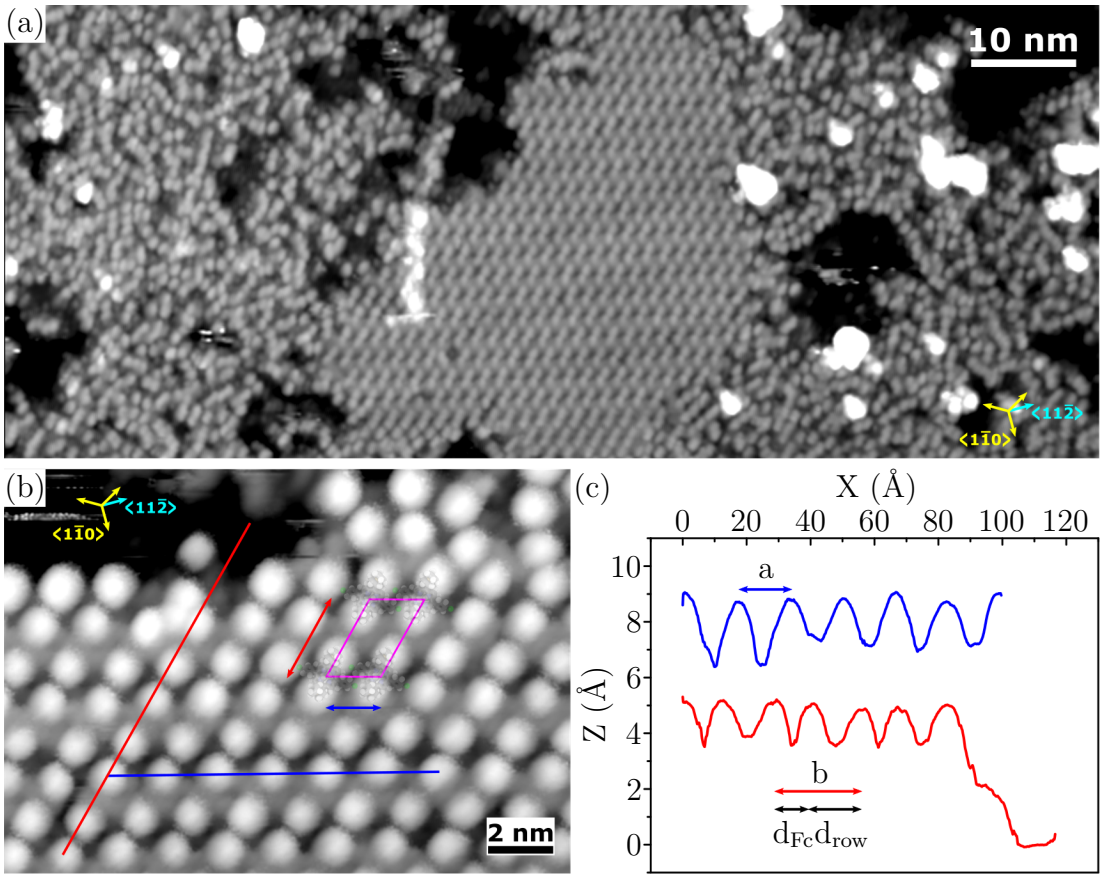

Figure 7.2: Self-assembled islands of $Fc_2(BrPh)_2P$ on Au(111). The large area scan in (a) shows both the ordered and disordered areas of the surface. A close-up of a molecular island is shown in (b), with the molecule and surface unit cell marked in. (c) topographic profiles along the lines indicated in (b). The unit cell parameters are a =17 Å, b =26.5 Å. The b parameter has dual periodicity stemming from the distance between the Fc groups within the molecule d_{Fc} =11 Å and the distance between nearest Fc groups in adjacent rows d_{row} =15.5 Å. Imaging conditions: (a) 15 pA, −2.5 V; (b) 20 pA, −1.25 V.

Waals interactions is expected to play a role in self-organisation of $Fc_2(BrPh)_2P$ on the surface. The lack of a strongly preferential packing structure, coupled with the non-trivial amount of impurities present due to ESD, explains why most of the surface is disordered, and only small well-organised islands are present, as shown in figure 7.2(a). Molecular ordering is increased after gentle annealing.

When the molecules do self-assemble, they first form lines at an angle of ∼15° to the ⟨11$\bar{2}$⟩ directions, as determined from the Au(111) herringbone ridges, with a repeat unit a measuring approximately 17 Å. Di(bromophenyl)-di(iodophenyl) porphyrin (Br_2I_2TPP) self-assembles with the Br atoms next to the porphyrinic β-hydrogens, giving a nearest neighbour distance of approximately 15 Å.[500] Similarly, $NiBr_4TPP$ packs with a square unit cell of side length 16 Å, where the

driver for self-assembly is attributed to the phenyl π-π interaction, as well as to the Br···H−C hydrogen bonds.[509] We believe that the same interactions drive self-assembly of $Fc_2(BrPh)_2P$ into lines. However, since the Fc groups obscure the rest of the molecule, it is not possible to confirm this without a relaxed molecular model.

The molecular rows pack with an inter-row periodicity of 26.5 Å. Adjacent rows are offset by half a unit cell length, giving a 60° angle between the surface unit cell vectors. The surface unit cell is indicated relative to the centre of the porphyrin core in figure 7.2(b). We note here that the unit cell periodicities are within the margin of error of distances corresponding to 6 and 9 Au(111) nearest neighbour distances (17.3 Å and 25.9 Å, respectively), indicating a commensurate unit cell. The red line in figure 7.2(b) has dual periodicity representing the intramolecular Fc-Fc distance and the spacing between adjacent rows, as can be seen in figure 7.2(c). The intramolecular Fc-Fc distance is 11 Å, while adjacent rows are separated by 15.5 Å. The expected intramolecular Fc-Fc distance is approximately 12 Å, and the small discrepancy observed could be either due to the inherent experimental error, or due to conformational relaxations upon adsorption.

The origin of the feature between the $Fc_2(BrPh)_2P$ rows is less clear. From the structure we have assigned to the islands, it does not appear to arise from any part of the molecule, in terms of geometry alone. It is present both before and after annealing up to 200 °C, which suggests that neither Au(111) adatoms nor residual solvent atoms are the cause. This does not rule out interaction with some less volatile impurity, however the regularity of the structure and its apparent thermodynamic stability make this very unlikely.

The fact that we see breaks in the inter-row feature at the island edges where packing is imperfect, as well as in the middle of the island, such as at the bottom left-hand corner of Fig. 7.2b, suggests that the feature is due to some easily removed part of the molecule. It is possible that the feature stems from an electronic interaction between the Br atoms in adjacent molecular rows. Close inspection of a Br_4TPP island reported by Grill *et al.*[212] shows a feature reminiscent of our zigzag feature between the Br atoms on adjacent molecules. This same feature can be seen more clearly in the cobalt 5,10,15,20-tetra(4-bromophenyl)porphyrin ($CoBr_4TPP$) islands in ref. 347. However, seeing as the distance between the molecular rows is significantly larger than the Br-Br distance in Br_4TPP/$CoBr_4TPP$ islands, and since the Br atoms seem not to be pointing directly into the gap between the rows, it is unlikely that this feature

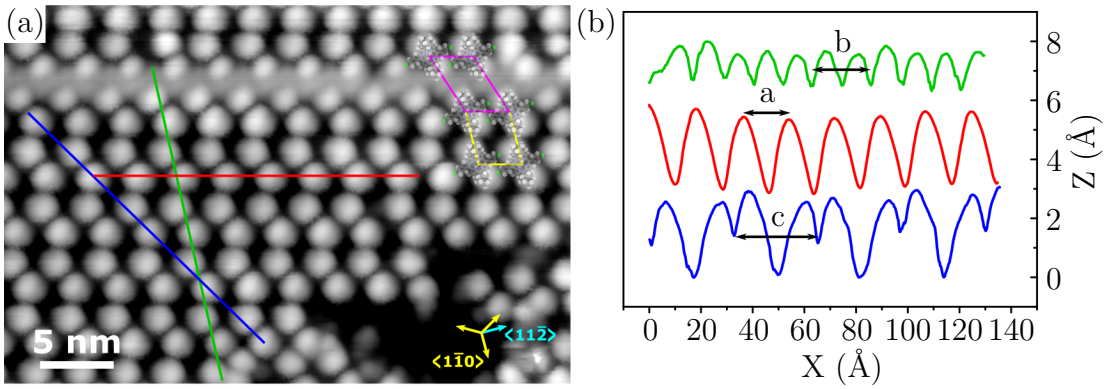

Figure 7.3: The minority packing phase of $Fc_2(BrPh)_2P$ on Au(111). (a) shows a transition between the majority phase and the minority phase, with the unit cells marked in pink and yellow, respectively. Imaging conditions: 20 pA, −1.8 V. (b) shows the apparent height profiles along the lines indicated in (a). The unit cell parameters for this structure are $a = 17.5$ Å and $b = 23.5$ Å. The period along the blue line is $c = 32.5$ Å.

can be attributed to the Br···Br interaction.

Other groups have observed a similar feature which they attribute to a perturbation in the surface charge density in the pores and around the edges of a covalently-bonded porphyrin network.[510] The topographic feature resulting from this perturbation looks very similar to our inter-row feature. However, we do not observe any such feature at the island edges, only between the molecular rows. Additionally, no such feature was observed for islands of unreacted Br_4TPP.[212,347] It is possible that the small intermolecular spacing obscures the feature in the Br_4TPP islands.

We also observed a minority phase where this feature does not appear. The row structure is identical to that in the majority phase, however the rows are shifted relative to each other so that Fc groups from molecules in different rows are beside each other, rather than interdigitated. This structure is shown in Fig. 7.3, and is described by the unit cell vectors $a = 17.5$ Å, which represents the intermolecular spacing along the row and is within the experimental error of that in the majority phase, and, $b = 23.5$ Å, representing the inter-row periodicity. The angle between the unit vectors is approximately 95°.

The fact that at the top of Fig. 7.3 we see the majority phase shifting to the minority phase with no disruption to the island, supports our assertion that the zigzag feature between molecular rows is not due to any species other than $Fc_2(BrPh)_2P$. The closer inter-row spacing may suppress the appearance of the zigzag feature, consistent with it originating in a surface charge density perturbation. However, we remain unable to definitively assign the origin of this feature.

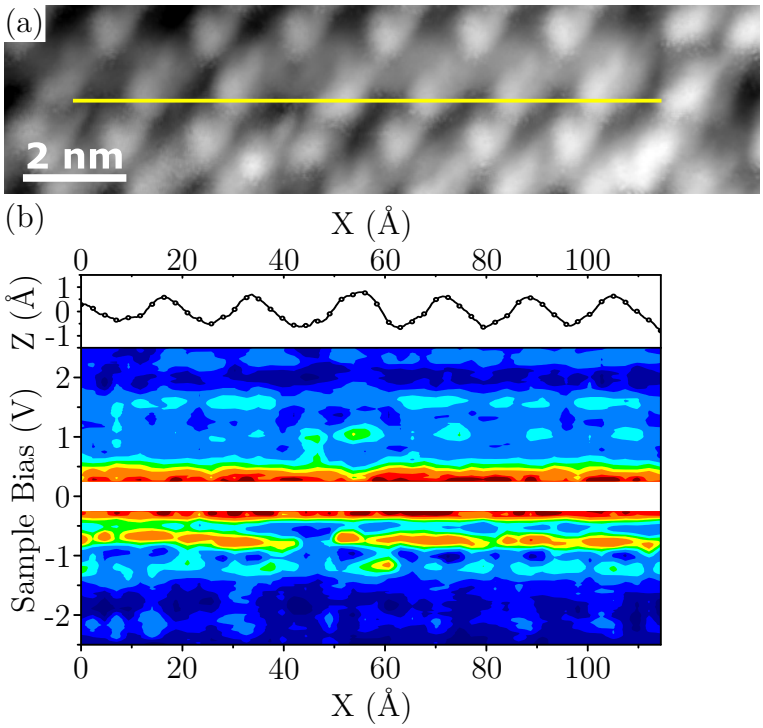

Figure 7.4: STS across a molecular row on Au(111). (b) shows a dI/dV colour map compiled from $Z(V_b)$ spectra measured along the yellow line in (a). Imaging conditions for (a): 20 pA, −1.3 V.

7.3.2 Electronic properties

We then investigated the electronic properties of these assemblies. We measured the dI/dV signal during $Z(V_b)$ spectra taken along the yellow line in figure 7.4(a), as described in section 2.3.3. These spectra were compiled into a colour map, shown in Fig. 7.4(b), which allows us to track the intensity of the various peaks along the molecular row.

The strong peaks below ±0.5 V are artefacts of the experiment, where the tip sharply approaches the surface to maintain the set-point current at low bias. The primary peaks observed occur at approximately 1.6 V, 1.0 V, −0.75 V and −1.2 V. The corresponding HOMO-LUMO gap is therefore 1.75 eV.

Nemykin *et al.*[353] have performed DFT calculations on a very similar molecule, differing only in that the phenyl Br atoms are replaced with H atoms. They found that HOMO-LUMO gap of 5,15-diferrocenyl-10,20-diphenylporphyrin (Fc_2Ph_2P) was ∼1.3 eV in the gas phase. DFT is known to underestimate the HOMO-LUMO gap, particularly when comparing gas phase calculations to measurements on adsorbed molecules.[511] Using the same methodology, Nemykin *et al.* calculate the HOMO-LUMO gap of TPP to be ∼1.85 eV, whereas TPP adsorbed on Au(111) shows a gap of ∼2.3 eV.[512] Additionally, STS transport gaps are similar for TPP

and 5,15-di(bromophenyl)-10,20-diphenylporphyrin (Br_2TPP),[358,512,513] supporting our expectation that the presence of Br atoms on the phenyl rings does not significantly alter the MO energetics. The gas phase calculations underestimate the gap of TPP/Au(111) by the same proportion as they differ from our measurements on $Fc_2(BrPh)_2P$.

Nemykin's group also calculated the spatial distribution of some of the MOs of Fc_2Ph_2P, and found that the HOMO was predominantly Fc-centred, while the LUMO was found on the porphyrin macrocycle. We have imaged the spatial distribution of the STS peaks, by measuring the $\mathrm{d}I/\mathrm{d}V$ signal, at a bias corresponding to the STS peaks, as the tip was scanned over the molecular island. The $\mathrm{d}I/\mathrm{d}V$ maps were recorded concurrently, by scanning each line backwards and forwards for each selected bias before moving on to the next line. The resulting topographic and differential conductance maps are shown in figure 7.5.

We expect the MOs to be broadened due to the hybridization with the Au(111) surface, as discussed in section 1.3, and therefore that the states we image in the STM differential conductance maps actually have contributions from several MOs. That being said, it is clear that at $-0.8\,\mathrm{V}$, corresponding to the HOMO level, we see that the state is localised on the Fc groups, as shown in figure 7.5(b). Additionally, we can see from figure 7.5(e) that differential conductance maps near the LUMO energy show the π-system of the molecule, again agreeing qualitatively with the DFT calculations. The higher energy states show very little spatial variation.

Closer analysis of Fig. 7.5 reveals that not all of the molecules show the same $\mathrm{d}I/\mathrm{d}V$ signal intensity at a given bias. Specifically, molecules exhibiting a strong $\mathrm{d}I/\mathrm{d}V$ signal intensity at $-0.8\,\mathrm{V}$ show no response at $-1.3\,\mathrm{V}$ and $0.8\,\mathrm{V}$, and *vice versa*. This on/off effect suggests a modulation of the STS peaks. Looking again at these states in Fig. 7.4(b), it is clear that on every molecule sampled there is appreciable $\mathrm{d}I/\mathrm{d}V$ intensity at both $-0.8\,\mathrm{V}$ and $-1.3\,\mathrm{V}$. Furthermore, the state at $-0.8\,\mathrm{V}$ appears to be stronger over every molecule. It is unclear why a difference is observed between the point spectroscopy and the $\mathrm{d}I/\mathrm{d}V$ maps.

The distribution of molecules "on" and "off" in the $\mathrm{d}I/\mathrm{d}V$ maps in Fig. 7.5 is reminiscent of that observed for the modulation in the LUMO observed by Auwärter *et al.*[364] for CoTPP islands. They attributed this effect to small variations in adsorption geometry caused by the incommensurate molecular adlayer. We have not been able to find molecular islands large enough to discern if there is a Moiré pattern corresponding to the MO modulation, however, since we believe the $Fc_2(BrPh)_2P$ overlayer structure to be commensurate with Au(111), we do

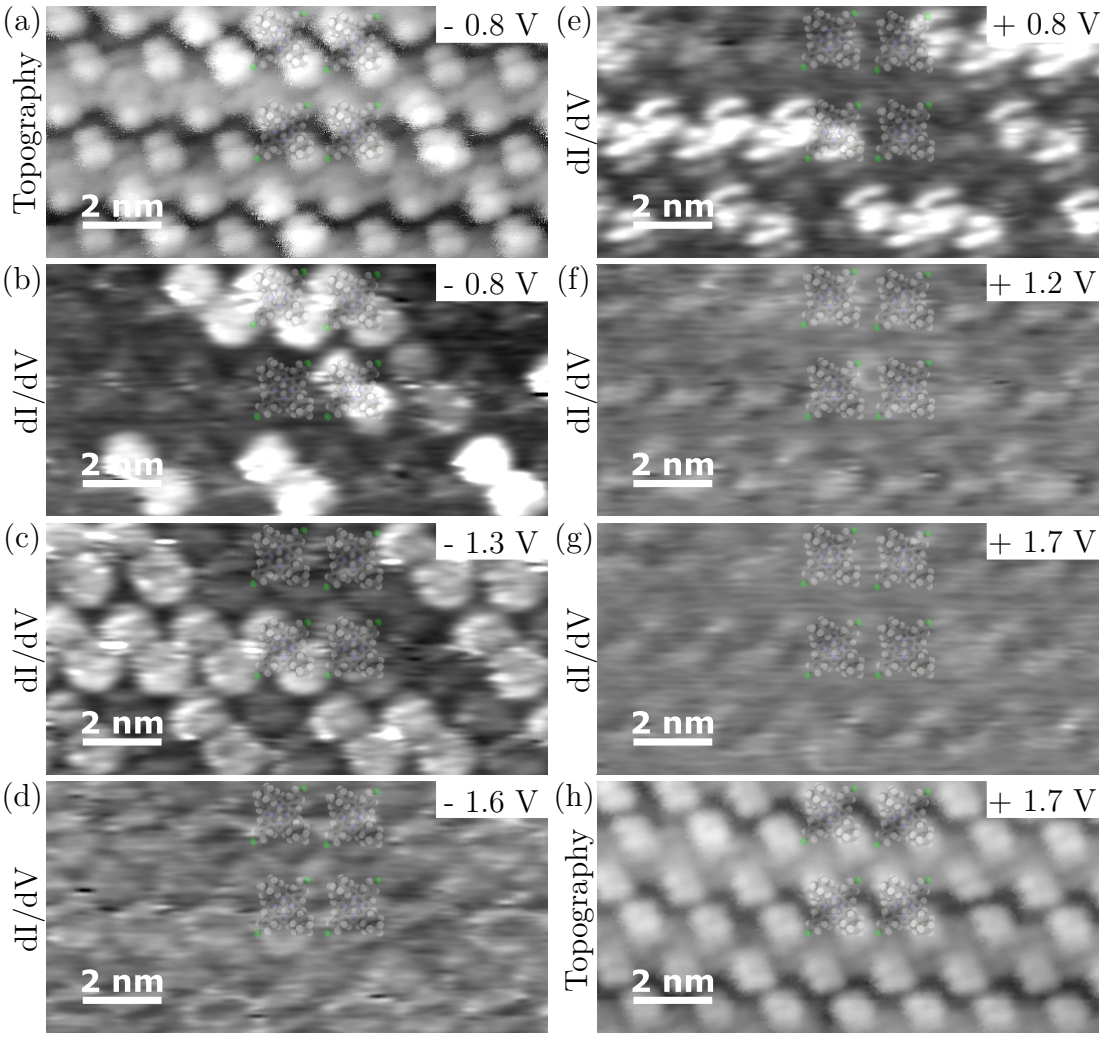

Figure 7.5: Topography [(a) and (h)] and dI/dV intensity maps (b)-(g) over a $Fc_2(BrPh)_2P$ island on Au(111) surface, recorded concurrently for bias values corresponding to STS peaks.

not expect this to be the case.

On the other hand, differences in adsorption site are not the only factor controlling the adsorption geometry. We saw in chapter 4 that adsorbed porphyrins can adopt different conformations. Zhang *et al.*[358] examined the adsorption configuration of Br_2TPP molecules on Au(111) and found that while the saddle geometry was the favoured conformation, the inverted dome conformation was also stable. They were able to distinguish between the configurations based on the topography, and induce switching between the two using the STM tip. They found a rigid shift of 0.5 V in the STS going from the inverted dome conformation to the saddle configuration, which they attributed to a different surface dipole for each geometry.

In our case, the bulky nature of the Fc groups makes it impossible to resolve

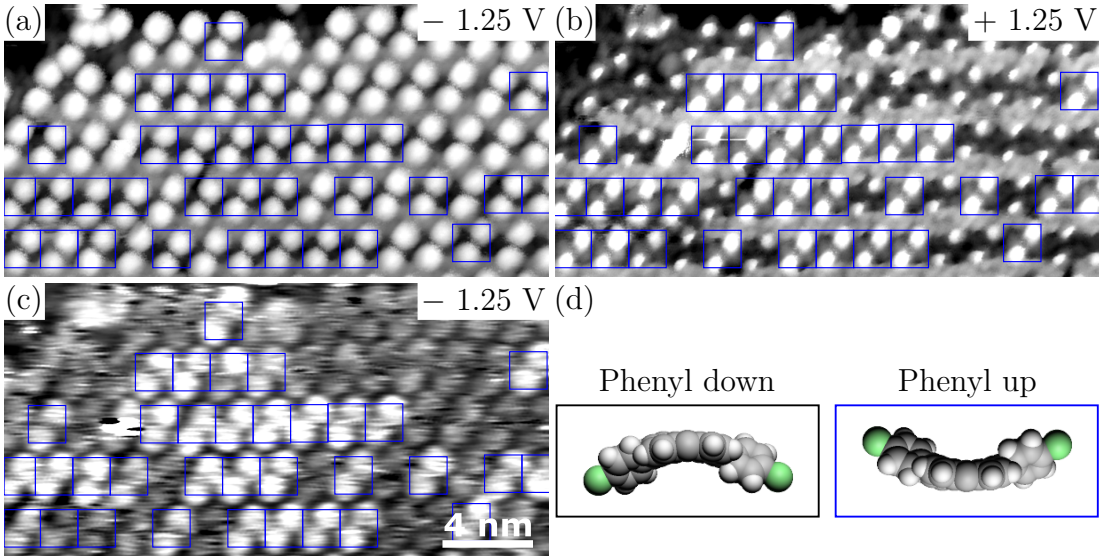

Figure 7.6: Molecules which appear identical in (a) when imaging at −1.25 V reveal subtle topographic differences in (b) when imaging at 1.25 V. Those molecules showing a weak feature perpendicular to those from the the Fc groups (indicated by a blue box) also show strong $\mathrm{d}I/\mathrm{d}V$ intensity at −1.25 V can be seen from (c). The effect of different conformations on the topography is shown schematically in (d), with the Fc groups removed for clarity. Imaging conditions: (a), (c) 20 pA, −1.25 V; (b) 20 pA, 1.25 V.

the core of $Fc_2(BrPh)_2P$ and assign the macrocycle conformation in the same way. We do, however, resolve subtle topographic differences between different molecules within an island when imaging at biases in the empty states, where the electronic contribution from the Fc groups is minimised. It can be seen in Fig. 7.6(a) that, at −1.25 V, the molecular topography looks identical at each site, however at 1.25 V some of the molecules have additional features along the opposite diagonal to the Fc groups, which are highlighted by the boxes in Fig. 7.6(b). We attribute these features to different porphyrin conformations which change the position of the bromophenyl groups, as shown schematically in Fig. 7.6(d). The molecules on which these topographic features are visible correspond almost exactly to those where the HOMO is close to −1.25 V, as can be seen by comparing figure 7.6(b) and (c).

The shifting STS reported by Zhang *et al.* was ascribed to modulation of the surface dipoles by different molecular conformations. The MO energy modulation observed here cannot be simply attributed to the surface dipole, since that would imply a rigid shift in energy, in which case we would expect figure 7.5(f) to resemble a contrast inversion of figure 7.5(e). However, conformational changes in the macrocycle also imply altered bond lengths and angles, and can therefore modify

the electronic properties of the isolated molecule.[514] It has been reported that deformation of the macrocycle narrows the HOMO-LUMO gap.[515,516] The main source of the HOMO-LUMO gap narrowing is attributed to the destabilisation of the HOMO; the LUMO is relatively unaffected.[517] This effect has been found to hold for porphyrins adsorbed on a surface.[335] However, the peripheral functional groups are also reported to play a large role in determining the energetic effects of modifying the porphyrin ring configuration.[363,518,519]

Conformational changes in the porphyrin core may have quite a complicated effect on this molecule since the HOMO and LUMO are localised on different parts of the molecule, and since the coupling between the Fc groups is conformation dependent (see section 1.1.3). In the gas phase, this molecule has a ruffled geometry, with the phenyl rings approximately orthogonal to the porphyrin macrocycle, and the attached Cp rings of the Fc moieties at an angle of ∼45° relative to the porphyrin core.[353] The phenyl rings of TPP are known to prefer an angle below 50° when adsorbed on a surface,[520] which induces non-planarity in the core due to steric interactions between the phenyl- and β-hydrogens.[354] Decreasing the angle between each of the Cp rings and the porphyrin core should increase the coupling between the two Fc groups and would be expected to alter the MO energies. Additionally, Br_2TPP tends to adsorb on a surface in the saddle conformation to maximise the interaction between the Br atoms and the surface,[358] and it is possible that the same may occur for $Fc_2(BrPh)_2P$.

In summary, we observe a modulation in the STS peak intensities, which we attribute to differences in the porphyrin ring conformation, however modelling of $Fc_2(BrPh)_2P$ adsorbed on the surface is necessary to elucidate this effect. Metalation of a porphyrin is known to change the ring conformation, dependent upon the size of the ion.[521] We intend to take advantage of this by inserting metal ions into the core to favour the saddle configuration and see if this suppresses the modulation of the MOs energies.

7.4 Templated Assembly of $Fc_2(BrPh)_2P$ on Cu_2N-Cu(100)

We require that the molecules be only weakly coupled to the substrate in order to be able to investigate their switching behaviour. In this section we discuss the structure and electronic properties of self-assembled molecular rows on the high coverage Cu_2N surface, which was introduced in section 5.1.2.

7.4.1 Surface-templated self-assembly

Mobile molecules tend to diffuse around the surface until they find a surface site at which the molecule-substrate interaction is sufficiently strong to render them immobile. Molecules deposited onto a surface held at a temperature at which the thermal energy is less than the diffusion barrier tend to be found in a random pattern, since they stick where they land. On the other hand, molecules deposited onto a surface held at a temperature at which they are mobile and subsequently cooled will tend to be found at more reactive surface sites, such as steps or vacancies, or if the coverage is sufficiently high, in closely-packed islands nucleated around some reactive site. The molecule-surface interactions tend to be very weak on an insulating substrate such that molecules are usually mobile at room temperature, and molecules tend to be found at reactive sites on the surface. For example, molecules tend to anchor at oxygen vacancies on Al_2O_3−NiAl(100).[197,432]

This helps explain the behaviour we observe when $Fc_2(BrPh)_2P$ is deposited onto the high-coverage Cu_2N surface. Here, molecules tend to accumulate on the exposed Cu(100) crosses or along the trenches. Since the exposed Cu reacts with the solvent (and possibly the molecule) we find organised molecules only along the trenches, as shown in Fig. 7.7(a). Closer analysis of the image in figure 7.7(b) reveals that they form rows identical to those found on the Au(111) surface.

There appeared to be more packing faults in the rows along the trenches than in the islands on Au(111). More specifically, sections of the rows with different orientations are often found along a single trench. We attribute this to the rotation barrier presented by the sides of the trench. On Au(111) when molecules meet they tend to stick together due to the interaction of the Br atoms with the porphyrin β-hydrogens or, if the alignment between them does not allow for that, due to Van der Waals interactions. Provided they have sufficient thermal energy, they will tend to move and/or rotate to adopt the most energetically stable packing configuration. When adsorbed in the Cu_2N trenches, however, the trench walls impede molecular rotations which results in an increased incidence of packing faults.

7.4.2 Electronic properties of molecular rows over trenches

We then investigated the electronic properties of these molecules along the Cu_2N trenches. First, we measured $Z(V_b)$ spectra at many points along each of the black lines in Fig. 7.8(a), which we then compiled into colour maps as already described. These are presented in Fig. 7.8(b)-(g). The primary features observed

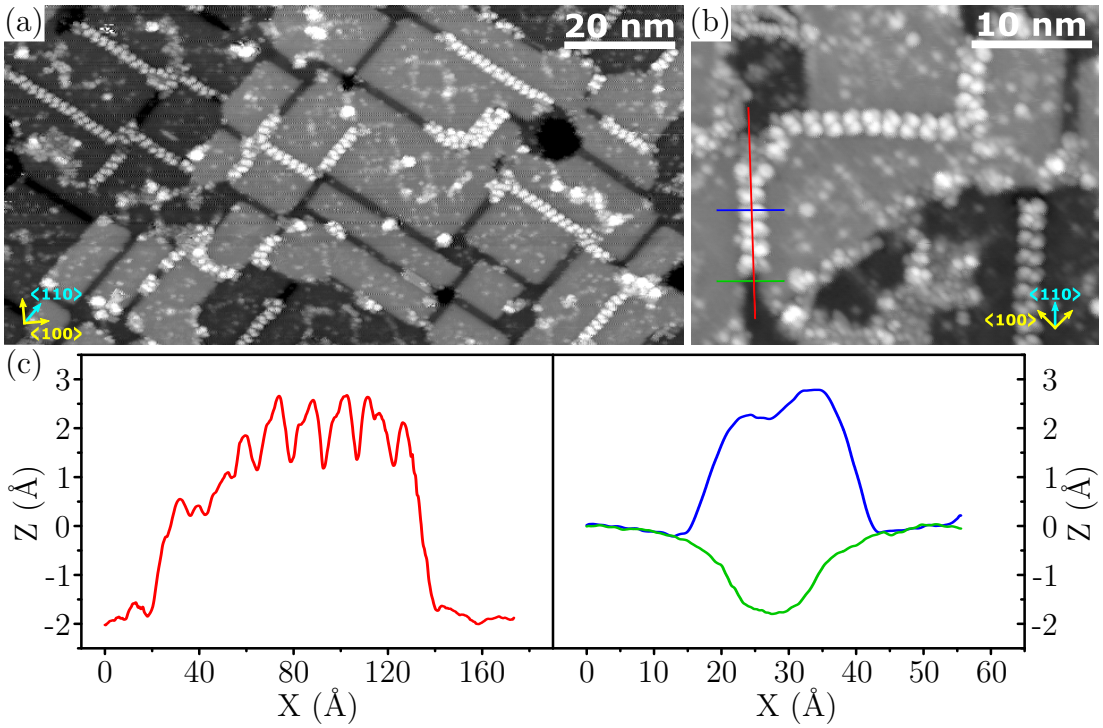

Figure 7.7: $Fc_2(BrPh)_2P$ adsorbs preferentially along the trenches on the high-coverage Cu_2N surface, as shown in (a). The smaller scale image in (b) shows that the molecular orientation is very similar to that along the rows on Au(111). Line profiles along the lines in (b) are shown in (c). Imaging conditions: (a) 20 pA, −2.5 V; (b) 20 pA, −2.25 V.

in these spectra occur at 1.4 V, 0.6 V, −1.25 V and −1.5 V. This gives a STM transport gap of ∼1.85 V, similar to that observed for molecules adsorbed on Au(111). The similarity of the gap on the different surfaces indicates that the coupling between the molecular and substrate states at the Cu_2N trenches is comparable to that on Au(111).

From analysis of how the peak intensity changes with position on the molecular row, we can assign the filled state peaks as being centred on the π-system of the molecule, and those in the empty states as originating from the Fc groups. The filled states on the molecule were mostly energy invariant, while there was some shifting of the peaks on the empty states side of the spectrum. This shift appeared to occur at regions in the wire where the molecular packing was imperfect.

We mapped out the dI/dV signal at a variety of different biases in order to investigate the spatial variation of the peak intensity, as we did for the islands on Au(111) in figure 7.5. As can be seen from Fig. 7.9(a), the tip used to make these measurements was not atomically sharp, causing it to image replicas of the surface features in the well-known multiple tip phenomenon.[437] Figure 7.9(b)

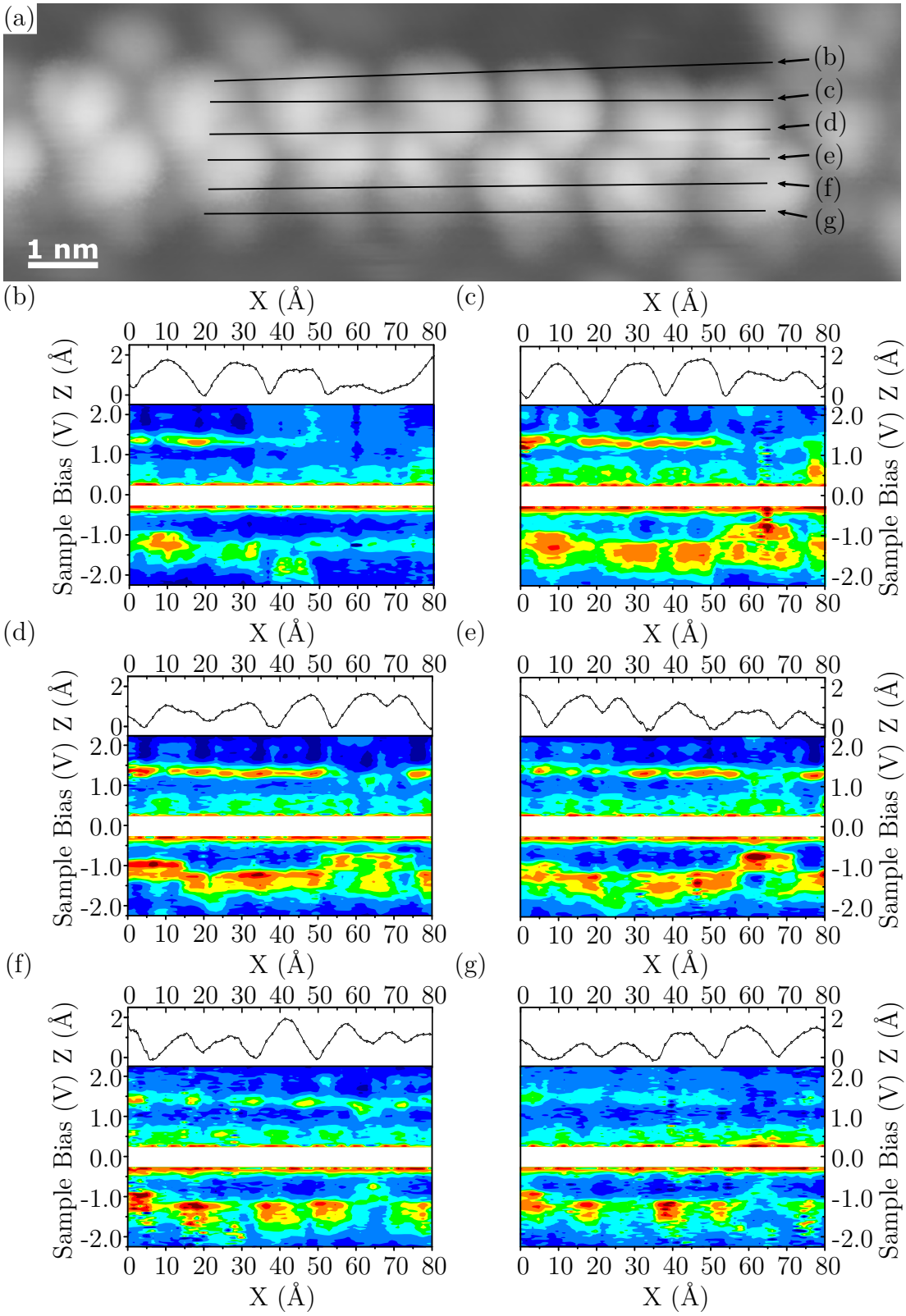

Figure 7.8: STS colour maps compiled from $Z(V_b)$ spectra recorded along the lines in (a) are shown in (b)-(g). Imaging conditions: 20 pA, −2.25 V.

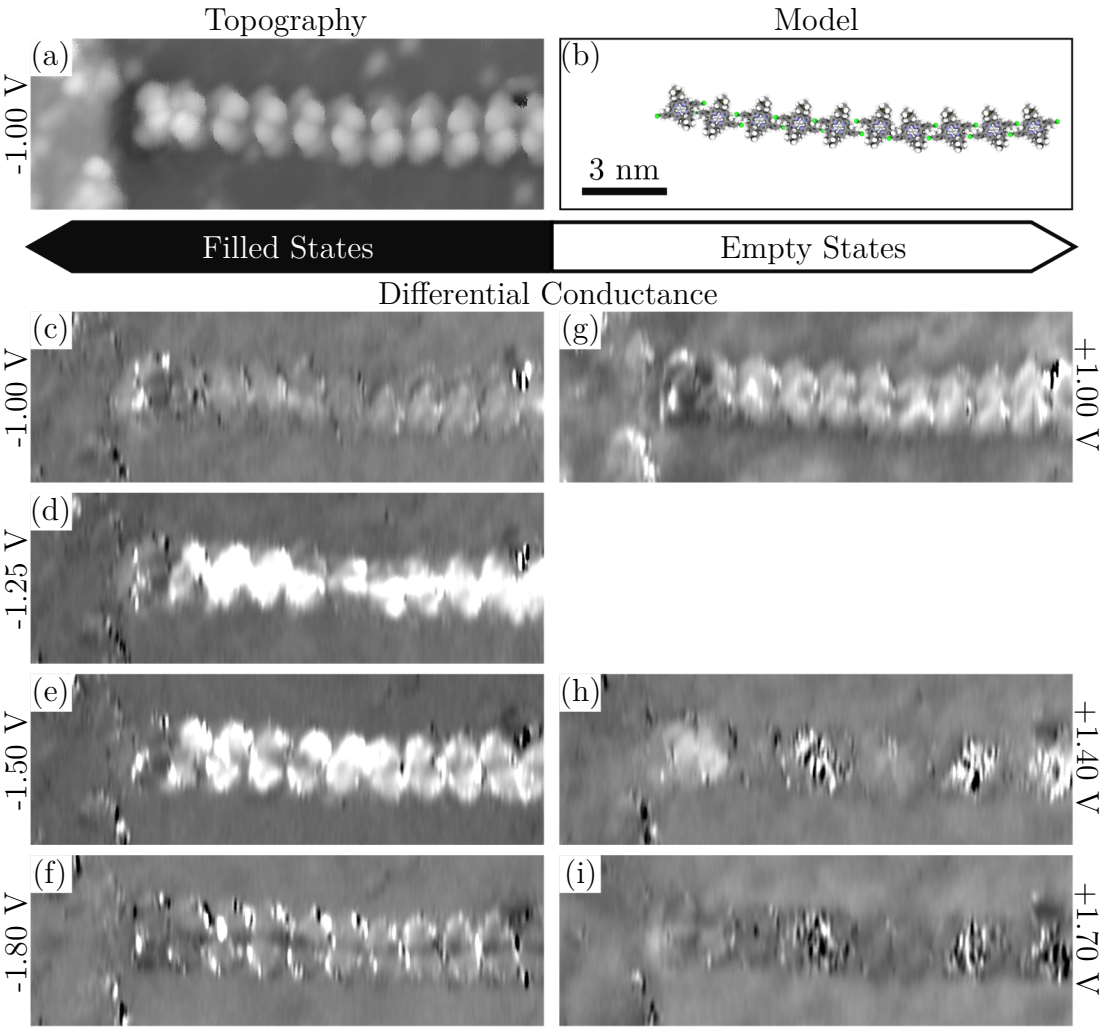

Figure 7.9: A molecular row adsorbed along a Cu_2N trench is shown in (a), with a corresponding molecular model in (b). dI/dV maps recorded concurrently for this row are shown for the sample biases indicated in (c)-(i).

shows a model of the packing structure along the trench.

Here we find significant intensity at 1.0 V, −1.25 V, and −1.5 V. It is unclear why we see greater signal at 1.0 V than at 1.4 V, since the STS colour maps in Fig. 7.8 suggest the reverse should be true. The state at 1.0 V appears to be delocalised throughout the molecular π-system, as expected for the LUMO. The OMOs closest to the Fermi level should be predominantly localised on the to the Fc positions, as already described, and this appears to be borne out by the dI/dV map in figure 7.9(d), recorded at −1.5 V.

The dI/dV map for −1.25 V [Fig. 7.9(d)] is particularly interesting. The state appears to encompass the entire molecule and not just the Fc groups as the HOMO-assigned peak was on Au(111). The dI/dV signal is strong even between the molecules which may suggest intermolecular π-interactions. Addi-

tionally it appears that the intensity of this state depends on the environment of the molecule and not just on the part of the molecule. It is not clear from looking at the molecular features we expect in these areas from our model in Fig. 7.9(b) why the intensity should be reduced close to the center of the wire, which supports the hypothesis that this state has some intermolecular electronic component.

Intermolecular coupling of MOs has been observed in the past.[522] Interestingly, Chen *et al.*[523] have observed that intermolecular delocalisation of π-MOs can occur along lines of 3,4,9,10-perylene-tetracarboxylicdianhydride (PTCDA). Co-adsorbed coronene molecules confine the PTCDA to 1D chains, where the distance between nearest neighbours is smaller than for a homogeneous PTCDA layer, allowing the HOMOs of adjacent molecules to overlap. We posit that the trenches confine the $Fc_2(BrPh)_2P$ molecules in a similar manner and slightly alter the packing, facilitating orbital overlap. However, no measurable difference in the packing periodicity was observed. Intermolecular coupling of MOs would critically depend on the phase of the MO at the point of overlap, which could be investigated with DFT. While including the substrate trench structure is not computationally feasible, the intermolecular distance could be fixed and a molecular row investigated in free space.

The aim of adsorbing $Fc_2(BrPh)_2P$ on a TIL was to attempt decouple it sufficiently in order to access its ionic resonances. However, after significant effort no spectroscopic signature of charging, or indeed of molecular vibronic states, was observed. Since it has been shown that Cu_2N is an effective decoupling layer,[387,524,525] we attribute this to the adsorption position of the molecules. The relatively strong interaction of $Fc_2(BrPh)_2P$ with the trenches in which they are adsorbed serves to immobilise them, but also couples them, so that the molecular states are hybridised with those of the surface, and the lifetime of electrons in the MOs is short. A similar effect is seen for molecules adsorbed on defect sites on Al_2O_3−NiAl(100),[197] and for the ZnTFcBP molecules investigated in chapter 5.

To be able to probe the excited states of the molecules we need to examine molecules adsorbed close to the center of the terraces. For this we need to move to areas of higher coverages where molecular rows nucleate at the trenches and grow out onto the Cu_2N island. Where this occurs the row tends not to adsorb in the center of the trench, instead one porphyrin center seems to rest on either trench edge, which allows each row to interact with the lower coordinated atoms at the trench edge. Unfortunately, in areas of higher coverage there are proportionally

more weakly-bound impurity species from the electrospray which makes STM very difficult. To date we have not been able to obtain reproducible data on these areas, however work in this area is ongoing.

7.5 Towards Covalently Bonded QCA Wires

As mentioned at the beginning of this chapter, the goal was to build covalently-bonded molecular wires using the Ullmann coupling reaction. To this end we have annealed the $Fc_2(BrPh)_2P$/Au(111) sample to progressively higher temperatures and examined the surface after each cycle. After deposition at room temperature, we have seen that the surface is mostly disordered with small organised areas. As after annealing to 100 °C for 10 minutes, the only noticeable difference is a slight increase in the number and size of organised areas.

As we noted already, intact $Fc_2(BrPh)_2P$ does not form strong intermolecular bonds, and combined with the presence of impurities introduced during ESD, this leads to a largely disordered surface with small areas of organised molecules. This disorder can make it difficult to discern morphological changes which occur during annealing, however we are confident that no such changes occur below 200 °C. Annealing the sample to approximately 300 °C produces significant changes in the surface structure, with many of the adsorbates desorbed and only the chain-like structures shown in Fig. 7.10(a) remaining. Upon further annealing, to ∼450 °C, we find dendritic structures which are characteristic of degraded polymeric networks.[526]

The chains shown in Fig. 7.10(a) resemble those shown in Fig. 7.10(b) which produced by Grill *et al.* *via* thermally-activated polymerisation of Br_2TPP.[212] They report that temperatures between 250 °C to 300 °C are required to break the C−Br bond and activate the Ullmann coupling reaction,[212,500] which matches the temperature used in our experiment. It is clear from Fig. 7.10(a) that no features corresponding to the Fc groups are present, indicating they dissociate at these temperatures.

The bond strength of C_6H_5−Br is ∼3.5 eV,[323] whereas ferrocene is reported to have a dissociation energy of ∼3.9 eV.[527] There is approximately a 0.7 eV difference between the bond strength of C_6H_5−Br and C_6H_5−I,[323] which resulted in a ∼80 °C difference in the annealing temperatures required to break the phenyl-iodine and phenyl-bromine bonds.[500] Since we expect that we have temperature control to within ∼20 °C, it should be possible, on the basis of the bond energetics alone, to activate the Ullmann coupling reaction without decomposition of the

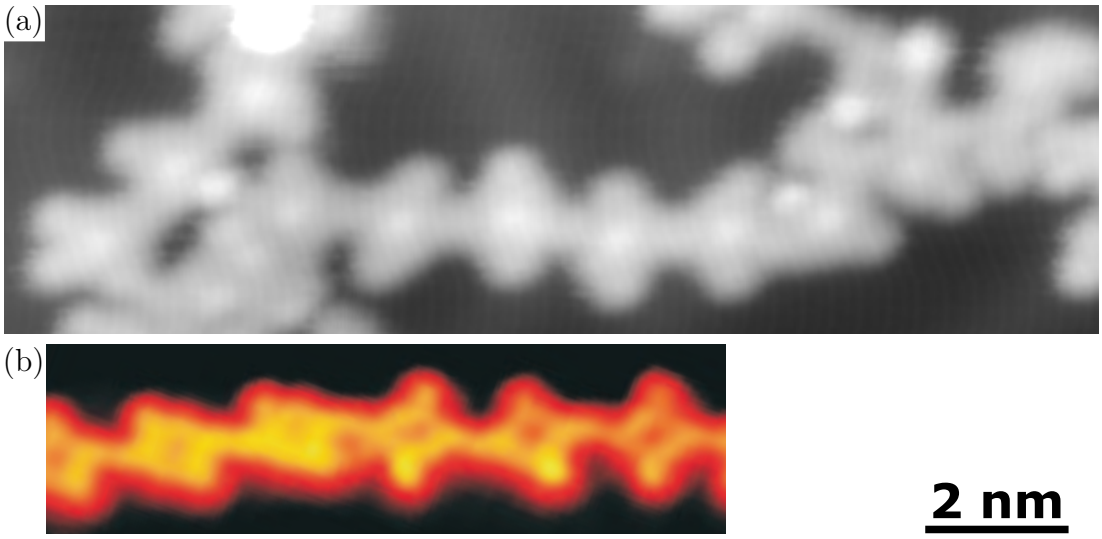

Figure 7.10: Upon annealing the $Fc_2(BrPh)_2P$/Au(111) system to approximately 300 °C structures such as that shown in (a) are observed on the surface. These resemble the 1D chains produced by Grill *et al.* *via* surface-catalysed coupling of Br_2TPP,[212] which are shown in (b). Imaging conditions: (a) 20 pA, −2.0 V.

Fc groups. However, the thermodynamics of molecular dissociation are modified on surfaces. As a clear illustration of this, ferrocene is known to dissociate on a Au(111) surface cooled to 80 K, whereas it dissociates in the gas phase only above 673 K.[528]

Another interesting observation is that there appears to be a feature in the center of most of the porphyrin macrocycles. The unreacted $Fc_2(BrPh)_2P$ molecule has a free base core, which usually appears hollow or with bright features at either side of the core, depending on the macrocycle conformation. Such a feature in the centre of a porphyrin ring can be due to the presence of some metal ions.[529–531] Self-metalation is known to occur on some surfaces,[532] but has never been reported to occur on Au(111). However, co-deposited Fe adatoms are known to be able to displace the inner porphyrinic H atoms, metallating the core.[533,534] Dissociation of the ferrocene groups may have made Fe adatoms available on the surface to participate in the metallation reaction. However, it is impossible to confirm this assignment without knowing the dissociation and reaction mechanism of the $Fc_2(BrPh)_2P$ molecule.

$Fc_2(BrPh)_2P$ is stable up until approximately 200 °C, indicating that if the activation temperature for the coupling reaction can be reduced below this, wires with intact Fc groups may be formed. Future work will focus on reducing the temperatures required for the coupling reaction. The simplest approach would be to use a more reactive substrate such as Ag(111) or Cu(111), or indeed one

of the non-close packed faces of a noble metal, which are known to reduce the energy required to break the Br−C bond.[507] However, this may introduce ESD compatibility issues as we saw in chapter 5, and may also reduce the dissociation temperature of the Fc groups. Additionally, we wish to examine these wires on a variety of surfaces and, as a result, surface-sensitive preparation conditions are not desirable.

Instead, we will take two approaches. The first approach will be to exchange the Br atoms for a functionality which has a lower activation temperature, such as iodine or an ethynyl group. The C−I bond is weaker than the C−Br bond, and is known to facilitate on-surface Ullmann coupling at approximately 120 °C.[500] Glaser coupling of acetyl groups has an lower activation temperature than the Ullmann coupling reaction,[535] and may therefore be feasible. The drawback of this approach is that it necessitates the synthesis of new molecules.

The second approach can be implemented with the $Fc_2(BrPh)_2P$ molecules, and involves coupling them in solution and subsequently depositing the wires. The reaction is more likely to be facile in solution than on a surface,[536–538] and therefore failure in solution would indicate that an alternative coupling mechanism should be attempted. Wires containing over 40 covalently-linked porphyrin subunits have already been deposited by ESD,[224] so that we would expect $Fc_2(BrPh)_2P$-derived porphyrin nanowires tens or hundreds of nm long to be ESD compatible. These long chains may be pinned at certain points on the Cu_2N surface, allowing those parts of the wire which are at the center of a Cu_2N terrace, and should therefore be decoupled from the underlying Cu(100), to be addressed.

7.6 Conclusions

We have deposited $Fc_2(BrPh)_2P$ on Au(111), where we have characterised its packing structure and electronic properties. We observed a modulation of the STS peaks over some molecules compared to others, which we believe is due to conformational differences. However, more experiments and/or modelling of the system are needed to confirm this.

We found that the trenches on the high-coverage Cu_2N−Cu(100) surface template self-assembly into molecular rows. These rows had the same periodicity as those on Au(111), yet gave rise to interesting electronic properties. We saw what we believe to be intermolecular coupling of MOs, facilitated by minor changes in the packing structure driven by the trenches. In this case too, we require DFT calculations for confirmation.

$Fc_2(BrPh)_2P$ was found to be coupled to the Cu_2N strongly enough at the trenches that its ion resonances were not sufficiently long-lived to be experimentally accessible. Molecules adsorbed close to the center of the Cu_2N islands are expected to be decoupled from the underlying metal. Molecular assemblies were found to nucleate from the trenches and grow outwards, so that molecules could be found near the middle of Cu_2N terraces. However, the presence of weakly-adsorbed species has to date prevented acquisition of reproducible data in the higher coverage regions of the sample, and work in this area is still ongoing.

We attempted to couple these molecules into covalently-bonded wires, but were unsuccessful. The carbon-bromine bond energy is quite similar to the Cp−Fe bond energy in a ferrocene molecule and, as a result, dissociation of both may occur at similar temperatures. We are planning to attempt to couple $Fc_2(BrPh)_2P$ in solution and deposit the pre-assembled wires onto both Au(111) and Cu_2N−Cu(100). Analogous molecules with the Br atoms replaced with I or ethynyl groups may also be synthesised in order to facilitate lower temperature on-surface coupling reactions.

8

Conclusions & Future Work

QCA presents a promising alternative computational paradigm to continue the computational power gains in the post-Moore world. Within QCA, binary states are represented by the charge configuration within a cell, and logic operations are implemented using patterned arrays of electrostatically-coupled cells. Molecular scale QCA should offer power dissipation approaching the theoretical minimum, as well as extremely high device densities. The aim of this work has been to make progress towards demonstrating MQCA.

The challenges associated with using STM to demonstrate switching in QCA cells built from molecular components include identifying suitable molecules, depositing and organising these molecules on passivated surfaces, and injecting charge into these decoupled assemblies. Once these challenges have been overcome, attempts to read-out and switch the charge states can be made. While progress has been made, work remains to be done in order to meet this goal.

We have investigated two candidate molecules here. The first of these is a TPP derivative, symmetrically functionalised with an amido-ferrocene. We have shown that these molecules, like other porphyrins, interact more strongly with Cu(111) than with Au(111), and that the higher surface energy on Cu(111) drives self-assembly into a more close-packed structure than is observed on Au(111). On Au(111), where intermolecular interactions govern the self-assembly, these molecules organise in a square motif which is desirable for QCA applications. We found good agreement between our STS measurements of the LDOS of these adsorbed layers and the theoretical predictions. The HOMO energy was observed to depend on the local conformation, but that these conformational differences do not propagate through a molecular layer.

To switch the charge state of the ferrocenyl moiety we needed to decouple the molecular states from the substrate states. This was particularly challenging given that the molecules were incompatible with standard deposition techniques. We found that NaCl(100) layers on Au(111) were incompatible with ESD, since their morphology was changed after exposure to the beam, resulting in a highly unstable surface. We believe that other ionic films would be similarly modified, and that only chemisorbed insulating films should be used in combination with ESD. We investigated two such systems, the nitrides of Cu(100) and Cu(110), and found that both are indeed ESD-compatible, however neither are well-suited for use with our molecule. The small terrace size of $Cu_2N-Cu(100)$ interferes with self-assembly, such that organised molecules are only found at trench edges, where they are not sufficiently decoupled. On $Cu_3N-Cu(110)$, on the other hand, we find evidence for deprotonation of the amide groups, leading to an upright adsorption geometry and strong coupling to the surface.

The final substrate investigated for this molecule was a chlorinated copper surface, which allowed higher resolution imaging, but no access to excited states. We did, however, provide new insight into the electronic properties of the Cl−Cu(111) surface in the coverage regime where the adlayer is uniaxially compressed. Here we detected an electronic state arising from the chlorine adsorption on Cu(111), which we attributed to an antibonding interaction between the Cl 3 p_z orbital and the Cu d states. The energy of this state was found to depend on the chlorine adsorption site, being higher for those adsorbed in fcc sites than hcp sites. The interface state energy was also found to depend on the size of the domain and on the distance from the domain edge.

The second molecule we investigated was a brominated ferrocenyl-porphyrin, designed to undergo a surface-catalysed polymerisation reaction. We found that the functional part of the molecule decomposed at temperatures similar to that required to cleave the bromine-phenyl bond, which activates the Ullmann coupling reaction. We believe that using the iodinated analogue of this molecule will facilitate the coupling reaction within the thermal budget for the intact molecule. In spite of the failure of the coupling reaction, we found interesting behaviour of the precursors, which were found to self-assemble on Au(111) where both the HOMO and LUMO energies were sensitive to the conformation of the central porphyrin macrocycle. We found that the $Cu_2N-Cu(100)$ trenches template the self-assembly of this molecule into wire structures, and we saw what we believe to be intermolecular overlap of MOs, however modelling of this system is required to confirm this.

As already mentioned, in future we plan to attempt the coupling reaction with the iodinated version of this molecule. Another avenue we intend to pursue is to couple these molecules in solution and deposit the resulting molecular wires *via* ESD. This should allow us to find wires with segments near the center of the Cu_2N terraces, which we expect to be less coupled than those at the trenches.

The major challenge remaining is to observe organised molecules on substrates where their electronic states are sufficiently decoupled to allow for charge injection. We have identified two new insulator-on-metal systems which we believe will solve the issues encountered to date, and facilitate demonstration of MQCA. These substrate systems, h-BN/Cu(111) and Al_2O_3−NiAl(100), have both been well-characterised and are capable of decoupling molecular states from those in the underlying metal. The next step for this research is to form these surfaces, and confirm their compatibility with ESD and with our MQCA candidates.

Bibliography

[1] C. S. Lent, P. D. Tougaw, W. Porod and G. H. Bernstein, *Nanotechnology*, 1993, **4**, 49–57.

[2] C. S. Lent, B. Isaksen and M. Lieberman, *J. Am. Chem. Soc.*, 2003, **125**, 1056–1063.

[3] A. O. Orlov, I. Amlani, G. H. Bernstein, C. S. Lent and G. L. Snider, *Science*, 1997, **277**, 928–930.

[4] G. Binnig, H. Rohrer, C. Gerber and E. Weibel, *Appl. Phys. Lett.*, 1982, **40**, 178–180.

[5] H. Ohtani, R. J. Wilson, S. Chiang and C. M. Mate, *Phys. Rev. Lett.*, 1988, **60**, 2398–2401.

[6] S. W. Wu, N. Ogawa, G. V. Nazin and W. Ho, *J. Phys. Chem. C*, 2008, **112**, 5241–5244.

[7] G. E. Moore, *Electronics*, 1965, **38**, 114.

[8] A. Aviram and M. A. Ratner, *Chem. Phys. Lett.*, 1974, **29**, 277–283.

[9] R. M. Metzger, B. Chen, U. Höpfner, M. V. Lakshmikantham, D. Vuillaume, T. Kawai, X. Wu, H. Tachibana, T. V. Hughes, H. Sakurai, J. W. Baldwin, C. Hosch, M. P. Cava, L. Brehmer and G. J. Ashwell, *J. Am. Chem. Soc.*, 1997, **119**, 10455–10466.

[10] N. Robertson and C. A. McGowan, *Chem. Soc. Rev.*, 2003, **32**, 96–103.

[11] L. A. Bumm, J. J. Arnold, M. T. Cygan, T. D. Dunbar, T. P. Burgin, L. Jones, D. L. Allara, J. M. Tour and P. S. Weiss, *Science*, 1996, **271**, 1705–1707.

[12] W. B. Davis, W. A. Svec, M. A. Ratner and M. R. Wasielewski, *Nature*, 1998, **396**, 60–63.

[13] H. W. Fink and C. Schönenberger, *Nature*, 1999, **398**, 407–410.

[14] P. Aich, S. L. Labiuk, L. W. Tari, L. J. Delbaere, W. J. Roesler, K. J. Falk, R. P. Steer and J. S. Lee, *J. Mol. Biol.*, 1999, **294**, 477–485.

[15] N. Hamada, S. I. Sawada and A. Oshiyama, *Phys. Rev. Lett.*, 1992, **68**, 1579–1581.

[16] S. J. Tans, M. H. Devoret, H. Dai, A. Thess, R. E. Smalley, L. J. Geerligs and C. Dekker, *Nature*, 1997, **386**, 474–477.

[17] A. Tsuda and A. Osuka, *Science*, 2001, **293**, 79–82.

[18] G. Sedghi, K. Sawada, L. J. Esdaile, M. Hoffmann, H. L. Anderson, D. Bethell, W. Haiss, S. J. Higgins and R. J. Nichols, *J. Am. Chem. Soc.*, 2008, **130**, 8582–8583.

[19] S. Im Jun, J. Wook Lee, S. Sakamoto, K. Yamaguchi and K. Kim, *Tetrahedron Lett.*, 2000, **41**, 471–475.

[20] M. D. Ward, *Chem. Soc. Rev.*, 1995, **24**, 121–134.

[21] C. Creutz and H. Taube, *J. Am. Chem. Soc.*, 1969, **91**, 3988–3989.

[22] C. Creutz and H. Taube, *J. Am. Chem. Soc.*, 1973, **95**, 1086–1094.

[23] M. B. Robin and P. Day, *Adv. Inorg. Chem. Radiochem.*, 1968, **10**, 247–422.

[24] P. J. Low, *Dalt. Trans.*, 2005, 2821–2824.

[25] W. Liang, M. P. Shores, M. Bockrath, J. R. Long and H. Park, *Nature*, 2002, **417**, 725–729.

[26] J. Park, A. N. Pasupathy, J. I. Goldsmith, C. Chang, Y. Yalsh, J. R. Petta, M. Rinkoski, J. P. Sethna, H. D. Abruña, P. L. McEuen and D. C. Ralph, *Nature*, 2002, **417**, 722–725.

[27] J. von Neumann, in *Cereb. Mech. Behav.*, Wiley, 1951, pp. 1–31.

[28] J. Conway, *Sci. Am.*, 1970, **223**, 120–123.

[29] S. Wolfram, *Nature*, 1984, **311**, 419–424.

[30] J. von Neumann, *The Theory of Self-Reproducing Automata*, University of Illinois Press, 1966, pp. 89–250.

[31] E. R. Banks, *Information Processing and Transmission in Cellular Automata*, Massachusetts Institute of Technology Technical Report MIT/LCS/TR-81, 1971.

[32] F. L. Carter, *Phys. D Nonlinear Phenom.*, 1984, **10**, 175–194.

[33] A. J. Heinrich, C. P. Lutz, J. A. Gupta and D. M. Eigler, *Science*, 2002, **298**, 1381–1387.

[34] A. Bandyopadhyay, R. Pati, S. Sahu, F. Peper and D. Fujita, *Nat. Phys.*, 2010, **6**, 369–375.

[35] J. Woodward, *Philos. Trans.*, 1724, **33**, 15–17.

[36] R. A. Marcus, *J. Chem. Phys.*, 1956, **24**, 966–978.

[37] R. A. Marcus, *J. Chem. Phys.*, 1957, **26**, 872–877.

[38] R. A. Marcus, *J. Chem. Phys.*, 1957, **26**, 867–871.

[39] N. S. Hush, *Prog. Inorg. Chem.*, 1967, **8**, 391–444.

[40] C. Creutz, *Prog. Inorg. Chem.*, 1983, **30**, 1–73.

[41] C. Lambert, C. Risko, V. Coropceanu, J. Schelter, S. Amthor, N. E. Gruhn, J. C. Durivage and J. L. Brédas, *J. Am. Chem. Soc.*, 2005, **127**, 8508–8516.

[42] A. Heckmann and C. Lambert, *Angew. Chemie - Int. Ed.*, 2012, **51**, 326–392.

[43] S. Barlow and D. O'Hare, *Chem. Rev.*, 1997, **97**, 637–670.

[44] S. B. Braun-Sand and O. Wiest, *J. Phys. Chem. A*, 2003, **107**, 285–291.

[45] K. D. Demadis, C. M. Hartshorn and T. J. Meyer, *Chem. Rev.*, 2001, **101**, 2655–2685.

[46] M. Parthey and M. Kaupp, *Chem. Soc. Rev.*, 2014, **43**, 5067–5088.

[47] R. A. Marcus, *Angew. Chemie - Int. Ed.*, 1993, **32**, 1111–1121.

[48] F. Ammar and J. M. Savéant, *J. Electroanal. Chem.*, 1973, **47**, 215–221.

[49] D. M. D'Alessandro and F. R. Keene, *Dalt. Trans.*, 2004, 3950–3954.

[50] F. Barrière, N. Camire, W. E. Geiger, U. T. Mueller-Westerhoff and R. Sanders, *J. Am. Chem. Soc.*, 2002, **124**, 7262–7263.

[51] D. M. D'Alessandro and F. R. Keene, *Chem. Rev.*, 2006, **106**, 2270–2298.

[52] C. A. Stein and H. Taube, *J. Am. Chem. Soc.*, 1981, **103**, 693–695.

[53] S. Roué, C. Lapinte and T. Bataille, *Organometallics*, 2004, **23**, 2558–2567.

[54] D. O. Cowan, C. Levanda, J. Park and F. Kaufman, *Acc. Chem. Res.*, 1973, **6**, 1–7.

[55] F. Delgado-Pena, D. R. Talham and D. O. Cowan, *J. Organomet. Chem.*, 1983, **253**, C43–C46.

[56] A.-C. Ribou, J.-P. Launay, M. L. Sachtleben, H. Li and C. W. Spangler, *Inorg. Chem.*, 1996, **35**, 3735–3740.

[57] C. Levanda, K. Bechgaard and D. O. Cowan, *J. Org. Chem.*, 1976, **41**, 2700–2704.

[58] J. Kotz, G. Neyhart, W. J. Vining and M. D. Rausch, *Organometallics*, 1983, **2**, 79–82.

[59] R. C. Haddon, *J. Am. Chem. Soc.*, 1987, **109**, 1676–1685.

[60] M. P. Samanta, W. Tian, S. Datta, J. I. Henderson and C. P. Kubiak, *Phys. Rev. B*, 1996, **53**, R7626–R7629.

[61] Z. J. Donhauser, B. A. Mantooth, K. F. Kelly, L. A. Bumm, J. D. Monnell, J. J. Stapleton, J. Price, A. M. Rawlett, D. L. Allara, J. M. Tour and P. S. Weiss, *Science*, 2001, **292**, 2303–2307.

[62] C. Patoux, C. Coudret, J.-P. Launay, C. Joachim and A. Gourdon, *Inorg. Chem.*, 1997, **36**, 5037–5049.

[63] A. Hildebrandt and H. Lang, *Dalt. Trans.*, 2011, **40**, 11831–11837.

[64] D. Siebler, C. Förster, T. Gasi and K. Heinze, *Organometallics*, 2011, **30**, 313–327.

[65] A. K. Burrell, W. M. Campbell, D. L. Officer, S. M. Scott, K. C. Gordon and M. R. McDonald, *J. Chem. Soc. Dalt. Trans.*, 1999, 3349–3354.

[66] C. S. Lent and P. D. Tougaw, *J. Appl. Phys.*, 1993, **74**, 6227–6233.

[67] P. D. Tougaw and C. S. Lent, *J. Appl. Phys.*, 1994, **75**, 1818–1825.

[68] C. S. Lent and P. D. Tougaw, *Proc. IEEE*, 1997, **85**, 541–557.

[69] M. T. Niemier and P. M. Kogge, Proc. ICECS'99. Int. Conf. Electron. Circuits Syst., 1999, pp. 1211–1215.

[70] J. Timler and C. S. Lent, *J. Appl. Phys.*, 2002, **91**, 823–831.

[71] C. Lent, P. Tougaw and W. Porod, Proc. PhysComp'94. Work. Phys. Comput., 1994, pp. 5–13.

[72] R. K. Kummamuru, J. Timler, G. Toth, C. S. Lent, R. Ramasubramaniam, A. O. Orlov, G. H. Bernstein and G. L. Snider, *Appl. Phys. Lett.*, 2002, **81**, 1332–1334.

[73] W. Porod, *Int. J. Bifurc. Chaos*, 1997, **7**, 2199–2218.

[74] G. Csaba, A. Imre, G. H. Bernstein, W. Porod and V. Metlushko, *IEEE Trans. Nanotechnol.*, 2002, **1**, 209–213.

[75] G. Csaba, W. Porod and Á. I. Csurgay, *Int. J. Circuit Theory Appl.*, 2003, **31**, 67–82.

[76] R. P. Cowburn and M. E. Welland, *Science*, 2000, **287**, 1466–1468.

[77] A. Imre, G. Csaba, L. Ji, A. Orlov, G. H. Bernstein and W. Porod, *Science*, 2006, **311**, 205–208.

[78] D. Loss and D. P. DiVincenzo, *Phys. Rev. A*, 1998, **57**, 120–126.

[79] G. Tóth and C. S. Lent, *Phys. Rev. A*, 2001, **63**, 052315.

[80] G. Tóth and C. S. Lent, *J. Appl. Phys.*, 1999, **85**, 2977–2984.

[81] A. O. Orlov, I. Amlani, G. Toth, C. S. Lent, G. H. Bernstein and G. L. Snider, *Appl. Phys. Lett.*, 1999, **74**, 2875–2877.

[82] R. K. Kummamuru, A. O. Orlov, G. Toth, J. Timler, R. Rajagopal, C. S. Lent, G. H. Bernstein and G. L. Snider, Proc. 1st IEEE Conf. Nanotechnology., 2001, pp. 431–436.

[83] I. Amlani, *Science*, 1999, **284**, 289–291.

[84] S. Gardelis, C. Smith, J. Cooper, D. Ritchie, E. Linfield and Y. Jin, *Phys. Rev. B*, 2003, **67**, 2–5.

[85] C. G. Smith, S. Gardelis, A. W. Rushforth, R. Crook, J. Cooper, D. A. Ritchie, E. H. Linfield, Y. Jin and M. Pepper, *Superlattices Microstruct.*, 2003, **34**, 195–203.

[86] F. Perez-Martinez, I. Farrer, D. Anderson, G. A. Jones, D. A. Ritchie, S. J. Chorley and C. G. Smith, *Appl. Phys. Lett.*, 2007, **91**, 032102.

[87] C. Single, R. Augke, F. E. Prins, D. A. Wharam and D. P. Kern, *Semicond. Sci. Technol.*, 1999, **14**, 1165–1168.

[88] C. Single, R. Augke, F. E. Prins, D. A. Wharam and D. P. Kern, *Superlattices Microstruct.*, 2000, **28**, 429–434.

[89] M. Macucci, M. Gattobigio, L. Bonci, G. Iannaccone, F. E. Prins, C. Single, G. Wetekam and D. P. Kern, *Superlattices Microstruct.*, 2003, **34**, 205–211.

[90] M. Mitic, M. C. Cassidy, K. D. Petersson, R. P. Starrett, E. Gauja, R. Brenner, R. G. Clark, A. S. Dzurak, C. Yang and D. N. Jamieson, *Appl. Phys. Lett.*, 2006, **89**, 013503.

[91] M. B. Haider, J. L. Pitters, G. A. Dilabio, L. Livadaru, J. Y. Mutus and R. A. Wolkow, *Phys. Rev. Lett.*, 2009, **102**, 046805.

[92] J. L. Pitters, L. Livadaru, M. B. Haider and R. A. Wolkow, *J. Chem. Phys.*, 2011, **134**, 064712.

[93] Y. Lu and C. S. Lent, *Chem. Phys. Lett.*, 2015, **633**, 52–57.

[94] A. Aviram, *J. Am. Chem. Soc.*, 1988, **110**, 5687–5692.

[95] N. S. Hush, A. T. Wong, G. B. Bacskay and J. R. Reimers, *J. Am. Chem. Soc.*, 1990, **112**, 4192–4197.

[96] E. P. Blair and C. S. Lent, Proc. SISPAD 2003. Int. Conf. Simul. Semicond. Process. Devices., 2003, pp. 14–18.

[97] C. S. Lent and B. Isaksen, *IEEE Trans. Electron Devices*, 2003, **50**, 1890–1896.

[98] J. Jiao, G. J. Long, F. Grandjean, A. M. Beatty and T. P. Fehlner, *J. Am. Chem. Soc.*, 2003, **125**, 7522–7523.

[99] J. Jiao, G. J. Long, L. Rebbouh, F. Grandjean, A. M. Beatty and T. P. Fehlner, *J. Am. Chem. Soc.*, 2005, **127**, 17819–17831.

[100] M. D. Rausch, F. A. Higbie, G. F. Westover, A. Clearfield, R. Gopal, J. M. Troup and I. Bernal, *J. Organomet. Chem.*, 1978, **149**, 245–264.

[101] J. Kotz, G. Neyhart, W. J. Vining and M. D. Rausch, *Organometallics*, 1983, **2**, 79–82.

[102] Y. Lu and C. S. Lent, *J. Comput. Electron.*, 2005, **4**, 115–118.

[103] V. Arima, M. Iurlo, L. Zoli, S. Kumar, M. Piacenza, F. Della Sala, F. Matino, G. Maruccio, R. Rinaldi, F. Paolucci, M. Marcaccio, P. G. Cozzi and A. P. Bramanti, *Nanoscale*, 2012, **4**, 813–823.

[104] A. Pulimeno, M. Graziano and G. Piccinini, Proc. 12th IEEE Conf. Nanotechnol., 2012, pp. 1–5.

[105] A. Pulimeno, M. Graziano, A. Sanginario, V. Cauda, D. Demarchi and G. Piccinini, *IEEE Trans. Nanotechnol.*, 2013, **12**, 498–507.

[106] Z. Li, A. M. Beatty and T. P. Fehlner, *Inorg. Chem.*, 2003, **42**, 5707–5714.

[107] Z. Li and T. P. Fehlner, *Inorg. Chem.*, 2003, **42**, 5715–5721.

[108] H. Qi, S. Sharma, Z. Li, G. L. Snider, A. O. Orlov, C. S. Lent and T. P. Fehlner, *J. Am. Chem. Soc.*, 2003, **125**, 15250–15259.

[109] H. Qi, A. Gupta, B. C. Noll, G. L. Snider, Y. Lu, C. Lent and T. P. Fehlner, *J. Am. Chem. Soc.*, 2005, **127**, 15218–15227.

[110] S. Guo and S. A. Kandel, *J. Phys. Chem. Lett.*, 2010, **1**, 420–424.

[111] Y. Lu, R. Quardokus, C. S. Lent, F. Justaud, C. Lapinte and S. A. Kandel, *J. Am. Chem. Soc.*, 2010, **132**, 13519–13524.

[112] R. C. Quardokus, Y. Lu, N. A. Wasio, C. S. Lent, F. Justaud, C. Lapinte and S. A. Kandel, *J. Am. Chem. Soc.*, 2012, **134**, 1710–1714.

[113] N. A. Wasio, R. C. Quardokus, R. P. Forrest, S. A. Corcelli, Y. Lu, C. S. Lent, F. Justaud, C. Lapinte and S. Alex Kandel, *J. Phys. Chem. C*, 2012, **116**, 25486–25492.

[114] V. N. Nemykin, G. T. Rohde, C. D. Barrett, R. G. Hadt, C. Bizzarri, P. Galloni, B. Floris, I. Nowik, R. H. Herber, A. G. Marrani, R. Zanoni and N. M. Loim, *J. Am. Chem. Soc.*, 2009, **131**, 14969–14978.

[115] T. J. Kealy and P. L. Pauson, *Nature*, 1951, **168**, 1039–1040.

[116] G. Wilkinson, M. Rosenblum, M. C. Whiting and R. B. Woodward, *J. Am. Chem. Soc.*, 1952, **74**, 2125–2126.

[117] M. Rosenblum and R. B. Woodward, *J. Am. Chem. Soc.*, 1958, **80**, 5443–5449.

[118] A. Haaland, *Acc. Chem. Res.*, 1979, **12**, 415–422.

[119] N. G. Connelly and W. E. Geiger, *Chem. Rev.*, 1996, **96**, 877–910.

[120] M. Jurow, A. E. Schuckman, J. D. Batteas and C. M. Drain, *Coord. Chem. Rev.*, 2010, **254**, 2297–2310.

[121] J. Otsuki, *Coord. Chem. Rev.*, 2010, **254**, 2311–2341.

[122] A. K. Burrell, W. M. Campbell, G. B. Jameson, D. L. Officer, P. D. W. Boyd, Z. Zhao, P. A. Cocks and K. C. Gordon, *Chem. Commun.*, 1999, 637–638.

[123] C. Bucher, C. H. Devillers, J. C. Moutet, G. Royal and E. Saint-Aman, *Coord. Chem. Rev.*, 2009, **253**, 21–36.

[124] R. G. Wollmann and D. N. Hendrickson, *Inorg. Chem.*, 1977, **16**, 3079–3089.

[125] E. S. Schmidt, T. S. Calderwood and T. C. Bruice, *Inorg. Chem.*, 1986, **25**, 3718–3720.

[126] P. V. Solntsev, J. R. Sabin, S. J. Dammer, N. N. Gerasimchuk and V. N. Nemykin, *Chem. Commun.*, 2010, **46**, 6581–6583.

[127] S. Venkatraman, V. Prabhuraja, R. Mishra, R. Kumar, T. K. Chandrashekar, W. Teng and K. R. Senge, *Indian J. Chem. - Sect. A Inorganic, Phys. Theor. Anal. Chem.*, 2003, **42**, 2191–2197.

[128] G. T. Rohde, J. R. Sabin, C. D. Barrett and V. N. Nemykin, *New J. Chem.*, 2011, **35**, 1440–1448.

[129] N. R. Erickson, C. D. Holstrom, H. M. Rhoda, G. T. Rohde, Y. V. Zatsikha, P. Galloni and V. N. Nemykin, *Inorg. Chem.*, 2017, **56**, 4716–4727.

[130] K. W. Poon, W. Liu, P. K. Chan, Q. Yang, T. W. Chan, T. C. Mak and D. K. Ng, *J. Org. Chem.*, 2001, **66**, 1553–1559.

[131] P. D. Beer, M. G. Drew and R. Jagessar, *J. Chem. Soc. Dalt. Trans.*, 1997, 881–886.

[132] J. Kim, S. W. Rhee, Y. H. Na, K. P. Lee, Y. Do and S. C. Jeoung, *Bull. Korean Chem. Soc.*, 2001, **22**, 1316–1322.

[133] V. N. Nemykin, G. T. Rohde, C. D. Barrett, R. G. Hadt, J. R. Sabin, G. Reina, P. Galloni and B. Floris, *Inorg. Chem.*, 2010, **49**, 7497–7509.

[134] A. Auger, A. J. Muller and J. C. Swarts, *Dalt. Trans.*, 2007, 3623–3633.

[135] A. Vecchi, N. R. Erickson, J. R. Sabin, B. Floris, V. Conte, M. Venanzi, P. Galloni and V. N. Nemykin, *Chem. - A Eur. J.*, 2015, **21**, 269–279.

[136] A. Zangwill, *Physics at Surfaces*, Cambridge University Press, 1988, pp. 183–232.

[137] R. Otero, A. L. Vázquez de Parga and J. M. Gallego, *Surf. Sci. Rep.*, 2017, **72**, 105–145.

[138] J. Bardeen, *Surf. Sci.*, 1964, **2**, 381–388.

[139] R. Hesper, L. H. Tjeng and G. A. Sawatzky, *Europhys. Lett.*, 1997, **40**, 177–182.

[140] J. B. Neaton, M. S. Hybertsen and S. G. Louie, *Phys. Rev. Lett.*, 2006, **97**, 216405.

[141] I. G. Hill, A. Rajagopal, A. Kahn and Y. Hu, *Appl. Phys. Lett.*, 1998, **73**, 662–664.

[142] G. Koller, R. I. R. Blyth, S. A. Sardar, F. P. Netzer and M. G. Ramsey, *Appl. Phys. Lett.*, 2000, **76**, 927–929.

[143] K. Wandelt, *Appl. Surf. Sci.*, 1997, **111**, 1–10.

[144] P. W. Anderson, *Phys. Rev.*, 1961, **124**, 41.

[145] D. M. Newns, *Phys. Rev.*, 1969, **178**, 1123–1135.

[146] W. Mönch, *Surf. Sci.*, 1994, **299**, 928–944.

[147] H. Vázquez, F. Flores, R. Oszwaldowski, J. Ortega, R. Pérez and A. Kahn, *Appl. Surf. Sci.*, 2004, **234**, 107–112.

[148] H. Ishii, K. Sugiyama, E. Ito and K. Seki, *Adv. Mater.*, 1999, **11**, 605–625.

[149] B. Hammer and J. K. Nørskov, *Nature*, 1995, **376**, 238–240.

[150] B. Hammer and J. K. Nørskov, *Surf. Sci.*, 1995, **343**, 211–220.

[151] E. W. Müller and K. Bahadur, *Phys. Rev.*, 1956, **102**, 624–631.

[152] R. Wiesendanger, *Scanning Probe Microscopy and Spectroscopy*, Cambridge University Press, 1994.

[153] O. K. Binnig, H. Rohrer, C. Gerber and E. Stoll, *Surf. Sci.*, 1984, **144**, 321–335.

[154] G. Binnig, H. Rohrer, C. Gerber and E. Weibel, *Phys. Rev. Lett.*, 1983, **50**, 120–123.

[155] G. Binnig and H. Rohrer, *Angew. Chemie - Int. Ed.*, 1987, **26**, 606–614.

[156] A. M. Bara, G. Binnig, H. Rohrer, C. Gerber, E. Stoll, A. Baratoff and F. Salvan, *Phys. Rev. Lett.*, 1984, **52**, 1304–1307.

[157] P. H. Lippel, R. J. Wilson, M. D. Miller, C. Wöll and S. Chiang, *Phys. Rev. Lett.*, 1989, **62**, 171–174.

[158] J. Repp, G. Meyer, F. E. Olsson and M. Persson, *Science*, 2004, **305**, 493–495.

[159] J. Repp, G. Meyer, S. Paavilainen, F. E. Olsson and M. Persson, *Science*, 2006, **312**, 1196–1199.

[160] D. M. Eigler and E. K. Schweizer, *Nature*, 1990, **344**, 524–526.

[161] K. Morgenstern, N. Lorente and K.-H. Rieder, *Phys. Status Solidi*, 2013, **250**, 1671–1751.

[162] M. F. Crommie, C. P. Lutz and D. M. Eigler, *Science*, 1993, **262**, 218–220.

[163] R. M. Feenstra, *Surf. Sci.*, 1994, **299**, 965–979.

[164] R. J. Hamers, *Annu. Rev. Phys. Chem.*, 1989, **40**, 531–559.

[165] L. Gross, F. Mohn, N. Moll, P. Liljeroth and G. Meyer, *Science*, 2009, **325**, 1110–1114.

[166] L. Gross, N. Moll, F. Mohn, A. Curioni, G. Meyer, F. Hanke and M. Persson, *Phys. Rev. Lett.*, 2011, **107**, 086101.

[167] J. Repp, G. Meyer, S. M. Stojković, A. Gourdon and C. Joachim, *Phys. Rev. Lett.*, 2005, **94**, 026803.

[168] G. Dujardin, R. E. Walkup and P. Avouris, *Science*, 1992, **255**, 1232–1235.

[169] S. W. Hla, L. Bartels, G. Meyer and K. H. Rieder, *Phys. Rev. Lett.*, 2000, **85**, 2777–2780.

[170] D. J. Griffiths, *Introduction to Quantum Mechanics*, Pearson, 2nd edn., 2005, pp. 315–354.

[171] J. Bardeen, *Phys. Rev. Lett.*, 1961, **6**, 57–59.

[172] A. Selloni, P. Carnevali, E. Tosatti and C. D. Chen, *Phys. Rev. B*, 1985, **31**, 2602–2605.

[173] V. A. Ukraintsev, *Phys. Rev. B*, 1996, **53**, 11176–11185.

[174] N. D. Lang, *Phys. Rev. B*, 1986, **34**, 5947–5950.

[175] J. A. Stroscio, R. M. Feenstra and A. P. Fein, *Phys. Rev. Lett.*, 1986, **57**, 2579–2582.

[176] N. Li, M. Zinke-Allmang and H. Iwasaki, *Surf. Sci.*, 2004, **554**, 253–261.

[177] M. Passoni and C. E. Bottani, *Phys. Rev. B*, 2007, **76**, 115404.

[178] B. Naydenov and J. J. Boland, *Phys. Rev. B*, 2010, **82**, 245411.

[179] A. E. Hanna and M. Tinkham, *Phys. Rev. B*, 1991, **44**, 5919–5922.

[180] H. Grabert and M. H. Devoret, *Single charge tunneling: Coulomb Blockade Phenomena in Nanostructures*, Springer, 1992, vol. 294, pp. 1–18.

[181] W. Zwerger and M. Scharpf, *Zeitschrift für Phys. B Condens. Matter*, 1991, **85**, 421–426.

[182] A. J. Fisher, *Phys. Rev. Lett.*, 1993, **70**, 3323–3326.

[183] R. Berndt, J. K. Gimzewski and P. Johansson, *Phys. Rev. Lett.*, 1991, **67**, 3796–3799.

[184] P. K. Hansma, *Phys. Rep.*, 1977, **30**, 145–206.

[185] K. Moth-Poulsen, *Handbook of Single-Molecule Electronics*, CRC Press, 2016, pp. 155–205.

[186] B. C. Stipe, M. A. Rezaei, W. Ho, S. Gao, M. Persson and B. I. Lundqvist, *Phys. Rev. Lett.*, 1997, **78**, 4410–4413.

[187] P. K. Hansma, *Tunneling Spectroscopy: Capabilities, Applications, and New Techniques*, Springer, 1982.

[188] M. Buttiker, *IBM J. Res. Dev.*, 1988, **32**, 63–75.

[189] A. Nitzan, *Annu. Rev. Phys. Chem.*, 2001, **52**, 681–750.

[190] D. V. Averin and Y. V. Nazarov, *Phys. Rev. Lett.*, 1990, **65**, 2446–2449.

[191] B. Wang, H. Wang, H. Li, C. Zeng, J. G. Hou and X. Xiao, *Phys. Rev. B*, 2000, **63**, 035403.

[192] I. Swart, L. Gross and P. Liljeroth, *Chem. Commun.*, 2011, **47**, 9011–9023.

[193] L. Liu, T. Dienel, R. Widmer and O. Gröning, *ACS Nano*, 2015, **9**, 10125–10132.

[194] S. W. Wu, G. V. Nazin, X. Chen, X. H. Qiu and W. Ho, *Phys. Rev. Lett.*, 2004, **93**, 236802.

[195] J. W. Gadzuk, *Phys. Rev. B*, 1991, **44**, 13466–13477.

[196] H. Park, J. Park, A. K. L. Lim, E. H. Anderson, A. P. Alivisatos and P. L. McEuen, *Nature*, 2000, **407**, 57–60.

[197] X. H. Qiu, G. V. Nazin and W. Ho, *Science*, 2003, **299**, 542–547.

[198] G. V. Nazin, S. W. Wu and W. Ho, *Proc. Natl. Acad. Sci.*, 2005, **102**, 8832–8837.

[199] X. H. Qiu, G. V. Nazin and W. Ho, *Phys. Rev. Lett.*, 2004, **92**, 206102.

[200] Y. Cui, N. Nilius, H. J. Freund, S. Prada, L. Giordano and G. Pacchioni, *Phys. Rev. B*, 2013, **88**, 205421.

[201] J. Repp, G. Meyer, F. E. Olsson and M. Persson, *Science*, 2004, **305**, 493–495.

[202] A. Bryant, D. P. Smith and C. F. Quate, *Appl. Phys. Lett.*, 1986, **48**, 832–834.

[203] C. J. Chen, *Introduction to Scanning Tunneling Microscopy*, Oxford University Press, 2nd edn., 2008, pp. 1–91.

[204] C. Wittneven, R. Dombrowski, S. H. Pan and R. Wiesendanger, *Rev. Sci. Instrum.*, 1997, **68**, 3806–3810.

[205] Y. J. Song, A. F. Otte, V. Shvarts, Z. Zhao, Y. Kuk, S. R. Blankenship, A. Band, F. M. Hess and J. A. Stroscio, *Rev. Sci. Instrum.*, 2010, **81**, 121101.

[206] J. P. Ibe, P. P. Bey, S. L. Brandow, R. A. Brizzolara, N. A. Burnham, D. P. DiLella, K. P. Lee, C. R. K. Marrian and R. J. Colton, *J. Vac. Sci. Technol. A*, 1990, **8**, 3570–3575.

[207] B. Naydenov, P. Ryan, L. C. Teague and J. J. Boland, *Phys. Rev. Lett.*, 2006, **97**, 098304.

[208] A. Y. Cho and J. R. Arthur, *Prog. Solid State Chem.*, 1975, **10**, 157–191.

[209] K. F. Jensen, in *Microelectron. Process. Chem. Eng. Asp.*, ACS Publications, 1989, ch. 5, pp. 199–263.

[210] A. Koma, *Prog. Cryst. Growth Charact. Mater.*, 1995, **30**, 129–152.

[211] L. Grill, *J. Phys. Condens. Matter*, 2010, **22**, 084023.

[212] L. Grill, M. Dyer, L. Lafferentz, M. Persson, M. V. Peters and S. Hecht, *Nat. Nanotechnol.*, 2007, **2**, 687–691.

[213] M. Bieri, M. Treier, J. Cai, K. Aït-Mansour, P. Ruffieux, O. Gröning, P. Gröning, M. Kastler, R. Rieger, X. Feng, K. Müllen and R. Fasel, *Chem. Commun.*, 2009, 6919–6921.

[214] J. Cai, P. Ruffieux, R. Jaafar, M. Bieri, T. Braun, S. Blankenburg, M. Muoth, A. P. Seitsonen, M. Saleh, X. Feng, K. Müllen and R. Fasel, *Nature*, 2010, **466**, 470–473.

[215] J. Liu, P. Ruffieux, X. Feng, K. Müllen and R. Fasel, *Chem. Commun.*, 2014, **50**, 11200–11203.

[216] M. Ammon, T. Sander and S. Maier, *J. Am. Chem. Soc.*, 2017, **139**, 12976–12984.

[217] M. Dole, L. L. Mack, R. L. Hines, D. O. Chemistry, R. C. Mobley, L. D. Ferguson and M. B. Alice, *J. Chem. Phys.*, 1968, **49**, 2240–2249.

[218] J. B. Fenn, M. Mann, C. K. Meng, S. F. Wong and C. M. Whitehouse, *Science*, 1989, **246**, 64–71.

[219] S. Rauschenbach, M. Ternes, L. Harnau and K. Kern, *Annu. Rev. Anal. Chem.*, 2016, **9**, 473–498.

[220] S. R. Forrest, *Chem. Rev.*, 1997, **97**, 1793–1896.

[221] K. Manandhar, T. Ellis, K. T. Park, T. Cai, Z. Song and J. Hrbek, *Surf. Sci.*, 2007, **601**, 3623–3631.

[222] G. Rapenne, L. Grill, T. Zambelli, S. Stojkovic, F. Ample, F. Moresco and C. Joachim, *Chem. Phys. Lett.*, 2006, **431**, 219–222.

[223] T. Kanno, H. Tanaka, T. Nakamura, H. Tabata and T. Kawai, *Jpn. J. Appl. Phys.*, 1999, **38**, L606–L607.

[224] A. Saywell, J. K. Sprafke, L. J. Esdaile, A. J. Britton, A. Rienzo, H. L. Anderson, J. N. O'Shea and P. H. Beton, *Angew. Chemie - Int. Ed.*, 2010, **49**, 9136–9139.

[225] R. C. Quardokus, N. A. Wasio, R. P. Forrest, C. S. Lent, S. A. Corcelli, J. A. Christie, K. W. Henderson and S. Alex Kandel, *Phys. Chem. Chem. Phys.*, 2013, **15**, 6973–6981.

[226] H. Kim, W. J. Son, W. J. Jang, J. K. Yoon, S. Han and S. J. Kahng, *Phys. Rev. B*, 2009, **80**, 245402.

[227] S. B. Lei, C. Wang, S. X. Yin, H. N. Wang, F. Xi, H. W. Liu, B. Xu, L. J. Wan and C. L. Bai, *J. Phys. Chem. B*, 2001, **105**, 10838–10841.

[228] F. Buchner, V. Schwald, K. Comanici, H. P. Steinrück and H. Marbach, *ChemPhysChem*, 2007, **8**, 241–243.

[229] R. J. Beuhler, E. Flanigan, L. J. Greene and L. Friedman, *J. Am. Chem. Soc.*, 1974, **96**, 3990–3999.

[230] H. J. Räder, A. Rouhanipour, A. M. Talarico, V. Palermo, P. Samorì and K. Müllen, *Nat. Mater.*, 2006, **5**, 276–280.

[231] R. Bernard, V. Hue, P. Reiss, F. Chandezon, P. Jegou, S. Palacin, G. Dujardin and G. Comtet, *J. Phys. Condens. Matter*, 2004, **16**, 7565–7579.

[232] P. M. Albrecht and J. W. Lyding, *Appl. Phys. Lett.*, 2003, **83**, 5029–5031.

[233] S. Clair, C. Rabot, Y. Kim and M. Kawai, *J. Vac. Sci. Technol. B*, 2007, **25**, 1143.

[234] Y. Terada, B. K. Choi, S. Heike, M. Fujimori and T. Hashizume, *Nano Lett.*, 2003, **3**, 527–531.

[235] L. Grill, I. Stass, K. H. Rieder and F. Moresco, *Surf. Sci.*, 2006, **600**, L143–L147.

[236] J. Laskin, P. Wang, O. Hadjar, J. H. Futrell, J. Alvarez and R. G. Cooks, *Int. J. Mass Spectrom.*, 2007, **265**, 237–243.

[237] G. E. Johnson, T. Priest and J. Laskin, *ACS Nano*, 2012, **6**, 573–582.

[238] K. D. D. Gunaratne, G. E. Johnson, A. Andersen, D. Du, W. Zhang, V. Prabhakaran, Y. Lin and J. Laskin, *J. Phys. Chem. C*, 2014, **118**, 27611–27622.

[239] M. S. B. Munson and F. H. Field, *J. Am. Chem. Soc.*, 1966, **88**, 2621–2630.

[240] D. I. Carroll, I. Dzidic, R. N. Stillwell, M. G. Horning and E. C. Horning, *Anal. Chem.*, 1974, **46**, 706–710.

[241] M. Barber, R. S. Bordoli, R. D. Sedgwick and A. N. Tyler, *J. Chem. Soc. Chem. Commun.*, 1981, 325–327.

[242] F. Hillenkamp, M. Karas, R. C. Beavis and B. T. Chait, *Anal. Chem.*, 1991, **63**, 1193A–1203A.

[243] J. B. Fenn, *Angew. Chemie - Int. Ed.*, 2003, **42**, 3871–3894.

[244] G. Siuzdak, B. Bothner, M. Yeager, C. Brugidou, C. M. Fauquet, K. Hoey and C. M. Chang, *Chem. Biol.*, 1996, **3**, 45–48.

[245] Z. X. Nie, Y. K. Tzeng, H. C. Chang, C. C. Chiu, C. Y. Chang, C. M. Chang and M. H. Tao, *Angew. Chemie - Int. Ed.*, 2006, **45**, 8131–8134.

[246] H.-C. Chang, *Annu. Rev. Anal. Chem.*, 2009, **2**, 169–185.

[247] L. P. Smith, W. E. Parkins and A. T. Forrester, *Phys. Rev.*, 1947, **72**, 989–1002.

[248] D. Carswell and J. Milsted, *J. Nucl. Energy*, 1957, **4**, 51–54.

[249] C. H. Chen, E. M. Kelder and J. Schoonman, *J. Mater. Sci.*, 1996, **31**, 5437–5442.

[250] J. Sobota and G. Sorensen, *Tribol. Lett.*, 1997, **3**, 161–164.

[251] K. Nakaso, B. Han, K. H. Ahn, M. Choi and K. Okuyama, *J. Aerosol Sci.*, 2003, **34**, 869–881.

[252] A. Jaworek, *Powder Technol.*, 2007, **176**, 18–35.

[253] B. Hoyer, G. Sørensen, N. Jensen, D. B. Nielsen and B. Larsen, *Anal. Chem.*, 1996, **68**, 3840–3844.

[254] N. V. Avseenko, T. Y. Morozova, F. I. Ataullakhanov and V. N. Morozov, *Anal. Chem.*, 2001, **73**, 6047–6052.

[255] V. N. Morozov, *J. Aerosol Sci.*, 2011, **42**, 341–354.

[256] T. Thundat, R. J. Warmack, D. P. Allison and T. L. Ferrell, *Ultramicroscopy*, 1992, **42-44**, 1083–1087.

[257] V. Franchetti, B. H. Solka, W. E. Baitinger, J. W. Amy and R. G. Cooks, *Int. J. Mass Spectrom. Ion Phys.*, 1977, **23**, 29–35.

[258] J. C. Swarbrick, J. B. Taylor and J. N. O'Shea, *Appl. Surf. Sci.*, 2006, **252**, 5622–5626.

[259] M. G. Ikonomou, A. T. Blades and P. Kebarle, *Anal. Chem.*, 1991, **63**, 1989–1998.

[260] L. B. Loeb, A. F. Kip, G. G. Hudson and W. H. Bennett, *Phys. Rev.*, 1941, **60**, 714–722.

[261] R. J. Pfeifer and C. D. Hendricks Jr, *AIAA J.*, 1968, **6**, 496–502.

[262] R. B. Cole, *J. Mass Spectrom.*, 2000, **35**, 763–772.

[263] M. Cloupeau and B. Prunet-Foch, *J. Electrostat.*, 1990, **25**, 165–184.

[264] J. Zeleny, *Phys. Rev.*, 1914, **3**, 69–91.

[265] J. Zeleny, *Phys. Rev.*, 1917, **10**, 1–6.

[266] G. Taylor, *Proc. R. Soc. A Math. Phys. Eng. Sci.*, 1964, **280**, 383–397.

[267] J. Fernández de la Mora, *Annu. Rev. Fluid Mech.*, 2007, **39**, 217–243.

[268] J. W. S. Rayleigh, *London, Edinburgh, Dublin Philos. Mag. J. Sci.*, 1892, **34**, 177–180.

[269] B. Vonnegut and R. L. Neubauer, *J. Colloid Sci.*, 1952, **7**, 616–622.

[270] J. W. S. Rayleigh, *London, Edinburgh, Dublin Philos. Mag. J. Sci.*, 1882, **14**, 184–186.

[271] M. Cloupeau and B. Prunet-Foch, *J. Electrostat.*, 1989, **22**, 135–159.

[272] A. Gomez and K. Tang, *Phys. Fluids*, 1994, **6**, 404–414.

[273] D. Duft, H. Lebius, B. A. Huber, C. Guet and T. Leisner, *Phys. Rev. Lett.*, 2002, **89**, 084503.

[274] G. Schmelzeisen-Redeker, L. Bütfering and F. W. Röllgen, *Int. J. Mass Spectrom. Ion Process.*, 1989, **90**, 139–150.

[275] J. V. Iribarne and B. A. Thomson, *J. Chem. Phys.*, 1976, **64**, 2287–2294.

[276] B. A. Thomson and J. V. Iribarne, *J. Chem. Phys.*, 1979, **71**, 4451–4463.

[277] S. Nguyen and J. B. Fenn, *Proc. Natl. Acad. Sci.*, 2007, **104**, 1111–1117.

[278] B. N. Pramanik, P. L. Bartner, U. A. Mirza, Y.-H. Liu and A. K. Ganguly, *J. Mass Spectrom.*, 1998, **33**, 911–920.

[279] C. Hamann, R. Woltmann, I.-P. Hong, N. Hauptmann, S. Karan and R. Berndt, *Rev. Sci. Instrum.*, 2011, **82**, 033903.

[280] Z. Ouyang, Z. Takáts, T. A. Blake, B. Gologan, A. J. Guymon, J. M. Wiseman, J. C. Oliver, V. J. Davisson and R. G. Cooks, *Science*, 2003, **301**, 1351–1354.

[281] V. H. Wysocki, K. E. Joyce, C. M. Jones and R. L. Beardsley, *J. Am. Soc. Mass Spectrom.*, 2008, **19**, 190–208.

[282] V. Grill, J. Shen, C. Evans and R. G. Cooks, *Rev. Sci. Instrum.*, 2001, **72**, 3149–3179.

[283] F. Pepi, A. Tata, S. Garzoli, P. Giacomello, R. Ragno, A. Patsilinakos, M. Fusco, A. D'Annibale, S. Cannistraro, C. Baldacchini, G. Favero, M. Frasconi and F. Mazzei, *J. Phys. Chem. C*, 2011, **115**, 4863–4871.

[284] G. Dubey, R. Urcuyo, S. Abb, G. Rinke, M. Burghard, S. Rauschenbach and K. Kern, *J. Am. Chem. Soc.*, 2014, **136**, 13482–13485.

[285] H. Tong, D. Bell, K. Tabei and M. M. Siegel, *J. Am. Soc. Mass Spectrom.*, 1999, **10**, 1174–1187.

[286] C. León, C. Sürgers, M. Mayor, M. Marz, R. Hoffmann and H. V. Löhneysen, *J. Phys. Chem. C*, 2009, **113**, 14335–14340.

[287] B. Naydenov, S. Torsney, A. S. Bonilla, M. El Garah, A. Ciesielski, A. Gualandi, L. Mengozzi, P. G. Cozzi, R. Gutierrez, P. Samorì, G. Cuniberti and J. J. Boland, *Langmuir*, 2018, **34**, 7698–7707.

[288] A. Santana-Bonilla, *Ph.D. Thesis*, Technische Universität Dresden, 2016.

[289] J. M. Lehn, *Science*, 2002, **295**, 2400–2403.

[290] T. Steiner, *Angew. Chemie - Int. Ed.*, 2002, **41**, 48–76.

[291] G. A. Jeffrey and W. Saenger, *Hydrogen Bonding in Biological Structures*, Springer-Verlag, 1st edn., 1991, pp. 1–49.

[292] C. L. Perrin and J. B. Nielson, *Annu. Rev. Phys. Chem.*, 1997, **48**, 511–44.

[293] S. Gronert, *J. Am. Chem. Soc.*, 1993, **115**, 10258–10266.

[294] J. A. Howard, V. J. Hoy, D. O'Hagan and G. T. Smith, *Tetrahedron*, 1996, **52**, 12613–12622.

[295] G. Gilli, F. Bellucci, V. Ferretti and V. Bertolasi, *J. Am. Chem. Soc.*, 1989, **111**, 1023–1028.

[296] V. Bertolasi, P. Gilli, V. Ferretti and G. Gilli, *J. Am. Chem. Soc.*, 1991, **113**, 4917–4925.

[297] T. Yokoyama, S. Yokoyama, T. Kamikado, Y. Okuno and S. Mashiko, *Nature*, 2001, **413**, 619–621.

[298] L. Smykalla, P. Shukrynau, C. Mende, T. Rüffer, H. Lang and M. Hietschold, *Surf. Sci.*, 2014, **628**, 132–140.

[299] Q. Yuan, Y. Xing and E. Borguet, *J. Am. Chem. Soc.*, 2010, **132**, 5054–5060.

[300] A. G. Slater, Y. Hu, L. Yang, S. P. Argent, W. Lewis, M. O. Blunt and N. R. Champness, *Chem. Sci.*, 2015, **6**, 1562–1569.

[301] S. Yoshimoto, N. Yokoo, T. Fukuda, N. Kobayashi and K. Itaya, *Chem. Commun.*, 2006, 500–502.

[302] V. V. Korolkov, S. A. Svatek, A. Summerfield, J. Kerfoot, L. Yang, T. Taniguchi, K. Watanabe, N. R. Champness, N. A. Besley and P. H. Beton, *ACS Nano*, 2015, **9**, 10347–10355.

[303] M. El Garah, A. Santana Bonilla, A. Ciesielski, A. Gualandi, L. Mengozzi, A. Fiorani, M. Iurlo, M. Marcaccio, R. Gutierrez, S. Rapino, M. Calvaresi, F. Zerbetto, G. Cuniberti, P. G. Cozzi, F. Paolucci and P. Samorì, *Nanoscale*, 2016, **8**, 13678–13686.

[304] E. S. Schmidt, T. S. Calderwood and T. C. Bruice, *Inorg. Chem.*, 1986, **25**, 3718–3720.

[305] P. J. de Rege, S. A. Williams and M. J. Therien, *Science*, 1995, **269**, 1409–1413.

[306] G. Canzi, J. C. Goeltz, J. S. Henderson, R. E. Park, C. Maruggi and C. P. Kubiak, *J. Am. Chem. Soc.*, 2014, **136**, 1710–1713.

[307] H. Sun, J. Steeb and A. E. Kaifer, *J. Am. Chem. Soc.*, 2006, **128**, 2820–2821.

[308] D. L. Sun, S. V. Rosokha, S. V. Lindeman and J. K. Kochi, *J. Am. Chem. Soc.*, 2003, **125**, 15950–15963.

[309] C. Kittel, *Introduction to Solid State Physics*, Wiley, 8th edn., 1976, p. 20.

[310] U. Harten, A. M. Lahee, J. P. Toennies and C. Wöll, *Phys. Rev. Lett.*, 1985, **54**, 2619–2622.

[311] Y. Okwamoto and K. H. Bennemann, *Surf. Sci.*, 1987, **186**, 511–522.

[312] C. Wöll, S. Chiang, R. J. Wilson and P. H. Lippel, *Phys. Rev. B*, 1989, **39**, 7988–7991.

[313] V. M. Hallmark, S. Chiang, J. F. Rabolt, J. D. Swalen and R. J. Wilson, *Phys. Rev. Lett.*, 1987, **59**, 2879–2882.

[314] J. Barth, H. Brune, G. Ertl and R. Behm, *Phys. Rev. B*, 1990, **42**, 9307–9318.

[315] F. Hanke and J. Björk, *Phys. Rev. B*, 2013, **87**, 235422.

[316] C. Ruggieri, S. Rangan, R. A. Bartynski and E. Galoppini, *J. Phys. Chem. C*, 2015, **119**, 6101–6110.

[317] W. Shockley, *Phys. Rev.*, 1939, **56**, 317–323.

[318] P. Heimann, H. Neddermeyer and H. F. Roloff, *J. Phys. C Solid State Phys.*, 1977, **10**, L17.

[319] W. Chen, V. Madhavan, T. Jamneala and M. F. Crommie, *Phys. Rev. Lett.*, 1998, **80**, 1469–1472.

[320] P. O. Gartland and B. J. Slagsvold, *Phys. Rev. B*, 1975, **12**, 4047–4058.

[321] M. F. Crommie, C. P. Lutz and D. M. Eigler, *Nature*, 1993, **363**, 524–527.

[322] B. W. Heinrich, L. Limot, M. V. Rastei, C. Iacovita, J. P. Bucher, D. M. Djimbi, C. Massobrio and M. Boero, *Phys. Rev. Lett.*, 2011, **107**, 216801.

[323] *CRC Handbook of Chemistry and Physics*, ed. D. R. Lide, CRC Press, 94th edn., 2013, pp. 12–114.

[324] I. Goldberg, *Chem. Commun.*, 2005, 1243–1254.

[325] P. Dastidar, Z. Stein, I. Goldberg and C. E. Strouse, *Supramol. Chem.*, 1996, **7**, 257–270.

[326] Y. Diskin-Posner and I. Goldberg, *Chem. Commun.*, 1999, 1961–1962.

[327] M. Ormaza, P. Abufager, N. Bachellier, R. Robles, M. Verot, T. Le Bahers, M. L. Bocquet, N. Lorente and L. Limot, *J. Phys. Chem. Lett.*, 2015, **6**, 395–400.

[328] A. Vargas-Caamal, S. Pan, F. Ortiz-Chi, J. L. Cabellos, R. A. Boto, J. Contreras-Garcia, A. Restrepo, P. K. Chattaraj and G. Merino, *Phys. Chem. Chem. Phys.*, 2016, **550**, 550–556.

[329] F. Buchner, E. Zillner, M. Röckert, S. Gläel, H. P. Steinrück and H. Marbach, *Chem. - A Eur. J.*, 2011, **17**, 10226–10229.

[330] D. A. Dixon, K. D. Dobbs and J. J. Valentini, *J. Phys. Chem.*, 1994, **98**, 13435–13439.

[331] R. Vargas, J. Garza, R. A. Friesner, H. Stern, B. P. Hay and D. A. Dixon, *J. Phys. Chem. A*, 2001, **105**, 4963–4968.

[332] C. H. Langley and N. L. Allinger, *J. Phys. Chem. A*, 2003, **107**, 5208–5216.

[333] S. Mathieu and G. Trinquier, *Phys. Chem. Chem. Phys.*, 2009, **11**, 8183–8190.

[334] K. Leung, S. B. Rempe, P. A. Schultz, E. M. Sproviero, V. S. Batista, M. E. Chandross and C. J. Medforth, *J. Am. Chem. Soc.*, 2006, **128**, 3659–3668.

[335] S. Müllegger, M. Rashidi, T. Lengauer, E. Rauls, W. G. Schmidt, G. Knör, W. Schöfberger and R. Koch, *Phys. Rev. B*, 2011, **83**, 1–4.

[336] L. Scudiero, D. E. Barlow and K. W. Hipps, *J. Phys. Chem. B*, 2000, **104**, 11899–11905.

[337] K. W. Hipps, L. Scudiero, D. E. Barlow and M. P. Cooke, *J. Am. Chem. Soc.*, 2002, **124**, 2126–2127.

[338] W. Deng and K. W. Hipps, *J. Phys. Chem. B*, 2003, **107**, 10736–10740.

[339] K. Suto, S. Yoshimoto and K. Itaya, *Langmuir*, 2006, **22**, 10766–10776.

[340] W. Auwärter, A. Weber-Bargioni, S. Brink, A. Riemann, A. Schiffrin, M. Ruben and J. V. Barth, *ChemPhysChem*, 2007, **8**, 250–254.

[341] J. Brede, M. Linares, S. Kuck, J. Schwöbel, A. Scarfato, S. H. Chang, G. Hoffmann, R. Wiesendanger, R. Lensen, P. H. Kouwer, J. Hoogboom, A. E. Rowan, M. Bröring, M. Funk, S. Stafström, F. Zerbetto and R. Lazzaroni, *Nanotechnology*, 2009, **20**, 275602.

[342] G. Rojas, X. Chen, C. Bravo, J. H. Kim, J. S. Kim, J. Xiao, P. A. Dowben, Y. Gao, X. C. Zeng, W. Choe and A. Enders, *J. Phys. Chem. C*, 2010, **114**, 9408–9415.

[343] F. Buchner, E. Zillner, M. Röckert, S. Gläel, H. P. Steinrück and H. Marbach, *Chem. - A Eur. J.*, 2011, **17**, 10226–10229.

[344] X. L. Zhang, J. W. Jiang, Y. T. Liu, S. T. Lou, C. L. Gao and Q. Y. Jin, *Sci. Rep.*, 2016, **6**, 22756.

[345] T. Lukasczyk, K. Flechtner, L. R. Merte, N. Jux, F. Maier, J. M. Gottfried and H. P. Steinrück, *J. Phys. Chem. C*, 2007, **111**, 3090–3098.

[346] V. Iancu, A. Deshpande and S.-W. Hla, *Nano Lett.*, 2006, **6**, 820–823.

[347] V. Iancu, A. Deshpande and S.-W. Hla, *Phys. Rev. Lett.*, 2006, **97**, 266603.

[348] Crljen, P. Lazić, D. Šokčević and R. Brako, *Phys. Rev. B*, 2003, **68**, 195411.

[349] F. Buchner, J. Xiao, E. Zillner, M. Chen, M. Röckert, S. Ditze, M. Stark, H. P. Steinrück, J. M. Gottfried and H. Marbach, *J. Phys. Chem. C*, 2011, **115**, 24172–24177.

[350] C. M. Doyle, S. A. Krasnikov, N. N. Sergeeva, A. B. Preobrajenski, N. A. Vinogradov, Y. N. Sergeeva, M. O. Senge and A. A. Cafolla, *Chem. Commun.*, 2011, **47**, 12134.

[351] K. Diller, F. Klappenberger, F. Allegretti, A. C. Papageorgiou, S. Fischer, A. Wiengarten, S. Joshi, K. Seufert, D. Écija, W. Auwärter and J. V. Barth, *J. Chem. Phys.*, 2013, **138**, 154710.

[352] G. Rojas, S. Simpson, X. Chen, D. A. Kunkel, J. Nitz, J. Xiao, P. A. Dowben, E. Zurek and A. Enders, *Phys. Chem. Chem. Phys.*, 2012, **14**, 4971–4976.

[353] V. N. Nemykin, G. T. Rohde, C. D. Barrett, R. G. Hadt, J. R. Sabin, G. Reina, P. Galloni and B. Floris, *Inorg. Chem.*, 2010, **49**, 7497–7509.

[354] T. Yokoyama, S. Yokoyama, T. Kamikado and S. Mashiko, *J. Chem. Phys.*, 2001, **115**, 3814–3818.

[355] L. Scudiero, D. E. Barlow, U. Mazur and K. W. Hipps, *J. Am. Chem. Soc.*, 2001, **123**, 4073–4080.

[356] S. Müllegger, W. Schöfberger, M. Rashidi, L. M. Reith and R. Koch, *J. Am. Chem. Soc.*, 2009, **131**, 17740–17741.

[357] Q. Li, S. Yamazaki, T. Eguchi, Y. Hasegawa, H. Kim, S. J. Kahng, J. Feng Jia and Q. K. Xue, *Nanotechnology*, 2008, **19**, 465707.

[358] Q. Zhang, X. Zheng, G. Kuang, W. Wang, L. Zhu, R. Pang, X. Shi, X. Shang, X. Huang, P. N. Liu and N. Lin, *J. Phys. Chem. Lett.*, 2017, **8**, 1241–1247.

[359] A. Savin, R. Nesper, S. Wengert and T. F. Fässler, *Angew. Chemie - Int. Ed.*, 1997, **36**, 1808–1832.

[360] K. Kandasamy, S. J. Shetty, P. N. Puntambekar, T. S. Srivastava, T. Kundu and B. P. Singh, *J. Porphyr. Phthalocyanines*, 1999, **3**, 81–86.

[361] M.-S. Liao and S. Scheiner, *J. Chem. Phys.*, 2002, **117**, 205–219.

[362] G. Zhang and C. B. Musgrave, *J. Phys. Chem. A*, 2007, **111**, 1554–1561.

[363] S. G. DiMagno, A. K. Wertsching and C. R. Ross, *J. Am. Chem. Soc.*, 1995, **117**, 8279–8280.

[364] W. Auwärter, K. Seufert, F. Klappenberger, J. Reichert, A. Weber-Bargioni, A. Verdini, D. Cvetko, M. Dell'Angela, L. Floreano, A. Cossaro, G. Bavdek, A. Morgante, A. P. Seitsonen and J. V. Barth, *Phys. Rev. B*, 2010, **81**, 1–14.

[365] A. Terentjevs, M. P. Steele, M. L. Blumenfeld, N. Ilyas, L. L. Kelly, E. Fabiano, O. L. A. Monti and F. Della Sala, *J. Phys. Chem. C*, 2011, **115**, 21128–21138.

[366] K. Lauwaet, K. Schouteden, E. Janssens, C. Van Haesendonck, P. Lievens, M. I. Trioni, L. Giordano and G. Pacchioni, *Phys. Rev. B*, 2012, **85**, 245440.

[367] L. Romaner, D. Nabok, P. Puschnig, E. Zojer and C. Ambrosch-Draxl, *New J. Phys.*, 2009, **11**, 053010.

[368] F. Matino, G. Schull, F. Kohler, S. Gabutti, M. Mayor and R. Berndt, *Proc. Natl. Acad. Sci.*, 2011, **108**, 961–964.

[369] L. Gross, F. Moresco, L. Savio, A. Gourdon, C. Joachim and K. H. Rieder, *Phys. Rev. Lett.*, 2004, **93**, 056103.

[370] F. Matino, G. Schull, F. Köhler, S. Gabutti, M. Mayor and R. Berndt, *Proc. Natl. Acad. Sci.*, 2011, **108**, 961–964.

[371] J. A. Smerdon, M. Bode, N. P. Guisinger and J. R. Guest, *Phys. Rev. B*, 2011, **84**, 165436.

[372] Z. H. Cheng, S. X. Du, N. Jiang, Y. Y. Zhang, W. Guo, W. A. Hofer and H. J. Gao, *Surf. Sci.*, 2011, **605**, 415–418.

[373] S. Schintke, S. Messerli, M. Pivetta, F. Patthey, L. Libioulle, M. Stengel, a. De Vita and W. D. Schneider, *Phys. Rev. Lett.*, 2001, **87**, 276801.

[374] N. Nilius, T. M. Wallis and W. Ho, *Phys. Rev. Lett.*, 2003, **90**, 046808.

[375] K. J. Franke, G. Schulze, N. Henningsen, I. Fernández-Torrente, J. I. Pascual, S. Zarwell, K. Rück-Braun, M. Cobian and N. Lorente, *Phys. Rev. Lett.*, 2008, **100**, 036807.

[376] T. G. Gopakumar, T. Brumme, J. Kröger, C. Toher, G. Cuniberti and R. Berndt, *J. Phys. Chem. C*, 2011, **115**, 12173–12179.

[377] N. Nilius, M. Kulawik, H. P. Rust and H. J. Freund, *Phys. Rev. B*, 2004, **69**, 121401.

[378] P. Liljeroth, J. Repp and G. Meyer, *Science*, 2007, **317**, 1203–1206.

[379] S. W. Wu, N. Ogawa and W. Ho, *Science*, 2006, **312**, 1362–1365.

[380] T. Leoni, O. Guillermet, H. Walch, V. Langlais, A. Scheuermann, J. Bonvoisin and S. Gauthier, *Phys. Rev. Lett.*, 2011, **106**, 216103.

[381] F. Mohn, J. Repp, L. Gross, G. Meyer, M. S. Dyer and M. Persson, *Phys. Rev. Lett.*, 2010, **105**, 266102.

[382] P. Liljeroth, I. Swart, S. Paavilainen, J. Repp and G. Meyer, *Nano Lett.*, 2010, **10**, 2475–2479.

[383] K. Glöckler, M. Sokolowski, A. Soukopp and E. Umbach, *Phys. Rev. B*, 1996, **54**, 7705.

[384] J. Viernow, D. Petrovykh, a. Kirakosian, J.-L. Lin, F. Men, M. Henzler and F. Himpsel, *Phys. Rev. B*, 1999, **59**, 10356–10361.

[385] J. Repp, S. Fölsch, G. Meyer and K. H. Rieder, *Phys. Rev. Lett.*, 2001, **86**, 252–255.

[386] R. Arita, Y. Tanida, K. Kuroki and H. Aoki, *Phys. Rev. B*, 2004, **69**, 115424.

[387] C. F. Hirjibehedin, C. P. Lutz and A. J. Heinrich, *Science*, 2006, **312**, 1021–1024.

[388] T. Choi, C. D. Ruggiero and J. A. Gupta, *J. Vac. Sci. Technol. B*, 2009, **27**, 887–890.

[389] V. C. Zoldan, R. Faccio, C. Gao and A. A. Pasa, *J. Phys. Chem. C*, 2013, **117**, 15984–15990.

[390] T. Bertrams, A. Brodde and H. Neddermeyer, *J. Vac. Sci. Technol. B*, 1994, **12**, 2122–2124.

[391] M. C. Gallagher, M. S. Fyfield, J. P. Cowin and S. A. Joyce, *Surf. Sci.*, 1995, **339**, L909–L913.

[392] T. Bertrams and H. Neddermeyer, *J. Vac. Sci. Technol. B*, 1996, **14**, 1141–1144.

[393] M. Kulawik, N. Nilius, H.-P. Rust and H.-J. Freund, *Phys. Rev. Lett.*, 2003, **91**, 256101.

[394] X. L. Zhang, L. G. Chen, P. Lv, H. Y. Gao, S. J. Wei, Z. C. Dong and J. G. Hou, *Appl. Phys. Lett.*, 2008, **92**, 223118.

[395] J. Repp, P. Liljeroth and G. Meyer, *Nat. Phys.*, 2010, **6**, 975–979.

[396] N. Pavliček, A. Mistry, Z. Majzik, N. Moll, G. Meyer, D. J. Fox and L. Gross, *Nat. Nanotechnol.*, 2017, **12**, 308–311.

[397] A. Bellec, F. Ample, D. Riedel, G. Dujardin and C. Joachim, *Nano Lett.*, 2009, **9**, 144–147.

[398] U. Barjenbruch, S. Fölsch and M. Henzler, *Surf. Sci.*, 1989, **211-212**, 749–758.

[399] C. Schwennicke, J. Schimmelpfennig and H. Pfnür, *Surf. Sci.*, 1993, **293**, 57–66.

[400] R. Bennewitz, V. Barwich, M. Bammerlin, C. Loppacher, M. Guggisberg, A. Baratoff, E. Meyer and H. Gu, *Surf. Sci.*, 1999, **438**, 289–296.

[401] M. Wagner, F. R. Negreiros, L. Sementa, G. Barcaro, S. Surnev, A. Fortunelli and F. P. Netzer, *Phys. Rev. Lett.*, 2013, **110**, 216101.

[402] S. Fölsch, A. Helms, S. Zöphel, J. Repp, G. Meyer and K. H. Rieder, *Phys. Rev. Lett.*, 2000, **84**, 123–126.

[403] E. Le Moal, M. Müller, O. Bauer and M. Sokolowski, *Surf. Sci.*, 2009, **603**, 2434–2444.

[404] W. Hebenstreit, J. Redinger, Z. Horozova, M. Schmid, R. Podloucky and P. Varga, *Surf. Sci.*, 1999, **424**, L321–L328.

[405] X. Sun, M. P. Felicissimo, P. Rudolf and F. Silly, *Nanotechnology*, 2008, **19**, 495307.

[406] F. Matthaei, S. Heidorn, K. Boom, C. Bertram, A. Safiei, J. Henzl and K. Morgenstern, *J. Phys. Condens. Matter*, 2012, **24**, 354006.

[407] J. Repp and G. Meyer, *Appl. Phys. A*, 2006, **85**, 399–406.

[408] Z. Li, H.-Y. T. Chen, K. Schouteden, E. Janssens, C. Van Haesendonck, P. Lievens and G. Pacchioni, *Nanoscale*, 2015, **7**, 2366–2373.

[409] K. Lauwaet, K. Schouteden, E. Janssens, C. Van Haesendonck and P. Lievens, *J. Phys. Condens. Matter*, 2012, **24**, 475507.

[410] J. Repp, G. Meyer and K. H. Rieder, *Phys. Rev. Lett.*, 2004, **92**, 036803.

[411] F. E. Olsson, M. Persson, A. G. Borisov, J. P. Gauyacq, J. Lagoute and S. Fölsch, *Phys. Rev. Lett.*, 2004, **93**, 206803.

[412] J. Repp, G. Meyer, S. Paavilainen, F. E. Olsson and M. Persson, *Phys. Rev. Lett.*, 2005, **95**, 1–4.

[413] G. Paniconi, Z. Stoeva, H. Doberstein, R. I. Smith, B. L. Gallagher and D. H. Gregory, *Solid State Sci.*, 2007, **9**, 907–913.

[414] H. Niehus, R. Spitzl, K. Besocke and G. Comsa, *Phys. Rev. B*, 1991, **43**, 12619–12622.

[415] F. M. Leibsle, C. F. J. Flipse and A. W. Robinson, *Phys. Rev. B*, 1993, **47**, 15865–15868.

[416] S. M. Driver and D. P. Woodruff, *Surf. Sci.*, 1999, **442**, 1–8.

[417] G. Ceballos, N. Haack, H. Wende, R. Püttner, K. Baberschke and D. Arvanitis, *Surf. Sci.*, 2000, **448**, 261–268.

[418] B. M. W. Trapnell, *Proc. R. Soc. A Math. Phys. Eng. Sci.*, 1953, **218**, 566–577.

[419] R. N. Lee and H. E. Farnsworth, *Surf. Sci.*, 1965, **3**, 461–479.

[420] R. Franchy, M. Wuttig and H. Ibach, *Zeitschrift für Phys. B Condens. Matter*, 1986, **64**, 453–459.

[421] T. Lederer, D. Arvanitis, M. Tischer, G. Comelli, L. Tröger and K. Baberschke, *Phys. Rev. B*, 1993, **48**, 11277–11286.

[422] F. M. Leibsle, C. F. J. Flipse and A. W. Robinson, *Phys. Rev. B*, 1993, **47**, 15865–15868.

[423] H. Yu and K. T. Leung, *J. Vac. Sci. Technol. A*, 1998, **16**, 30–34.

[424] F. M. Leibsle, S. S. Dhesi, S. D. Barrett and A. W. Robinson, *Surf. Sci.*, 1994, **317**, 309–320.

[425] F. Komori, S. Y. Ohno and K. Nakatsuji, *Prog. Surf. Sci.*, 2004, **77**, 1–36.

[426] R. M. Feenstra, J. A. Stroscio, J. Tersoff and A. P. Fein, *Phys. Rev. Lett.*, 1987, **58**, 1192–1195.

[427] D. P. Woodruff, S. L. Hulbert, P. D. Johnson and N. V. Smith, *Phys. Rev. B*, 1985, **31**, 4046–4048.

[428] C. D. Ruggiero, T. Choi and J. A. Gupta, *Appl. Phys. Lett.*, 2007, **91**, 7–10.

[429] T. Choi, M. Badal, S. Loth, J. W. Yoo, C. P. Lutz, A. J. Heinrich, A. J. Epstein, D. G. Stroud and J. A. Gupta, *Nano Lett.*, 2014, **14**, 1196–1201.

[430] A. Soon, L. Wong, B. Delley and C. Stampfl, *Phys. Rev. B*, 2008, **77**, 1–13.

[431] T. Choi, C. Ruggiero and J. Gupta, *Phys. Rev. B*, 2008, **78**, 1–5.

[432] M. Bäumer and H. J. Freund, *Prog. Surf. Sci.*, 1999, **61**, 127–198.

[433] D. Wei-Dong, Z. Han-Jie and B. Shi-Ning, *Chinese Phys. B*, 2010, **19**, 026803.

[434] X. D. Ma, D. I. Bazhanov, O. Fruchart, F. Yildiz, T. Yokoyama, M. Przybylski, V. S. Stepanyuk, W. Hergert and J. Kirschner, *Phys. Rev. Lett.*, 2009, **102**, 3–6.

[435] J. Berger, K. Kośmider, O. Stetsovych, M. Vondráček, P. Hapala, E. J. Spadafora, M. Švec and P. Jelínek, *J. Phys. Chem. C*, 2016, **120**, 21955–21961.

[436] K. Bhattacharjee, X. D. Ma, Y. Q. Zhang, M. Przybylski and J. Kirschner, *Surf. Sci.*, 2012, **606**, 652–658.

[437] M. Stedman, *J. Microsc.*, 1988, **152**, 611–618.

[438] C. Bombis, N. Kalashnyk, W. Xu, E. Lægsgaard, F. Besenbacher, T. R. Linderoth, Besenbacher and T. R. Linderoth, *Small*, 2009, **5**, 2177–2182.

[439] A. Scarfato, S. H. Chang, S. Kuck, J. Brede, G. Hoffmann and R. Wiesendanger, *Surf. Sci.*, 2008, **602**, 677–683.

[440] E. Le Moal, M. Müller, O. Bauer and M. Sokolowski, *Phys. Rev. B*, 2010, **82**, 045301.

[441] L. Ramoino, M. Von Arx, S. Schintke, A. Baratoff, H. J. Güntherodt and T. A. Jung, *Chem. Phys. Lett.*, 2006, **417**, 22–27.

[442] W. Hebenstreit, M. Schmid, J. Redinger, R. Podloucky and P. Varga, *Phys. Rev. Lett.*, 2000, **85**, 5376–5379.

[443] T. Kakudate, M. Nakaya and T. Nakayama, *Thin Solid Films*, 2012, **520**, 2004–2008.

[444] J. Kolodziej, B. Such, P. Czuba, F. Krok, P. Piatkowski, P. Struski, M. Szymonski, R. Bennewitz, S. Schär and E. Meyer, *Surf. Sci.*, 2001, **482-485**, 903–909.

[445] S. R. Saeed, O. P. Sinha, F. Krok and M. Szymonski, *Appl. Surf. Sci.*, 2008, **255**, 1766–1775.

[446] A. Hinaut, B. Eren, R. Steiner, S. Freund, R. Jöhr, T. Glatzel, L. Marot, E. Meyer and S. Kawai, *Phys. Chem. Chem. Phys.*, 2017, **19**, 16251–16256.

[447] A. Hinaut, R. Pawlak, E. Meyer and T. Glatzel, *Beilstein J. Nanotechnol.*, 2015, **6**, 1927–1934.

[448] R. Ryberg, *J. Chem. Phys.*, 1985, **82**, 567–573.

[449] O. Karis, J. Hasselström, N. Wassdahl, M. Weinelt, A. Nilsson, M. Nyberg, L. G. Pettersson, J. Stöhr and M. G. Samant, *J. Chem. Phys.*, 2000, **112**, 8146–8155.

[450] R. González-Moreno, A. Garcia-Lekue, A. Arnau, M. Trelka, J. M. Gallego, R. Otero, A. Verdini, C. Sánchez-Sánchez, P. L. De Andrés, J. Á. Martín-Gago and C. Rogero, *J. Phys. Chem. C*, 2013, **117**, 7661–7668.

[451] M. Furukawa, T. Yamada, S. Katano, M. Kawai, H. Ogasawara and A. Nilsson, *Surf. Sci.*, 2007, **601**, 5433–5440.

[452] P. R. Davies, D. Edwards and D. Richards, *J. Phys. Chem. B*, 2004, **108**, 18630–18639.

[453] S. Joshi, D. Ecija, R. Koitz, M. Iannuzzi, A. P. Seitsonen, J. Hutter, H. Sachdev, S. Vijayaraghavan, F. Bischoff, K. Seufert, J. V. Barth and W. Auwärter, *Nano Lett.*, 2012, **12**, 5821–5828.

[454] N. Garro, A. Cantarero, M. Cardona, T. Ruf, A. Göbel, C. Lin, K. Reimann, S. Rübenacke and M. Steube, *Solid State Commun.*, 1996, **98**, 27–30.

[455] S. Schintke, S. Messerli, M. Pivetta, F. Patthey, L. Libioulle, M. Stengel, A. De Vita and W. D. Schneider, *Phys. Rev. Lett.*, 2001, **87**, 276801.

[456] P. J. Goddard and R. M. Lambert, *Surf. Sci.*, 1977, **67**, 180–194.

[457] D. P. Woodruff, D. L. Seymour, C. F. McConville, C. E. Riley, M. D. Crapper, N. P. Prince and R. G. Jones, *Phys. Rev. Lett.*, 1987, **58**, 1460–1462.

[458] K. Motai, T. Hashizume, H. Lu, D. Jeon, T. Sakurai and H. W. Pickering, *Appl. Surf. Sci.*, 1993, **67**, 246–251.

[459] B. Andryushechkin, K. Eltsov and V. Shevlyuga, *Surf. Sci.*, 2000, **470**, L63–L68.

[460] B. V. Andryushechkin, V. V. Zheltov, V. V. Cherkez, G. M. Zhidomirov, A. N. Klimov, B. Kierren, Y. Fagot-Revurat, D. Malterre and K. N. Eltsov, *Surf. Sci.*, 2015, **639**, 7–12.

[461] S. Torsney, B. Naydenov and J. J. Boland, *Phys. Rev. B*, 2017, **96**, 245411.

[462] M. D. Crapper, C. E. Riley, P. J. Sweeney, C. F. McConville, D. P. Woodruff and R. G. Jones, *Surf. Sci.*, 1987, **182**, 213–230.

[463] M. D. Crapper, C. E. Riley, P. J. J. Sweeney, C. F. McConville, D. P. Woodruff and R. G. Jones, *Europhys. Lett.*, 1986, **2**, 857–861.

[464] M. F. Kadodwala, A. A. Davis, G. Scragg, B. C. C. Cowie, M. Kerkar, D. P. Woodruff and R. G. Jones, *Surf. Sci.*, 1995, **324**, 122–132.

[465] G. Binnig, H. Rohrer, C. Gerber and E. Weibel, *Appl. Phys. Lett.*, 1982, **40**, 178–180.

[466] W. K. Walter, D. E. Manolopoulos and R. G. Jones, *Surf. Sci.*, 1996, **348**, 115–132.

[467] S. Peljhan and A. Kokalj, *J. Phys. Chem. C*, 2009, **113**, 14363–14376.

[468] N. D. Spencer, P. J. Goddard, P. W. Davies, M. Kitson and R. M. Lambert, *J. Vac. Sci. Technol. A*, 1983, **1**, 1554–1555.

[469] R. G. Jones and C. A. Clifford, *Phys. Chem. Chem. Phys.*, 1999, **1**, 5223–5228.

[470] B. V. Andryushechkin, V. V. Cherkez, B. Kierren, Y. Fagot-Revurat, D. Malterre and K. N. Eltsov, *Phys. Rev. B*, 2011, **84**, 205422.

[471] T. V. Pavlova, B. V. Andryushechkin and G. M. Zhidomirov, *J. Phys. Chem. C*, 2016, **120**, 2829–2836.

[472] K. Doll and N. M. Harrison, *Chem. Phys. Lett.*, 2000, **317**, 282–289.

[473] H. Fu, L. Jia, W. Wang and K. Fan, *Surf. Sci.*, 2005, **584**, 187–198.

[474] K. Doll and N. M. Harrison, *Phys. Rev. B*, 2001, **63**, 165410.

[475] Z. Li, K. Schouteden, V. Iancu, E. Janssens, P. Lievens, C. Van Haesendonck and J. I. Cerdá, *Nano Res.*, 2015, **8**, 2223–2230.

[476] P. H. Citrin, P. Eisenberger and R. C. Hewitt, *Surf. Sci.*, 1979, **89**, 28–40.

[477] S. Haq, F. Hanke, J. Sharp, M. Persson, D. B. Amabilino and R. Raval, *ACS Nano*, 2014, **8**, 8856–8870.

[478] M. Lackinger and W. M. Heckl, *J. Phys. D. Appl. Phys.*, 2011, **44**, 464011.

[479] J. Sakamoto, J. Van Heijst, O. Lukin and A. D. Schlüter, *Angew. Chemie - Int. Ed.*, 2009, **48**, 1030–1069.

[480] D. V. Kondratuk, L. M. A. Perdigaõ, A. M. S. Esmail, J. N. O'Shea, P. H. Beton and H. L. Anderson, *Nat. Chem.*, 2015, **7**, 317–322.

[481] S. J. Jethwa, M. Madsen, J. B. Knudsen, L. Lammich, K. V. Gothelf and T. R. Linderoth, *Chem. Commun.*, 2017, **53**, 1168–1171.

[482] P. A. Held, H. Fuchs and A. Studer, *Chem. - A Eur. J.*, 2017, **23**, 5874–5892.

[483] M. Lackinger, *Chem. Commun.*, 2017, **53**, 7872–7885.

[484] R. Gutzler and D. F. Perepichka, *J. Am. Chem. Soc.*, 2013, **135**, 16585–16594.

[485] M. In't Veld, P. Iavicoli, S. Haq, D. B. Amabilino and R. Raval, *Chem. Commun.*, 2008, 1536–1538.

[486] A. Saywell, A. S. Browning, P. Rahe, H. L. Anderson and P. H. Beton, *Chem. Commun.*, 2016, **52**, 10342–10345.

[487] D. Zhong, J. H. Franke, S. K. Podiyanachari, T. Blömker, H. Zhang, G. Kehr, G. Erker, H. Fuchs and L. Chi, *Science*, 2011, **334**, 213–216.

[488] N. A. Zwaneveld, R. Pawlak, M. Abel, D. Catalin, D. Gigmes, D. Bertin and L. Porte, *J. Am. Chem. Soc.*, 2008, **130**, 6678–6679.

[489] H. Y. Gao, P. A. Held, M. Knor, C. Mück-Lichtenfeld, J. Neugebauer, A. Studer and H. Fuchs, *J. Am. Chem. Soc.*, 2014, **136**, 9658–9663.

[490] S. Weigelt, C. Busse, C. Bombis, M. M. Knudsen, K. V. Gothelf, T. Strunskus, C. Wöll, M. Dahlbom, B. Hammer, E. Lœgsgaard, F. Besenbacher and T. R. Linderoth, *Angew. Chemie - Int. Ed.*, 2007, **46**, 9227–9230.

[491] M. Treier, N. V. Richardson and R. Fasel, *J. Am. Chem. Soc.*, 2008, **130**, 14054–14055.

[492] M. Matena, T. Riehm, M. Stöhr, T. A. Jung and L. H. Gade, *Angew. Chemie - Int. Ed.*, 2008, **47**, 2414–2417.

[493] F. Bebensee, C. Bombis, S. R. Vadapoo, J. R. Cramer, F. Besenbacher, K. V. Gothelf and T. R. Linderoth, *J. Am. Chem. Soc.*, 2013, **135**, 2136–2139.

[494] Q. Sun, C. Zhang, Z. Li, H. Kong, Q. Tan, A. Hu and W. Xu, *J. Am. Chem. Soc.*, 2013, **135**, 8448–8451.

[495] F. Ullmann, *Berichte der Dtsch. Chem. Gesellschaft*, 1903, **36**, 2382–2384.

[496] I. Goldberg, *Berichte der Dtsch. Chem. Gesellerschaft*, 1906, **39**, 1691–1692.

[497] J. Lindley, *Tetrahedron*, 1984, **40**, 1433–1456.

[498] J. Hassan, M. Sévignon, C. Gozzi, E. Schulz and M. Lemaire, *Chem. Rev.*, 2002, **102**, 1359–1469.

[499] M. Xi and B. E. Bent, *Surf. Sci.*, 1992, **278**, 19–32.

[500] L. Lafferentz, V. Eberhardt, C. Dri, C. Africh, G. Comelli, F. Esch, S. Hecht and L. Grill, *Nat. Chem.*, 2012, **4**, 215–220.

[501] L. Dong, P. N. Liu and N. Lin, *Acc. Chem. Res.*, 2015, **48**, 2765–2774.

[502] J. A. Lipton-Duffin, O. Ivasenko, D. F. Perepichka and F. Rosei, *Small*, 2009, **5**, 592–597.

[503] M. Kittelmann, P. Rahe, M. Nimmrich, C. M. Hauke, A. Gourdon and A. Kühnle, *ACS Nano*, 2011, **5**, 8420–8425.

[504] T. Dienel, J. Gómez-Díaz, A. P. Seitsonen, R. Widmer, M. Iannuzzi, K. Radican, H. Sachdev, K. Müllen, J. Hutter and O. Gröning, *ACS Nano*, 2014, **8**, 6571–6579.

[505] M. B. Wieland, A. G. Slater, B. Mangham, N. R. Champness and P. H. Beton, *Beilstein J. Nanotechnol.*, 2014, **5**, 394–401.

[506] J. Wen, D. Luo, L. Cheng, K. Zhao and H. Ma, *Macromolecules*, 2016, **49**, 1305–1312.

[507] M. Bieri, M. T. Nguyen, O. Gröning, J. Cai, M. Treier, K. Aït-Mansour, P. Ruffieux, C. A. Pignedoli, D. Passerone, M. Kastler, K. Müllen and R. Fasel, *J. Am. Chem. Soc.*, 2010, **132**, 16669–16676.

[508] R. Gatti, J. M. Macleod, J. A. Lipton-du, A. G. Moiseev, D. F. Perepichka and F. Rosei, *J. Phys. Chem. C*, 2014, **118**, 25505–25516.

[509] S. A. Krasnikov, C. M. Doyle, N. N. Sergeeva, A. B. Preobrajenski, N. A. Vinogradov, Y. N. Sergeeva, A. A. Zakharov, M. O. Senge and A. A. Cafolla, *Nano Res.*, 2011, **4**, 376–384.

[510] C. Doyle, *Ph.D. Thesis*, Dublin City University, 2013.

[511] F. Buchner, K. G. Warnick, T. Wölfle, A. Görling, H. P. Steinrück, W. Hieringer and H. Marbach, *J. Phys. Chem. C*, 2009, **113**, 16450–16457.

[512] J. Mielke, F. Hanke, M. V. Peters, S. Hecht, M. Persson and L. Grill, *J. Am. Chem. Soc.*, 2015, **137**, 1844–1849.

[513] G. Kuang, S. Z. Chen, W. Wang, T. Lin, K. Chen, X. Shang, P. N. Liu and N. Lin, *J. Am. Chem. Soc.*, 2016, **138**, 11140–11143.

[514] M. O. Senge, *Chem. Commun.*, 2006, 243–256.

[515] K. M. Barkigia, L. Chantranupong, J. Fajer and K. M. Smith, *J. Am. Chem. Soc.*, 1988, **110**, 7566–7567.

[516] K. M. Barkigia, J. Fajer, M. W. Renner, M. Dolores Berber, C. J. Medforth and K. M. Smith, *J. Am. Chem. Soc.*, 1990, **112**, 8851–8857.

[517] A. B. Parusel, T. Wondimagegn and A. Ghosh, *J. Am. Chem. Soc.*, 2000, **122**, 6371–6374.

[518] A. K. Wertsching, A. S. Koch and S. G. DiMagno, *J. Am. Chem. Soc.*, 2001, **123**, 3932–3939.

[519] H. Ryeng and A. Ghosh, *J. Am. Chem. Soc.*, 2002, **124**, 8099–8103.

[520] J. Brede, M. Linares, R. Lensen, A. E. Rowan, M. Funk, M. Bröring, G. Hoffmann and R. Wiesendanger, *J. Vac. Sci. Technol. B Microelectron. Nanom. Struct.*, 2009, **27**, 799–804.

[521] J. A. Shelnutt, X.-Z. Song, J.-G. Ma, S.-L. Jia, W. Jentzen and C. J. Medforth, *Chem. Soc. Rev.*, 1998, **27**, 31–42.

[522] M. Feng, J. Zhao and H. Petek, *Science*, 2008, **320**, 359–362.

[523] L. Chen, H. Li and A. T. S. Wee, *Phys. Rev. Lett.*, 2010, **105**, 2–5.

[524] S. Wang, W. Wang, Y. Hong, B. Z. Tang and N. Lin, *Phys. Rev. B*, 2011, **83**, 115431.

[525] T. Miyamachi, M. Gruber, V. Davesne, M. Bowen, S. Boukari, L. Joly, F. Scheurer, G. Rogez, T. K. Yamada, P. Ohresser, E. Beaurepaire and W. Wulfhekel, *Nat. Commun.*, 2012, **3**, 938.

[526] R. Gutzler, H. Walch, G. Eder, S. Kloft, W. M. Heckl and M. Lackinger, *Chem. Commun.*, 2009, 4456–4458.

[527] K. E. Lewis and G. P. Smith, *J. Am. Chem. Soc.*, 1984, **106**, 4650–4651.

[528] K. F. Braun, V. Iancu, N. Pertaya, K. H. Rieder and S. W. Hla, *Phys. Rev. Lett.*, 2006, **96**, 1–4.

[529] L. A. Zotti, G. Teobaldi, W. A. Hofer, W. Auwärter, A. Weber-Bargioni and J. V. Barth, *Surf. Sci.*, 2007, **601**, 2409–2414.

[530] A. C. Papageorgiou, S. Fischer, S. C. Oh, Ö. Sağlam, J. Reichert, A. Wiengarten, K. Seufert, S. Vijayaraghavan, D. Écija, W. Auwärter, F. Allegretti, R. G. Acres, K. C. Prince, K. Diller, F. Klappenberger and J. V. Barth, *ACS Nano*, 2013, **7**, 4520–4526.

[531] A. Rieger, S. Schnidrig, B. Probst, K. H. Ernst and C. Wäckerlin, *J. Phys. Chem. Lett.*, 2017, **8**, 6193–6198.

[532] K. Diller, A. C. Papageorgiou, F. Klappenberger, F. Allegretti, J. V. Barth and W. Auwärter, *Chem. Soc. Rev.*, 2016, **45**, 1629–1656.

[533] F. Buchner, K. Flechtner, Y. Bai, E. Zillner, I. Kellner, H. P. Steinrück, H. Marbach and J. M. Gottfried, *J. Phys. Chem. C*, 2008, **112**, 15458–15465.

[534] G. Di Santo, C. Castellarin-Cudia, M. Fanetti, B. Taleatu, P. Borghetti, L. Sangaletti, L. Floreano, E. Magnano, F. Bondino and A. Goldoni, *J. Phys. Chem. C*, 2011, **115**, 4155–4162.

[535] Y.-Q. Zhang, N. Kepčija, M. Kleinschrodt, K. Diller, S. Fischer, A. C. Papageorgiou, F. Allegretti, J. Björk, S. Klyatskaya, F. Klappenberger, M. Ruben and J. V. Barth, *Nat. Commun.*, 2012, **3**, 1286.

[536] M. D. Rausch, *J. Am. Chem. Soc.*, 1960, **82**, 2080–2081.

[537] M. D. Rausch, *J. Org. Chem.*, 1961, **26**, 1802–1805.

[538] M. D. Rausch, *Inorg. Chem.*, 1962, **1**, 414–417.